TUDelft

Delft University of Technology

Reliability of long heterogeneous slopes in 3d
Model performance and conditional simulation

Li, Yajun

Important note
To cite this publication, please use the final published version (if applicable).
Please check the document version above.

RELIABILITY OF LONG HETEROGENEOUS SLOPES IN 3D

MODEL PERFORMANCE AND CONDITIONAL SIMULATION

RELIABILITY OF LONG HETEROGENEOUS SLOPES IN 3D

MODEL PERFORMANCE AND CONDITIONAL SIMULATION

Proefschrift

ter verkrijging van de graad van doctor
aan de Technische Universiteit Delft,
op gezag van de Rector Magnificus prof. ir. K. C. A. M. Luyben,
voorzitter van het College voor Promoties,
in het openbaar te verdedigen op vrijdag 24 februari 2017 om 10:00 uur

door

Yajun LI (李亚军)

Bachelor of Science in Agricultural Hydraulic Engineering,
Northwest A&F University, Yangling, Shaanxi, China,
geboren te Shanxi, China.

Dit proefschrift is goedgekeurd door de promotor:

Prof. dr. M. A. Hicks

Samenstelling promotiecommissie:

Rector Magnificus,	voorzitter
Prof. dr. M. A. Hicks,	Technische Universiteit Delft, promotor

Onafhankelijke leden:

Prof. dr. G. A. Fenton,	Dalhousie University
Prof. dr. A.-H. Soubra,	Université de Nantes
Prof. dr. K. G. Gavin,	Technische Universiteit Delft
Prof. dr. ir. P. H. A. J. M. van Gelder,	Technische Universiteit Delft
Prof. dr. ir. S. N. Jonkman,	Technische Universiteit Delft

Overige leden:

Dr. P. J. Vardon,	Technische Universiteit Delft

To my parents

CONTENTS

1

INTRODUCTION

1

1.1. Background and Motivation

The variability of soil properties existed long before it was acknowledged and dealt with by humans. Engineers have always been interested in designing the safest structures (built on, surrounded by, or made of soils) economically (i.e. at a reasonable cost). In the process of approaching a more realistic description of soils and thus advancing civil engineering designs, researchers have started to relax one of the primary assumptions used in traditional analysis; that is, that the ground is idealised as layers of material with uniform properties. For example, the series of ICASP conferences (the International Conferences on Applications of Statistics and Probability in Civil Engineering), has been following the use of statistical concepts since 1971, when the first ICASP conference was held in Hong Kong. Moving on to the 21st century, the need for adequate representation of in-situ soil variability has been recognised in recent design codes such as Eurocode 7 (Frank, 2004; Hicks and Nuttall, 2012). As such, reliability assessments in geotechnical projects have been receiving increasing attention from regulatory bodies in recent years, promoting the concept of reliability-based design (Phoon, 2008).

In the field of slope engineering, reliability-based design calculations can be carried out using modern geotechnical design software, such as the Bishop random field module used in Deltares' D-GeoStability software (essentially an extended 2D model based on Calle (1985) that was documented in GeoDelft (1994)). There is also Vanmarcke's (1977b; 2011) simplified 3D model for slope stability calculations. However, there are certain assumptions made in these two currently available models for 3D slope reliability, not least the assumption of a single rigid failure of a cylindrical soil mass. Also, field (e.g. CPT) measurements are not directly used in these calculations. In contrast, 3D random finite element models (Spencer and Hicks, 2007; Spencer, 2007; Hicks et al., 2008; Griffiths et al., 2009b; Hicks and Spencer, 2010; Hicks et al., 2014) are able to seek out the 3D failure surface more naturally, based on the stress–strain response of the soil, without any prior assumptions regarding the failure mechanism attached to the method itself.

To provide a rational reliability analysis of systems such as flood defence dykes or levees, cut slopes and highways, either for designing new structures or for strengthening existing ones, there is a need for a performance assessment of the currently available slope reliability models. This thesis, building on previous 2D and 3D investigations by other researchers (Calle, 1985; Vanmarcke, 1977b; Hicks et al., 2008, 2014), investigates the influence of spatial variability of undrained shear strength on 3D slope stability and compares the relative performance of three methods for computing slope reliability.

1.2. Objectives and Scope

The objectives of this research are:

- To investigate the influence of heterogeneity of undrained shear strength on the stability and failure consequence of slopes that are long in the third, out-of-plane, direction; that is, for slopes in which the length over height ratio is in the range 10-100. In particular, to investigate the influence of heterogeneity on failure volumes and lengths and the probability of failure;

- To investigate extended 2D and simplified 3D stochastic models for simulating

slope reliability. In particular, by comparing with solutions obtained using the random finite element method (RFEM), to assess the applicability of current simpler methods of analysis for dykes; that is, to identify when these simpler models may reasonably be used to assess slope stability and when caution may be needed;

- To demonstrate how the random finite element method may be used to conduct a detailed 3D analysis of a representative section of a slope, and the results then extrapolated to take account of the length effect in much longer slopes (based on Hicks and Spencer (2010));

- To demonstrate how field measurements can be used to reduce uncertainties in structural response, thereby resulting in a cost-effective design and/or site investigation.

In order to achieve the research objectives, a number of related topics have been covered:

- A detailed evaluation of Vanmarcke's (1977b) model for a range of values of the horizontal scale of fluctuation. (Chapter 4)

- The implementation of a version of Calle's (1985) model based on finite elements. (Chapter 5)

- An investigation of the Dutch α factor, which is used in quantifying the spatial variability of soil properties in geotechnical design. (Chapter 5)

- An investigation of the boundary conditions used in 3D finite element analysis. (Chapter 5)

- The quantification of potential failure volumes and lengths in 3D RFEM analyses using a displacement threshold approach. (Chapters 4 and 5)

- The development of a high performance computing (HPC) strategy based on a CouchDB pool server. (Chapter 3 and Appendix A)

- An investigation of the slope length effect and evaluation of a proposed power law equation for predicting the reliability of very long slopes based on 3D RFEM (Hicks and Spencer, 2010). (Chapter 5)

- A detailed comparison of the factor of safety distributions obtained using RFEM and the models of Vanmarcke (1977b) and Calle (1985), for a range of horizontal scales of fluctuation. (Chapter 5)

- The implementation and validation of a 3D conditional simulation strategy based on Kriging for regularly spaced CPTs. (Chapter 6)

- The quantification of uncertainty reduction in structural response in terms of a sampling efficiency index. (Chapter 6)

- An investigation into the influence of sample density on the cost-effectiveness of site investigation. (Chapter 6)

1

1.3. OVERVIEW

The outline of this thesis is as follows:

Chapter 1 introduces the objectives and scope of the thesis.

Chapter 2 gives a literature review, mainly concerning the relevant geotechnical background. Starting with a statistical description of soil variability, the chapter goes on to discuss various stochastic methods, of differing degrees of complexity, for use in geotechnics. The review highlights 3D applications of the random finite element method for slope stability problems, as well as for other geotechnical applications, and related fields. The general review of literature in this chapter is supplemented by more focused reviews that are contained within the later problem-specific chapters.

Chapter 3 briefly explains the methodology used in this thesis. The procedure to carry out an RFEM analysis is outlined first. Some specific aspects related to 3D RFEM, such as how random fields of soil properties are generated, post-processed (i.e. squashed and/or stretched) and mapped onto finite elements, are covered. In order to carry out the investigations in the following chapters in a reasonable time, an HPC computing strategy suitable for Monte Carlo simulations is developed. Specifically, the pilot framework based on a PiCaS module from SurfSARA is introduced.

Chapter 4 compares the relative performances of the RFEM and Vanmarcke models for a slope that is 10 times longer than it is high (in this case, the slope length effect can be neglected). Detailed comparisons for a range of horizontal scales of fluctuation are provided; these include the probability density functions of the factor of safety, the potential failure volumes and lengths, the differences in the means and standard deviations of the factor of safety, and the reliability indices. The reasoning behind the differences are explained and some insights into Vanmarcke's model are provided.

Chapter 5 continues on from Chapter 4 to look at the reliability of much longer slopes, where the length effect should not be neglected. It compares the relative performance of RFEM with respect to both Vanmarcke's and Calle's models, taking account of length effects for slope lengths up to 100 times the slope height. A version of Calle's model is implemented based on finite element analysis and the Dutch α factor used in design is evaluated via random fields. A power law equation is validated for predicting the reliability of longer slopes based on a detailed 3D RFEM analysis of a shorter representative slope section. The performance of this approach is investigated by evaluating its accuracy for a range of slope lengths.

Chapter 6 is dedicated to the implementation and application of conditional simulation in cost-effective designs and site investigations based on 3D Kriging theory, in view of the fact that the simulations in the previous two chapters do not incorporate field measurements directly (i.e. by honoring the spatial distributions). This extends research in the Author's team in the field of uncertainty reduction from 2D to 3D. The development in this chapter is used to investigate the sampling efficiencies at various locations in a clay deposit that is to be excavated to form a slope, so as to provide valuable additional information compared to an unconditional simulation. The required sampling intensity is also investigated to avoid redundant information in site investigations.

Chapter 7 concludes the thesis and gives recommendations for further research.

2

LITERATURE REVIEW

If I have seen further,
it is by standing on the shoulders of giants.

Isaac Newton

Reliability is, after all, engineering in its most practical form.

James R. Schlesinger

2

2.1. INTRODUCTION

Soil properties vary spatially in the ground as a result of the combined action of physical, chemical and/or biological processes that act at different spatial and/or temporal scales, i.e. they fluctuate over various distances. Characterisation and modelling of spatial variability is essential to achieve a better understanding of the relationships between soil properties and geotechnical soil–structure performance. For example, in the Netherlands, it is particularly important to realistically assess the reliability of existing line infrastructures such as dykes and embankments (see Fig. 2.1), as well as the risks posed by their failure. As such structures are characterised by a large length to cross-section ratio, and by the three dimensional (3D) nature of soil heterogeneity, both locally and regionally, the length effect must be considered, e.g. by a full 3D analysis (Hicks and Spencer, 2010; Hicks et al., 2014). The benefits are cost-effective maintenance of existing dykes and new construction of dykes with lower risk.

Real dyke failures often involve a long term behaviour under complex environmental conditions, as in the levee failure shown in Fig. 2.2. However, cut clay slopes can sometimes fail shortly after excavation. In this case, an undrained total stress analysis can be carried out to investigate the short term behaviour. Fig. 2.3 shows an example of a cut clay slope failure, in a slope which was part of a large project involving the creation of a new 8.7 km rail bed alignment at acceptable grades through the relatively mountainous terrain of southwestern Pennsylvania (Kutschke, 2011). The failures shown in Figs. 2.2 and 2.3 are both localised 3D failures (most likely influenced by soil property spatial variations) despite the apparent plane strain conditions.

This chapter provides a literature review related to the subject of this thesis and, in particular, concentrates on the use of 3D methods of analysis in geotechnics (Sections 2.5 and 2.6). First, some evidence is given for the point and spatial characteristics of soil parameter variability (Section 2.2); in particular relating to undrained shear strength, which is the property considered in the current investigation. Secondly, some probabilistic methods used in geotechnical engineering are summarised (Section 2.3). Thirdly, the discretisation approaches for random fields are reviewed (Section 2.4), which are followed by an introduction to the random finite element method (Section 2.5). Finally, currently available approaches to 3D slope reliability analysis are reviewed (Section 2.6).

2.2. PROBABILISTIC CHARACTERISATION OF SOIL VARIABILITY

Geotechnical soil variability results mainly from three sources: inherent variability, measurement error and transformation uncertainty (Phoon and Kulhawy, 1999a,b). Soil inherent properties fluctuate over various distances in space due to complex mineralogical and geological reasons. Measurement errors are caused by equipment, operator and random testing errors including statistical uncertainty due to limited samples. Transformation uncertainty is introduced when transforming field or laboratory measurements into design soil properties using empirical equations. The role of the probabilistic characterisation of soil variability is two-fold (Vanmarcke, 1978): (a) it provides a format for quantifying engineering information (gathered during site investigation, sampling and testing) about the subsurface conditions at a site; and (b) it provides the basis for quan-

Figure 2.1: A long river levee (source: Rijkswaterstaat), from Schweckendiek (2014)

Figure 2.2: A levee failure in Ascension Parish, Louisiana, from Rogers (2016)
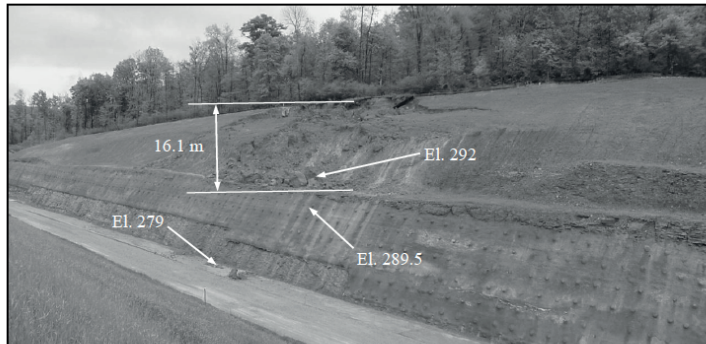
(a) Overview of slope.

(b) View of 7.6 meter tall main scarp.

Figure 2.3: An example of a cut clay slope failure, based on Kutschke (2011)

tifying the variability and reliability of geotechnical performance predictions.

Classical statistical characteristics of soil properties, in the case of describing the soil properties as single variables, include the parameters defining the probability distribution, such as the mean value (μ), standard deviation (σ) or variance (σ^2), and coefficient of variation (COV) ($V = \sigma/\mu$). In the case of spatial variability, an additional parameter, the scale of fluctuation (SOF) (Vanmarcke, 1978), which measures the distance over which soil property values show relatively strong correlation from point to point in space (see, e.g., Figs. 5.8 and 5.9 for the effect of varying SOF), should be introduced.

Phoon and Kulhawy (1999a) provided a good summery of the COVs of inherent variability, scale of fluctuation and measurement error for different soil types and field tests. In their companion paper (Phoon and Kulhawy, 1999b), they used a second-moment probabilistic approach to evaluate the variability of design soil properties, combining all available uncertainties consistently, based on the type of transformation model used.

2.2.1. POINT STATISTICS OF UNDRAINED SHEAR STRENGTH

The undrained shear strength (s_u) can be obtained by direct laboratory testing (e.g. unconfined compression (UC) test, unconsolidated undrained (UU) triaxial compression test, and consolidated isotropic undrained triaxial compression (CIUC) test), by direct use of the in-situ vane shear test (VST), or by correlation with corrected cone tip resistance, with standard penetration test (SPT) blow count N value, with dilatometer test (DMT) horizontal stress index or with plasticity index (Phoon and Kulhawy, 1999b). According to Phoon and Kulhawy (1999a), the COV of inherent variability of undrained shear strength of London Clays is in the range 0.1-0.3 for UU, and 0.2-0.4 for CIUC, indicating the importance of mentioning the test type when reporting the COVs. The COV of s_u from VST is in the range 0.1-0.4. In their companion paper (Phoon and Kulhawy, 1999b), they reported the total COV (including the COV of inherent variability, the COV of measurement error and the COV of transformation uncertainty) of undrained shear strength of clay to be in the range 0.1-0.6 for different types of tests (laboratory and insitu). A likely range for COV (of s_u) of 0.1-0.5 was suggested by Lee et al. (1983). Among other examples: Lumb (1966) published COVs of 0.18 and 0.16 for marine and London clays, respectively, based on in-situ testing; Soulie et al. (1990) reported 0.21 and 0.23 for two marine clays; Asaoka and Grivas (1982) reported values of 0.18 to 0.30 for New York City clay; Vanmarcke (1977b) found a value of 0.32 for varved clay; Hicks and Samy (2002) inferred a value of around 0.2 from the data of Chiasson et al. (1995).

Also, based on the results of two sampling groups (i.e. hydraulically-jacked specimens and open-drive specimens) for an extensive laboratory investigation of London clay, Hooper and Butler (1966) reported COV values ranging from 0.11 to 0.33. However, although similar trends in the mean s_u were found in both groups, the average COVs differed (0.14 and 0.28, respectively). It therefore seems probable that higher values of COV may sometimes result from a different sampling technique, rather than from actual (inherent) material variability (Hicks and Samy, 2002).

Low et al. (2010) reported the results of an international collaborative project, in which a worldwide high-quality database of lightly over-consolidated clays was assembled, and used to evaluate resistance factors for the estimation of intact and re-moulded undrained shear strength from the penetration resistance of piezocone, T-bar and ball

Table 2.1: Different measures of spatial correlation (based on Elkateb et al. (2003); Elkateb (2003))

Type of correlation	Model equation	Autocorrelation distance (r)	Scale of fluctuation (θ)	Spatial range (a)
Exponential	$\rho(\tau) = exp(-\frac{\tau}{r})$	r	$\theta = 2r$	$a = 3r$
Gaussian	$\rho(\tau) = exp(-(\frac{\tau}{r})^2)$	r	$\theta = \sqrt{\pi}r$	$a = \sqrt{\pi}r$
Spherical	$\rho(\tau) = 1 - 1.5\frac{\tau}{r} + 0.5(\frac{\tau}{r})^3$	r	$\theta = 0.55r$	$a = r$

penetration tests. A COV range of 0.02-0.34 for the resistance factors was found from all the sites.

Ching and Phoon (2013b) reported a range of COVs for s_u/σ'_v (in which σ'_v is the effective vertical stress) of 0.316–0.611 from various test procedures based on a large clay database, highlighting that s_u values of a clay evaluated by different test procedures are different due to the tests possibly involving different stress states, stress histories, degrees of sampling disturbance, and strain rates.

Lundberg and Li (2015) reported a COV of 0.32 for the undrained shear strength of a soft Scandinavian clay based on CPT and VST tests.

Note that, if a mean s_u increasing with depth is present in a deposit, as is often the case, then COV should be computed based on residuals by removing the depth trend; otherwise, it may be overestimated (Hicks and Samy, 2002).

2.2.2. Published values of the scale of fluctuation

There are some commonly used correlation functions to model the spatial correlation structure of soil variability. Different researchers use different measures. In particular, the correlation nature can be expressed in terms of the autocorrelation distance (e.g. DeGroot and Baecher, 1993), the scale of fluctuation (SOF) (e.g. Vanmarcke, 1977a), or the spatial range in geostatistics (e.g. Pyrcz and Deutsch, 2014). These three commonly used correlation models are listed in Table 2.1, together with the relationships between the three measures of spatial correlation. Geotechnical engineers tend to use the first two measures, i.e. the scale of fluctuation (θ) and the autocorrelation distance (r).

Some commonly used techniques to estimate θ are as follows:

- Conduct a regression analysis (e.g. ordinary least squares) to fit an assumed theoretical correlation function to the sample correlation function (e.g. Jaksa et al., 1999; Phoon et al., 2003; Uzielli et al., 2005; O'Connor and Kenshel, 2012; Firouzianbandpey et al., 2014; Lloret-Cabot et al., 2014; Lundberg and Li, 2015);

- Use the variance function approach suggested by Vanmarcke (1977a) (e.g. Wickremesinghe and Campanella, 1993; Wong, 2004; Hicks and Onisiphorou, 2005; Kenarsari et al., 2013);

- Use maximum likelihood estimation to estimate unknown parameters (mean, variance and SOF), assuming a joint distribution of the soil property with the corresponding correlation function model (e.g. DeGroot and Baecher, 1993; Fenton, 1999a; O'Connor and Kenshel, 2012);

Table 2.2: Summary of scales of fluctuation for soil parameters (based on El-Ramly et al. (2003); Kim (2005); Li et al. (2015a); Hicks and Samy (2002))

Property [a]	Soil type	Scale of fluctuation		References
		θ_v (m)	θ_h (m)	
CI	Sand	–	55	Vanmarcke (1977a)
c,ϕ	Clay	0.1-5	2-30	Hsu and Nelson (2006)
c,ϕ	Clay	0.5-3	10-40	Suchomel et al. (2010)
N(SPT)[b]	Sandy soil	2.4	–	Vanmarcke (1977a)
N(SPT)	Akita sandy soil	1.8	–	Popescu et al. (1995)
N(SPT)	Alluvial	–	34	DeGroot (1996)
P_o(SPT)	Varved clay	2.0	–	DeGroot (1996)
q_c(CPT)	Clay	~1.2	–	Tantalla et al. (2001)
q_c(CPT)	–	~1.2–1.3	–	Vanmarcke (1977a)
q_c(CPT)	Silty clay	2.0	10-24	Lacasse and de Lamballerie (1995)
q_c(CPT)	Clean sand North sea soil	3.2	–	Kulatilake and Ghosh (1988)
q_c(CPT)	Sensitive clay	4.0	–	Chiasson et al. (1995)
q_c(CPT)	Laminated clay	–	19.2	Lacasse and Nadim (1997)
q_c(CPT)	Dense sand	–	75	Lacasse and Nadim (1997)
q_c(CPT)	North sea soil	–	28-76	Keaveny et al. (1989)
q_c(CPT)	North sea clay	–	60	Tang (1979)
q_c(CPT)	Taranto clay	0.29-0.40	–	Cafaro and Cherubini (2002)
q_c(CPT)	Clay, sand	0.13-1.11	–	Uzielli et al. (2005)
q_c(CPT)	Silty clay	0.8-6.1	–	Haldar and Babu (2009)
q_c(CPT)	Clay	1.3-4	10-62	Salgado and Kim (2013)
q_c(CPT)	Sand	2.2-3	35-75	Salgado and Kim (2013)
q_c(CPT)	Sand	0.3	–	Wickremesinghe and Campanella (1993)
q_c(CPT)	Tarsiut core sand	1.9	24.2	Popescu et al. (1997)
S_p(CPT)	Sand	0.3-0.7	3.5-15	Wong (2004); Hicks and Onisiphorou (2005)
s_u(VST)	Sensitive clay	2	–	Baecher (1983)
s_u(VST)	Soft marine clay	–	46	DeGroot and Baecher (1993)
s_u(VST)	Very soft clay	2.2	44.2	Bergado et al. (1994)
s_u(VST)	Sensitive clay	4.0	–	Chiasson et al. (1995)
s_u(VST)	Sensitive clay	2.0	20	Soulie et al. (1990)
s_u(VST)	Saturated soft clay	2.4-6.2	–	Asaoka and Grivas (1982)
s_u(VST)	Soft to medium clay	–	42.8-49	Bergado et al. (1994)
s_u(VST)	Clay	2-6.2	46-60	Phoon and Kulhawy (1999a); Ching and Phoon (2013a)
s_u(UU)	Offshore soil	7.2	–	Keaveny et al. (1989)
s_u(DST)	Offshore soil	2.8	–	Keaveny et al. (1989)
s_u(UC)	Soft clay	4.0	80	Honjo and Kuroda (1991)
s_u(UC)	Chicago clay	0.8	–	Wu (1974)
s_u	Marine clay, Japan	1.3-2.7	–	Matsuo (1976)
s_u	Ontario varved clay	–	46	Vanmarcke (1977b)
s_u(DST)	Clay	1.1-1.23	92.4	Ronold (1990)
s_u,c,ϕ	In-situ soils	1-6	30-60	Ji et al. (2012)

[a] Measurement: q_c –CPT tip resistance; s_u –Undrained shear strength; P_o –DMT lift-off pressure; N –Blow count per foot; S_p –State parameter; CI –Compressibility index.

[b] Type of test: VST –Field vane shear test; UC –Unconfined compression test; UU –Unconsolidated undrained triaxial test; DST –Direct shear test; CPT –Cone penetration test; DMT –Dilatometer test; SPT –Standard penetration test.

- Use Bartlett's limit (e.g. Jaksa et al., 1999; Jamshidi Chenari and Oloomi Dodaran, 2010; Kenarsari et al., 2013).

Due to the general lack of measurement intensity when carrying out routine site investigations in geotechnical engineering, spatial correlation data are scarce; however, it has been improving in recent years, as more people start to recognize the importance of risk analysis in the decision making process. Some published values for the spatial correlation of soil properties are listed in Table 2.2, in terms of scale of fluctuation for the exponential correlation function (i.e. 2 times the originally published data for those cases in which autocorrelation distances were reported, as in El-Ramly et al. (2003) and many other publications; therefore, the magnitudes of θ will be smaller for the Gaussian correlation model than those shown in the table). Note that it is not uncommon for researchers to misuse the terms 'scale of fluctuation' and 'autocorrelation distance', which could lead to erroneous estimates of the correlation distance by a factor of 2 or 1.77 ($\approx \sqrt{\pi}$). For the common exponential and Gaussian correlation functions, the scale of fluctuation is equal to 2 and 1.77 times the autocorrelation distance, respectively. The typical range of scale of fluctuation is between 1 m to 6 m in the vertical direction and 10-80 m in the horizontal direction, although the vertical SOF could be as small as 0.1 m and the horizontal SOF as small as 2.0 m (Jaksa et al., 1999) (see Table 2.2).

It is noted that data for correlations in the horizontal plane are even more rare than for the vertical direction. This is mainly due to the fact that fewer samples are usually obtained in the horizontal plane in routine geotechnical site investigation (e.g. in the case of CPT measurements, there will be relatively few CPTs in the lateral plane). Also, it is not common practice to carry out tests horizontally (see Chapter 3 in Broere (2001)), as was done by Jaksa et al. (1999) who performed a horizontal CPT into the face of a slope; in that case, the amount of data points in the horizontal direction allowed an estimate of the horizontal scale of fluctuation. However, a much higher degree of correlation is generally assumed in the horizontal plane than in the vertical direction, this being supported by the process of deposition and available evidence. For example, the scales of fluctuation in the horizontal direction were found to be, on average, 12 times greater than in the vertical direction in Popescu et al. (1995) and Popescu et al. (1997), by comparing closely-spaced CPT profiles taken from a hydraulic sandfill. Some values for the degree of anisotropy of the heterogeneity of sands are: 11 in Lloret-Cabot et al. (2012), a range of 4–40 in Lloret-Cabot et al. (2014), and 2.4–7 in Firouzianbandpey et al. (2014). Similar values for the degree of anisotropy of the heterogeneity of clays have been reported: e.g. 10 in Soulie et al. (1990), and 13 in Phoon and Kulhawy (1999a).

Soil properties are often depth dependent, and hence field test measurements (e.g. cone tip resistance from CPT) often exhibit a depth trend. In the case of significant trends in soil measurement data, these need to be removed before estimating the scale of fluctuation to ensure stationarity (Wickremesinghe and Campanella, 1993; Jaksa et al., 1999). Non-removal of mean trends can lead to overestimation of the scale of fluctuation.

Although many researchers have assumed that soil variability exhibits a finite scale of fluctuation, which can be described by a single value of SOF, Fenton (1999b) suggested that the nature of variability in soil parameters is best represented using a fractal stochastic model corresponding to so-called Brownian motion. Based on a large database of

CPT samples, a long memory was found in the vertical direction, due to the maximum likelihood estimates of SOF being dependent on the size of sampling domain. A fractal model in the horizontal direction was also supported by Jaksa and Fenton (2002), who based their findings on 50 CPTs carried out adjacent to one another along a line, at horizontal spacings of 0.5 m. In their investigation, several hundred horizontal data sets were established by placing the tip resistance (q_c) data into a matrix, with each column representing one of the 50 CPTs, and each row being a 5 mm increment of depth. Consequently, each row yielded a 24.5 m long horizontal data set, 5 mm in thickness.

2.3. PROBABILISTIC ANALYSIS METHODS

There are various methods to conduct probabilistic analysis. These can be categorized into three groups:

- Single variable approach

  In this approach, the problem domain is assumed to have the same soil property value throughout, sampled randomly from the assumed distribution function. This implies an infinite spatial correlation length, so that no spatial averaging is applicable, e.g. Duncan (2000); Nguyen and Chowdhury (1984), and results in an overestimation of the probability of failure, implying that a cost-effective design often cannot be reached. Examples highlighting this include El-Ramly et al. (2002); Griffiths and Fenton (2004), among others.

  Note that, although the concept of spatial averaging is not included in this approach, the effect can be accounted for by applying a reduction coefficient to the variance of the input variables. The problem is then to determine the appropriate reduction factors for the range of potential failure surfaces. For example, Christian et al. (1994) found this factor by integrating the statistically varying shear strength over the failure surface for the James Bay dyke, while El-Ramly (2002) conducted a so-called MC−Christian (MC stands for Monte Carlo) analysis for the same dyke by imposing the same reduction factor (as used by Christian et al. (1994)) on the input variance.

- Multiple variable approach

  In contrast to the above approach, this one introduces more variables; each variable occupies a block of the domain, with block sizes being approximately of the order of the SOF. The approach takes account of spatial variability in its simplest form; that is, through a 1D consideration by incorporating the autocorrelation function into the model, either along the critical failure surface (El-Ramly et al., 2002) or solely along the vertical or horizontal directions (Wang et al., 2010).

  A moderate number of variables is used to simulate the random field and often these approaches facilitate a practical spreadsheet-based reliability tool by either approximate methods or Monte Carlo simulation. However, the sacrifice is that the anisotropic structure of the variability, which is always present whether the

ground is natural or manmade, cannot be captured accurately, and this approach may therefore not be applicable for some practical applications. In addition, a potential drawback lies in the determination of an equivalent scale of fluctuation (El-Ramly et al., 2006).

- Many variable approach

  This approach takes full account of the spatial variability, either by 2D or 3D random fields. Hundreds of variables are introduced into much smaller blocks within the problem domain, taking account of both the horizontal and vertical SOFs; thus 2D or 3D random fields can be generated according to isotropic or anisotropic correlation structures, by incorporating various autocorrelation functions. Its application to various practical engineering problems can be found in Fenton et al. (2003), Griffiths et al. (2009a), Hicks and Samy (2002) and Hicks and Onisiphorou (2005) for 2D, and in Griffiths et al. (2009b), Hicks and Spencer (2010), Hicks et al. (2008) and Spencer and Hicks (2007) for 3D.

An overview of the stochastic methods used for analysing slope stability problems is shown in Fig. 2.4. Generally, slope reliability can be assessed by direct methods without needing to know the performance function explicitly, or by using some meta-model, surrogate model or response surface model to explicitly approximate the performance function. Some commonly used methods, namely the first order reliability method (FORM), first order second moment method (FOSM), Monte Carlo Simulation (MCS) and the response surface method, are introduced in the following sections.

2.3.1. FORM

The matrix formulation (Ditlevsen, 1981) of the Hasofer and Lind (1974) or FORM index is

$$\beta = \min_{x \in F} \sqrt{(\mathbf{x} - \boldsymbol{\mu})^T \mathbf{C}^{-1} (\mathbf{x} - \boldsymbol{\mu})} \tag{2.1}$$

or equivalently,

$$\beta = \min_{x \in F} \sqrt{(\mathbf{x}^N)^T \mathbf{R}^{-1} (\mathbf{x}^N)} \tag{2.2}$$

where

$$x_i^N = \frac{x_i - \mu_i}{\sigma_i} \tag{2.3}$$

and $\mathbf{x}$ is a vector representing the set of random variables x_i, $\boldsymbol{\mu}$ is a vector of mean values μ_i, $\mathbf{C}$ is the covariance matrix, $\mathbf{R}$ is the correlation matrix, σ_i is the standard deviation, and x_i^N is a component of $\mathbf{x}^N$ (i.e. the standardised $\mathbf{x}$). F is the failure domain, which is separated from the safe domain by the limit state surface/function (see Fig. 2.5), defined as

$$G(\mathbf{x}) = G(x_1, x_2, \ldots, x_n) = 0 \tag{2.4}$$

In this equation, $G(\mathbf{x}) = 0$ represents the limit state and failure occurs for $G(\mathbf{x}) \leq 0$; for $G(\mathbf{x}) > 0$, the system is safe.

2
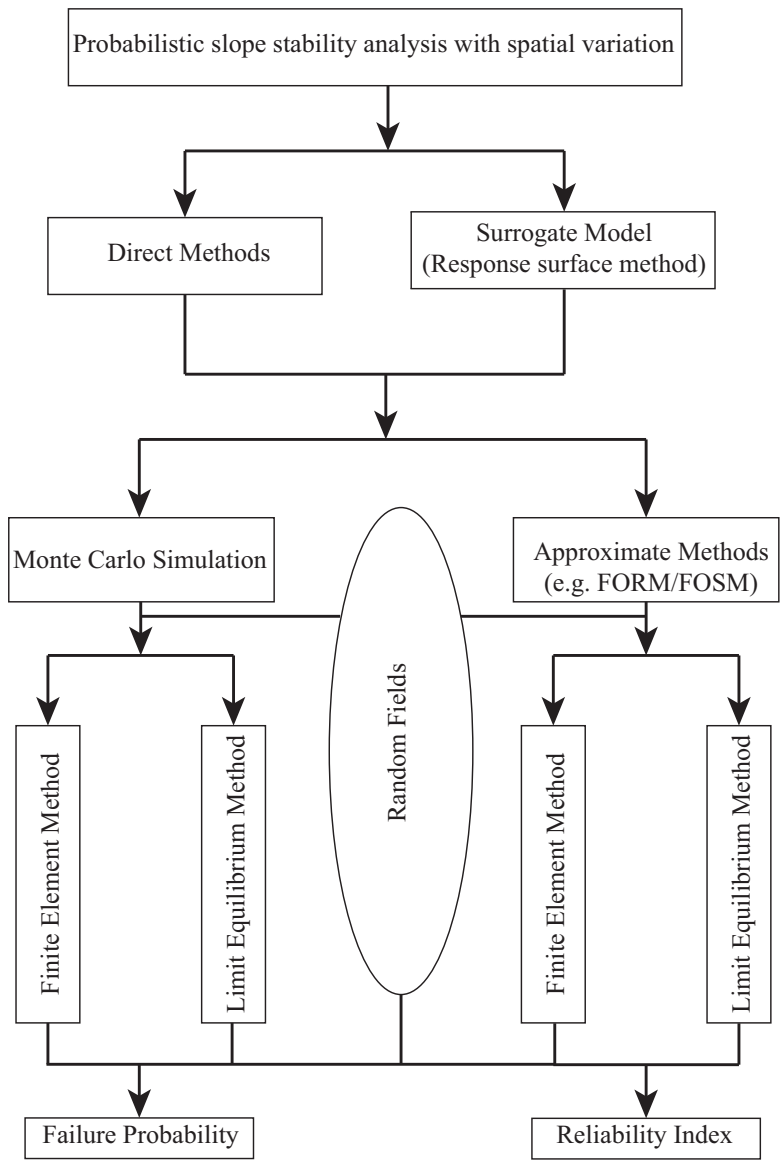
Figure 2.4: An overview of probabilistic slope stability methods considering spatial variability

2
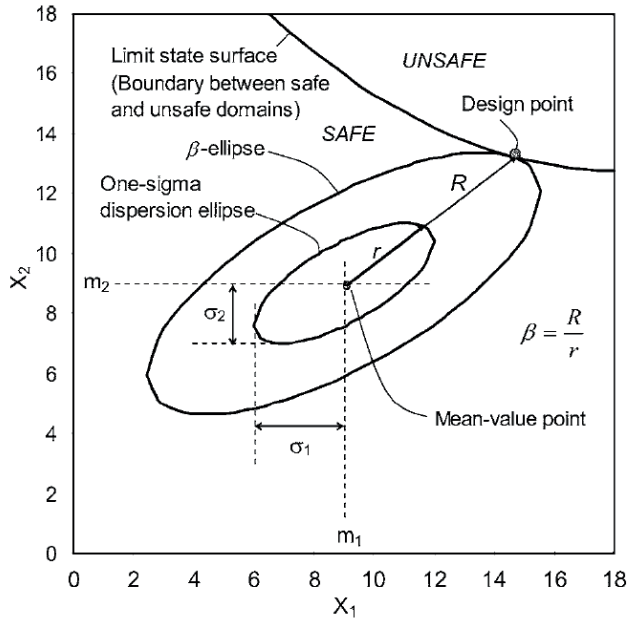
Figure 2.5: Schematic view of the FORM reliability index, based on Xu and Low (2006)

A widely used procedure for computing β (i.e. the reliability index) is to transform the limit state surface into the space of reduced variates (x_i^N), whereby the shortest distance from the transformed limit state surface to the origin of the reduced variates is the reliability index. The computation procedure is explained in Ang and Tang (1984).

Low and Tang (1997a) provided an alternative, more intuitive interpretation in the original space; that is, the point denoted by the value x_i which minimises the square root in the above equation (Eq. 2.1 or 2.2) and satisfies F is the design point; that is, the point of tangency of an expanding dispersion ellipsoid with the limit state surface separating safe combinations of random values from unsafe combinations. The reliability index β is the axis ratio R/r (Fig. 2.5) of the ellipse that touches the limit state surface (i.e. the $\beta\sigma$ ellipse) and the 1 standard deviation dispersion ellipse (i.e. the σ ellipse). The method deals with correlations without orthogonal transformation (e.g. eigen-decomposition or singular value decomposition) of the covariance matrix. The advantage of Low and Tang's (1997a) spreadsheet method is that iterative searching is performed automatically by invoking a spreadsheet's optimisation tool; hence partial derivatives are not part of the input, which is attractive for cases with complicated or implicit performance functions. This methodology was combined with a limit equilibrium method and demonstrated in Low and Tang (1997b) for a reinforced embankment on soft ground.

As a simple illustration of the use of FORM, Fig. 2.6 shows the contours (1, 2, 3, 4, 5 and 6σ ellipses and the $\beta\sigma = 2.4\sigma$ ellipse) of the probability density function of the binormal distribution of two correlated variables, for an explicit performance function.

Low and Tang (2004) presented a cell-object-oriented constrained optimization approach based on the expanding ellipsoid concept and equivalent normal transformation (e.g. Rosenblatt (1952) transformation and Rackwitz and Flessler (1978) transformation), for a reliability analysis involving correlated non-normals, and gave a detailed comparison between this approach and the Hasofer–Lind method for uncorrelated and correlated normal variates and the first order reliability method (FORM) for correlated non-normals. Low and Tang (2007) then improved the efficiency of their methodology by obviating the need for computations of equivalent normal means and equivalent normal standard deviations, and by changing (automatically) the dimensionless equivalent standard normal vector.

Although FORM has the advantage of being easily embedded in an easy-to-use spreadsheet, which makes it available to most engineers, Griffiths et al. (2009a) found that it may lead to unconservative estimates of the failure probability if the coefficient of variation of the shear strength parameters exceeds a critical value, due to the spatial variability not being modelled within their FORM implementation (i.e. no spatial variability involved), for example, compared to the random finite element method (RFEM, see Section 2.5). Note that, in their paper, no comparisons were made between RFEM and FORM involving spatial variability in the vertical or horizontal directions as in Low et al. (2007) and Low (2014). However, even if FORM with spatial variability is used to model slope reliability, it would still suffer from the constraint that the number of random variables (e.g. used in the built-in optimisation tool in a spreadsheet) should not be too large, in order to avoid a 'fake' local minimum being mistaken as the global minimum (Wang et al., 2010). Moreover, it can only model the spatial variability partially, along one direction (i.e. only vertical or horizontal spatial variation, or spatial variation along the failure surface), in contrast to RFEM which is capable of fully modelling the spatial variability in all directions.

2.3.2. FOSM

The FOSM method is an approximate approach based on a first order Taylor series expansion of the performance function (or limit state function, see Section 2.3.1) around its mean value. In the case of slope stability, the performance function can be assessed, for example, by Bishop's method of slices or the finite element method.

The reliability index for the first order second moment method (Hassan and Wolff, 1999) is

$$\beta = \frac{\mathrm{E}[FS] - 1}{\sigma[FS]} \tag{2.5}$$

in which the mean (E[.]) and standard deviation (σ[.]) of the factor of safety (FS) (which is a function of the random variables X_i) are

$$\mathrm{E}[FS] = FS(\mu_{X_i}) \tag{2.6}$$

$$\mu_{X_i} = \mathrm{E}[X_i] \tag{2.7}$$
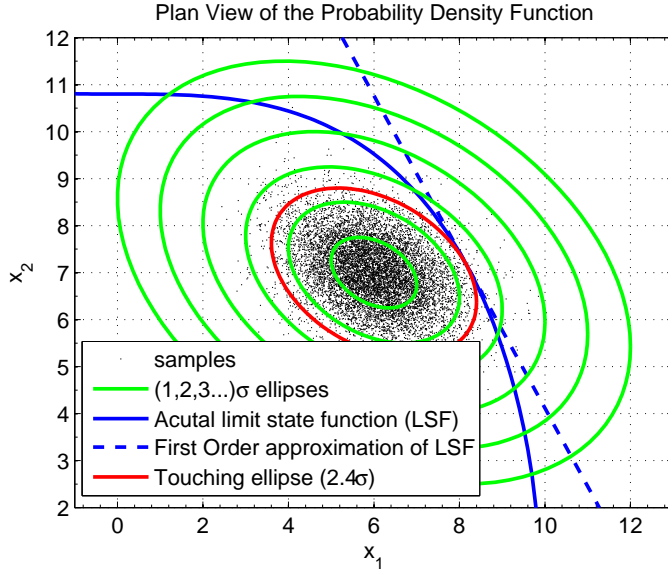
Figure 2.6: An example showing FORM for two normally distributed variables x_1 and x_2, correlated by ρ, with the explicit limit state function $g(x_1, x_2) = -0.03x_1^3 - 0.25x_2^2 + 29.16$ ($\mu_{x_1} = 6.0, \sigma_{x_1} = 1.0, \mu_{x_2} = 7.0, \sigma_{x_2} = 0.75, \rho_{x_1,x_2} = -0.35$), based on Griffiths et al. (2007)

and

$$\sigma[FS] = \sqrt{\sum_{i=1}^{n}\left(\frac{\partial FS}{\partial X_i}\right)^2 \sigma^2[X_i] + 2\sum_{\substack{i,j=1 \\ i<j,or,i>j}}^{n}\left(\frac{\partial FS}{\partial X_i}\right)\left(\frac{\partial FS}{\partial X_j}\right)\rho_{ij}\sigma[X_i]\sigma[X_j]}$$

$$= \sqrt{\sum_{i=1}^{n}\left(\frac{\partial FS}{\partial X_i}\right)^2 \sigma^2[X_i] + \sum_{\substack{i,j=1 \\ j\neq i}}^{n}\left(\frac{\partial FS}{\partial X_i}\right)\left(\frac{\partial FS}{\partial X_j}\right)\rho_{ij}\sigma[X_i]\sigma[X_j]} \tag{2.8}$$

$$= \sqrt{\sum_{i,j=1}^{n}\left(\frac{\partial FS}{\partial X_i}\right)\left(\frac{\partial FS}{\partial X_j}\right)\rho_{ij}\sigma[X_i]\sigma[X_j]} = \sqrt{\nabla_g^{\mathrm{T}}\mathbf{C}\nabla_g}$$

with

$$\nabla_g = \left(\frac{\partial FS}{\partial X_1}, \frac{\partial FS}{\partial X_2}, \ldots, \frac{\partial FS}{\partial X_n}\right)^{\mathrm{T}} \tag{2.9}$$

$$C_{ij} = \sigma^2 \rho_{ij} \tag{2.10}$$

The partial derivatives can be evaluated by

$$\frac{\partial FS}{\partial X_i} = \frac{FS_i^+ - FS_i^-}{2m\sigma[X_i]} \tag{2.11}$$

where

$$FS_i^+ = FS(\mu_{X_i} + m\sigma[X_i], \mu_{X_j}(j = 1, \ldots, n, j \neq i)) \qquad (2.12)$$

$$FS_i^- = FS(\mu_{X_i} - m\sigma[X_i], \mu_{X_j}(j = 1, \ldots, n, j \neq i)) \qquad (2.13)$$

where, for example, $m = 1$ was used in El-Ramly et al. (2002).

Note that, using FOSM, the reliability index fails to be constant under different but mechanically equivalent formulations of the same performance function. Such an invariant problem can be prevented if the first-order approximations are evaluated at a point on the failure surface, e.g. as is the case with FORM.

2.3.3. MONTE CARLO SIMULATION

In this approach, a large number of sets of randomly generated values for the uncertain parameters is created and the performance function for each set is computed. The statistics of the resulting set of values of the function can be computed and the probability of failure p_f calculated directly. The method has the advantage of conceptual simplicity, but it can require a large number of values of the performance function to obtain adequate accuracy. Furthermore, the method does not give insight into the relative contributions of the uncertain parameters that may be obtained from other methods (e.g. FORM). The computational effort can be reduced significantly by using variance reduction (which is something of a misnomer, and not the same thing as the 'variance reduction' in local averages) statistical techniques, such as importance sampling (Baecher and Christian, 2005; Ching et al., 2009) and subset simulation (Ahmed and Soubra, 2012; Phoon, 2008), and these should be employed whenever possible.

To give an example, consider the problem of determining the probability of failure of a system which has two random inputs, X_1 and X_2 (Fenton and Griffiths, 2008). The response of the system to these inputs is some function $g(X_1, X_2)$, which is also random because the inputs are random. For example, X_1 could be soil cohesion c, X_2 could be soil friction angle ϕ, and $g(X_1, X_2)$ could be the factor of safety of a slope (in this example, it is assumed that there are 2 random soil properties, although in RFEM (Section 2.5) it is more likely that g is a function of a large number of random variables). Now, assume that system failure will occur whenever $g(X_1, X_2) > g_c$. In the space of (X_1, X_2) values, there will be some region in which $g(X_1, X_2) > g_c$, as illustrated in Fig. 2.7, and the problem is then to assess the probability that the particular (X_1, X_2) which actually occurs will fall into the failure region. Mathematically, the goal is to try to determine the probability p_f, where

$$p_f = P[g(X_1, X_2) > g_c] \qquad (2.14)$$

Suppose, for example, that X_1 and X_2 follow a bivariate lognormal distribution with the mean response well within the safe region and a correlation coefficient between X_1 and X_2 of $\rho = 0.6$ (a negative correlation implies that, as X_1 increases, X_2 tends to decrease); this example is shown in Fig. 2.7.

The above is a simple example for two correlated random variables. However, the concept is exactly the same for RFEM (see Section 2.5), except that the number of correlated random variables is then scaled to hundreds or thousands. In fact, if X_1 represents c_1 and X_2 represents c_2 (where c_1 and c_2 are the autocorrelated cohesion), the above example can be considered as the case for a two-variable random field (where each point in
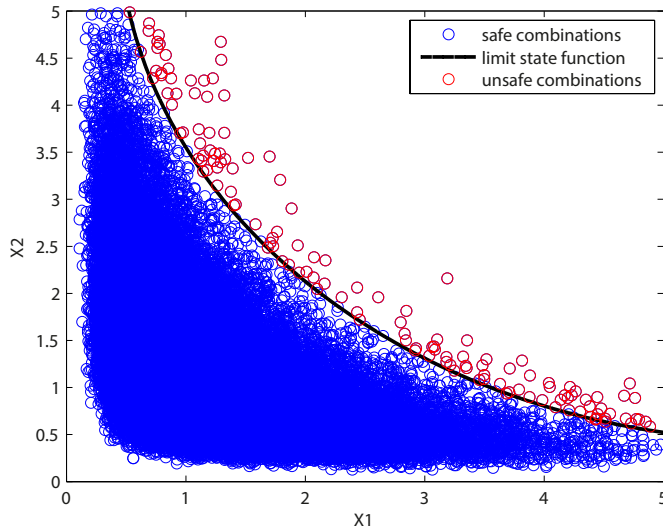
Figure 2.7: Monte Carlo simulation of two correlated lognormal variables with ρ=-0.6, after Fenton and Griffiths (2008)

Fig. 2.7 can be considered as an independent random field with two random variables). The Monte Carlo framework is central to the RFEM process outlined in Section 2.5.

2.3.4. RESPONSE SURFACE METHOD

The response surface method (RSM) is a statistical technique proposed by Box and Wilson (1951) to determine the optimum conditions in chemical investigations at which some response is a maximum or minimum. The main idea of RSM is to approximate the unknown implicit performance/response function (with regards to the input variables) by conducting a sequence of designed experiments. It is therefore a surrogate model that mimics the behavior of some simulation model. To explicitly constructs the relationship between the response and the input variables, a simple nth order polynomial (Wong, 1985; Xu and Low, 2006) may be used. In the case of a slope reliability problem involving k random variables, it is sufficient to take a second-order polynomial approximation function (Low et al., 1998),

$$G'(\mathbf{x}) = l + \sum_{i=1}^{k} m_i x_i + \sum_{i=1}^{k} n_i x_i^2 \qquad (2.15)$$

where $\mathbf{x}$ is the random variable vector with components $x_i (i = 1, 2, \ldots, k)$, $G'(\mathbf{x})$ is the approximate performance function and l, m_i and n_i are the coefficients that need to be determined by experiments.

First, the values at sampling points for each variable are selected (i.e. by choosing $x_i = \mu_{x_i} \pm m\sigma_{x_i}$ and $x_j = \mu_{x_j}$ for $j \neq i$, where the value of m is usually selected to be 1.0);

then the sampling function values (i.e. values of the function at the sampling points) can be determined by carrying out a number of traditional slope stability analyses (i.e. limit equilibrium analysis, limit analysis or finite element analysis). It then involves fitting a second order polynomial to the sampling function values (at least $2k+1$ model evaluations are needed in order to solve for the unknown coefficients). Note that interaction terms (i.e. $x_i x_j$, $i \neq j$) may be included to form a complete second-order polynomial function, which could possibly lead to a better approximation of the performance function. However, the inclusion of these terms also means an increasing number of model evaluations. For the results of example reliability analyses in Xu and Low (2006), the effect of interaction terms on the reliability index was shown to be negligible; therefore, the interaction terms may be omitted in some cases.

Provided that the model under consideration is sufficiently smooth, quadratic polynomials (Eq. 2.15) may be sufficiently accurate approximations. This is especially true for studying the model response not too far from its mean value, i.e. for a central trend analysis. Nonetheless, one should be careful when the estimation of the probability of exceeding a threshold is of interest, since the polynomial approximation in the tails of the response distribution may be poor.

After the polynomial response surface is approximated, one can proceed with either Monte Carlo simulation by directly using the approximated function g (i.e. Eq. 2.14), or FORM analysis by constraining x_i on the explicitly approximated limit state surface G' (i.e. for the approximation of G in Eq. 2.4, x_i is the design point when the reliability index is minimised), or FOSM analysis by explicitly defining the derivatives (i.e. Eq. 2.9).

The advantage of using the response surface method is that an explicit performance function, which builds up the relationship between the input variables and the geotechnial system response, can be approximated. This function can later be used repeatedly in a structural response analysis in a timely fashion, effectively avoiding the computationally expensive process of carrying out a detailed analysis of a structure by, for example, the nonlinear finite element method. However, this also means that the accuracy of the method relies on how close the true performance function is approximated. Note that the approximation can be improved in a FORM analysis via iterations (Tandjiria et al., 2000); i.e. by taking, for the approximated response surface at the current iteration, the 'optimal' values of the random variables that 'minimise' the reliability index as the basis for sampling points for the next iteration (i.e. for updating the response and thereby improving the approximation). For more information, the readers are refered to Tandjiria et al. (2000), Babu and Srivastava (2007), Youssef Abdel Massih and Soubra (2008) and Zhang et al. (2012).

A conceptual extension of the above deterministic response surface method, that is, the stochastic response surface method (SRSM) using polynomial chaos, can also be used for the reliability analysis of slopes (Li et al., 2011). The basic idea of SRSM is to approximate model inputs and outputs in terms of random variables by a polynomial chaos expansion. The unknown coefficients in the polynomial chaos expansion are determined using a probabilistic collocation method (Huang et al., 2009). The major advantage of SRSM is that it allows existing deterministic numerical codes, such as a finite element code, to be used as a 'black-box' within the method. Applications of SRSM can be found in, for example, Huang and Kou (2007), Huang et al. (2007), Gavin and Yau

([2008](#)), [Mollon et al.](#) ([2010](#)) and [Jiang et al.](#) ([2014](#)).

2.4. DISCRETISATION OF RANDOM FIELDS

Random fields, used for representing spatially variable soil properties, have found extensive use in practical geotechnical applications ([Fenton and Griffiths](#), [2008](#)). There are various methods of representing random fields in finite element analysis ([Li and Der Kiureghian](#), [1993](#); [Matthies et al.](#), [1997](#)), including:

- Mid-point or nodal point method ([Der Kiureghian and Ke](#), [1987](#)), in which the field within the domain of an element is described by a single random variable representing the value of the field at a central point of the element.

- Spatial averaging method ([Vanmarcke and Grigoriu](#), [1983](#)), which describes the field within each element in terms of the spatial average of the field over the element;

- Shape function method ([Liu et al.](#), [1986](#)), which describes the random field within an element in terms of a set of nodal values and corresponding shape functions.

- Series expansion method, such as Karhunen–Loeve expansion, which expresses the field in terms of its spectral decomposition ([Phoon et al.](#), [2002](#)).

Much discussion is available on the relative merits of the various methods of representing random fields in finite element analysis ([Li and Der Kiureghian](#), [1993](#); [Matthies et al.](#), [1997](#)). The spatial averaging discretisation of the random field is used in this thesis, due to it reflecting the simplest form of finite element representation of a continuum, as well as the way that soil samples are typically taken and tested in practice, i.e. as local averages. Another advantage of this method is that it yields accurate results even for rather coarse meshes, according to [Der Kiureghian and Ke](#) ([1987](#)), which was also highlighted by [Matthies et al.](#) ([1997](#)). In the Author's opinion, this is largely due to the consistent modelling of the variance for different element sizes.

2.5. RANDOM FINITE ELEMENT METHOD IN GEOTECHNICAL ENGINEERING

The random finite element method (RFEM) is often used to compute geotechnical structure (e.g. slope) response (e.g. factor of safety and displacement) within a Monte Carlo framework ([Fenton and Griffiths](#), [2008](#)). The procedure is as follows:

1. Generate random property fields, for example, using the local average subdivision (LAS) method ([Fenton and Vanmarcke](#), [1990](#)), based on the soil property statistics, e.g. mean, standard deviation and spatial correlation structure (type of correlation function, and horizontal and vertical scales of fluctuation, θ_h and θ_v, respectively);

2. Map random field cell values onto the Gauss points within the finite element mesh modelling the given problem (in this case, a slope stability problem);

3. Carry out a traditional finite element (e.g. slope stability) analysis (Smith and Griffiths, 2005);

4. Repeat the above steps for multiple realisations in a Monte Carlo analysis (see Section 2.3.3), until the output statistics (e.g. mean and standard deviation of the factor of safety) converge.

For a given set of statistics, a probability distribution of the factor of safety can be obtained. Moreover, the potential consequences (e.g. failure volume and failure length in the case of slope stability) may also be quantified for each realised factor of safety.

The method has found widespread use in the field of geotechnics, as it is relatively simple to implement and enables a comprehensive analysis of the effects of soil spatial variability. It is widely considered to be the baseline stochastic method, against which other methods may be compared (Spencer, 2007); for example, Fenton et al. (2003) used RFEM as a means of validating their proposed approximate solution model (i.e. based on the harmonic mean of random field cells within some area behind the slope face) for slope stability. As a simulation method, RFEM can be applied to large and complex systems, without the need to include the rigid idealisations and/or simplifications necessary for analytical solutions, resulting in more realistic models. Therefore, RFEM can be used to test if and when analytical solution methods are ineffective (e.g., because of gross idealizations). Its biggest disadvantage is that it tends to be computationally expensive.

Griffiths and Fenton (1997, 1998) investigated the effects of spatially random permeability values on seepage in 2D and 3D. They found that the ability of the flow to move in three dimensions allowed it to more easily avoid areas of low permeability. This had the effect of increasing the mean flow rate while reducing its variance, when compared to the 2D solution. However, the absolute difference from 2D was not great and it was concluded that, for the case considered, a 2D stochastic analysis provided a good, conservative, computationally cheaper, estimate of the global stochastic response.

Fenton and Vanmarcke (1998) used a 3D random field combined with a 1D nonlinear finite element program to investigate the liquefaction risk accounting for local spatial variation, due to the enormous computational requirements of a nonlinear, time-stepping (i.e. subject to earthquake ground motion), Monte Carlo analysis in the 1990s.

Kuo et al. (2004) presented a parametric study of the effects of a layered spatially random soil on the displacement of a pad footing, and used 3D random fields combined with elastic–plastic FEA. They concluded that layered soils reduced the variation in footing settlement and that the soil layer closest to the foundation had the largest effect on the settlement variance.

Jaksa et al. (2005) presented the results of Monte Carlo simulations incorporating many 3D single-layer soil profiles with different statistical characteristics. A three-storey building, founded on nine pad footings, was used to assess the reliability of various site investigation strategies and test methods. They showed that the likelihood of under-designing or over-designing a footing decreases as the scope of the investigation increases.

Spencer (2007) and Spencer and Hicks (2007) used 3D RFEM with parallel computing to investigate the influence of heterogeneity on the reliability and failure of a long

undrained clay slope, and this was extended by Hicks et al. (2008) to investigate the potential failure consequences associated with different reliability levels. A comprehensive study of the influence of spatial variability on reliability and failure consequence can be found in Hicks and Spencer (2010) and Hicks et al. (2014). The same methodology was used to investigate the performance of simpler 3D slope reliability methods by Li et al. (2013) and Li and Hicks (2014).

Paiboon et al. (2013) investigated the influence of porosity and void size on effective elastic geotechnical engineering properties, using a 3D model incorporating random fields and finite elements. The study also investigated the representative volume element (RVE) needed to capture the essential properties of a heterogeneous material containing voids. It was found that, for the same porosity, the larger the size of the voids, the greater the size of the RVE. In addition, when the 3D results were compared with 2D results obtained by the authors in a previous study (Griffiths et al., 2012), it was found that the effective elastic stiffness was consistently greater in 3D than in 2D.

Arregui-Mena et al. (2015) carried out a stochastic thermo-mechanical analysis using Monte Carlo simulation combined with 3D random fields of material properties for nuclear graphite reactor bricks. They found that the pre-service von Mises stress is around twenty times higher when the spatial variability of material properties is introduced, and that tiny spatial variations in the coefficient of thermal expansion and Young's modulus can lead to the presence of thermal stresses in bricks that are free to expand.

2.6. STOCHASTIC ANALYSIS OF 3D SLOPES

Vanmarcke (1977b) presented the first stochastic analysis of a 3D slope, considering an idealised cylindrical failure through a slope with a heterogeneous Gaussian strength distribution. Methods for calculating the expected length of a failure, as well as the probability of failure for a given slope length, were presented. Also, predictions were compared to the failure of a long embankment in Canada, with good agreement. The techniques from this paper are summarised in greater detail in Chapter 4. Vanmarcke's model led to the investigation of Yücemen and Al-Homoud (1990), who highlighted the importance of the critical and total slope lengths in a 3-D analysis.

Auvinet and Gonzalez (2000) concluded that, for materials that are homogeneous only in a statistical sense, i.e. for most natural and compacted materials, the commonly accepted concept that 2D stability analyses give results that are on the safe side with respect to those given by three-dimensional analyses is not valid, based on a generalization of simplified Bishop's method and autocorrelated soil properties at the base of vertical columns in a 3D limit equilibrium analysis. This suggests that 3D models are needed. The following sections briefly review three currently available 3D approaches for slope stability.

2.6.1. VANMARCKE'S SIMPLIFIED 3D MODEL

The first paper treating the three-dimensional slope stability problem within a probabilistic framework was by Vanmarcke (1977b). In his paper, Vanmarcke considered the reliability of earth slopes for a stochastic cohesive soil characterized by the undrained shear strength. By considering the averaging of strength values over the failure surface of

a cylinder and including the end resistance, Vanmarcke (1977b) developed a simplified 3D model for estimating the probability of failure of a long slope. The equilibrium equation for the cylindrical failure in a 3D slope was proposed based on an extension of the circular arc method. Estimates for the probability of failure for a single cylindrical failure of finite length were derived, assuming the spatially averaged shear strength over a finite length followed a Gaussian probability distribution and had a structure controlled by a single 'characteristic distance'; that is, by the scale of fluctuation of the derived 'moving average' variable (for a unit length) along the longitudinal direction of the slope. The theoretical risk analysis predicted the most probable length of the failure zone along the embankment axis, the probability of occurrence of a slope failure centered at a specified point along the embankment axis, and the probability of a slope failure anywhere along an embankment of given total length. This was later extended to drained slopes by Vanmarcke (1980), who accommodated frictional and cohesive components of shear strength as well as a spectrum of drainage conditions. His approach has gained continuous attention in recent years, due to its ability to account for the so-called length effect in long soil structures (Vanmarcke, 2011; Vanmarcke and Otsubo, 2013). A detailed description is given in Chapters 4 and 5.

2.6.2. CALLE'S 2.5D MODEL

Calle (1985) proposed an extended/upgraded 2D probabilistic Bishop model for the analysis of long earth slopes and the method was incorporated in Mstab (GeoDelft, 1994). The estimation of the probability of failure anywhere along the slope axis involves three steps; the first step is to calculate the cross-section reliability index, using Bishop's model linked to a first order second moment method; the second step determines the probability of occurrence of a potentially unstable zone using down-crossing theory (Papoulis and Pillai, 2002); the third step evaluates the probability of a real failure mode, taking account of the contribution to the resistance of the end sections and given the presence of a potentially unstable zone. The basic failure model and method of analysis are presented in detail in Chapter 5.

2.6.3. 3D RFEM

Spencer and Hicks (2006, 2007) and Hicks and Spencer (2010) used RFEM to compute the reliability of a long slope cut in clay. The results showed that, for a given factor of safety based on the mean property value, reliability is a function of the degree of anisotropy of the heterogeneity. In particular, there are three possible failure modes, depending on the degree of anisotropy of the heterogeneity relative to the slope geometry. 2D analysis was shown to be equivalent to the 3D problem for an infinite scale of fluctuation in the horizontal plane. For low and intermediate horizontal scales of fluctuation (i.e. relative to the slope length), there are large differences between the 2D and 3D solutions. The same methodology was extended by Hicks et al. (2008) to look at the consequences in terms of volumes of material associated with potential slides, and by Hicks et al. (2014) to look at the integrated failure length along the third dimension of the slope. They also used this approach to demonstrate how characteristic values can be determined according to Eurocode 7 (Hicks and Nuttall, 2012).

Griffiths et al. (2009b) found that two-dimensional probabilistic analysis, which implicitly assumes perfect spatial correlation in the out-of-plane direction, may underestimate the probability of failure of slopes.

3D RFEM will be used in this thesis and its performance compared with the methods of Vanmarcke and Calle. This will be presented in detail in Chapters 4-6.

2.7. CONCLUSIONS

A literature review relating to the work presented in this thesis has been presented. This has covered:

1. evidence relating to the characterisation of soil variability; the COV of undrained shear strength is in the range of 0.1–0.4 and the vertical and horizontal SOFs for clay are in the range of 0.1–4 m and 10–90 m, respectively.

2. stochastic analysis methods; e.g. FOSM, FORM, MC and RSM.

3. the application of the random finite element method in geotechnical engineering; this has been mainly focused on 3D applications involving seepage, liquefaction, footings, slopes and nuclear engineering.

4. a summary of currently available methods dealing with 3D slope reliability; i.e. the Vanmarcke, Calle and RFEM models.

Detailed literature studies relating to specific topics will be included in Chapters 4-6.

3

RFEM FOR LONG SLOPE STABILITY AND ITS HPC IMPLEMENTATION

In the field of dyke engineering, soil strength heterogeneity and the so-called length effect have drawn much attention in recent years. Reliability and risk analysis of dykes, taking account of the length effect, poses a great challenge for engineers and researchers. This chapter presents the general outline of the random finite element method (RFEM) used to investigate the length effect; that is, by analysing the reliability of longer and longer slopes using a 3D nonlinear finite element code within a Monte Carlo framework. However, this is computationally prohibitive for a standard desktop computer, as both the memory and run-time requirements can be very high. Moreover, thousands of realisations of soil strength spatial variability are sometimes required to get a meaningful reliability result, although, usefully, each realisation is a largely independent calculation. To this end, Cloud and Grid computing technologies are naturally the most suitable for running multiple independent jobs. In this chapter, an HPC computing strategy based on Grid computing has been developed to carry out the work presented in later chapters.

3

3.1. INTRODUCTION

This chapter starts with a brief introduction to the random finite element method (RFEM) (Section 3.2), which is used in this thesis to analyse the stability of long slopes. It is then followed by a general description of the local average subdivision (LAS) algorithm developed by Fenton and Vanmarcke (1990), as well as its implementation by Spencer (2007) for generating anisotropic random fields of soil property values (Section 3.3). Section 3.4 is dedicated to solving the particular challenges posed when analysing very large problems, by means of HPC computing based on Grid e-infrastructures. Section 3.5 concludes the chapter.

3.2. RFEM IN LONG SLOPE STABILITY

As described in Section 2.5, RFEM combines the finite element method with random field generation techniques (Section 2.4). In slope reliability and risk assessments, this involves generating multiple realisations of the spatial variability of soil property values and carrying out a finite element analysis for each realisation to assess the factor of safety, as well as the potential sliding volume and length (see Fig. 3.1).

The generated random field cell values are mapped onto the slope mesh at the Gauss point level, so as to adequately represent the spatial variability. In order to minimise the computer run-time, a larger finite element size in the horizontal plane has been used in this thesis; this has a negligible influence on the computed factor of safety and the quality of the random field, due to the horizontal scale of fluctuation generally being larger than the vertical one. Note that, in the case of an element that has a horizontal dimension twice the vertical dimension, the value applied to each Gauss point is the average of four adjoining random field cells (i.e. the average of two cells in both the x and y directions), as illustrated in Fig. 3.2.

After mapping, the slopes are analysed with the strength reduction method to obtain a distribution of the realised factor of safety (F_R) and all possible failure mechanisms (as inferred from the computed displacements). In a detailed quantitative risk assessment (QRA) framework, reliability (or the probability of failure not occuring) and failure consequence evaluation are the two fundamental components (e.g. Huang et al., 2013). Reliability is the probability of a structure to perform a required function under stated conditions for a specified period of time. It is theoretically defined as the probability of success (i.e. reliability = 1 - probability of failure) and plays a key role in the cost-effectiveness of systems, in terms of minimizing costs and designing reliable engineering works. In the case of slope stability, reliability can be inferred from the computed histogram of F_R (with the probability of failure being found by integrating the area under the normalised histogram for $F_R < 1.0$) (e.g. Hicks and Spencer, 2010). Consequence analysis provides quantitative information on the risk and potential hazards that may be caused by the failure of engineering structures (e.g. Hicks et al., 2014). With this information it is possible to improve the original design, incorporate mitigation measures, or devise hazard and management strategies to keep the risk at acceptable levels. In long slope engineering, the potential failure volume and length are two important indicators of failure consequence, and therefore they are herein included in the RFEM analysis by post-processing the displacement fields. Detailed analyses will be presented in Chapters

4 and 5.

This thesis uses the local average subdivision method (Fenton, 1990; Fenton and Vanmarcke, 1990) to generate random fields, as it fully accounts for spatial correlation and averaging. The algorithm and implementation of LAS are briefly summarised in the following sections.

3.3. RANDOM FIELD GENERATION

3.3.1. LOCAL AVERAGE SUBDIVISION

The local average subdivision process (Fenton, 1990; Fenton and Vanmarcke, 1990) proceeds in a top-down recursive manner, and a brief overview of the 3D implementation of LAS will be covered here. LAS in 3D involves the subdivision of a parent cell (or cube) into 8 smaller cells of the same size. Initially, the random field domain is represented by a single cell (or cube). This is uniformly subdivided into smaller cells, stage by stage, until the required level of subdivision of the random field has been attained.

Fig. 3.3 shows the subdivision of a parent cell at an arbitrary location within the larger random field domain. The parent cells that are illustrated in the figure are denoted as $P_i, i = 1, 2, \ldots, 3^3$ and the child or subdivided cells are denoted as $Q_j, j = 1, 2, \ldots, 2^3$. Fig. 3.3 only shows the subdivision of the parent cell P_{14}. The algorithm will be represented here using vector notation (Fenton, 1994).

The values of $\mathbf{Q}^T = \{Q_1, Q_2, Q_3, \ldots, Q_8\}$ are obtained by adding a random component to a weighted mean. The mean term is derived from a best linear unbiased estimate using a $3 \times 3 \times 3$ neighborhood of the parent cell values, i.e. $\mathbf{P}^T = \{P_1, P_2, P_3, \ldots, P_{27}\}$. Hence,

$$\mathbf{Q} = \mathbf{A}^T \mathbf{P} + \mathbf{C} \mathbf{U} \tag{3.1}$$

where $\mathbf{U}$ is a random vector with independent standard normal elements.

Defining the covariance matrices as

$$\mathbf{R} = \mathrm{E}\left[\mathbf{P}\mathbf{P}^T\right] \tag{3.2a}$$

$$\mathbf{S} = \mathrm{E}\left[\mathbf{P}\mathbf{Q}^T\right] \tag{3.2b}$$

$$\mathbf{B} = \mathrm{E}\left[\mathbf{Q}\mathbf{Q}^T\right] \tag{3.2c}$$

where E[.] denotes the expectations which are derived using local average theory (i.e. variance reduction, see Vanmarcke (1983) and Vanmarcke (1977a)) over the cell domains.

The matrix $\mathbf{A}$ is determined by

$$\mathbf{A} = \mathbf{R}^{-1} \mathbf{S} \tag{3.3}$$

while the lower triangular matrix $\mathbf{C}$ satisfies

$$\mathbf{C}\mathbf{C}^T = \mathbf{B} - \mathbf{S}^T \mathbf{A} \tag{3.4}$$

At the start of the LAS process, in stage 0, a random global average is generated. In stage 1, the domain is subdivided into 8 cells whose local averages should average to
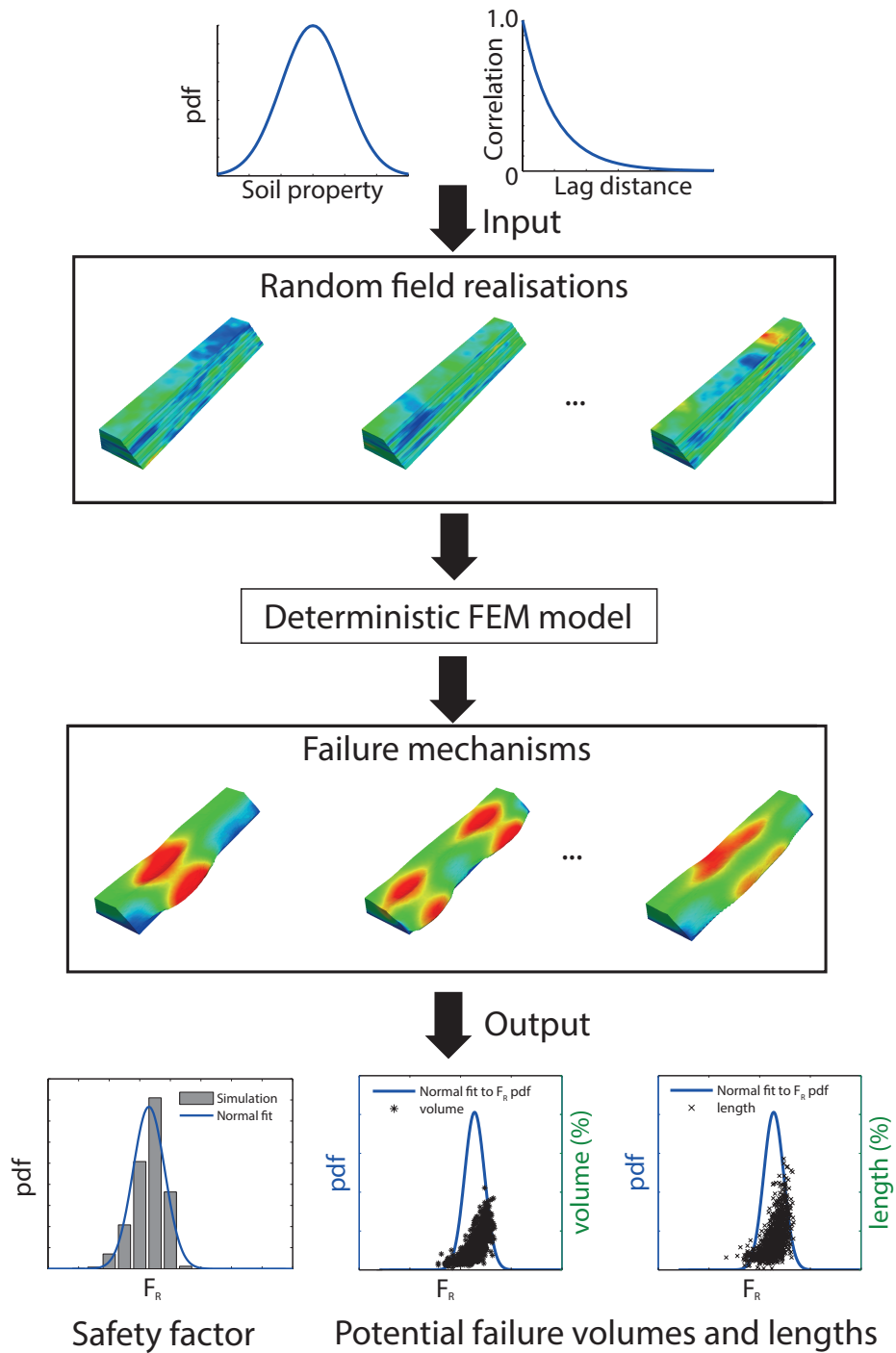
Figure 3.1: Schematic RFEM flowchart for slope stability assessment

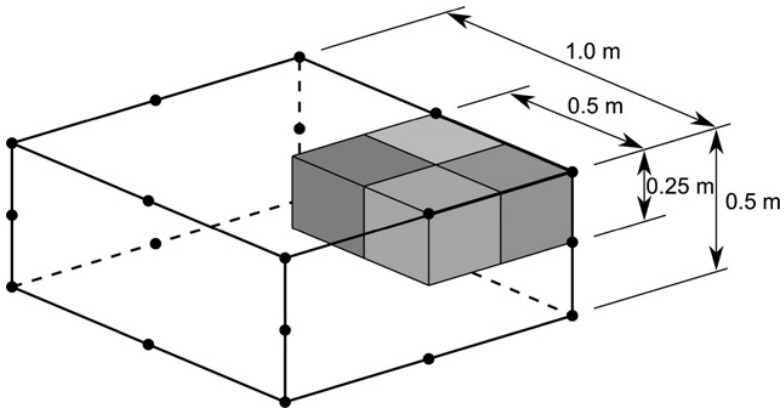Figure 3.2: One finite element and four random field cells (element size 1.0 × 1.0 × 0.5 m, random field cell size 0.25 × 0.25 × 0.25 m), after Hicks and Spencer (2010)

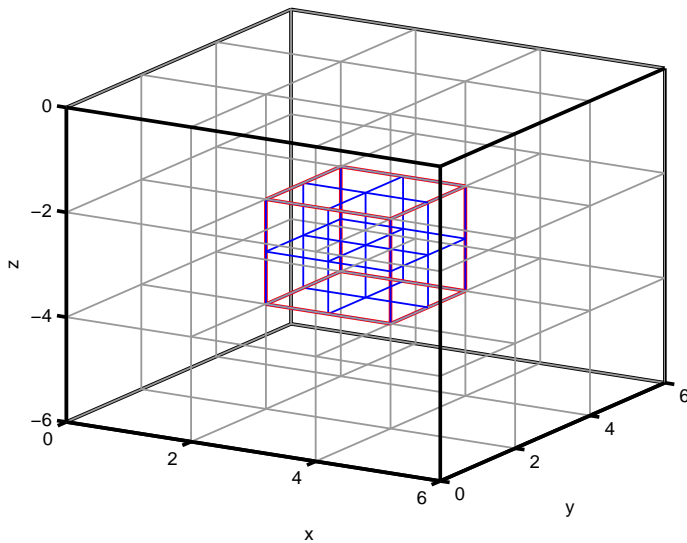
Figure 3.3: Cell subdivision in 3D with a 3 × 3 × 3 neighborhood size (subdivided cell size = 2)

preserve the global or parent average value, i.e. upwards averaging is preserved. Hence, for the subdivision of an arbitrary parent cell at any stage in the subdivision process, such as that illustrated in Fig. 3.3,

$$P_{14} = \frac{1}{8} \sum_{i=1}^{8} Q_i \qquad (3.5)$$

The above procedure proceeds recursively until the stage that satisfies the required field resolution.

3.3.2. SPENCER'S IMPLEMENTATION

An existing LAS program implemented by Spencer (2007) has been used in this thesis. The implementation uses the following 3D covariance function:

$$C(\tau_1, \tau_2, \tau_3) = \sigma^2 \exp\left(-\frac{2|\tau_3|}{\theta_3} - \sqrt{\left(\frac{2\tau_1}{\theta_1}\right)^2 + \left(\frac{2\tau_2}{\theta_2}\right)^2} \right) \qquad (3.6)$$

where τ and θ are the lag distance and scale of fluctuation, subscripts 1–3 denote the two lateral and vertical coordinate directions, respectively, and σ^2 is the variance of the relevant soil property. However, because the subdivision algorithm itself is incapable of preserving anisotropy (Fenton, 1994), in this implementation an isotropic random field is initially generated, and this field is then post-processed to give the target anisotropic random field; that is, by squashing and/or stretching the field in the vertical and/or horizontal directions, respectively.

Note that the vertical correlation structure is separated from the two horizontal directions in Eq. 3.6 (Fenton and Vanmarcke, 1998); this represents the separation in the assumed long-term laminar deposition process of the soils being modelled. Hence, it is assumed that horizontal layers are deposited at one time, giving them linked correlation, whereas vertical deposition occurs through time, making the correlation separate.

3.3.3. SQUASHING/STRETCHING IN 2D

Figs. 3.4–3.6 show three possible ways of post-processing an isotropic random field to produce an anisotropic field ready for mapping to a finite element mesh. In each figure, the starting point is an isotropic random field comprising 512×512 cells (i.e. as has been generated by 9 LAS sudivision stages).

Fig. 3.4 shows an example of squashing the starting isotropic random field vertically. In this example, the target square domain size is $D = 5.0$ m, the vertical scale of fluctuation is $\theta_v = 0.5$ m, and the anisotropy of the heterogeneity is $\xi = 6$, i.e. the horizontal scale of fluctuation is $\theta_h = 3.0$ m. The final cell size is $d_c = 0.1$ m, and therefore 50 cells are needed in the horizontal direction and $50 \times 6 = 300$ cells (before squashing) in the vertical direction, as these are to be squashed and replaced by 50 new square cells. The starting isotropic field has a scale of fluctuation of $\theta_{iso} = 3.0$ m, to ensure that the final target field has the required horizontal and vertical SOFs. Note that, by squashing vertically (and averaging each group of 6 cells to form a single new cell of 0.1 m dimension), the vertical scale of fluctuation is scaled down to the target 0.5 m.
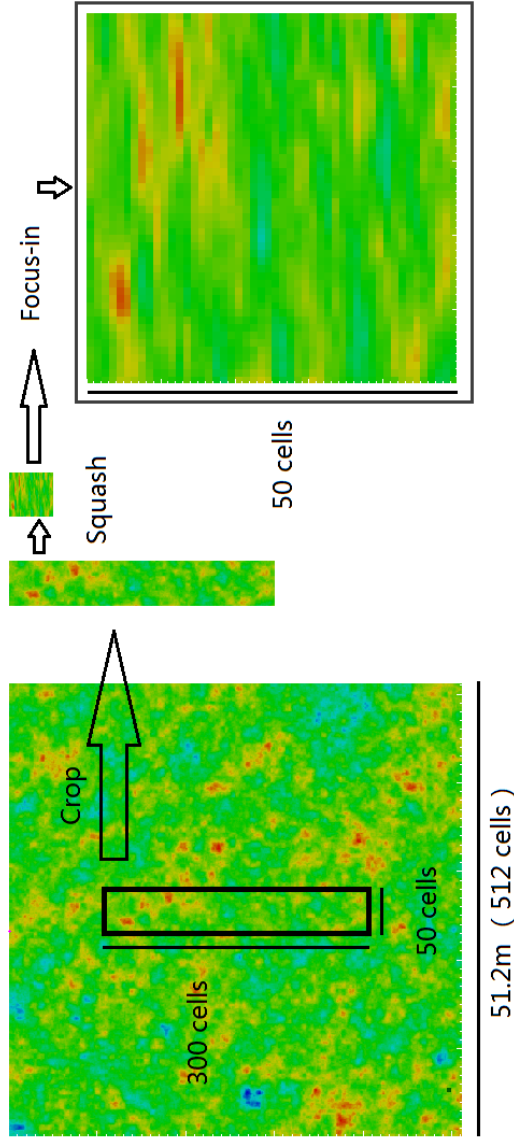
Figure 3.4: Post-processed anisotropic random field produced by squashing ($\xi = 6$)
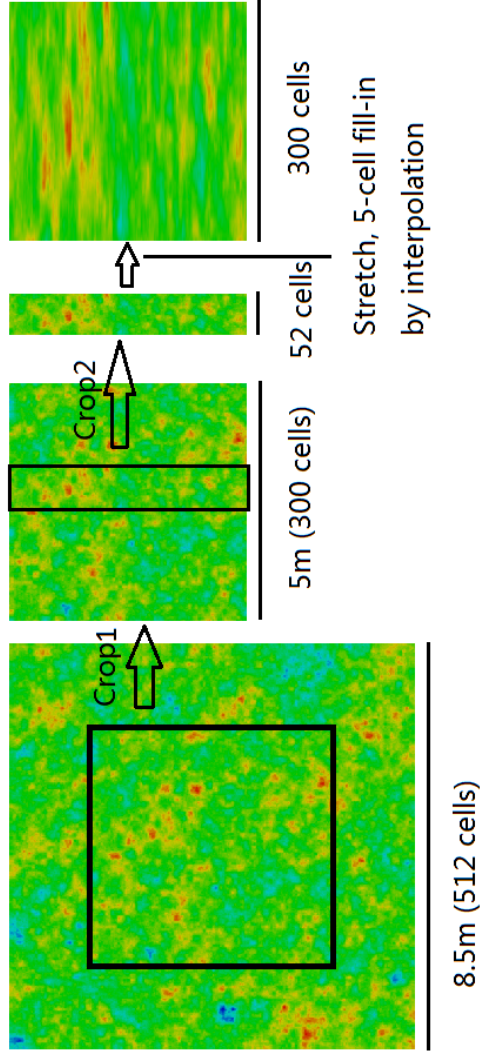
Figure 3.5: Post-processed anisotropic random field produced by stretching ($\xi = 6$) (52 cells after Crop2 to be able to interpolate between the last two columns of cells)
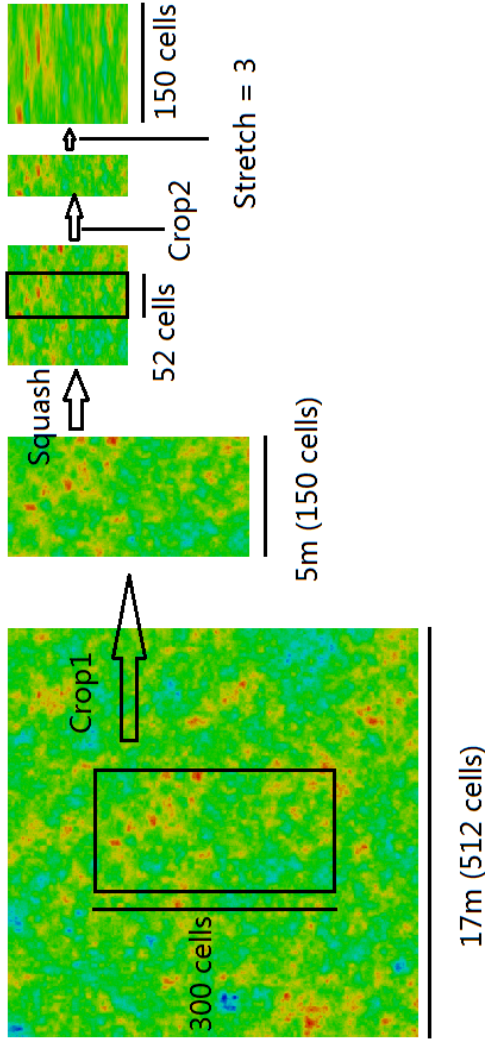
Figure 3.6: Post-processed anisotropic random field produced by squashing and stretching ($\xi = 6$) (52 cells after Crop2 to be able to interpolate between the last two columns of cells)

The same target field can also be produced by stretching an isotropic random field with $\theta_{iso} = \theta_v = 0.5$ m, as illustrated in Fig. 3.5. In this example, the horizontal SOF is scaled up to 3.0 m and so each of the original square cells needs to be replaced by 6 new square cells (each with their own cell value). The extra cell values can be assigned by linear interpolation between neighbouring columns of cells in the original field (Spencer, 2007), as illustrated in Fig. 3.5. Note that the original field before cropping is exactly the same as the original field from Fig. 3.4, due to the different random field cell sizes. Here, the cell size is $d_c = 1/60$ m, i.e. by keeping the ratio $\theta_{iso}/d_c = 30$ the same as in Fig. 3.4 to ensure the same amount of variance reduction at the 'point' level.

Squashing and stretching may also be combined to give the target field. For example, the same target field as shown in Figs. 3.4 and 3.5 can be produced by first squashing by a factor of 2 from an isotropic field having $\theta_{iso} = 2 \times \theta_v = 1.0$ m (Fig. 3.6). After squashing, the intermediate field has a vertical SOF of $\theta_v = 0.5$ m and a horizontal SOF of $\theta_h = 1.0$ m. Hence, by stretching the squashed field horizontally by a factor of 3, the resultant field will have a horizontal SOF of $\theta_h = 3.0$ m. Note that, in order to make the variance reduction in the final field consistent with the above figures, the cell size here is set to $d_c = 1/30$ m, so that θ_{iso}/d_c is the same as above.

3.3.4. SQUASHING/STRETCHING IN 3D

For 3D problems, squashing, which occurs in the vertical direction, is exactly the same as when it is done in 2D, except that multiple slices (i.e. x–z or y–z plane, see Fig. 3.7 for the coordinate system) are being squashed. Stretching in 3D is essentially a 2D stretching in the x–y plane, whereas stretching in 2D is a 1D stretching along the x or y axis.

Bilinear interpolation was used in the implementation of Spencer (2007) to stretch (in the horizontal plane) 3D isotropic random fields to produce the required anisotropic 3D random fields. An example is shown in Fig. 3.7 for a target field of 19 m × 19 m × 19 m with $\theta_v = 5.0$ m, $\theta_h = 30$ m and a cell size of $d_c = 1.0$ m. The stretching is illustrated in Fig. 3.8 for the top layer in the vertical direction (i.e. the x–y plane at the maximum z). Note that the field shown in Fig. 3.7 comprises 19 cells in each direction whereas the field shown in Fig. 3.8b has 25 cells along each side. That is, the final field is produced by first stretching a group of a 5 × 5 cells by a factor of $\xi = 6$ (Fig. 3.8a, this has to be at least 5 cells along each direction to be able to interpolate between the last two cells in each direction, due to $(4-1) \times 6 < 19 < (5-1) \times 6$) and then cropping from the stretched field (Fig. 3.8b). Therefore, the first layer in Fig. 3.7 corresponds to the 3/4 of Fig. 3.8b in the up-left corner. Note that a local colour scale is used for Fig. 3.8 and that the black dots represent the known grid/cell values.

3.4. COMPUTATIONAL CHALLENGES FOR LONGER SLOPES

In Chapter 5 of this thesis, the 3D slope analysed by Hicks et al. (2014) is increased in size to a length of 500 m. The aim has been to quantify the range of discrete failures and their relative frequencies in a longer slope than analysed previously, thereby enabling a comparative investigation of slope length dependency with other available models. This has necessitated a 3D finite element mesh comprising 40,000 twenty-node brick elements, 191,281 nodes and 573,843 degrees of freedom. Hence, for such a physically large prob-
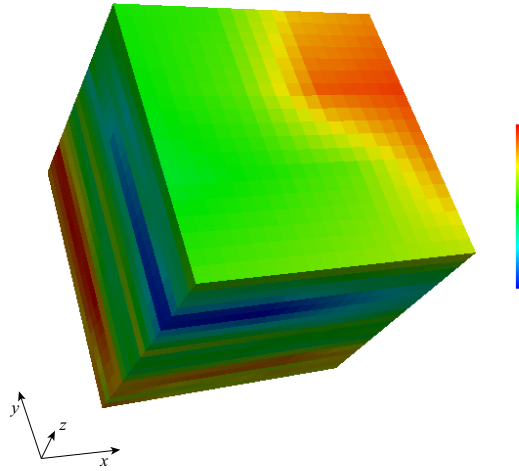
Figure 3.7: Stretched 3D random field ($19 \times 19 \times 19$ cells, $\xi = 6$)
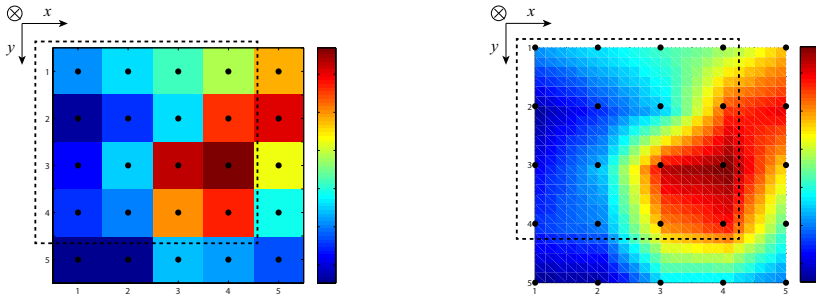
(a) Before stretching; cell size enlarged 5 times

(b) After stretching; cell size $d_c = 1.0$ m

Figure 3.8: Demonstration of stretching an $x - y$ plane ($\theta_{iso} = 5.0$ m) to produce the top layer of the 3D random field shown in Fig. 3.7: bilinear interpolation, $\otimes$ means z coordinates directed into the paper, the dotted area indicates the zone to be cropped to produce the target top layer, and a local color scale is used in both subfigures.

3

lem the computational requirements are substantial, with regards to both run-time and memory. A computing strategy has therefore been developed, based on Grid computing, so that the computational analysis can be undertaken in a significantly reduced time.

Spencer (2007) showed that the direct solver was approximately ten times faster than the iterative solver in his nonlinear plasticity, iterative factor of safety analyses. Therefore, the direct solver has been used in this thesis. However, as the problem becomes large, in terms of the total number of degrees of freedom or total numbers of equations (e.g. 509,760 equations are involved in the investigation presented in Chapter 5), it requires more computer memory to store the global stiffness matrix, and also more time to factorise it and run the equilibrium iterations. For a 500 m long slope, such as that investigated in Chapter 5, around 6 GB of memory is needed; therefore, a standard desktop computer, which usually has ≥ 8 GB of standard memory, is adequate for a single realisation. However, hundreds of Monte Carlo realisations are needed to simulate the range of spatial variability in the ground and, on average, it takes 3 hours to run a single realisation for a problem of this size. If, for example, 2000 realisations need be run on a desktop computer, it would take 250 days to finish. It is therefore not a feasible task for such a machine.

As each realisation or job can be run independently on a single serial computer, Grid computing, which is generally the allocation of jobs over a network of distributed computers, is ideally suitable for Monte Carlo simulation.

The Author was granted access to the Dutch grid infrastructure and was authenticated as a member in a virtual organization where 3 computing clusters were available (4400 cores for the gina cluster, 900 cores for the rug cluster and 3800 cores for the nikhef cluster (data from Sep. 2014)). For high memory jobs (as is the case in Chapter 5), it was the gina cluster that was used. The computing capacity is 4400/2 = 2200 jobs (it has 3-8 GB of memory per core and therefore 2 free cores are needed for a single 6 GB job). With these available resources, it was possible to carry out the investigation for a 500 m long slope in a reasonable time. Usually it takes 15-18 hours (i.e. 5-6 times that of a single realisation) to finish 2000 jobs/realisations, including the waiting time in the queue (Li et al., 2015d). A detailed description of the computing strategy based on HPC can be found in Appendix A.

3.5. CONCLUSIONS

This chapter has outlined the methodology used in this thesis to carry out the RFEM analyses in the following chapters, including aspects relating to the random field generator such as squashing and stretching post-processing techniques for producing anisotropic random fields. An HPC computing strategy based on Grid computing (Appendix A) has been developed to carry out the work much more efficiently, especially for very large problems. Specifically, one year of serial computational analysis can be undertaken in a single day in parallel.

4

RELIABILITY ANALYSIS OF A LONG SLOPE IN 3D: COMPARING RFEM WITH VANMARCKE'S MODEL

An idealised 3D slope stability problem, incorporating spatial variability of undrained shear strength, has been analysed by Vanmarcke's (1977b) simplified method and the more advanced random finite element method (RFEM), and the two solutions compared. Both methods lead to predictions of reliability (or, alternatively, to probability of failure), as opposed to a single factor of safety. However, they may give significantly different results, depending on the scale of fluctuation (SOF) of undrained shear strength in the horizontal direction relative to the slope dimensions. It is shown that, in a heterogeneous soil, failure mechanisms seek out the weakest path. It is therefore the spatial average of material properties over this general failure surface that determines slope stability, rather than simple spatial averages over a pre-defined failure surface such as the cylindrical surface assumed in the simpler model. The results demonstrate that the RFEM response of the slope is weaker than the Vanmarcke solution in most cases and that the difference is greatest for small SOFs, due to differences in the predicted failure length and thereby to the exaggerated contribution to resistance then predicted by the cylinder ends in the Vanmarcke solution. In contrast, for large horizontal SOFs relative to the slope length, the two methods agree. This is because the failure surfaces in the RFEM analyses then tend to be cylindrical and propagate along the entire length of the slope, thereby matching Vanmarcke's solution for this limiting case. The investigation highlights the merits of advanced methods of analysis in assessing the performance of simpler methods used in design. Moreover, by giving a detailed comparative analysis between the RFEM and Vanmarcke models for the stability of a slope of finite length at a single point, the chapter acts as a springboard to the more complicated slope length dependency investigation in Chapter 5.

4.1. INTRODUCTION

The spatial variability of soil property values influences soil behaviour and the performance of geotechnical structures (Hicks, 2007). For example, spatial variability promotes the development of failure mechanisms along so-called 'paths of least resistance' (Hicks and Samy, 2002; Fenton and Griffiths, 2002, 2003; Fenton et al., 2003; Hicks and Spencer, 2010), causing an apparent reduction in the property mean (Hicks and Nuttall, 2012), while, at the same time, it has the effect of variance reduction due to spatial averaging of properties along the failure path (El-Ramly et al., 2002; Duncan et al., 2003; Ji et al., 2012). However, spatial variability also increases uncertainty in design, due to lack of knowledge regarding the actual heterogeneity existing at a site (Lloret-Cabot et al., 2012, 2014). This has led to the increasing use of probabilistic methods to quantify the effects of spatial variability and uncertainty in geotechnical assessments (Baecher and Christian, 2005; Hicks, 2007; Phoon, 2008; Arnold et al., 2012).

Slope stability has been identified as an application for which a consideration of spatial variability is particularly relevant. For this purpose, spatial variability has often been modelled in 2D using an isotropic correlation structure; for example, as in Paice and Griffiths (1997), Griffiths and Fenton (2004), Schweiger and Peschl (2005), Griffiths et al. (2009a) and Suchomel et al. (2010). Relatively fewer studies have considered anisotropic heterogeneity in 2D; for example, as in Hicks and Samy (2002, 2004), Hicks and Onisiphorou (2005), Cho (2007, 2009), Arnold and Hicks (2011), Jiang et al. (2014) and Li et al. (2015a).

However, 2D analysis represents, at best, a spatial average of properties over the third (slope length) dimension (Catalan and Cornell, 1976). That is, the input point statistics of the soil properties in a 2D model generally represent spatial averages over the length dimension, as site characterisation programs are often carried out in 3D space instead of at a particular cross-section. Hence, the derived '2D' point properties are dependent on the slope length and on the correlation distance of the property in that direction. For an infinite correlation distance, the 2D statistics are a good representation; however, in reality, this is rarely the case. Therefore, the performance prediction from a 2D probabilistic analysis is indicative of, at best, an average performance in the slope length direction. The implication is that the reliability of some segments will be overestimated (i.e. unconservative) and that of other segments will be underestimated (i.e. conservative). As a result, mitigation measures may not be carried out effectively.

The importance of tackling slope reliability in 3D was first recognised by Vanmarcke (1977b), who considered, from an analytical point of view, the three-dimensional slope stability problem within a probabilistic framework, by simplifying the complicated 3D problem to one involving a single cylindrical failure mechanism of finite length. This was followed by Calle (1985), who developed a variation of Vanmarcke's (1977b) model for aiding dyke safety assessments in the Netherlands. However, it is only in recent years that numerical methods have been used to analyse the 3D problem in greater detail; for example, as in Spencer and Hicks (2006, 2007), Spencer (2007), Hicks et al. (2008), Griffiths et al. (2009b), Hicks and Spencer (2010), Nuttall (2011), Hicks et al. (2014) and Ji and Chan (2014).

In particular, Spencer and Hicks (2006, 2007), Spencer (2007) and Hicks and Spencer (2010) used the random finite element method (RFEM) (Fenton and Griffiths, 2008) to in-

vestigate the influence of anisotropy of the heterogeneity of undrained shear strength on the performance of a slope that was long in the third dimension, and identified three categories of failure mode, depending on the horizontal scale of fluctuation (SOF) relative to the slope geometry. They showed that 2D analysis is only justified for long slopes with two dimensional failure mechanisms; moreover, discrete failures, which mainly result from intermediate levels of anisotropy, demonstrate that the 3D nature of heterogeneity should be considered and that 3D analysis should be carried out to assess slope reliability in these (i.e. most) situations. However, Hicks and Spencer (2010) also showed that, for very long slopes, such as highway embankments and flood defences, system reliability may be assessed by carrying out a detailed analysis of a relatively short, representative section of the slope, and then, by assuming stationarity of the property statistics, extrapolating the results to the system by means of simple probability theory.

This chapter investigates the relative performance of two contrasting approaches to accounting for soil heterogeneity in analysing 3D slope reliability; that is, the analytical method of Vanmarcke (1977b) and the more versatile (but computationally more expensive) random finite element method. By considering a simple idealised slope stability problem, the aim is to identify and evaluate those situations in which the two solutions are similar, as well as those situations in which they are significantly different.

For this purpose, the focus is on uncertainty relating to the spatial variability of properties relative to the problem geometry, rather to uncertainty relating to (for example) the soil constitutive behaviour. Hence, the RFEM model idealises the soil as a linear elastic, perfectly plastic Tresca material, to make the soil behaviour consistent with Vanmarcke's (1977b) model which assumes only a cohesive shear strength for the soil. However, the same methodology has also been successfully applied using more realistic models of soil behaviour (e.g. Hicks and Onisiphorou, 2005; Arnold and Hicks, 2011).

In the following sections, Vanmarcke's (1977b) simplified 3D model is reviewed (Section 4.2) and the 3D RFEM model briefly introduced (Section 4.3). The relative performance of the two approaches in analysing a simple 3D slope stability problem is then investigated in Section 4.4.

4.2. VANMARCKE'S SIMPLIFIED 3D MODEL

Vanmarcke (1977b) was the first to consider three-dimensional slope stability within a probabilistic framework, based on his work on the probabilistic characterisation and modelling of soil profiles (Vanmarcke, 1977a, 1978) and the first passage time problem (Vanmarcke, 1975). He investigated the reliability of earth slopes for cohesive soils characterised by a stochastic undrained shear strength s, which was assumed to be stationary (i.e. statistically homogeneous, implying that the first two moments are constant within the domain of interest) along the entire slope length. Estimates of the failure probability for a single cylindrical failure mechanism of finite length b, centred at a given point along a slope of indeterminate length, were derived, assuming the spatially averaged shear strength over that finite length s_b (and therefore the factor of safety F_b, see equation 4.1 below) followed a Gaussian (i.e. normal) probability distribution and had a correlation structure controlled by a single 'characteristic distance', δ. This distance is herein taken to be the scale of fluctuation θ used by Vanmarcke (1983), i.e. $\theta = \delta$. By considering the averaging of strength values over the cylindrical failure surface, and by including the end

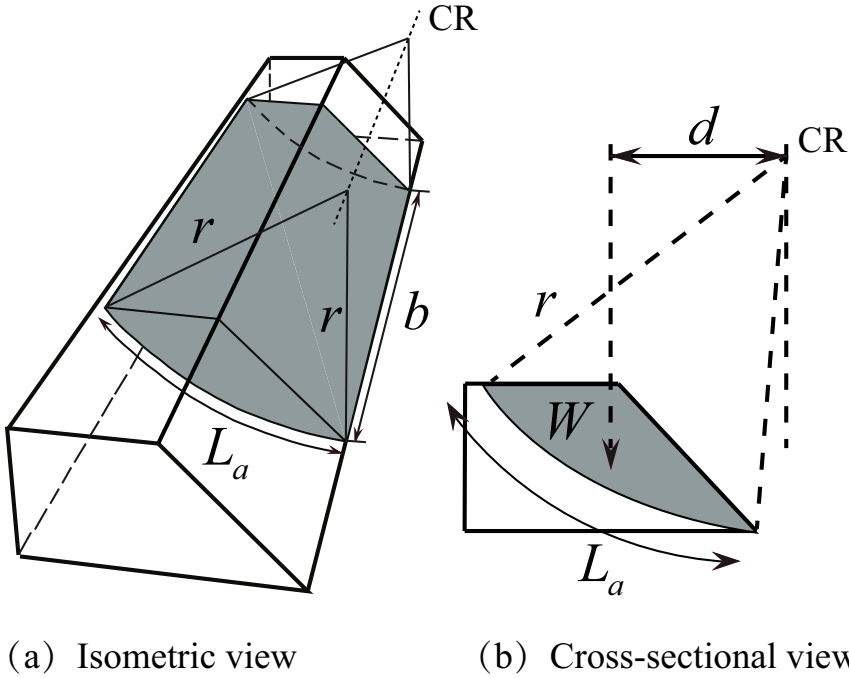(a) Isometric view   (b) Cross-sectional view

Figure 4.1: Diagrams showing the failure mass within a long 3D slope (based on Vanmarcke (1977b))

resistance, Vanmarcke (1977b) developed a simplified 3D model for estimating the probability of failure of a slope (of constant cross-section) that is long in the third dimension.

The proposed equilibrium equation for a cylindrical failure in a 3D slope was based on an extension of the circular arc method in 2D, but also included a term for the added resistance from the two vertical end faces. Hence,

$$F_b = \frac{M_r(b)}{M_o(b)} = \frac{s_b L_a r b + R_e}{W d b} \tag{4.1}$$

where F_b is the traditional factor of safety for the failure length b; M_r and M_o are the resisting and overturning moments, respectively; s_b is the average shear strength on the cylindrical failure surface of length b; L_a is the length of the assumed circular failure arc; r is the radius of the failure arc; W is the weight per unit length of the material located above the sliding surface; d is the horizontal distance from the centre of rotation to the centre of gravity of the rotating body; and R_e is the contribution to the resisting moment from the end sections. These variables are depicted in Fig. 4.1, in which CR is the centre of rotation of the failure arc.

Using the First Order Second Moment (FOSM) approach (Section 2.3.2), Vanmarcke (1977b) first considered the mean factor of safety, $\bar{F}_b$, for a cylindrical failure of length b, by separating equation 4.1 into components for the cylindrical surface and end faces,

i.e.

$$\bar{F}_b = \bar{F}\left(1 + \frac{d_0}{b}\right) \tag{4.2}$$

where $\bar{F}$ is the mean factor of safety for the plane strain condition (noting that, in equation 4.1, s_b is a variable while $\bar{s}_b$ denotes its mean),

$$\bar{F} = \frac{\bar{s}_b L_a r}{W d} \tag{4.3}$$

and d_0 is twice the ratio of the cross-sectional sliding area, A, to the arc length, L_a, i.e.

$$d_0 = \frac{2A}{L_a} \tag{4.4}$$

Hence, the term d_0/b in equation 4.2, as a multiplier of $\bar{F}$, accounts for the increased resistance to failure caused by the end faces of the cylinder. The extra term increases the mean factor of safety, making the slope less likely to fail compared to a 2D analysis, especially for small values of b. In addition, the resisting moment due to the end faces is approximated by taking the length of the 'lever arm' to be the radius r, thereby resulting in an upper bound for the end resistance.

The standard deviation of F_b, $\tilde{F}_b$, as a result of the variation of the shear strength s_b over the cylindrical surface (but neglecting any uncertainty in the end resistance R_e), was given as

$$\tilde{F}_b = \Gamma(b) V_{s_1} \bar{F} \tag{4.5}$$

where

$$\Gamma(b) = 1 \; ; \; b \leq \theta \tag{4.6a}$$

$$\Gamma(b) = \left(\frac{\theta}{b}\right)^{1/2} \; ; \; b > \theta \tag{4.6b}$$

and

$$V_{s_1} = \Gamma(L_a) V_s \tag{4.7}$$

$\Gamma(b)$ is a variance reduction factor for the shear strength averaged over the length b, V_s is the coefficient of variation of the 'point' shear strength (although some averaging is already implied), V_{s_1} is the coefficient of variation of the average strength over a unit length of the failure surface, and $\Gamma(L_a)$ is obtained by replacing b with L_a and θ with θ_e, the equivalent SOF along the failure arc, in equation 4.6. The term $\Gamma(b) V_{s_1}$ in equation 4.5, which equals $\Gamma(b)\Gamma(L_a)V_s$, represents the variance reduction as a result of averaging over both the cross-sectional arc L_a and slope length b. Thus, as b increases relative to θ, $\Gamma(b)$ reduces and so does $\tilde{F}_b$. That is, as the length of the failed section of the slope increases relative to θ, the effect of greater averaging of values over the failure surface is to reduce the variance of the result.

Note that no distinction is made between the scale of fluctuation of s_1 and that of the point process s. Thus, θ in equation 4.6 is taken to be the horizontal SOF. Note also that the variance reduction factor given by equation 4.6 is an appropriate idealisation that may be compared with other approximations to the actual variance reduction factor
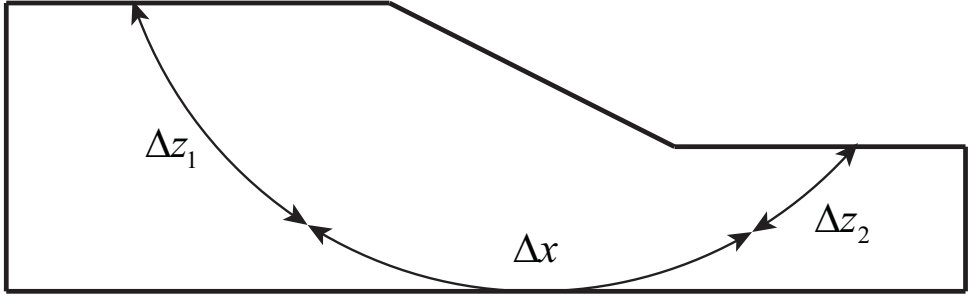
Figure 4.2: Subdivision of the failure arc for a slope with a foundation layer

(equation 4.13), which may be obtained through adopting a specific form of the underlying correlation function (e.g. such as the exponential form used for the RFEM analyses in this thesis, equation 4.14).

According to Vanmarcke (1977b), the equivalent SOF in the cross-sectional plane, θ_e, can be approximated by subdividing the failure arc L_a into segments ($\Delta z_1 + \Delta z_2 + \Delta x$) and using the equation

$$\frac{L_a}{\theta_e} = \frac{(\Delta z_1 + \Delta z_2)}{\theta_v} + \frac{\Delta x}{\theta_h} \tag{4.8}$$

where $L_a = \Delta z_1 + \Delta z_2 + \Delta x$, and θ_v and θ_h are the vertical and horizontal SOFs, respectively. The circular arc segments ($\Delta z_1, \Delta z_2$ and Δx) subdivide the failure surface into sections that are mainly vertical (Δz_1 and Δz_2) or mainly horizontal (Δx), as illustrated in Fig. 4.2 for a slope failure involving a foundation layer. For a slope failure in which there is no foundation layer, as is the case for the analyses in this chapter, $\Delta z_2 = 0$.

This method of approximating θ_e may be compared with the approach of El-Ramly et al. (2006), which assumed $\theta_e = \sqrt{\theta_v \theta_h}$. Hence there was no consideration of the failure surface dependency, in contrast to Vanmarcke (1977b) who considered the equivalent SOF as a function of the length and shape of the failure surface, which, in turn, is constrained by the problem geometry. Further details on calculating θ_e are given in Section 4.4.2.

Once θ_e is defined, it is straightforward to use equation 4.7, and then equation 4.5, to get $\tilde{F}_b$. As seen in equations 4.2 and 4.5, $\bar{F}_b$ and $\tilde{F}_b$ are both dependent on the slope failure length. For any b, the probability of failure, for a slope section centred at some defined point along the longer slope, is the probability that F_b is less than or equal to 1.0, i.e. $P(F_b \leq 1)$. As a Gaussian distribution is assumed for s_b (and thereby F_b), $P(F_b \leq 1)$ can be calculated using the cumulative standard Gaussian distribution function Φ. Over the range of possible values of b, $P(F_b \leq 1)$ varies due to $\bar{F}_b$ and $\tilde{F}_b$ being functions of b for any given $\bar{F}$, θ_v and θ_h. This probability reaches a maximum at the critical failure length b_c, which, by assessing a reliability function (Vanmarcke, 1977b) as a function of b, was derived as

$$b_c = \frac{\bar{F}}{\bar{F} - 1} d_0 \; ; \; b_c > \theta_h \tag{4.9a}$$

$$b_c = \theta_h \; ; \; b_c \le \theta_h \tag{4.9b}$$

Hence, the most likely failure length depends only on $\bar{F}$, θ_h and d_0 (the factor accounting for failure surface end effects). Note that $\bar{F}$ has to be larger than 1.0 in equation 4.9a to ensure a positive and meaningful failure length.

By using equations 4.2–4.9 for a given slope, the probability that a failure of length b_c will occur, $p_f(b_c)$, can be found by calculating the mean and standard deviation of the factor of safety, and utilising the properties of the standard Gaussian distribution function, i.e.

$$p_f(b_c) = P(F_{b_c} \le 1) = P(U \le -\beta_{b_c}) = \Phi(-\beta_{b_c}) \tag{4.10}$$

where

$$\beta_{b_c} = (\bar{F}_{b_c} - 1)/\tilde{F}_{b_c} \tag{4.11}$$

is the reliability index for the failure length b_c, and

$$U = \frac{F_{b_c} - \bar{F}_{b_c}}{\tilde{F}_{b_c}} \tag{4.12}$$

is a standardised random variable with zero mean and unit standard deviation.

4.3. RFEM MODELLING OF 3D SLOPE RELIABILITY AND RISK

The 3D RFEM approach used in this thesis combines random fields for modelling the spatial variability of material properties (in this case, the undrained shear strength s) and finite elements for computing geo-structural response (in this case, the factor of safety in a slope stability application).

The random fields of s have been generated using local average subdivision (LAS) (Fenton and Vanmarcke, 1990), which requires as input the property mean $\bar{s}$, standard deviation $\tilde{s}$ and scale of fluctuation θ. The anisotropy of the heterogeneity ($\xi = \theta_h/\theta_v$) is modelled by defining different values of SOF in the vertical and horizontal directions (i.e. θ_v and θ_h, respectively), as has previously been reported and implemented, for example, by Hicks and Samy (2002) and Hicks and Spencer (2010) in 2D and 3D, respectively.

A fundamental part of the LAS algorithm is the variance function, which measures the reduction in variance caused by averaging over a domain. It is related to the correlation function for a stationary process as follows (Fenton and Griffiths, 2008):

$$\Gamma^2(T) \equiv \gamma(T) = \frac{2}{T} \int_0^T \rho(\tau) d\tau - \frac{2}{T^2} \int_0^T \tau \rho(\tau) d\tau \tag{4.13}$$

where T is the averaging interval and ρ is the correlation function in 1D. This equation can be used to construct equation 3.2 in the LAS algorithm presented in Chapter 3, while the adopted 3D exponential correlation function is given as

$$\rho(\tau_1, \tau_2, \tau_3) = \exp\left(-\frac{2|\tau_1|}{\theta_1} - \sqrt{\left(\frac{2\tau_2}{\theta_2}\right)^2 + \left(\frac{2\tau_3}{\theta_3}\right)^2}\right) \tag{4.14}$$

where τ is the lag distance, and subscripts 1–3 denote the vertical and two lateral coordinate directions, respectively. Note that, for a stationary random process, $\rho(\tau_1, \tau_2, \tau_3) = C(\tau_1, \tau_2, \tau_3)/\sigma^2$, where σ^2 is the variance of the random soil property and $C(\tau_1, \tau_2, \tau_3)$ is refered to in equation 3.6 in Chapter 3.

Based on a series of Monte Carlo realisations, with each realisation involving a different random field and a finite element analysis of the slope, a distribution of the realised factor of safety (denoted as F_R) may be obtained for a given set of input statistics (i.e. $\bar{s}, \tilde{s}, \theta_v, \theta_h$). The reliability of the slope can then be assessed, by calculating the reliability index β using equation 4.11, based on the estimates of the mean and standard deviation of F_R, or by calculating the failure probability using equation 4.10, assuming a normal distribution of F_R.

In order to assess the risk associated with a given $\bar{F}$, the consequences have to be assessed first. The consequence associated with each potential slope failure is here quantified by estimating the slide volume, using the same strategy as reported by Hicks et al. (2008, 2014). The computed slide volumes are a vital component in understanding the relationship between the 3D RFEM analysis and the simplified 3D Vanmarcke solution, as will become clear in the next section.

4.4. COMPARATIVE ANALYSES OF A SLOPE PROBLEM

Three categories of failure mode have previously been identified in the analysis of a long 3D slope in a heterogeneous soil, as reported by Spencer and Hicks (2006, 2007), Spencer (2007) and Hicks and Spencer (2010). The occurrence of these failure mode categories was shown to be strongly influenced by the magnitude of θ_h relative to the slope geometry, as represented by the slope height H and length L, and may be simply summarised as follows:

- Mode 1: For $\theta_h < H$, the slope fails along its entire length and the failure mechanism, which initiates from the slope toe for a depth independent $\bar{s}$, passes through weak and strong zones alike, due to the scale of fluctuation being too small to promote failure through semi-continuous weaker zones. There is therefore considerable variance reduction due to the averaging of property values over the large failure surface and this leads to a narrow range of solutions. Indeed, in the limit when $\theta_v = \theta_h \rightarrow 0$, this case is analogous to a conventional 2D deterministic analysis based on $\bar{s}$.

- Mode 2: For $H < \theta_h < L/2$, it is more likely for failure to propagate through semi-continuous weaker zones, thereby forming discrete 3D failures that can either be separate or inter-connected. In this case, there is a wide range of solutions and slope reliability decreases as the slope length increases, due to the increased chance of encountering a weak zone that is capable of triggering failure.

- Mode 3: For $\theta_h > L/2$, there is an increasing likelihood of the failure surface extending along the slope length, in a similar manner to Mode 1, due to the spatial variability taking on a more layered appearance. However, in contrast to Mode 1, there is a wide range of solutions (i.e. with failure mechanisms initiating from any depth), mainly due to the wide range of strengths possible for the soil 'layers' in

the vicinity of the slope toe. In the limit when $\theta_h \to \infty$, this case is analogous to a 2D stochastic analysis.

Note that the above classification was based on a vertical SOF equal to one fifth of the slope height and that, for a larger θ_v, there may be a greater possibility of failure being attracted to semi-continuous weaker zones (i.e. Mode 2 failure). Also, the value of θ_h/L at which the predominant failure mode changes from 2 to 3 is rather subjective. Although $\theta_h/L = 1/2$ seems logical (Hicks and Spencer, 2010), $\theta_h/L > 1$ is more apparent from the results in the present study, as will be observed in due course. Indeed, Hicks et al. (2014) carried out detailed studies for long slopes, with and without a foundation layer, and, through automatically computing slide volumes and lengths, demonstrated that the above values of θ_h (relative to H and L) are merely guidelines for the transition from one failure mode to another. In particular, they showed that Mode 2 failures are possible for virtually any value of θ_h, thereby highlighting the difficulty of computing a 2D failure mechanism in a heterogeneous soil.

Keeping in mind the above failure mode categories, a series of RFEM analyses has been conducted to compare with Vanmarcke's (1977b) theoretical solution.

4.4.1. PROBLEM DESCRIPTION

The reliability assessment has been made for a $L = 50$ m long slope, of the same cross-sectional dimensions as studied by Hicks and Spencer (2010). Hence it is $H = 5$ m high, with a 45° slope angle, and has no foundation layer. Note that Hicks et al. (2014) carried out detailed RFEM analyses of a similar slope, with and without a foundation layer, and demonstrated that the absence of a foundation layer had little influence on the general findings. Hence, no foundation layer has been considered here, in order to reduce the computational effort. Moreover, the slope angle and height have been chosen as being reasonable dimensions for this type of comparison, based partly on previous experience in analysing slopes of differing angles and heights (Hicks and Samy, 2004; Fenton et al., 2013).

Figure 4.3 shows the 3D finite element mesh discretisation used in the RFEM analyses, as well as a 2D cross-section, relative to a Cartesian (i.e. x–y–z) coordinate system. The mesh comprises 4000 20-node hexahedral elements. Each element uses $2 \times 2 \times 2$ Gaussian integration, and each has dimensions of 1.0×1.0 m in plan and 0.5 m in depth, except for along the slope face where the elements have been distorted to model the correct slope angle, as indicated in Fig. 4.3(a). The boundary conditions are a fixed base, rollers on the back (y–z) face preventing displacement perpendicular to the face, and rollers on the end (x–z) faces allowing only vertical displacement. Detailed explanations for this choice of boundary conditions are given in Spencer (2007), Hicks and Spencer (2010) and Hicks et al. (2014). In particular, Spencer (2007) discussed the various options for the end boundaries, which can have a significant influence on the response of relatively shorter slopes as demonstrated by Griffiths et al. (2009b) who considered both perfectly smooth and perfectly restrained boundaries for slopes up to $L/H = 16$. Spencer (2007) found that restraining only the y-direction led to a bias in failures near the mesh ends, probably due to the greater influence of weaker zones arising from the implied symmetry of the random field about the mesh ends when allowing free movement in the x–z plane. In contrast, he observed no such bias when restraining the mesh in both the
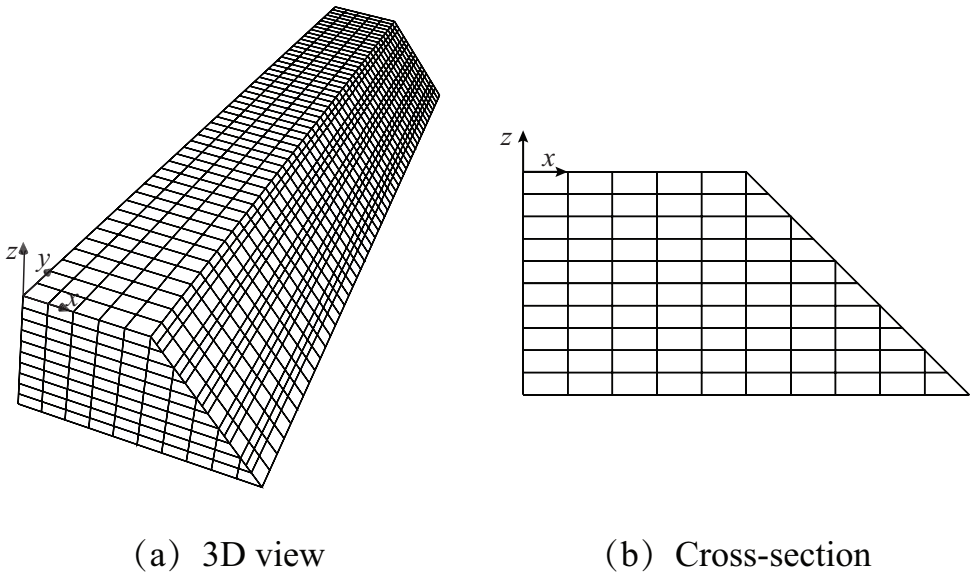
(a) 3D view   (b) Cross-section

Figure 4.3: Finite element mesh discretisation for a 50 m long slope

x and y directions, while leaving the z-direction free, and obtained results for slopes of different lengths that were supported by probabilistic theory. Note that the Author has investigated the location of the back ($x = 0$) boundary, for different values of θ_h, for two cases; one with the boundary 5 m from the slope crest and the other with the boundary at a distance of 10 m. As the differences in the computed results between the two cases were negligible, the more efficient 5 m case has been used here.

The calculations are for a soil with a unit weight of 20 kN/m^3 and a spatially varying undrained shear strength s represented by a normal distribution. The mean undrained shear strength is $\bar{s} = 26$ kPa, which corresponds to $\bar{F} = 1.6$ for a plane strain homogenous analysis based on Taylor's (1937) stability factor. The coefficient of variation of s is $V_s = \tilde{s}/\bar{s} = 0.2$, which is within the range of commonly found values in practice (Hicks and Samy, 2002) and also small enough to ensure that truncating the normal distribution, to prevent the possibility of negative values, has a negligible effect on the analysis. In practice, the vertical scale of fluctuation can easily be found from in-situ (e.g. cone penetration) testing and is generally small relative to the height of a slope (e.g. θ_v is often between 0.5-1.0 m). In contrast, the horizontal scale of fluctuation is difficult to measure, although it is generally much larger than the vertical scale of fluctuation. Hence, in this chapter θ_v is held constant at 1.0 m (= $H/5$) throughout the investigation, whereas a wide range of values has been considered for θ_h (in which $\theta_h = \xi\theta_v$).

In the RFEM analysis, the random field cell values of undrained shear strength are mapped onto the finite element mesh at the Gauss point level (see Hicks and Spencer (2010) for more details). As $2 \times 2 \times 2$ Gaussian integration has been employed, this means that, in the vertical direction, the random field cell size is $0.25 \times \theta_v$, whereas, in the horizontal direction, the cell size is usually much smaller than θ_h, thereby ensuring that the

spatial variability is modelled in sufficient detail. The clay stress–strain response is modelled using an elastic–perfectly plastic Tresca soil model with the following elastic model parameters: Young's modulus $E = 1.0 \times 10^5$ kPa, and Poisson's ratio $v = 0.3$ (Griffiths and Lane, 1999). Note that, although an undrained analysis implies a Poisson's ratio of 0.5, the smaller value used herein aids numerical stability and efficiency, as well as promoting a more realistic in-situ stress field (Wang et al., 2016). Moreover, it has negligible influence on the predicted factor of safety in slope stability analysis using simple elasto-plastic models.

The mesh is loaded by applying gravitational loading to generate the in situ stresses and the factor of safety is computed using the strength reduction method (Smith and Griffiths, 2005; Hicks and Spencer, 2010); i.e. for each realisation, the slope is repeatedly analysed for progressively lower shear strengths, with the factor of safety (F_R) being the amount by which the original random field cell values are scaled down to cause failure. Hence each realisation involves taking the slope to failure and, at failure, the value of F_R is recorded, as are the slide volume and slide length.

4.4.2. VANMARCKE SOLUTION

In order to investigate Vanmarcke's (1977b) analytical solution, an estimation of A and L_a is required (equations 4.2–4.4). This follows the work of Hicks et al. (2008) and Nuttall (2011), and involves locating the rupture surface in a plane strain finite element (FE) analysis of a homogeneous slope that is taken to failure using the strength reduction method. Note that the same values of A, L_a and $\bar{F}$ (resulting from the same critical slip surface) can be obtained via the circular arc method within a limit equilibrium context, although the definition of the factor of safety is different to the strength reduction method within a finite element context; this is because only a purely cohesive soil is considered herein.

Figure 4.4(a) shows that an imaginary point in space, well above the centre of the slope face, is chosen. Next, a series of lines radiating out from this point (across the slope mesh) are considered. The maximum value of the shear strain invariant along each line is detected and, by connecting the locus of the maxima from all the lines, the rupture surface is defined. The surface may then be smoothed by polynomial curve fitting using a least squares approach, and the arc length and slip area then found by numerical integration (Fig. 4.4(b)). For the present slope geometry and failure mechanism, the integrated length of the rupture surface is $L_a = 12.0$ m and the slip area is $A = 23.0$ m^2.

To illustrate the use of Vanmarcke's (1977b) solution, the case of $\theta_h = 6$ m is used as an example. Calculating the slope's mean factor of safety, $\bar{F}_{b_c}$, for the probable failure length, b_c, is equivalent to calculating the factor of safety for a homogenous 3D cylindrical failure, assuming $s = \bar{s} = 26$ kPa and taking account of the end contributions. Firstly, using equation 4.4 and the estimates of $L_a = 12.0$ m and $A = 23.0$ m^2, d_0 is calculated to be 3.83 m. This is substituted into equation 4.9, along with the factor of safety based on a plane strain analysis, $\bar{F} = 1.6$, to give the most probable failure length of $b_c = 10.2$ m (i.e. based on $\theta_h = 6$ m). This is substituted into equation 4.2 to give the mean traditional factor of safety for a slope failure of that length, $\bar{F}_{b_c} = 2.2$. Note that this is considerably higher than $\bar{F} = 1.6$, demonstrating the large increase in resistance to failure, due to the end resistance, for the predicted short failure length.

4
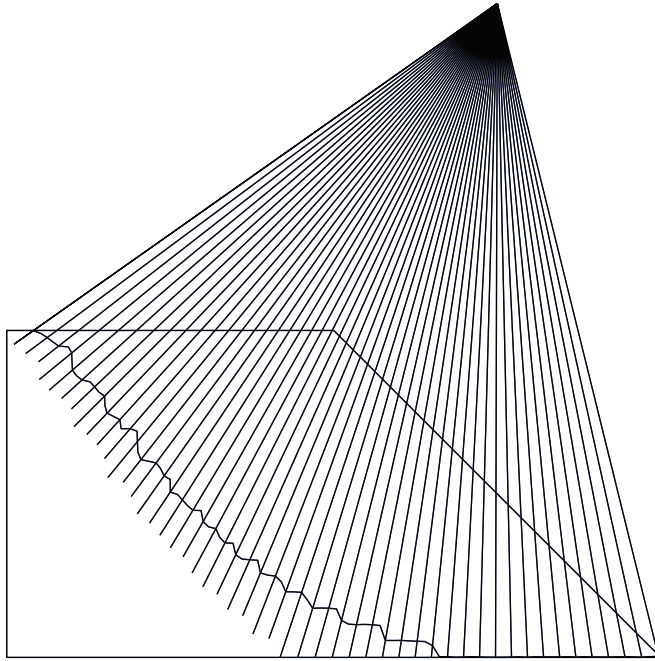
(a) Radial scan method and rupture surface
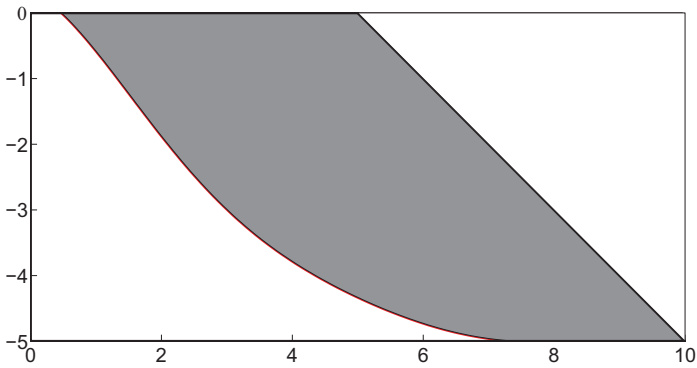
(b) Smoothed surface and slip area shown shaded

Figure 4.4: Determination of cross-section failure geometry

For estimating the standard deviation of the safety factor, the equivalent SOF is determined using equation 4.8. For a slope with no foundation layer, Δz_2 equals zero, as discussed earlier. With reference to Fig. 4.4, the 12.0 m long failure arc may be crudely approximated as a horizontal 4 m segment starting at the slope toe, plus a second 8 m segment from the base to the top of the soil layer. Therefore, as a first approximation $\Delta x \approx 8$ m (i.e. the horizontal segment plus half the inclined segment) and $\Delta z_1 \approx 4$ m (i.e. half the inclined segment). (Note that this ratio of Δx to Δz_1 is also the approximate ratio of the lateral to vertical dimensions of the slide extent; i.e. 9.5/5.0, as seen in Fig. 4.4(b).) By substituting these values, as well as $\theta_v = 1$ m and $\theta_h = 6$ m, into equation 4.8, θ_e is evaluated.

Although this is a rather subjective method of obtaining θ_e, the approximated values for different θ_h were found to be in good agreement with the values back-figured from 2D RFEM analyses using a numerical procedure (Jaksa et al., 1999). Specifically, for an ensemble of random fields, the failure surfaces computed in the corresponding slope stability analyses were identified using the ridge-finding technique illustrated in Fig. 4.4(a), and the spatial variation of soil properties along each failure surface then determined by identifying the random field cells through which the failure surface propagated. The sample correlation functions were then calculated for all the realisations, and a 1D exponential correlation function (i.e. equation 4.14 for only the term in τ_1) then fitted to the averaged sample correlation function to find the scale of fluctuation along the failure surface. This was done for various horizontal scales of fluctuation (for a given θ_v), and the back-figured equivalent scales of fluctuation were found to be in good agreement with the estimated value based on equation 4.8 and the chosen values of Δx and Δz_1.

Finally, $\tilde{F}_{b_c}$ is estimated using equations 4.5–4.7 and $V_s = 0.2$, to give $\Gamma(b) = 0.77$ and thereby $\tilde{F}_{b_c} = 0.106$ for $\theta_h = 6$m. Table 4.1 lists the theoretical means and standard deviations of F_{b_c} for all values of θ_h considered in this chapter. Note that, in contrast to the RFEM analysis which considers a slope of fixed length (L), the Vanmarcke solution is independent of slope length and that, for $\theta_h > L = 50$ m, the derived value of b_c used to calculate $\bar{F}_{b_c}$ and $\tilde{F}_{b_c}$ is also greater than 50 m (from equation 4.9). Table 4.1 shows that, although $\tilde{F}_{b_c}$ has almost converged by the time $\theta_h = 50$ m (i.e. corresponding to when $b_c = L$), $\bar{F}_{b_c}$ continues to reduce towards $\bar{F} = 1.6$ as θ_h increases further. Hicks et al. (2014) showed that, for the same cross-section, a homogeneous slope of $L/H \geq 10$ behaves in a similar manner to plane strain. The fact that a larger L/H is implied for the Vanmarcke solution is likely to be due to the overestimated end resisting moment (referred to earlier).

4.4.3. RFEM results and comparison

Numerical simulations based on RFEM analyses comprising $N = 500$ realisations have been conducted for values of θ_h in the range $1 \leq \theta_h \leq 1000$ m (with $\theta_v = 1$ m in all cases). Each realisation involves the generation of a random field of s, based on the statistics of s and using local average subdivision (Fenton and Vanmarcke, 1990), and the subsequent FE analysis of the slope to find the factor of safety (see Table A.1 for an indication of the calculation times, noting that the time needed for the generation of the random field is negligible compared to the FE calculation). Further details of the methodology can be

Table 4.1: Means and standard deviations of Vanmarcke and RFEM factors of safety ($\theta_v = 1.0$ m, $\bar{F} = 1.60$)

	Vanmarcke		RFEM	
SOF (θ_h: m)	Mean	Standard deviation	Mean	Standard deviation
1	2.2	0.029	1.59	0.014
2	2.2	0.050	1.58	0.027
6	2.2	0.106	1.55	0.064
12	2.11	0.148	1.53	0.100
24	1.86	0.154	1.52	0.126
50	1.72	0.157	1.54	0.137
100	1.66	0.158	1.57	0.147
1000	1.61	0.160	1.59	0.157

found in, for example, Hicks and Spencer (2010).

Figure 4.5 shows the resulting histograms of the realised factor of safety, F_R, as well as fitted normal distributions, for θ_h= 6, 24 and 100 m. For each value of θ_h, the mean ($\bar{F}_R$) and standard deviation ($\tilde{F}_R$) of F_R are indicated. The figure shows that the normal distribution fits the results of the Monte Carlo simulations reasonably well and the same was also found for other values of θ_h. Moreover, the output (i.e. factor of safety) means and standard deviations were found to have converged (see Appendix B for the convergence plots), indicating that enough realisations were used in the simulations. Although more realisations would have led to a further increase in accuracy, especially for cases in which the reliability index is high, the Author has followed the suggestion of Fenton and Griffiths (2010); i.e. to employ the continuous fitted distribution, based on the assumption that the distribution of factor of safety continues to be modelled by the fitted distribution in the distribution tails. As this approach was considered to be sufficient for the purposes of the comparative study in this chapter, it is the fitted normal probability density functions (PDFs) that have been used to compare with the results obtained via Vanmarcke's (1977b) model.

Figure 4.6 shows the RFEM PDFs of F_R, and also the slide volumes (as a percentage of the total mesh volume) associated with individual realisations, for each value of θ_h; i.e. the slide volume is computed for each realisation and plotted as a single cross corresponding to the value of F_R for that realisation. Fig. 4.7 summarises the results of all realisations in terms of (a) the mean and standard deviation of F_R, and (b) the mean slide volume and mean slide length, indicating trends consistent with the longer slopes analysed by Hicks and Spencer (2010) and Hicks et al. (2014). The corresponding solutions based on Vanmarcke's (1977b) 3D model are also shown in both figures, as is the computed (FE) slide volume for an analysis based on a homogeneous soil (indicated by the horizontal broken line). Note that, in Fig. 4.7(b), the Vanmarcke solutions for slide volume and length (which are based on a slope failure at a given location within a slope of infinite length) have been truncated at $\theta_h = 50$ m, to make them consistent with the finite slope length analysed using RFEM. Note also that, for both the RFEM and Vanmarcke approaches, the terms 'slide/failure volume' and 'slide/failure length' here

(a) $\theta_h = 6\,\text{m}$

(b) $\theta_h = 24\,\text{m}$
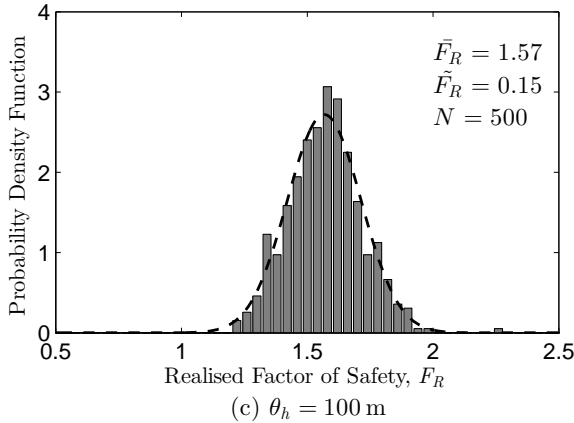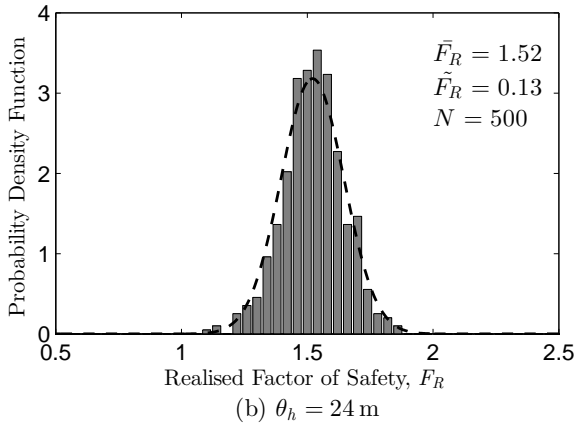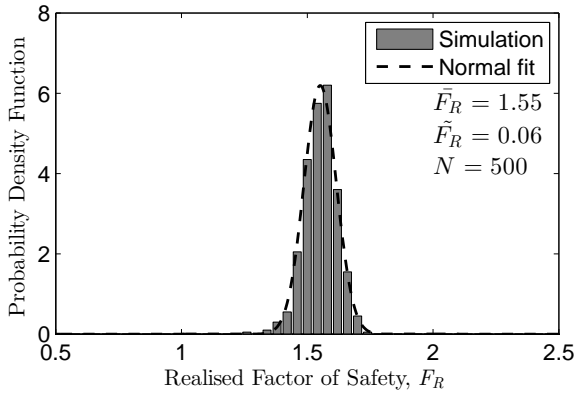

(c) $\theta_h = 100\,\text{m}$

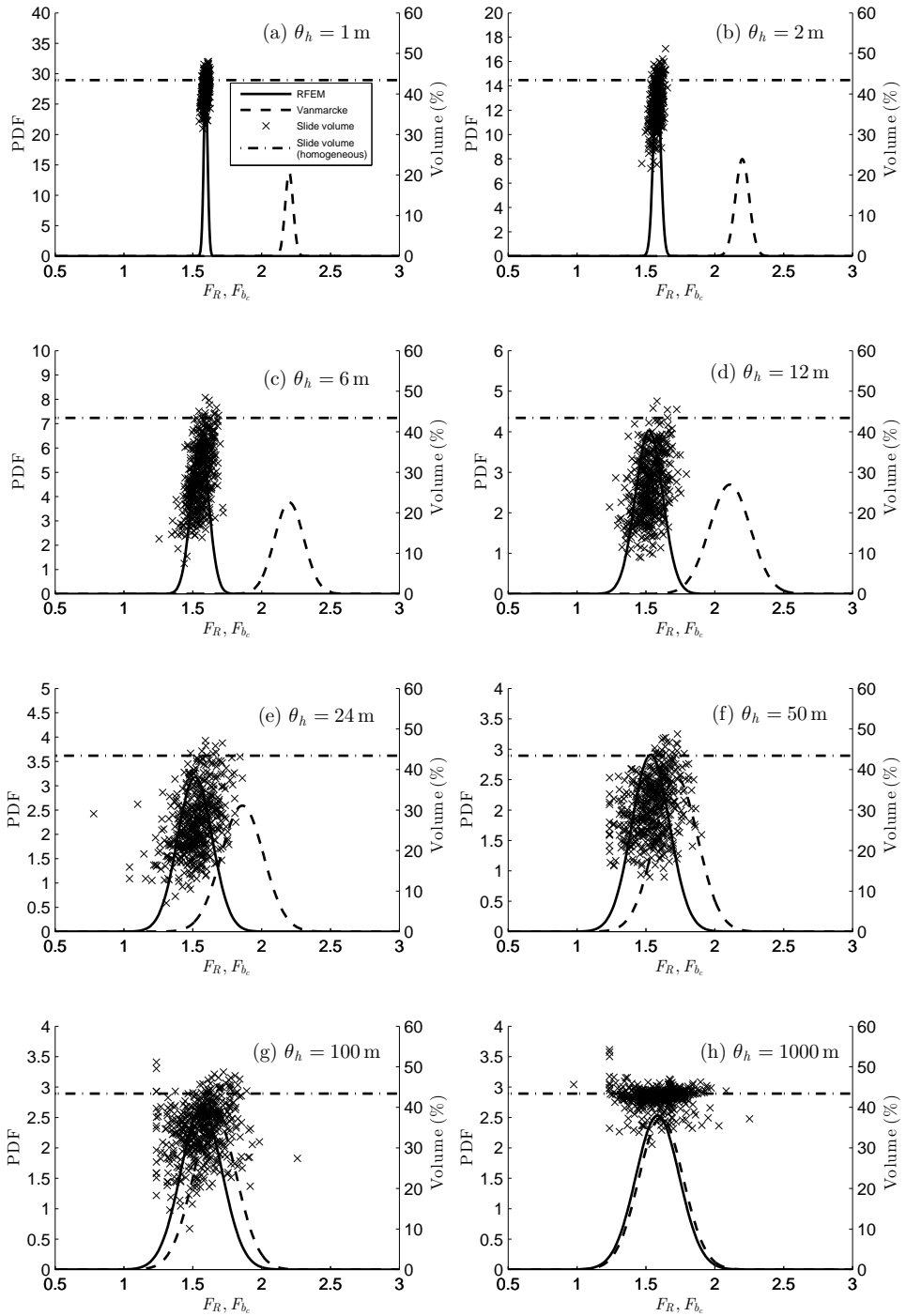Figure 4.5: Probability density functions of the realised factor of safety for a 50 m long slope

Figure 4.6: Influence of θ_h on PDF of factor of safety and range of RFEM slide volumes

refer to the geometry of the mass of soil that dictates the factor of safety of the slope; i.e. they represent the geometry of the soil mass that slides along the 3D failure surface that would form should the shear strength in the slope be scaled down (by the factor of safety) to cause slope failure.

The slide volume for each realisation is approximated as the volume of all elements with an average nodal x (out-of-slope-face direction) displacement greater than some threshold value, which is calibrated against the more rigorous ridge-finding technique for a 2D slice taken through the centre of a homogeneous slope; i.e. it is the displacement iso-surface that bounds the same failed volume as obtained by locating the critical slip surface using contours of shear strain invariant (see Hicks et al. (2014) for further details). For the present problem, this threshold value is estimated to be 26% of the maximum computed x displacement. The mean slide volume, as plotted in Fig. 4.7(b), is then the average of the slide volumes from all the realisations.

As the failure length constitutes an explicit part of the Vanmarcke solution, to facilitate understanding, the procedure of Hicks et al. (2014) is implemented to estimate the mean failure length in an RFEM analysis. In each realisation, the failure length is estimated to be the integrated length, along the slope in the longitudinal direction, for which the x displacement is greater than the threshold displacement (for the row of elements directly above the slope toe); the failure length is then averaged over the ensemble of realisations for a given θ_h. The results are shown in Fig. 4.7(b) for different values of θ_h. The strong positive correlation between the mean failure length and mean failure volume indicates that the above estimation is reasonable. Note that the estimated failure lengths for very small and very large θ_h are slightly less than the slope length, due to the boundary conditions constraining the failure mechanism and displacement magnitudes near the mesh ends (thereby making the threshold displacement less applicable in these locations). Moreover, the estimated failure length does not differentiate between the number of slides over the slope length (Hicks et al., 2014).

Figures 4.6(a) and (b) suggest that, for $\theta_h = 1$ m and $\theta_h = 2$ m, most failures may be categorised as Mode 1, as indicated by both the narrow range of RFEM safety factors and narrow range of slide volumes. Moreover, most slide volumes are relatively large (30-50% of the total mesh volume, as compared to 43.4% for the homogeneous case), indicating failure along most of the slope length, as is also highlighted by the mean slide volumes and lengths plotted in Fig. 4.7(b). As θ_h increases, the Mode 2 failure mechanism becomes dominant (Fig. 4.6(c-e)), as indicated by the wider distributions of both F_R and the slide volumes. As θ_h increases to still larger values (Figs. 4.6(f-h)), Mode 3 mechanisms become more apparent, with the possible slide volumes now distributed over a still larger range of F_R. However, Figs. 4.6(f-g) also indicate that a high proportion of Mode 2 failure mechanisms remain, even for values of θ_h around or above the slope length, which supports the previous finding of Hicks et al. (2014) that 2D failure mechanisms are very difficult to compute in a 3D heterogeneous soil slope. The results in Fig. 4.6(h) represent the limiting condition, for when $\theta_h \rightarrow \infty$; in this case, the slide volume remains rather stable at around 40-45%, indicating that most failure mechanisms are Mode 3.

The corresponding solution due to Vanmarcke (1977b) is also plotted in Fig. 4.6. It can be seen that, for values of θ_h associated with RFEM failure Modes 1 and 2, the RFEM
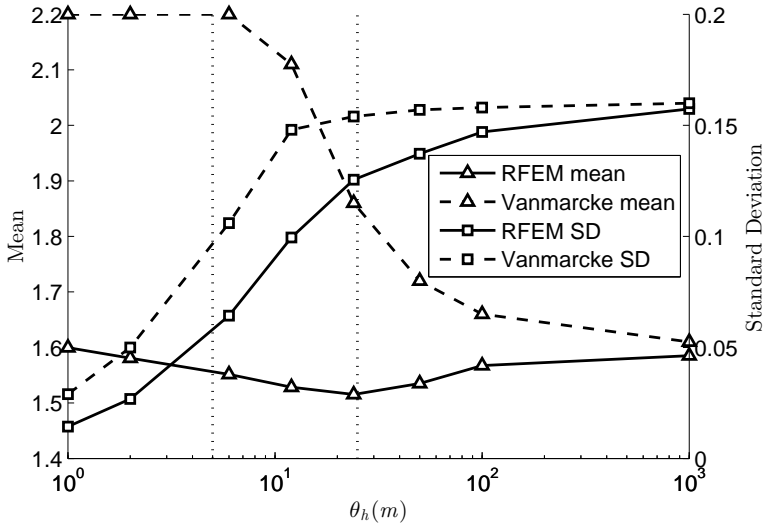
(a) Mean and standard deviation (SD) of factor of safety versus θ_h
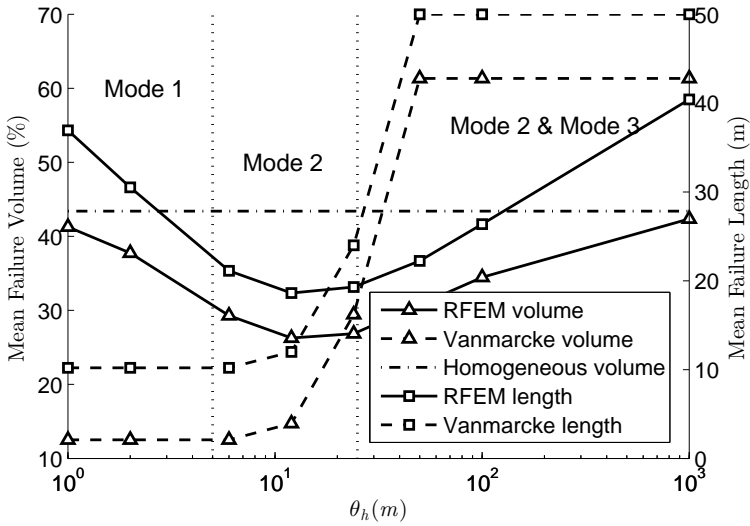
(b) Failure volume and length versus θ_h

Figure 4.7: Comparison between RFEM results and Vanmarcke's (1977b) solution

response (e.g. the mean factor of safety) is significantly lower than the corresponding Vanmarcke solution: the predicted curves from the Vanmarcke solution have values of F_{b_c} well above the mean plane strain factor of safety of $\bar{F} = 1.6$, whereas, for RFEM analyses, most F_R values are slightly below this value. For larger values of θ_h that are nominally associated with the RFEM transition to Mode 3, the two solutions get closer, and, for the limiting condition of $\theta_h = 1000$ m, when nearly all RFEM failures are Mode 3, there is close agreement between the two solutions.

The above observations may be explained by the way in which the Vanmarcke solution evolves (i.e. how the PDF changes with θ_h). For $\theta_h \le b_c$ ($\theta_h = 1, 2, 6$ m in Figs. 4.6(a-c)), the mean of F_{b_c} does not change (see equations 4.2 and 4.9(a)). In this case, the Vanmarcke solution predicts a most probable failure length of 10.2 m, as shown in Fig. 4.7(b). Equation 4.2 implies that these predicted short slides are heavily influenced by the end resistance of the failure surface, leading to a very high mean factor of safety of $\bar{F}_{b_c} = 2.2$ (Fig. 4.7(a)). In contrast, the RFEM results predict failure along most of the slope length (Fig. 4.7(b)) and a much lower mean factor of safety (Fig. 4.7(a)), the larger failure length being due to the small SOF causing the soil mass to behave like a homogeneous material (i.e. promoting a Mode 1 type failure).

For $\theta_h \ge b_c$ ($\theta_h = 12, 24, 50, 100, 1000$ m in Figs. 4.6(d-h)), the mean of F_{b_c} decreases (equations 4.2 and (4.9b)). The case of $\theta_h \approx 12$ m can be considered as when the Vanmarcke PDF starts moving to the left, so giving a decreasing mean factor of safety as shown in Fig. 4.7(a). For the limiting condition of $\theta_h = 1000$ m, the influence of the end resistance becomes negligible in the Vanmarcke solution (equation 4.2), and the two solutions then coincide (Figs. 4.6(h) and 4.7(a)). In this case, the RFEM failure mechanism fits the assumption made in Vanmarcke's simplified model; i.e. a cylindrical failure surface, as indicated in Fig. 4.6(h) by the narrow range of slide volumes which approximate to the homogeneous slide volume of 43.4%. Moreover, the slope failure propagates along the entire slope length (see Fig. 4.7(b)), which is also consistent with Vanmarcke's model.

For comparative purposes, the mean and standard deviation (SD) of F_{b_c} and F_R, plotted in Fig. 4.7(a), are listed in Table 4.1. Note that only the critical failure length b_c is considered in obtaining the mean and standard deviation of F_{b_c}, whereas the mean and standard deviation of the factor of safety F_R, from the RFEM simulation, includes the effect of failures of various lengths (especially for Mode 2 failures). It can be seen that the mean Vanmarcke solution reduces as θ_h increases, i.e. due to the reduced influence of the end contribution in equation 4.2. On the other hand, the mean RFEM solution reduces (from 1.59 to 1.52) as θ_h increases to 24 m, due to the relatively greater influence of weaker zones as the failure mechanism seeks out the weakest path. Typical RFEM failure mechanisms are illustrated in Fig. 4.8; i.e. in terms of computed x-displacement (out-of-slope-face) contours, for $\theta_h = 12$ m. The estimated slide volumes indicate that the automated method of estimation has been successful.

Figure 4.7(a) and Table 4.1 show that the standard deviation of the RFEM results is less than that of the Vanmarcke results, especially for lower values of θ_h. This is partly due to the approximate form of the variance reduction factor used in equation 4.6 in Vanmarcke's (1977b) model, compared to the variance function derived from the correlation function (equation 4.14) used in the current RFEM model; specifically, the variance reduction factor is approximated as, or close to, unity in Vanmarcke's model for most val-

4
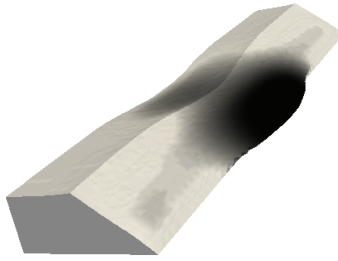
(a) Vol = 16.2%

(b) Vol = 26.5%
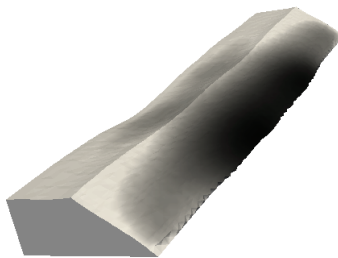
(c) Vol = 35.7%

Figure 4.8: Example failure mechanisms for θ_h = 12 m (Vol indicates the slide volume as a percentage of mesh volume; displacement magnification scale = 400)

ues of θ_h, whereas some reduction should be introduced (Vanmarcke, 2011), as has been done in the RFEM model. Although the variance reduction factor in Vanmarcke's model is less than unity for $\theta_h = 1$ m, $\theta_h = 2$ m and $\theta_h = 6$ m, the resulting standard deviation is still much greater than the RFEM result, due to the short predicted failure length in this case (equation (4.6b)). As the horizontal SOF becomes large and Mode 3 failures start to dominate in the RFEM analyses, $\bar{F}_R$ approaches 1.6 (from below) and $\bar{F}_R$ tends to a maximum which is closely related to the equivalent SOF for a cross-section taken through the slope (i.e. using equations 4.5–4.7, with $\theta = \theta_e$ in equation 4.7). Indeed, the RFEM standard deviation converges toward the solution predicted by equation 4.5 as θ_h becomes very large. Note that this solution is less than that for the isotropic case, i.e. for $\theta_v = \theta_h = \infty$, in which the coefficient of variation of the factor of safety would tend to the coefficient of variation of the undrained shear strength (i.e. the input V_s). This is due to the failure surface needing to pass upwards through 'layers' in the slope with s values 'uncorrelated' to those for the 'layer' in which failure initiates (due to the small θ_v of 1.0 m).

4.4.4. SUMMARISING COMMENTS

Figure 4.9 shows the difference between the Vanmarcke and RFEM solutions, as a percentage of the RFEM solution and as a function of θ_h. It is seen that the relative differences in the mean and SD of the factor of safety generally reduce as θ_h increases.

The biggest differences occur for values of θ_h associated with Mode 1 failure (in the RFEM model), and are due to the two models predicting completely different failure lengths; as already discussed, the Vanmarcke model predicts a 10.2 m failure (and thereby a large relative contribution from the end resistance), whereas the RFEM model predicts failure along the entire slope length (see Fig. 4.7(b)).

The large differences for values of θ_h associated with Mode 2 failure (in the RFEM model) are due to 3 factors: 1) the reduction in $\bar{F}_R$ (in the RFEM model) due to failure seeking to follow the weakest path; 2) the RFEM model including a wide range of possible failure surface geometries and failure lengths; and 3) the overestimated end resistance in the Vanmarcke model. As Mode 3 is approached (in the RFEM model), the differences between the two solutions become smaller than 10%, due to the two methods then accounting for similar failure mechanisms. Note that, although the difference between the two solutions is relatively modest for values of θ_h around 50–100 m, which may be considered a reasonable range of θ_h for some practical applications, this is partly due to the slope being only 50 m long (thereby encouraging more Mode 3 failures). The Author has found that the difference between the two solutions becomes larger as the slope length is increased for a given θ_h.

Interestingly, although there can be a big difference in the means and standard deviations of the factor of safety predicted by the two approaches, this does not necessarily imply a large difference in the reliability index β (equation 4.11), due to the Vanmarcke mean and standard deviation both being larger than the mean and standard deviation in the RFEM analysis for values of θ_h associated with RFEM Modes 1 and 2 (Fig. 4.7(a)). This is illustrated in Fig. 4.10, in which β is plotted as a function of θ_h for four values of $\bar{F}$, the mean factor of safety for the plane strain condition. Note that only those reliability indices corresponding to Modes 2 and 3 are plotted, in order to improve the visualisation

4
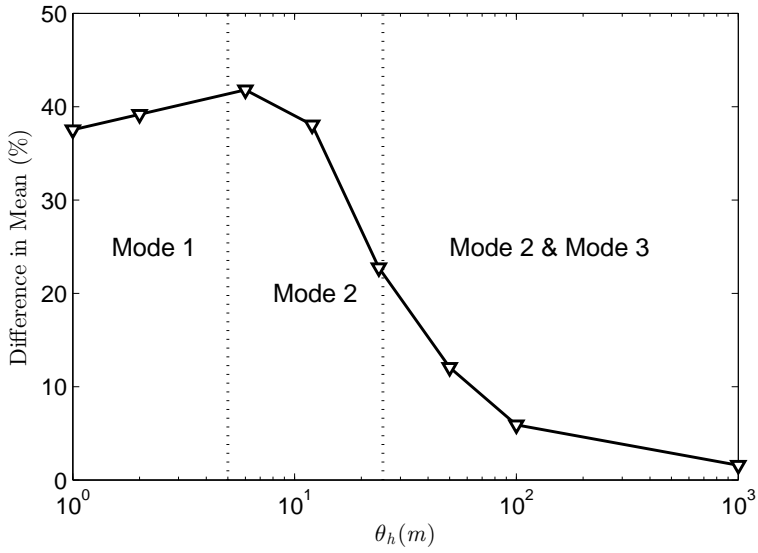
(a) Difference in mean factor of safety versus θ_h
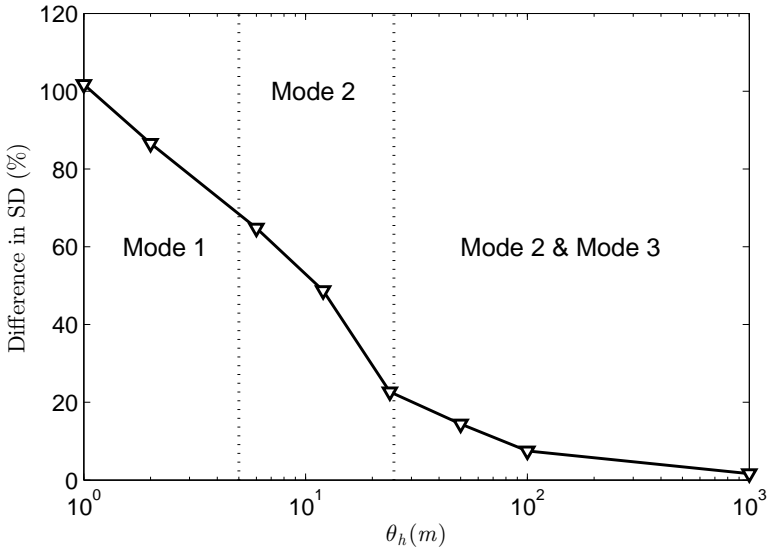
(b) Difference in SD of factor of safety versus θ_h

Figure 4.9: Difference between Vanmarcke and RFEM solutions as a function of θ_h, expressed as a percentage of the RFEM solution
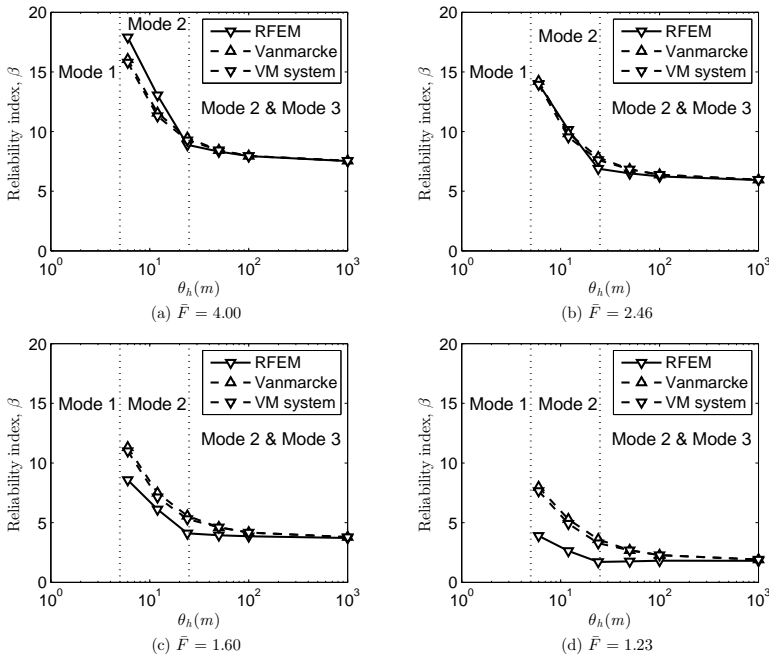
Figure 4.10: Reliability index versus θ_h for different mean plane strain factors of safety

of the differences for more likely values of θ_h. It is seen in Fig. 4.10(c) that, for $\bar{F} = 1.6$ (i.e. the base case), the analytical approach gives an un-conservative solution for the reliability index relative to RFEM. Moreover, in both solutions, the reliability decreases with an increasing SOF. This can be explained by Table 4.1, which shows an increasing SD in the factor of safety due to a decreasing variance reduction. In general, for smaller (and generally more practical) values of $\bar{F}$ (i.e. based on a smaller mean undrained shear strength), the difference is much larger, as seen in Fig. 4.10(d) for $\bar{F} = 1.23$.

Note that, in the above comparison, Vanmarcke's (1977b) approach is based on estimating the probability of failure of the slope for a cylindrical mechanism of the critical length, at some given point along a slope of indeterminate length, whereas the RFEM approach estimates the probability of failure of the slope 'system' for a slope of a fixed length; i.e. all failure mechanisms are possible and these may initiate anywhere over the slope length. However, in his paper, Vanmarcke (1977b) also considered the probability of failure with respect to length effects, using a 'first crossing' technique (Vanmarcke, 1975). This was investigated by the Author (Li and Hicks, 2014) to see how, for the Vanmarcke solution, the probability of failure of a section of length b_c increased with slope length (i.e. assuming that the failed section might occur at any location along the slope). Based on the mean rate of increase of the failure probability per unit length of the slope (Vanmarcke, 1977b), only a small increase in the probability of failure was observed for the 50 m long slope considered in this chapter (corresponding to a reduction in the reliability index of 1-9%, see Fig. 4.10). However, research to investigate the length effect for

much longer slopes is presented in Chapter 5.

4.5. Conclusions

A simple three dimensional slope stability problem has been analysed probabilistically
by both Vanmarcke's (1977b) analytical approach and the random finite element method
(RFEM). For horizontal scales of fluctuation (θ_h) that are large compared to the slope
length, the two approaches give similar results, because most of the failure surfaces com-
puted in the RFEM analyses are then approximately cylindrical and propagate along the
entire length of the slope, thereby matching Vanmarcke's assumption and resulting fail-
ure length for this limiting condition. In contrast, for smaller values of θ_h (i.e. less than
the slope length), the two approaches can give significantly different results, with the
RFEM response of the slope generally being much weaker than the Vanmarcke solution.

The large differences may be attributed to 3 factors. Firstly, there is the ability of the
RFEM simulation to seek out the weakest failure path through the slope, thereby reduc-
ing the average shear strength over the failure surface. Secondly, in reality there are many
possible failure surfaces of varying location, size and shape (as may be computed using
RFEM), and it is the spatial averages of material properties over these surfaces that are
influential, not simple spatial averages over a single predefined failure surface (of one
critical length) such as the cylindrical surface assumed in Vanmarcke's solution. Thirdly,
the cylinder ends can significantly increase the resistance to failure in Vanmarcke's anal-
ysis for small values of θ_h (cf. equation 4.2), so that the factor of safety may be greatly
overestimated.

The advantages of Vanmarcke's solution are that it is elegant and simple to use, and
may be considered a useful and practical tool to aid in the design of slopes that are very
long in the third dimension. However, this investigation has highlighted the merits of
more advanced methods of analysis for gaining insight into the performance of simpler
models in general. In particular, they can have an important role to play in identifying
and quantifying the limitations of such models, as well as providing a possible means for
identifying how they may be improved.

5

INFLUENCE OF LENGTH EFFECT ON EMBANKMENT SLOPE RELIABILITY IN 3D

Embankment slopes composed of spatially variable soils have a variety of different failure modes that are affected by the correlation distances of the material properties and the geometry and total length of the slope. This chapter examines the reliability of soil slopes for embankments of different length and utilises parallel computing to analyse very long embankments (up to 100 times the slope height) for a clay soil characterised by a spatially varying undrained shear strength. Based on a series analyses using the 3D random finite element method (RFEM), it is first shown that the reliability of slopes of various length can be efficiently computed by combining simple probability theory with a detailed 3D RFEM analysis of a representative shorter slope of length 10 times the slope height. RFEM predictions of reliability index for long slopes are then compared with results obtained via Vanmarcke's (1977b) simplified 3D method and Calle's (1985) extended 2D approach. It is shown that these methods can give significantly different results, depending on the horizontal scale of fluctuation (SOF) relative to the slope length, with RFEM predicting a lower slope reliability than the Vanmarcke and Calle solutions in all cases. The differences in the solutions for the three methods are attributed to differences in the assumed and computed failure surface geometries.

5.1. INTRODUCTION

A feature of civil infrastructures such as railway embankments, river banks, highways, and levees (or dykes) is a large ratio of the length dimension to the cross-sectional dimension. The stability of these structures is of great concern to geotechnical engineers, due to the potential for huge economic and social impact should they fail (Wolff, 2008). Traditionally, deterministic plane strain analyses have been carried out to assess slope stability via a single factor of safety. More recently, probabilistic plane strain analyses have been used to account for the uncertainty due to soil heterogeneity in slope reliability assessments (Hicks and Samy, 2002; Cho, 2007; Ji et al., 2012; Jiang et al., 2014; Li et al., 2015a). Due to such analyses quantifying the probability of failure, they are a useful supplement to conventional deterministic analyses. However, in both approaches, an infinitely long failure is implied in the third dimension, which is not physically realistic due to the spatial variability of soil properties (as well as variations in slope geometry). The fact that soil heterogeneity is three dimensional can make the use of a 2D analysis debatable (Spencer and Hicks, 2006, 2007; Spencer, 2007; Griffiths et al., 2009b). Indeed, a 3D analysis may be desirable for more realistic predictions of slope reliability (Hicks and Spencer, 2010; Hicks et al., 2008, 2014; Li et al., 2013, 2015c; Ji and Chan, 2014; Ji, 2014).

For the aforementioned structures, the variability in the third dimension can be very important when assessing the reliability of very long infrastructures. This is because the longer the total length of a slope, the greater the chance that a 'weak spot' exists somewhere, and thus the higher the probability of a 'system' failure (Christian and Baecher, 2011). This total length dependency is sometimes referred to as the 'length effect' for long slopes.

In order to allow adequate consideration of the total slope length, which is always missed in conventional slope stability calculations, Vanmarcke (1977b) and Calle (1985) proposed methods for accounting for the length effect in the selection of design factors of safety. Vanmarcke (1977b, 2011) demonstrated analytically that the length effect can be determined by considering the first crossings (or first passage, as in Vanmarcke (1975)) of a random process in the slope length direction, so that the probability of failure can be evaluated as a function of the total slope length. Based on Vanmarcke's (1977a) concept of modelling the spatial variability of soil strength as a random process, Calle (1985) proposed a semi-analytical model for long soil slopes using first-crossing theory (referred to as down-crossing by Calle (1985) and out-crossing by Vrouwenvelder (2006)). He argued that a real finite failure can only occur in a potentially unstable zone in the longitudinal direction; that is, when, in the longitudinal direction, the average soil strength along the potential cross-sectional failure surface drops below the strength required for stability along the finite length.

In contrast to the methods of Vanmarcke (1977b) and Calle (1985), where a cylindrical failure surface is assumed, Hicks and Spencer (2010) investigated length effects for slopes up to 200 m long using RFEM, which makes no prior assumptions regarding the shape of the failure surface. However, a disadvantage of the numerical model was that it was computationally expensive for a full 3D analysis. Fortunately, computing technologies have advanced significantly in recent years, with computational capacity being extended substantially with the aid of grid and cloud computing technologies (Li et al.,

2015d). This chapter uses these new technologies to build on the work of Hicks and Spencer (2010) and Li et al. (2013, 2015c), with particular emphasis on the length effect and a comparative study to compare the relative performance of the above three methods for much longer slopes (up to 500 m long).

Note that the investigation focuses on the length effect within a long 'statistically homogeneous' segment of, for example, a dyke ring system, as such a system is generally idealised in this way, with each segment characterised by statistically homogeneous soil strength properties and loads, as well as similar cross-sectional geometries. A typical segment has a length of 200-1000 m according to Jongejan et al. (2013). For assessing the reliability of an embankment slope with multiple segments having distinctly different properties (e.g. strength, load and geometry), the extended methodology presented by Vanmarcke and Otsubo (2013) can be used by taking account of the correlations between the segments.

In the following sections, Vanmarcke's (1977b) model is briefly revisited (Section 5.2), followed by an explanation of the Author's implementation of Calle's (1985) model (Section 5.3). For both models, only those equations necessary for evaluating the results are presented; for further details, the reader is referred to the original publications. Then, after a brief review of relevant RFEM research (Section 5.4), the relative performance of the three methods is assessed for a simple benchmark problem (Section 5.5).

5.2. Vanmarcke's 3D Model Considering Length Effect

The basic Vanmarcke model based on random field theory is presented in Chapter 4 (Section 4.2). The 'system failure' aspect, i.e. the dependence of failure probability on the total length L, based on 'first crossing' (Vanmarcke, 1975), is presented below. Note that, throughout this chapter, a 'bar' over a symbol denotes the mean of a variable and a 'tilde' denotes its standard deviation.

5.2.1. First crossing of spatial averages along a long embankment

By idealising the 3D failure surface as a cylinder of length b in the longitudinal direction, bounded by two vertical ends, and considering the limit equilibrium of the failure mass, Vanmarcke (1977b) derived the factor of safety F_b (Eq. 4.1). Using FOSM, the reliability index is defined as

$$\beta_b = \frac{\bar{F}_b - 1}{\tilde{F}_b} \tag{5.1}$$

where the value of b that gives the minimum reliability index is the critical failure length b_c (given by Eq. 4.9).

Recall that the probability that a failure of length b_c will occur, $p_f(b_c)$, is given by $p_f(b_c) = P(F_{b_c} \leq 1) = P(U \leq -\beta_{b_c}) = \Phi(-\beta_{b_c})$, where $U = (F_{b_c} - \bar{F}_{b_c})/\tilde{F}_{b_c}$ is a standard normal random variable. By assuming that the failure length b is fixed at its critical value, so that the reliability is minimised, the factor of safety $F_b = F_{b_c}$ of the finite length $b = b_c$, is viewed as a function of y_o, the position of the centre of the failure surface along the longitudinal axis of the slope, as is U. The variation of U in the slope length direction, i.e. $U(y)$, can be viewed as a random function derived from the random process $s(y)$ (recalling that s is the random undrained shear strength), by keeping the length $b = b_c$

fixed and moving the failure cylinder along the slope length axis.

With reference to equations 4.10 and 4.12, a slope failure will occur if the safety factor, F_{b_c}, crosses into the unsafe domain $F_{b_c} \leq 1$ at any location y_o, where $b_c/2 \leq y_o \leq L - b_c/2$ (and L is the slope length). That is, the slope fails if $U(y)$ crosses the failure threshold $(-\beta_{b_c})$ within the length interval $b_c/2 \leq y \leq L - b_c/2$ (see Fig. 5.1). The random function $U(y)$ will be Gaussian (since the moving average strength s_b is assumed to be Gaussian) and the slope reliability (or probability of no down-crossings) will have the form:

$$P_S(L) = \begin{cases} \left[1 - p_f(b_c)\right] e^{-v_{\beta_{b_c}}(L - b_c)}; L \geq b_c \\ 1 - p_f(L); L \leq b_c \end{cases} \tag{5.2}$$

where

$$v_{\beta_{b_c}} = \frac{1}{2\pi} \exp(-\frac{\beta_{b_c}^2}{2}) \sqrt{-\rho''_b(0)} \tag{5.3}$$

is the average number of excursions per unit length, or mean (decay) rate of the threshold level down-crossings.

The term $\rho''_b(0)$ in equation 5.3 is the second derivative of the correlation function $\rho_b(\Delta y)$ of the moving average s_b with respect to Δy, evaluated at $\Delta y = 0$. According to Vanmarcke (1977a), the correlation function $\rho_b(\Delta y)$ has the form,

$$\rho_b(\Delta y) = 1 - \frac{(\Delta y)^2}{b\theta} \tag{5.4}$$

where Δy is the distance between spatial averages s_b. By assuming $v_{\beta_{b_c}} \ll 1$ and $p_f(b_c) \ll 1$, and thereby replacing the exponential form e^{-u} by $1 - u$ in equation 5.2, the probability of slope failure can be expressed as

$$P_F(L) = 1 - P_S(L) \approx \begin{cases} p_f(b_c) + (L - b_c)\, v_{\beta_{b_c}}; L \geq b_c \\ p_f(L); L \leq b_c \end{cases} \tag{5.5}$$

where the term $(L - b_c)\, v_{\beta_{b_c}}$ represents the length effect. The equation only works if the resulting value of $P_F(L)$ is well below one; otherwise, the original expression (equation 5.2) must be used.

5.3. IMPLEMENTATION OF CALLE'S 2.5D MODEL

Whereas Vanmarcke's basic model is based on variance reduction theory in the longitudinal direction, Calle (1985) argued that there is not much variance reduction in that direction for a finite length slope failure, due to real failure only being able to occur in a so-called unstable zone where the factor of safety is less than unity. Calle (1985) first carried out a basic 2D probabilistic (FOSM) Bishop slope stability analysis. This was then extended to determine the probability of occurrence of a potentially unstable zone using the down-crossing method. Finally, the probability of failure was calculated by taking account of the end effect (i.e. the resisting moment due to the ends of the cylindrical failure surface). As the basic probabilistic analysis is a 2D analysis and the length effect is incorporated by the analytical solution of a first excursion problem (Papoulis and Pillai, 2002), this model has often been referred to as a '2.5D' model. The basic procedure is
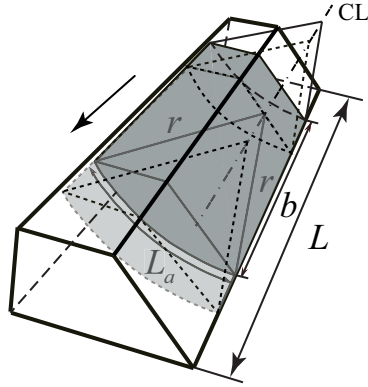
(a) Isometric view
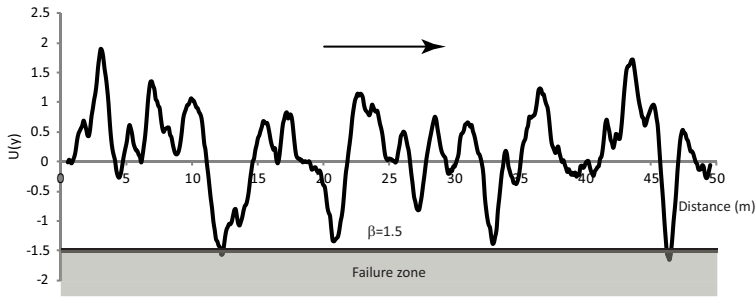
(b) Moving average process $U(y)$

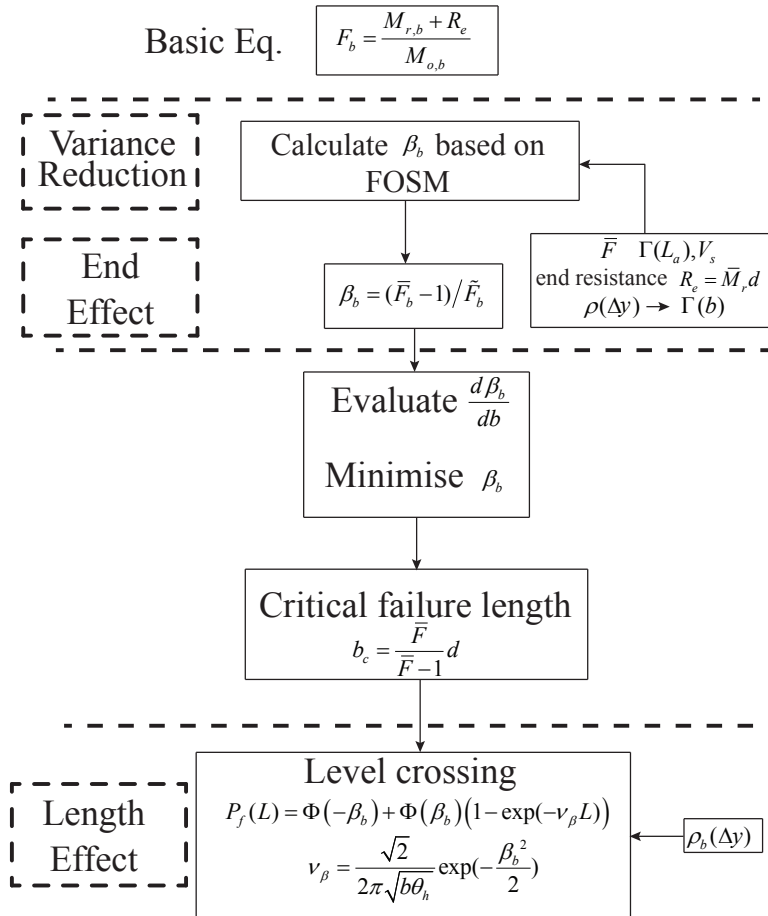Figure 5.1: Vanmarcke's (1977b; 1980) simplified model considering system effect

5

Basic Eq.

$$F_b = \frac{M_{r,b} + R_e}{M_{o,b}}$$

Variance Reduction

Calculate β_b based on FOSM

End Effect

$$\beta_b = (\bar{F}_b - 1)/\tilde{F}_b$$

$$\bar{F} \quad \Gamma(L_a), V_s$$
end resistance $R_e = \bar{M}_r d$
$$\rho(\Delta y) \rightarrow \Gamma(b)$$

Evaluate $\dfrac{d\beta_b}{db}$

Minimise β_b

Critical failure length

$$b_c = \frac{\bar{F}}{\bar{F} - 1} d$$

Length Effect

Level crossing

$$P_f(L) = \Phi(-\beta_b) + \Phi(\beta_b)(1 - \exp(-\nu_\beta L))$$

$$\nu_\beta = \frac{\sqrt{2}}{2\pi\sqrt{b\theta_h}} \exp(-\frac{\beta_b^2}{2})$$

$$\rho_b(\Delta y)$$

Figure 5.2: Flowchart of Vanmarcke's model

Basic Eq. $$F_l = F + \frac{2M_e}{M_o l}$$

| | Calculate cross-sectional β based on FOSM/FORM | mean μ variance σ^2 $\rho(\Delta z)$ |

Bishop Stability Analysis

$$\beta = \frac{\overline{F} - 1}{\tilde{F}}$$

Level crossing

$$P(F(y) < 1) = \Phi(-\beta) + \Phi(\beta)\big(1 - \exp(-N_\beta L)\big)$$

$$N_\beta = \frac{\sqrt{2}}{2\pi\delta_h} \exp(-\frac{\beta^2}{2})$$

$\rho(\Delta y)$

Length Effect

Average failure length

$$l = \Phi(-\beta)/N_\beta$$

End Effect

Add end resistance

$$P_f = P(F_l < 1) = \frac{\Phi(-\beta_l)}{\Phi(-\beta)} P(F(y) < 1)$$

$$\beta_l = \beta + 2M_e / \tilde{F} M_o l$$
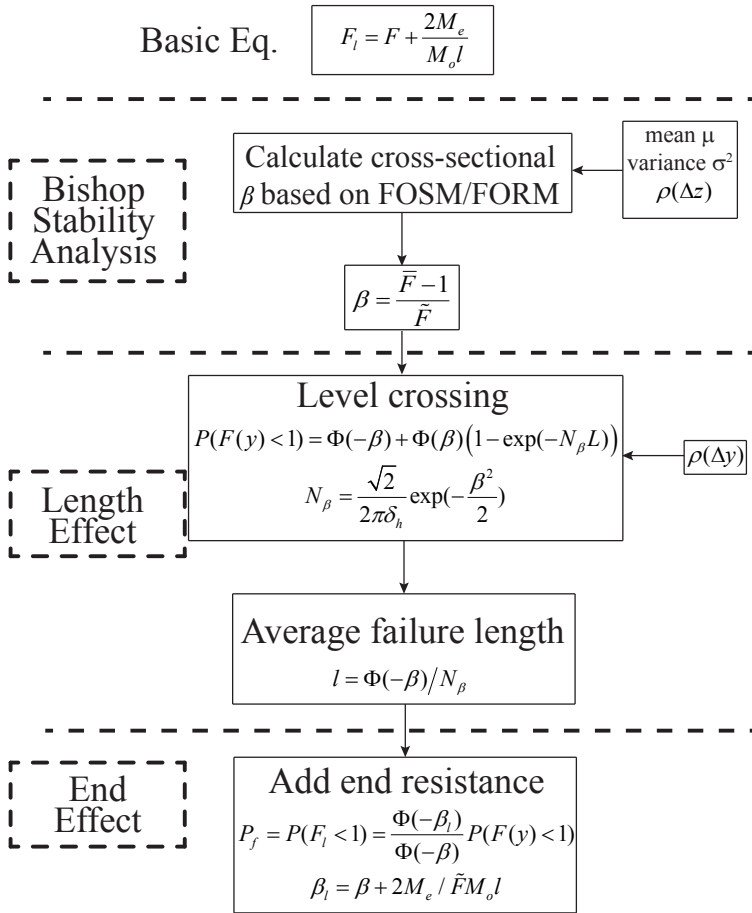
Figure 5.3: Flowchart of Calle's model

presented as follows, whereas, for comparative purposes, Figs. 5.2 and 5.3 compare the main features of the Vanmarcke and Calle models in flowchart form.

The equation defining the factor of safety associated with a finite length failure, F_l, is

$$F_l = F + \frac{2M_e}{M_o l} \tag{5.6}$$

where M_e is the end resisting moment for one of the two end boundaries of the cylinder, l is the expected length of the unstable zone, and F is the cross-sectional (i.e. plane strain) safety factor.

5.3.1. CROSS-SECTIONAL FOSM ANALYSIS
The performance function is defined as

$$G = F - 1 = M_r/M_o - 1 \tag{5.7}$$

where M_o and M_r are the cross-sectional overturning and resisting moments, respectively, and the random variable M_r is a function of the spatially varying undrained shear strength. The first order approximation of the performance function at the 'mean value' point is

$$G' = F' - 1 = F(\bar{\mathbf{s}}) + \{\nabla F_s\}^{\mathrm{T}}(\mathbf{s} - \bar{\mathbf{s}}) - 1 \tag{5.8}$$

where $\mathbf{s}$ is a vector of n random variables (i.e. undrained shear strength $s_1, s_2, \ldots, s_n$), $\bar{\mathbf{s}}$ is a vector of the means $(\bar{s}_1, \bar{s}_2, \ldots, \bar{s}_n)$ of the random variables, and $\{\nabla F_s\}$ is a gradient vector, i.e.

$$\{\nabla F_s\} = \left(\frac{\partial F}{\partial s_1}, \ldots, \frac{\partial F}{\partial s_i}, \ldots, \frac{\partial F}{\partial s_n}\right)^{\mathrm{T}} \tag{5.9}$$

The mean and variance of G' are

$$\bar{G}' = \bar{F}' - 1 = F(\bar{\mathbf{s}}) - 1 \tag{5.10a}$$

$$\tilde{G}'^2 = \tilde{F}'^2 = \{\nabla F_s\}^{\mathrm{T}}[C]\{\nabla F_s\} \tag{5.10b}$$

where [C] is the covariance matrix and its elements are determined by the correlation coefficients between variables s_i and s_j, and by their standard deviations $\tilde{s}_i$ and $\tilde{s}_j$, i.e.

$$C_{ij} = \rho_{ij}\tilde{s}_i\tilde{s}_j \tag{5.11}$$

Due to the horizontal SOF in practice generally being larger than the horizontal dimension of the cross-section, the slope is here simply modelled by n random variables in the vertical direction (Wang et al., 2010) in the Author's current implementation of Calle's model. That is, the undrained shear strength s is assumed to be fully correlated at any given depth, while the n random variables are correlated in the vertical direction via a squared exponentially decaying correlation function involving the vertical lag Δz, modified by an α factor (GeoDelft, 1994), i.e.

$$\rho(\Delta z) = (1 - \alpha) + \alpha \exp(-\frac{\Delta z^2}{\delta_v{}^2}) \tag{5.12}$$

where

$$\alpha = \frac{\tilde{s}_v^2}{\tilde{s}^2} \tag{5.13}$$

and δ_v is the vertical correlation distance, which is related to the scale of fluctuation θ (Vanmarcke, 1983) by a factor of $\sqrt{\pi}$ (i.e. $\theta = \sqrt{\pi}\delta$, see Table 2.1 where $\delta = r$). Typical values of θ_v may range between 0.3 m and 3 m (Hicks and Samy, 2002), corresponding to a range of δ_v of 0.17-1.7 m.

The α factor defined in equation 5.13 is based on the equality,

$$\tilde{s}^2 = \tilde{s}_v^2 + \tilde{s}_h^2 \tag{5.14}$$

in which $\tilde{s}_v^2$ is the average of the variances of different individual vertical boreholes, $\tilde{s}^2$ is the total 'point' variance and $\tilde{s}_h^2$ indicates the variance of the average values of individual boreholes. The derivation of equation 5.14 is given in Appendix C. It may be noticed that, when $\alpha = 1.0$, equation 5.12 simplifies to the conventional squared exponential correlation function often used in literature. In Dutch practice, α values ranging from 0.5 to 1.0 have been used (GeoDelft, 1994). The incorporation of α is to represent lateral variations (of the average values of individual boreholes) that often exist in extensive soil deposits (TAW, 2001); $(1 - \alpha)$ effectively limits the variance reduction function via Eqs. 5.10b and 5.11, thereby taking account of soil variability in the third dimension within a 2D framework. A detailed explanation of the α factor will be given in Section 5.5.1.

The probability of failure is expressed as

$$P\left[G' < 0\right] = P\left[\frac{G' - \bar{G}'}{\tilde{G}'} < \frac{0 - \bar{G}'}{\tilde{G}'}\right] = \Phi\left(-\beta\right) \tag{5.15}$$

where

$$\beta = \frac{\bar{G}'}{\tilde{G}'} = \frac{\bar{F}' - 1}{\tilde{F}'} \tag{5.16}$$

is the cross-sectional reliability index that can be evaluated from equations 5.10. As in Hassan and Wolff (1999), the partial derivatives of the factor of safety with respect to the random variables in equation 5.9 are calculated numerically, by evaluating F using strength parameter values equal to the mean plus or minus one standard deviation, to obtain F^+ and F^-, respectively, i.e.

$$\frac{\partial F}{\partial s_i} = \frac{F^+ - F^-}{2\tilde{s}_i} \tag{5.17}$$

where F^+ and F^- have here been calculated by the finite element method, rather than by a limit equilibrium analysis such as Bishop's method of slices (as used by Calle (1985)).

5.3.2. Determination of the Unstable Zone

The probability that the factor of safety $F(y) = M_r(y)/M_o$, $0 \le y \le L$, is less than unity somewhere along the slope axis is given by

$$P(F(y) < 1) = \Phi(-\beta) + \Phi(\beta)\left(1 - \exp(-N_\beta L)\right) \tag{5.18}$$

where $F(y) < 1$ denotes the event of down-crossing anywhere along the slope axis, L is the total length of the slope, and

$$N_\beta = \frac{1}{2\pi} \exp(-\frac{\beta^2}{2})\sqrt{-\rho''_F(0)} \qquad (5.19)$$

is the average number of excursions per unit length (or mean down-crossing rate).

Note that equation 5.19 is equivalent to equation 5.3, the difference being that equation 5.19 takes $F(y) < 1$ as the down-crossing event, whereas equation 5.3 takes $F_{b_c}(y) < 1$ as the down-crossing event. Therefore, the cross-sectional β is used equation 5.19 and the β_{b_c} for a failure of length b_c is used in equation 5.3. Furthermore, the second term on the right-hand-side of equation 5.18 represents the length effect, so that equation 5.18 would simply be the probability of failure of a cross section should this term be left out.

The expected width of a potentially unstable zone can be expressed as

$$l = \Phi(-\beta)/N_\beta = 2\pi\Phi(-\beta)\exp(\frac{\beta^2}{2})/\sqrt{-\rho''_F(0)} \qquad (5.20)$$

The double prime used in equations 5.19 and 5.20 denotes the second derivative of the correlation function with respect to Δy. The correlation function in the out-of-plane direction takes the form,

$$\rho_F(\Delta y) = (1 - \alpha) + \alpha \exp(-\frac{\Delta y^2}{\delta_h^2}) \qquad (5.21)$$

which leads to

$$\sqrt{-\rho''_F(0)} = \sqrt{2\alpha}/\delta_h \qquad (5.22)$$

Typical values of δ_h range between 25 m and 100 m (GeoDelft, 1994), which is a lot larger than the vertical correlation distance mentioned earlier.

5.3.3. PROBABILITY OF SLOPE FAILURE
Taking into account the end resistance, the probability of failure can be evaluated as

$$P_f = P(F_l < 1) = \frac{\Phi(-\beta_l)}{\Phi(-\beta)} P(F(y) < 1) \qquad (5.23)$$

where the term $\Phi(-\beta_l)/\Phi(-\beta)$ represents the end effect and

$$\beta_l = \frac{\bar{F}_l - 1}{\tilde{F}_l} \qquad (5.24)$$

With reference to equation 5.6, as M_o and M_e are treated as deterministic variables, the mean and standard deviation of F_l are given as

$$\bar{F}_l = \bar{F} + \frac{2M_e}{M_o l} \qquad (5.25a)$$

$$\tilde{F}_l = \tilde{F} \qquad (5.25b)$$

Note that no variance reduction in the length direction is taken into account in equation 5.25b (in contrast with equation 4.5), so this assumption implies that there is not much averaging in the horizontal direction over the failure domain.

Substituting equations 5.25 into equation 5.24 gives the reliability index considering the end effect, i.e.

$$\beta_l = \frac{\bar{F}_l - 1}{\tilde{F}_l} = \beta + \frac{2M_e}{\bar{F}M_o l} = \beta + \frac{2M_e}{\tilde{M}_r l} \tag{5.26}$$

5.4. LENGTH EFFECT USING 3D RFEM

Sections 5.4.1-5.4.4 focus on how RFEM has been used to model the idealised slope that forms the basis of the comparative study reported in Section 5.5.

5.4.1. PROBLEM DESCRIPTION

The reliability assessment has been made for a slope with the same cross-sectional dimensions as that studied by Hicks and Spencer (2010), but for much longer slope lengths varying from 50 m to 500 m. The finite element mesh discretisation is also the same, and is illustrated in Fig. 4.3 for the example of a 50 m long slope. The slope is inclined at 45°, of height $H = 5$ m and rests on a firm base, while the undrained shear strength has a coefficient of variation of $V = 0.2$, a vertical scale of fluctuation of $\theta_v = 1$ m and a horizontal scale of fluctuation θ_h that takes on different values for different groups of analyses. The clay is modelled by an elastic, perfectly plastic Tresca soil model, with an elastic modulus, $E = 1.0 \times 10^5$ kPa, and Poisson's ratio, $v = 0.3$ (Smith and Griffiths, 2005). The random field cell values are mapped onto the 8 Gaussian integration points within each 20-node finite element, instead of onto the element itself, in order to emulate the spatial variability as accurately as possible (Hicks and Samy, 2002; Hicks and Spencer, 2010).

5.4.2. BOUNDARY CONDITIONS

The applied boundary conditions are a fixed base, rollers on the back (y-z) face preventing displacement perpendicular to the face, and rollers on the end (x-z) faces allowing only vertical displacement.

Spencer (2007) investigated two options for the end-boundaries of slopes up to L/H = 40, and found that restraining only the y-direction (i.e. to give '2D' boundary conditions) led to a bias in failures near the mesh ends, probably due to the greater influence of weaker zones arising from the implied symmetry of the random field about the mesh ends when allowing free movement in the x-z plane. In contrast, he observed no such bias when applying an intermediate boundary condition (i.e. restraining the mesh ends in both the x- and y-directions, while leaving the z-direction free). Meanwhile, Griffiths et al. (2009b) investigated perfectly smooth and perfectly restrained end-boundaries, demonstrating that the choice of boundary can have a significant influence on the response of relatively shorter slopes up to $L/H = 16$.

The influence of free (i.e. 2D), 'intermediate' and rough end-boundary conditions (BCs) on the response of heterogeneous slopes of different length has here been investigated for slopes up to 500 m long (i.e. $L/H = 100$). Fig. 5.4 shows that intermediate and rough BCs give almost the same result for two example slope lengths. However,
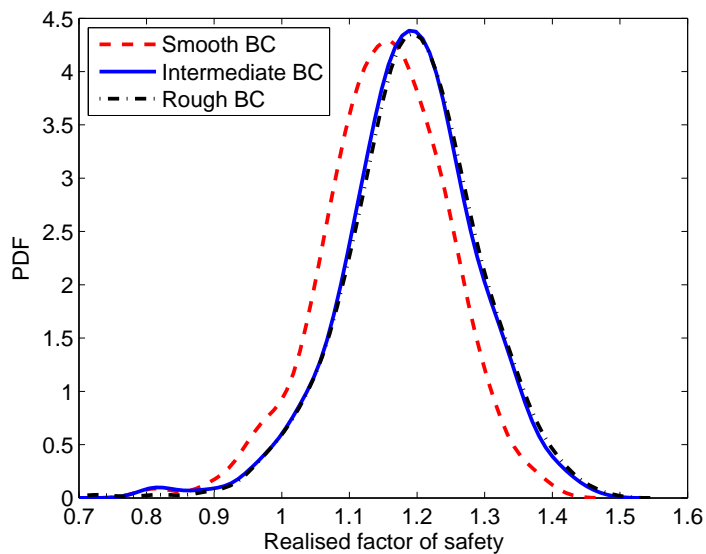
(a) 50 m long slope with $\theta_h = 24$ m
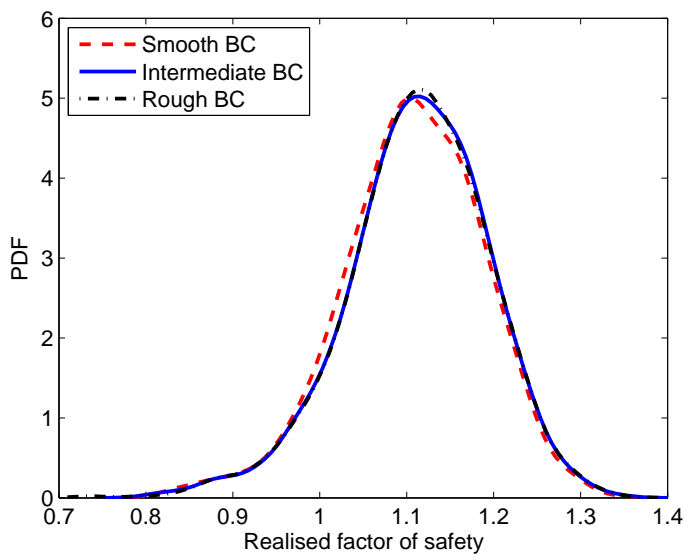
(b) 500 m long slope with $\theta_h = 200$ m

Figure 5.4: Influence of end-boundary conditions on realised factor of safety computed using RFEM
($F_T = 1.25$)

whereas all three boundary conditions give consistent results for the 500 m long slope, the smooth boundary condition leads to a weaker response for the 50 m long slope (for a similar ratio of θ_h/L).

5.4.3. RFEM RELIABILITY

In the RFEM analysis, for a given mean undrained shear strength, the slope reliability may be defined as,

$$R = \frac{N_f}{N} \tag{5.27}$$

where N_f is the number of realisations in which the slope fails under its self weight (i.e. the realised factor of safety is smaller than 1.0), and N is the total number of realisations.

Two kinds of factor of safety should be clearly defined here. The first is the factor of safety (F_T) based on the mean undrained shear strength; that is, the safety factor obtained by carrying out a (traditional) single deterministic analysis based only on the mean strength. The second is the realised factor of safety (F_R) based on a Monte Carlo simulation; that is, the distribution of realised factors of safety obtained by analysing the stability of a slope for multiple soil strength realisations based on the same soil strength input statistics. There is a different distribution of F_R for each traditional F_T and, as mentioned above, the reliability may be assessed from the distribution of F_R. Therefore, each F_T is associated with a particular reliability level, and this provides a way to link traditional and reliability-based designs (i.e. by determining the reliability associated with a traditional F_T).

5.4.4. LENGTH EFFECT

The influence of slope length on slope reliability was investigated by Hicks and Spencer (2010), by assuming that the event of failure not occurring in each section (of representative length in the longitudinal direction) of the slope is independent. This assumption is thought to be reasonable for small θ_h relative to slope length, as 3D failures then tend to be relatively small. Hicks and Spencer (2010) suggested a simple equation to estimate the system reliability based on the computed reliability of a (usually shorter) representative section, i.e.

$$R(L_A) = R(L_B)^{\frac{L_A}{L_B}} \tag{5.28}$$

where R denotes the reliability for a given mean shear strength, and L_A and L_B are the respective lengths of the whole slope and the representative section.

Alternatively, equation 5.28 can be expressed in terms of the failure probability:

$$1 - P_f(L_A) = \left[1 - P_f(L_B)\right]^{\frac{L_A}{L_B}} \tag{5.29}$$

By taking the natural logarithm of both sides of the equation,

$$\ln\left[1 - P_f(L_A)\right] = \frac{L_A}{L_B}\ln\left[1 - P_f(L_B)\right] \tag{5.30}$$

Hence, the probability of failure of a slope of length L_A, for small $P_f(L_A)$, may be given as

$$P_f(L_A) \approx \frac{L_A}{L_B}P_f(L_B) \tag{5.31}$$
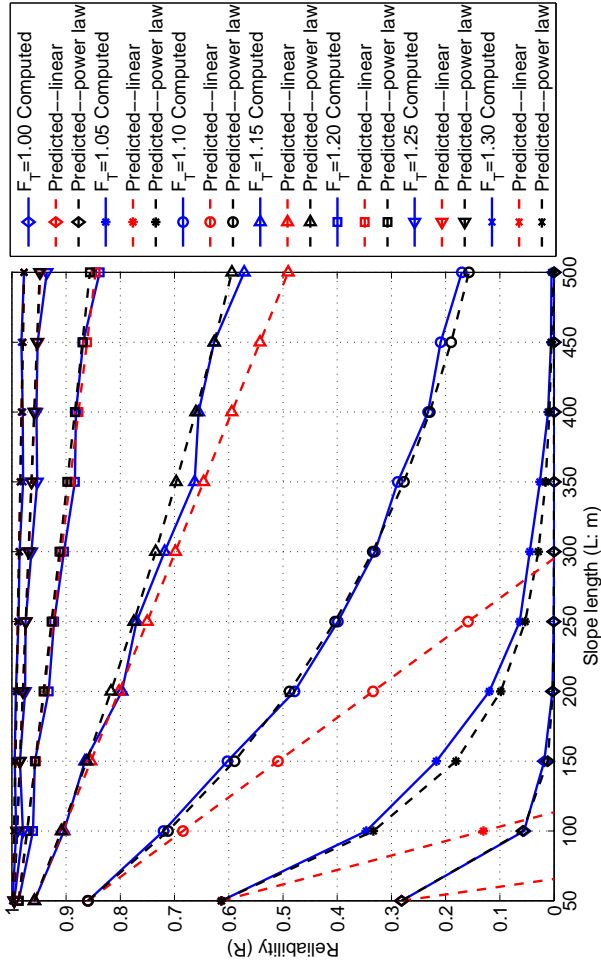
Figure 5.5: Influence of slope length on the reliability of a statistically homogeneous slope, for different factors of safety (F_T) based on the mean strength

This approximation is obtained by assuming $P_f(L_A) \ll 1$ (and therefore $P_f(L_B) \ll 1$ for $L_A > L_B$) and replacing $\ln(1-u)$ with $-u$ in equation 5.30, noting that the following approximation holds for $u \ll 1$:

$$e^{-u} = 1 - u \Leftrightarrow -u = \ln(1-u) \tag{5.32}$$

When expressed in terms of reliability, equation 5.31 becomes

$$R(L_A) \approx 1 - \frac{L_A}{L_B} + \frac{L_A}{L_B} R(L_B) \tag{5.33}$$

Generally, equations 5.31 and 5.33 are a good approximation provided that $P_f(L_A) \leq 0.05$ or $R(L_A) \geq 0.95$, which is the usual range of practical interest. For larger $P_f(L_A)$, the original equation 5.28 should instead be used. Hicks and Spencer (2010) suggested that equation 5.28 may be modified to give more precise predictions, by replacing L_A/L_B with $(L_A - 2H)/(L_B - 2H)$ to eliminate the end-boundary effect. In this case, equations 5.31 and 5.33 will change accordingly.

The influence of slope length on reliability is investigated here for a 'statistically homogeneous' slope with a length of up to 500 m, for the case of $\theta_h = 12$ m. Specifically, Fig. 5.5 compares the results of 3D RFEM simulations with the predictions given by equations 5.28 and 5.33, based on the RFEM results for a 50 m long slope (i.e. $L_B = 50$ m). The RFEM results have been obtained by analysing 10 slopes, from 50 m to 500 m in length, in steps of 50 m. For each slope length, $N = 1000$ realisations were used, except for $L = 50$ m which used 5000 realisations. This was to obtain as accurate an estimate as possible for $L = 50$ m, due to this result being used to predict (using equations 5.28 and 5.33) the R-F_T responses for other slope lengths. The distribution of realised factor of safety (F_R) for $L = 50$ m is shown in Fig. 5.6 (for $F_T = 1.25$), to highlight that $N = 5000$ realisations have been enough to generate a 'converged' distribution that is accurate enough for the purpose of predicting the reliability distributions for other slope lengths. The figure demonstrates that the computed results are closely approximated by a normal distribution, although it is the former that have been used to derive the predicted distributions.

The slope reliability predicted using equation 5.28 shows good agreement with the computed RFEM results, as seen in Fig. 5.5. It is also clear that the linear prediction (equation 5.33) is sufficiently accurate for probabilities of failure less than 5%, but significantly in error for failure probabilities greater than 20%.

5.5. ANALYSIS AND COMPARISON OF METHODS

The reliability predictions based on RFEM analyses, as described in the previous section, are used for $\theta_h = 12$, 24, 50 and 100 m to compare the relative performance of the three models (i.e. Vanmarcke, Calle and RFEM) as a function of slope length. Before carrying out a detailed comparison, some observations on the α factor (Eq. 5.13, Section 5.3.1) (GeoDelft, 1994) based on random field simulations will be presented; the results of this preliminary study will be used later in the performance evaluation.

5.5.1. OBSERVATIONS ON α FACTOR BASED ON RANDOM FIELD SIMULATION

Fig. 5.7(b) shows the horizontal variation, over a distance of 50 m, of the average undrained shear strength in a 5 m deep soil layer, together with three examples of the
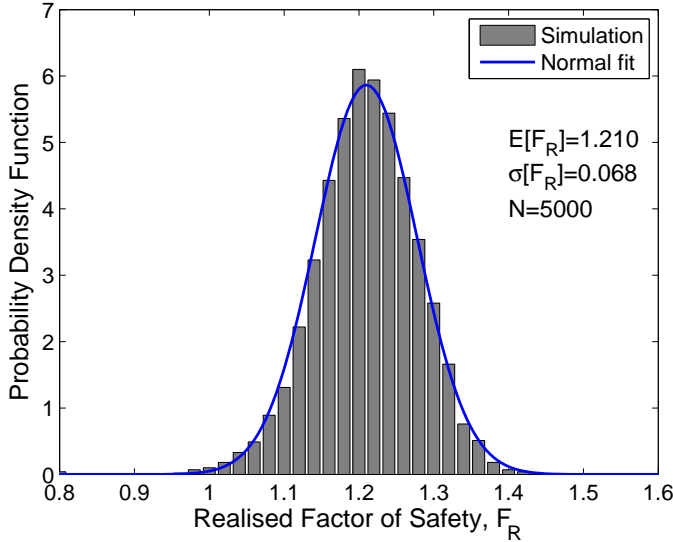
Figure 5.6: PDF of realised factor of safety for $L = 50$ m and $\theta_h = 12$ m ($F_T = 1.25$)

variation in the point strength with depth taken from three borehole locations (see plan view in Fig. 5.7(a)). For this illustration, the shear strength values have been extracted from a single 3D random field of undrained shear strength (with a $0.5 \times 0.5 \times 0.5$ m cell size) generated using $\bar{s} = 40$ kPa, $V = 0.2$, $\theta_v = 2.0$ m and $\theta_h = 8.0$ m. Clearly, the average value of s shows significant lateral variation. In this case, $\alpha = 0.87$ according to equation 5.13, in which $\tilde{s}^2$ and $\tilde{s}_v^2$ are based on all columns of random field cells making up the 50×5 m cross-section.

For the limiting case when there is no lateral variation in the average value of s, i.e. due to $\theta_h \gg L$, $\alpha \approx 1.0$ due to $\tilde{s}_h^2 \approx 0$. However, this is unlikely in practice, as analyses based on α are generally carried out at a regional scale that includes large-scale variations within the sampling domain; that is, if θ_h is relatively large compared to the cross-section and initial sampling domain, the only way to get a good estimate of the mean and variance is to increase the size of the sampling domain (Fenton and Griffiths, 2008)). Typical random field realisations, with the respective α values back-calculated from the cross-sections shown, are illustrated in Fig. 5.8 for a finite sampling domain of $L = 50$ m and $H = 5$ m, for $\theta_v = 1.0$ m. Note that, as θ_h / L becomes larger, α gets nearer to 1.0 due to the spatial variability taking on a more layered and predictable appearance. However, for a given value of θ_h / L, it is not a unique value due to the influence of the spatial distribution of weaker and stronger zones (compare, for example, Figs. 5.8(a) and (b)). Fig. 5.9 shows an equivalent set of results for $\theta_v = 3$ m, revealing a smaller α for a larger θ_v (i.e. compared to Fig. 5.8), due to the larger values of $\tilde{s}_h^2$.

To investigate the relationship between α and the horizontal and vertical SOFs, 200 random field realisations have been used to back-figure the average horizontal and vertical variances for a vertical slice of 5 m depth over horizontal distances of both 50 m
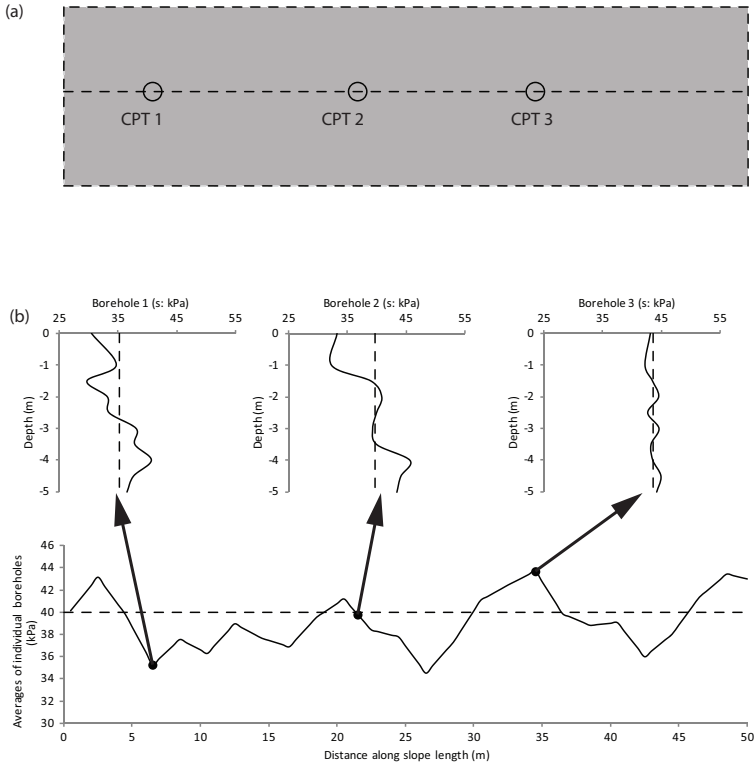
Figure 5.7: Illustration of cross-sectional variation in shear strength over a 50 m length of a 5 m deep clay deposit (modelled by a 3D random field based on $\mu_s = 40$ kPa, $V = 0.2$, $\theta_v = 2.0$ m and $\theta_h = 8.0$ m): (a) plan view of borehole locations; (b) variation of s in each borehole and variation of their means
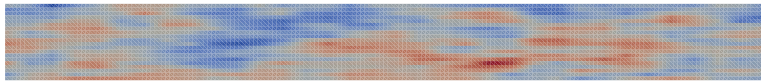
(a) θ_h = 6 m (giving $\alpha = 0.82$)
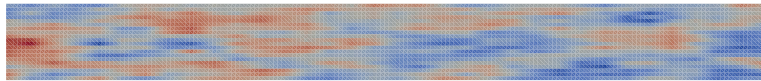
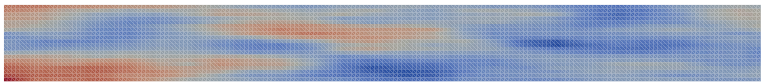(b) θ_h = 6 m (giving $\alpha = 0.79$)
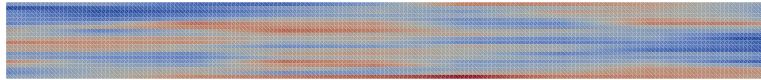
(c) θ_h = 24 m (giving $\alpha = 0.92$)
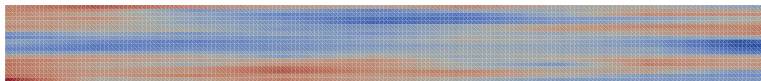
(d) θ_h = 24 m (giving $\alpha = 0.94$)
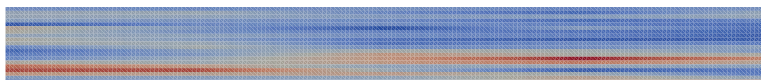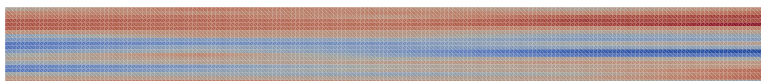
(e) θ_h = 50 m (giving $\alpha = 0.97$)

(f) θ_h = 50 m (giving $\alpha = 0.99$)

Figure 5.8: Computed α factors based on cross-sections from typical random fields of shear strength ($L = 50$ m, $H = 5$ m and $\theta_v = 1.0$ m)
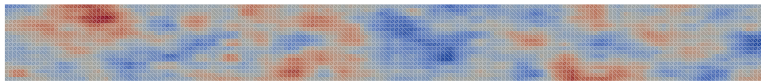
(a) θ_h = 6 m (giving $\alpha = 0.63$)
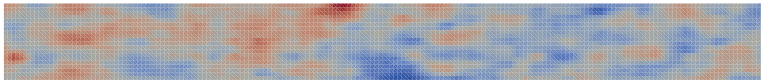
(b) θ_h = 6 m (giving $\alpha = 0.65$)
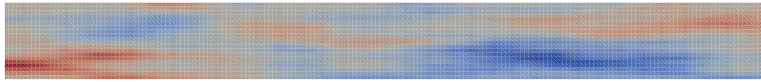
(c) θ_h = 24 m (giving $\alpha = 0.75$)

(d) θ_h = 24 m (giving $\alpha = 0.71$)
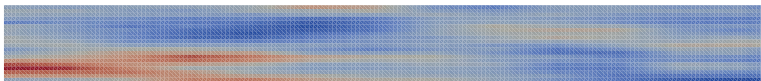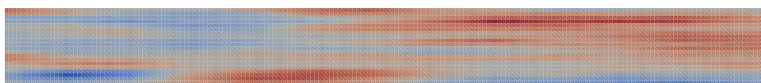
(e) θ_h = 50 m (giving $\alpha = 0.87$)

(f) θ_h = 50 m (giving $\alpha = 0.79$)

Figure 5.9: Computed α factors based on cross-sections from typical random fields of shear strength ($L = 50$ m, $H = 5$ m and $\theta_v = 3.0$ m)
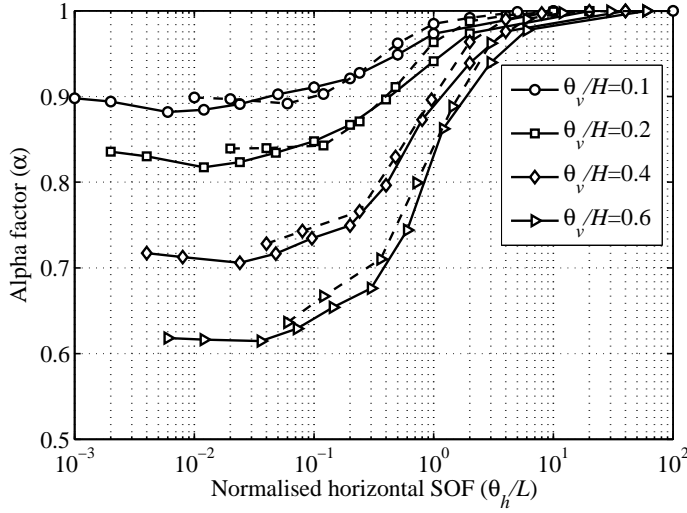
Figure 5.10: Alpha factor as a function of the horizontal and vertical scales of fluctuation (solid lines for $L = 500$ m, dashed lines for $L = 50$ m)

5

and 500 m. The random fields have been generated using a random field cell size of $0.25 \times 0.25 \times 0.25$ m and various combinations of θ_v and θ_h, with $\theta_v = 0.5$, 1.0, 2.0 and 3.0 m and $0.5 \le \theta_h \le 30,000$ m. For each combination of θ_v and θ_h, α has been computed for all 200 realisations and then averaged to give a single value. Fig. 5.10 shows the results for the averaged α as a function of the horizontal SOF, normalised with respect to layer length L, and vertical SOF normalised with respect to layer depth H. It is seen that α decreases as θ_h/L decreases, for all values of θ_v considered. A smaller α basically means that the total variance (equation 5.13) is the sum of a proportionately larger horizontal variance and a proportionately smaller vertical variance (equation 5.14). For a large ratio of θ_h/L there is not much difference between the means of each borehole. This results in a value of α close to 1, due to the horizontal variance $\tilde{s}_h^2$ being relatively small. Conversely, for a smaller ratio of θ_h/L, the borehole means exhibit a larger variation, as indicated by a larger $\tilde{s}_h^2$, and thereby a smaller α (i.e. further away from 1) is obtained. Moreover, as θ_v increases relative to the layer depth, α decreases further. This is because there is less potential for the strengths of stronger and weaker zones to 'cancel each other out' along each vertical borehole for a relatively larger ratio of θ_v/H, and this tends to increase the variance between the borehole means.

According to variance reduction theory (Vanmarcke, 1977a), $\tilde{s}_h^2 = (\theta_v/H)\tilde{s}^2$ for relatively small values of θ_h/L (i.e. such that the assumption that each column of cells in the cross-section is an independent realisation is valid) and relatively small values of θ_v/H (i.e. such that $\tilde{s}^2$ from one realisation approximates closely to the point variance; i.e. the ergodicity condition, which can only be theoretically achieved by a realisation of infinite extent (Fenton and Griffiths, 2008)). Therefore, α can be theoretically predicted for the case of $\theta_v/H = 0.1$ in the range of $0.001 \le \theta_h/L \le 0.1$ in Fig. 5.10; i.e. $\alpha = \tilde{s}_v^2/\tilde{s}^2 = (\tilde{s}^2 - \tilde{s}_h^2)$
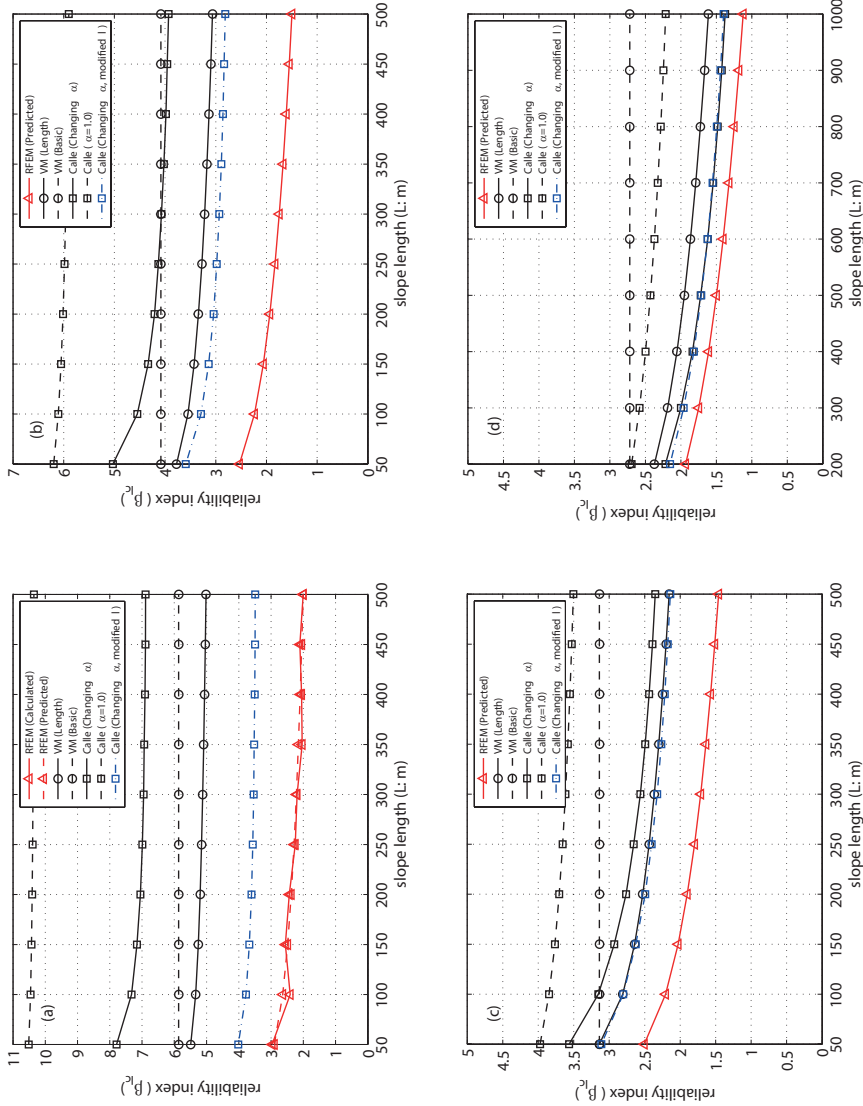
Figure 5.11: Comparing reliability index versus slope length for three models ($F_T = 1.30$): (a) $\theta_h = 12$ m; (b) $\theta_h = 24$ m; (c) $\theta_h = 50$ m; (d) $\theta_h = 100$ m

$/\tilde{s}^2 = 1 - \tilde{s}_h^2/\tilde{s}^2 = 1 - \theta_v/H = 1 - 0.1 = 0.9$, which closely matches the computed response.

The range of α factors found in this study (for typical values of θ_v/H) is consistent with the Dutch practice, i.e. $0.5 \le \alpha \le 1.0$ (GeoDelft, 1994).

5.5.2. RFEM RESULTS AND COMPARISON WITH FIRST CROSSING RESULTS

Figs. 5.11(a) to (d) show results for reliability index (β_{lc}) versus slope length, for a factor of safety of 1.30 based on the mean undrained shear strength, and for θ_h values of 12, 24, 50 and 100 m, respectively. These have been obtained from the inverse of the cumulative normal distribution function (i.e. $\beta_{lc} = -\Phi^{-1}(P_F)$, $-\Phi^{-1}(P_f)$ or $-\Phi^{-1}(P_f(L_A))$, using equations 5.5, 5.23 or 5.29, respectively). For the RFEM analyses, $N = 1000$ realisations have been conducted for the case of $L_B = 500$ m (see Appendix B for the convergence plots), and this has been used to compute results for other lengths via equation 5.29. Note that in Figs. 5.11(a) to (d), the case of $L_B = 500$ m is used as the RFEM reference analysis for making further predictions, due to equation 5.29 being based on discrete 3D failures and the suggestion by Hicks and Spencer (2010) that $\theta_h \le L/2$ to ensure the occurrence of this type of failure; note that, in Fig. 5.11(c), $\theta_h = 50$ m, which is equal to L for the shortest slope. Also, for the same reason, the slope length in Fig. 5.11(d) is kept in the range of 200-1000 m for the case of $\theta_h = 100$ m.

Six groups of results are shown in the figures: the RFEM-based prediction using equation 5.29, Vanmarcke's prediction based on the basic (i.e. slope length independent) model, Vanmarcke's prediction based on the level crossing model, the predictions based on Calle's model using both $\alpha = 1$ and a value of α that is a function of θ_h/L, and a further prediction based on Calle's model using a changing α and a modified failure length l (see Section 5.5.4). These are denoted in the figures as RFEM (predicted), VM (basic), VM (length), Calle ($\alpha = 1$), Calle (changing α) and Calle (changing α, modified l), respectively. In addition, a full 3D RFEM analysis is shown in Fig. 5.11(a), this being the same $F_T = 1.30$ analysis as appears in Fig. 5.5. Note that, in this case, the comparison between 3D RFEM and equation 5.29 is excellent, regardless of whether equation 5.29 uses the 3D $L = 50$ m results (as in Fig. 5.5) or the $L = 500$ m results (as in Fig. 5.11(a)) to make the prediction for other slope lengths, due to θ_h being 4 times smaller than the shortest ($L = 50$ m) slope.

As seen in Fig. 5.11, the analytical solution based on Vanmarcke's (1977b) simplified 3D (basic) model is independent of the slope length, whereas the reliability decreases with increasing slope length for all other models; i.e. the longer the slope, the smaller the reliability index. For the Author's implementation of Calle's model, the predictions based on a changing α, i.e. where $\alpha = f(\theta_v, \theta_h, H, L)$, show a larger length effect than those based on $\alpha = 1.0$. This can be explained relative to the modified correlation function (equation 5.12); i.e. α decreases as the ratio of the horizontal scale of fluctuation to soil layer length decreases (Fig. 5.10) and, as a smaller α effectively increases the variance of G' via equations 5.10-5.12, this results in a decreased reliability index in equation 5.16. The use of a smaller α in equation 5.12 reduces the exponential part of the variance that can be reduced in the cross-sectional analysis, over the failure surface, and increases the other part (i.e. the $(1-\alpha)$ part when considered in equation 5.11) if the total variance is kept constant.

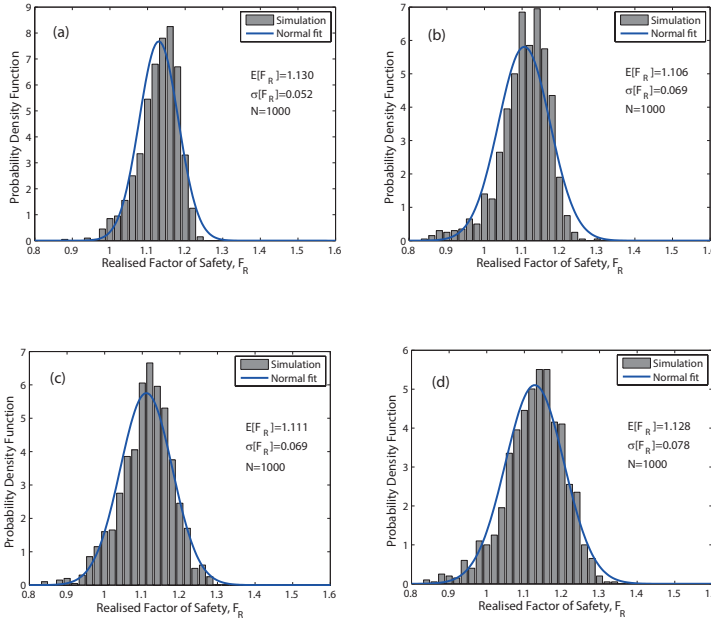Fig. 5.11 shows that RFEM predicts the smallest reliability indices for the range of

Figure 5.12: PDF of realised factor of safety for the four θ_h cases considered ($F_T = 1.30$, $L = 500$ m): (a) $\theta_h = 12$ m; (b) $\theta_h = 24$ m; (c) $\theta_h = 50$ m; (d) $\theta_h = 100$ m

cases considered. However, as the horizontal scale of fluctuation increases from 12 to 50 m, the results predicted by Vanmarcke's length-effect model and Calle's model with the modified correlation function move closer to the RFEM results and, for $\theta_h = 100$ m, the results are closer still, in particular with Calle's α modified solution approaching the RFEM solution. The differences with respect to the Vanmarcke and Calle models may partly be explained by the cylinder end effects (Li et al., 2015c): specifically, through overestimating the end resistance by assuming the mean strength in equations 4.2 and 5.25a, and by underestimating the variance of the factor of safety in equations 4.5 and 5.25b, i.e. the variance in the end resistance is not considered in Vanmarcke's (1977b) and Calle's models. Vanmarcke (1980) stated that the variance associated with the end resistance is proportional to the following factor:

$$c = \frac{\theta_v}{\theta_h} \frac{d}{b} \tag{5.34}$$

For a smaller horizontal SOF (note that a smaller θ_h is associated with a smaller b_c in equation 4.9), neglecting that part of the variance associated with the end resistances would result in a smaller $\tilde{F}_b$, and thus a higher (overestimated) β_b (see equations 4.5 and 4.11). Note that the RFEM predictions for β_{lc} are based on the computed $P_f(L_A)$, in conjunction with equation 5.29 and the inverse of the cumulative normal distribution function Φ^{-1}, even though the distributions of realised factor of safety are slightly non-normal for the reference length of $L_A = 500$ m, as illustrated in Fig. 5.12. This is in
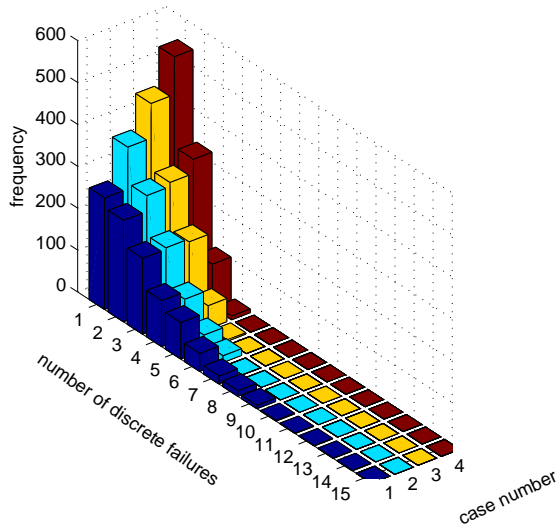
Figure 5.13: Frequency distributions of discrete failures for a 500 m long slope, for the four θ_h cases considered: (1) θ_h = 12 m; (2) θ_h = 24 m; (3) θ_h = 50 m; (4) θ_h = 100 m

5

contrast to the result shown in Fig. 5.6 for L_A = 50 m, and may be due (at least in part) to the smaller number of realisations in combination with a larger domain size and an associated greater range of possible failure mechanisms. When the computed $P_f(L_A)$ was replaced by the probability of failure based on the fitted normal PDF, there was only a relatively small shift in the β_{lc} predictions and the general findings of the comparative study remained unchanged. However, further comparative studies may be appropriate for situations in which the probability of failure is very small, as is often the case in practice.

5.5.3. Discrete failures in RFEM

Hicks et al. (2014) quantified the potential failure volume and length by a simple procedure using the out-of-slope-face displacement in their Monte Carlo simulations of a 100 m long slope. The failure length here refers to the unstable length computed in any realisation due to scaling down the soil strength profile to reach slope failure using the strength reduction method, and was estimated to be the integrated length along the row of elements directly above the slope toe, in the longitudinal direction, for which the displacement was greater than some calibrated threshold displacement. It may not be necessary to differentiate between multiple failures for a relatively short (e.g. 50-100 m long) slope, due to the relatively lower probability of encountering multiple failures. However, for a slope length of 500 m, for example, it is informative to quantify the number of discrete failures. Hence, the approach of Hicks et al. (2014) has been extended to quantify discrete failures: i.e. it is considered to be a separate failure if the failed elements directly above the slope toe are not continuously linked (Li et al., 2015e). The frequency

Table 5.1: Comparison of predicted failure lengths (units: m) for the three models ($F_T = 1.3$, $L = 500$ m)

SOF (θ_h: m)	RFEM		Vanmarcke	Calle (Changing α)	Calle ($\alpha = 1$)
	Mean	SD[a]	Critical b_c	Unstable zone l	Unstable zone l
12	13.3	8	16.6	6.0	4.7
24	17.7	9.9	24	11.8	9.3
50	27.4	15.2	50	24.2	19.5
100	47.5	27.3	100	47.1	39

[a] standard deviation

distributions for the number of discrete failures are shown in Fig. 5.13, for the four θ_h cases considered and a 500 m long slope. It is seen that, for a small θ_h, there can be many discrete failures, although the number decreases to 1-3 failures when θ_h is 100 m. Note that, although multiple failures are possible, their extents can be quite variable, with some failures having larger displacements than others. In reality, those failures involving larger displacements tend to fail first, which, in the case of a sea dyke failure for example, will usually release the hydraulic loading before some other failures of smaller extent develop fully themselves, resulting in fewer failures.

5.5.4. FAILURE LENGTH
In the case of multiple failures, the discrete failure length may be considered a more consistent measure of potential failure length for slopes of different total length; that is, in contrast to the integrated failure length, which may be more closely related to some specific slope length. Therefore, discrete failure lengths are quantified herein for the four values of θ_h considered and, for each case, the mean and standard deviation of the failure length have been computed based on all the discrete failures identified over $N = 1000$ Monte Carlo realisations. The results based on a 500 m long slope are shown in Table 5.1, as are the predicted failure (i.e. critical) lengths from Vanmarcke's model and Calle's model with changing α and with $\alpha = 1$. It is seen that the failure length from Vanmarcke's model is the largest of the three models. The RFEM potential failure lengths compare favourably with those from Vanmarcke's model for $\theta_h = 12$ m and 24 m. However, for $\theta_h = 50$ m and 100 m, the potential failure lengths from RFEM are less than those from Vanmarcke's model, although they show good agreement with those of Calle's model with changing α. However, the failure length from Calle's model with a changing α is smaller than those from Vanmarcke's model for the case of $\theta_h = 12$ m and 24 m.

Fig. 5.14 illustrates how the failure length changes with θ_h for the various models. It is clear that, for any given θ_h, the wide range of possible failure lengths computed using RFEM accounts for both the Vanmarcke and Calle solutions, although the mean response tends to the Vanmarcke solution for smaller θ_h and to the Calle solution for larger θ_h. However, note that for very small θ_h relative to the slope height (not investigated in this chapter), Hicks and Spencer (2010), Hicks et al. (2014) and Li et al. (2015c) showed that the RFEM failure length could become very long (cf. a 2D mechanism) due to the soil then resembling a homogeneous deposit based on the mean property value.
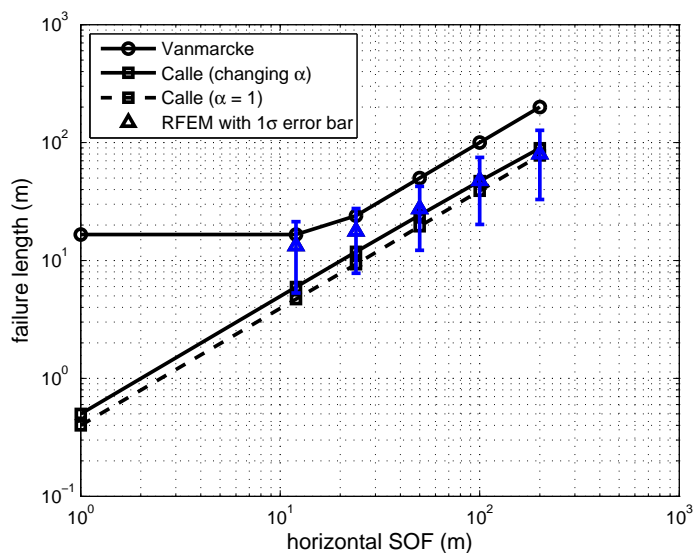
Figure 5.14: Potential failure length versus horizontal scale of fluctuation for the various models ($F_T = 1.30$, five RFEM results corresponding to θ_h = 12, 24, 50, 100 and 200 m shown with their means and associated one σ error bars)

Note that the predicted failure length in Calle's model is the expected length of the unstable zone (Section 5.3.2) before taking account of the end resistance. For a relatively short unstable zone (e.g. 6.0 m in the case of θ_h = 12 m and 11.8 m in the case of θ_h = 24 m), the probability of failure decreases substantially when taking account of the end resistance (Section 5.3.3), due to the end resistance contributing a relatively large proportion of the total resisting moment. Therefore, the potential failure length is likely to be underestimated in Calle's model for those cases having a smaller θ_h, when compared to the critical failure length in Vanmarcke's model, which defines the smallest reliability index incorporating the influence of the end resistance (Section 4.2). This is considered to be the reason why the results are closer between Vanmarcke and RFEM, than between Calle and RFEM, for these values of θ_h.

The differences in the predicted failure lengths for the three models may contribute to the differences in reliability index highlighted in Section 5.5.2. As shown in Fig. 5.11, if the expected failure length (l) in Calle's model is modified to be the mean failure length found using RFEM (i.e. larger), the reliability curve for various total slope length gets closer to the reliability curves obtained from Vanmarcke's model and RFEM.

5.6. CONCLUSIONS

This chapter has highlighted the length effect in the 3D reliability analysis of slopes that are very long in the third dimension. This has been achieved by comparing and evaluating the relative performance of three currently available methods of analysis: the random finite element method (RFEM), and two simpler methods proposed by Vanmarcke

(1977b) and Calle (1985).

Based on 3D RFEM analyses and the assumption of a series system composed of multiple independent elements, a power law equation was used to predict the reliability of longer slopes based on the detailed analysis of a shorter slope with the same statistical characteristics. This was shown to be accurate by comparing with RFEM analyses of slopes of various length. The RFEM-based predictions were then compared with the two simpler (level crossing) approaches, to investigate the relative performance of the three models for different horizontal scales of fluctuation. It was found that the two simpler models predict higher reliability indices compared to RFEM for all horizontal scales of fluctuation relative to slope length, but especially for shorter horizontal SOFs. It has been postulated that the differences in the results are related, at least in part, to the different approaches regarding failure mechanism. In particular, whereas RFEM automatically takes account of various possible failure surface geometries, the two simpler methods assume a cylindrical failure surface. Discrete failure lengths in RFEM analyses were quantified, and the differences with respect to the failure lengths predicted by the other two models were able to provide a reasonable explanation for the differences in reliability indices observed for the different slope lengths.

The α factor used in Dutch practice has been investigated in detail using random fields. It was shown to be a function of both the horizontal and vertical scales of fluctuation, as well as of the depth and lateral extent of a soil structure or deposit.

5

6

CONDITIONAL SIMULATION OF RANDOM FIELDS IN LONG 3D SLOPES

A method of combining a 3D Kriging algorithm for geotechnical sampling schemes (e.g. CPTs), with an existing 3D random field generator, is presented, to enable the simulation of conditional random fields of soil heterogeneity. The conditional random fields match the measurement data at the borehole locations and honour the spatial correlations of the soil properties. The approach, Kriging combined with 3D random field generation, is validated by demonstrating the consistency in the covariance structures and PDFs before and after conditioning. Both isotropic and anisotropic random fields, conditioned upon the measurement data, can be generated and used in subsequent analyses of structure performance. Although the theory for generating the conditional random fields is nothing new, the conditional random fields are here linked with finite elements, within a Monte Carlo framework, to investigate optimum sampling locations in 3D space and the cost effective design of a slope. The results demonstrate the potential of a 3D conditional simulation in directing exploration programs and designing cost saving structures in geotechnical engineering; that is, by reducing uncertainty and improving the confidence in a project's success.

6.1. Introduction

Soil properties exihibit three dimensional spatial variability (i.e. heterogeneity). In geotechnical engineering, a site investigation may be carried out, and the data collected and processed in a statistical way to characterise the variability (DeGroot and Baecher, 1993; Fenton, 1999a,b; Hicks and Onisiphorou, 2005; Jaksa et al., 1999; Lundberg and Li, 2015; Lloret-Cabot et al., 2014; Phoon and Kulhawy, 1999a; Uzielli et al., 2005; Zhao et al., 2013). The outcomes of the statistical treatment, e.g. the mean property value, the standard deviation or coefficient of variation, and the spatial correlation distance, may be used as input to a geotechnical model capable of dealing with the spatial variation (e.g. a random field simulation). However, when it comes to making use of the field data, there arises the question: How can we make best use of the available data? The idea is to use the data more effectively, so that it is worth the effort or cost spent in carrying out the investigation, as well as the additional effort in post-processing the data. The aim of this chapter is to contribute towards answering this question.

For example, cone penetration tests (CPTs) are often carried out in geotechnical field investigations, in order to obtain data used in implementing the design of a structure. The amount of data from CPT measurements is often larger than from conventional laboratory tests. This is useful, as a large database is needed to accurately estimate the spatial correlation structure of a soil property. For example, Fenton (1999b) used a database of CPT profiles from Oslo to estimate the correlation statistics in the vertical direction, and Jaksa et al. (1999) used a database from Adelaide to estimate the correlation distances in both the vertical and horizontal directions.

In geotechnical engineering, a substantial amount of numerical work has been done using idealised 2D simulations based on collected in-situ data (e.g. Hicks and Onisiphorou, 2005), although a 3D simulation would be preferable due to site data generally being collected from a 3D space. However, there are relatively few studies simulating the effect of 3D heterogeneity due to the high computational requirements. Examples include the effect of heterogeneity on shallow foundation settlement (Fenton and Griffiths, 2005; Jaksa et al., 2005; Kuo et al., 2004), on steady state seepage (Griffiths and Fenton, 1995, 1997, 1998) and on slope reliability (Spencer and Hicks, 2006, 2007; Spencer, 2007; Griffiths et al., 2009b; Hicks and Spencer, 2010; Li et al., 2013, 2015c,e; Hicks et al., 2008, 2014; Li and Hicks, 2014).

The above investigations all used random fields to represent the soil spatial variability and the finite element method to analyse geotechnical performance within a Monte Carlo framework, a form of analysis sometimes referred to as the random finite element method (RFEM) (Fenton and Griffiths, 2008). However, they did not make use of the spatial distribution of related measurement data to constrain the random fields. In other words, for those applications that are based on real field data, many realisations not complying with the field data at the measurement locations will be included in the simulation, which, in turn, will result in an exaggerated range of responses in an analysis of geotechnical performance.

Studies on conditional simulations are available in geostatistics in the field of reservoir engineering (Chiles and Delfiner, 2009). However, there are not many studies dealing with soil spatial variability in geotechnical engineering that utilise conditional simulation (some 2D exceptions include, e.g., Vanmarcke and Fenton (1991); Lloret-Cabot

et al. (2012); van den Eijnden and Hicks (2011); Lloret-Cabot et al. (2014)). This is partly due to the smaller amount of data generally available in geotechnical engineering, and partly due to there often not being a computer program specially implemented for those situations where there are sufficient data (e.g. CPT, VST), especially in 3D. However, unconditional random fields can easily be conditioned to the known measurements by Kriging (Journel, 1974; Chiles and Delfiner, 2009). Hence, following the previous 2D work of van den Eijnden and Hicks (2011) and Lloret-Cabot et al. (2012), this chapter seeks to implement and apply conditional simulation in three dimensional space, in order to reduce uncertainty in the field where CPT measurements are carried out.

Usually, site investigation plans are designed to follow some regular pattern. For example, a systematic grid of sample locations is generally used due to its simplicity to implement (Jaksa et al., 1999). Moreover, although there are various sampling plans in terms of layouts, it is found that systematically ordered spatial samples are superior in terms of the quality of estimates at unsampled locations (Olea, 1984). Therefore, this chapter will be devoted to implementting a 3D Kriging algorithm for sampling schemes following a regular grid. This will then be combined with an existing 3D random field generator to implement a conditional simulator. However, extension to irregular sampling patterns is straightforward based on the presented framework.

The implemented approach has been applied in two idealised slope stability examples. The first demonstrates how the approach may be used to identify the best locations to conduct borehole testing, and thereby allow an increased confidence in a project's success or failure to be obtained. While it is very important to pay sufficient attention to the required intensity of a site investigation (i.e. the optimal number of boreholes) with respect to the site-specific spatial variability, as highlighted in Jaksa et al. (2005), the first example starts by focusing on the optimum locations for carrying out site investigations for a given number of boreholes, before moving on to consider the intensity of testing. The second example compares different candidate slope designs, in order to choose the best (most cost-effective) design satisfying the reliability requirements.

For simplicity, this chapter focuses on applications involving only a single soil layer (i.e. a single layer characterised by a statistically homogeneous undrained shear strength), although the extension to multiple soil layers is straightforward. Moreover, the effect of random variation in the boundary locations between different soil layers can also be easily incorporated by conditioning to known boundary locations (e.g. corresponding to where the CPTs have been carried out).

6.2. CONDITIONAL SIMULATION

A conditional random field, which preserves the known values at the measurement locations, can be formed from three different fields (Journel and Huijbregts, 1978; Frimpong and Achireko, 1998; Fenton and Griffiths, 2008):

$$Z_{rc}(\mathbf{x}) = Z_{ru}(\mathbf{x}) + (Z_{km}(\mathbf{x}) - Z_{ks}(\mathbf{x})) \tag{6.1}$$

where $\mathbf{x}$ denotes a location in space, $Z_{rc}(\mathbf{x})$ is the conditionally simulated random field, $Z_{ru}(\mathbf{x})$ is the unconditional random field, $Z_{km}(\mathbf{x})$ is the Kriged field based on measured values at $\mathbf{x}_i (i = 1, 2, \ldots, N)$, $Z_{ks}(\mathbf{x})$ is the Kriged field based on unconditionally (or ran-

domly) simulated values at the same positions $\mathbf{x}_i$ ($i = 1, 2, \ldots, N$), and N is the number of measurement locations.

The unconditional random field can be simulated via several methods (Fenton, 1994); for example, interpolated autocorrelation (Ji et al., 2012), covariance matrix decomposition, discrete Fourier transform or Fast Fourier transform, turning bands, local average subdivision (LAS), and Karhunen–Loeve expansion (Phoon et al., 2002), among others. The LAS method (Fenton and Vanmarcke, 1990) is used in this thesis. The Kriged fields are obtained by Kriging (Krige, 1951), which has found extensive usage in geostatistics (Cressie, 1990; Wackernagel, 2003). The Kriging method is briefly reviewed in the following section. For a brief description of the LAS algorithm, the readers are referred to Chapter 3.

6.3. Kriging Theory

In contrast to conventional deterministic interpolation techniques, such as moving least squares and the radial point interpolation method, Kriging incorporates the variogram (or covariance) into the interpolation procedure; specifically, information on the spatial correlation of the measured points is used to calculate the weights. Moreover, standard errors of the estimation can also be obtained, indicating the reliability of the estimation and the accuracy of the prediction. Kriging is a method of interpolation for which the interpolated values are modelled by a Gaussian process governed by prior covariances and for which confidence intervals can be derived. While interpolation methods based on other criteria need not yield the most likely intermediate values, Kriging provides a best linear unbiased prediction of the soil properties (Z) between known data (Fenton, 2007; Wackernagel, 2003) by assuming the stationarity of the mean and of the spatial covariances, or variograms. A brief review is first given to facilitate understanding of the implementation.

Suppose that Z_1, Z_2, …, Z_N are observations of the random field $Z(\mathbf{x})$ at points $\mathbf{x}_1$, $\mathbf{x}_2$, …, $\mathbf{x}_N$ (i.e. $Z_i = Z(\mathbf{x}_i)$ ($i = 1, 2, \ldots, N$)). The best linear unbiased estimation (BLUE) of the soil property at some location $\mathbf{x}_0$ is given by

$$\hat{Z}(\mathbf{x}_0) = \sum_{i=1}^{N} \lambda_i Z_i = \sum_{i=1}^{N} \lambda_i(\mathbf{x}_0) Z(\mathbf{x}_i) \tag{6.2}$$

in which N denotes the total number of observations and λ_i denotes the unknown weighting factor associated with observation point $\mathbf{x}_i$, which needs to be determined.

The Kriging estimation is a weighted average of the values of Z at each observation point, in which the unbiased estimation requires the weights to sum up to 1, i.e.

$$\sum_{i=1}^{N} \lambda_i = 1 \tag{6.3}$$

It is the best estimator in the sense that the estimated field has the smallest variance error σ_e^2 with respect to the true field. The weights in Eq. 6.2, for the estimation at any point $\mathbf{x}_0$, can be found by minimising the variance of the Kriging error σ_e^2, which is given

as

$$\sigma_e^2 = \mathrm{var}\left[\hat{Z} - Z\right] = \mathrm{E}\left[(\hat{Z} - Z)^2\right] - \left(\mathrm{E}\left[\hat{Z} - Z\right]\right)^2$$
$$= \mathrm{E}\left[(\hat{Z} - Z)^2\right] + 0 \tag{6.4}$$
$$= \mathrm{E}\left[\hat{Z}^2\right] - 2\mathrm{E}\left[\hat{Z}Z\right] + \mathrm{E}\left[Z^2\right]$$

where var[] and E[] denote the variance and expectation operators, respectively, and where the equation makes use of the unbiasedness, that is, $\mathrm{E}\left[\hat{Z} - Z\right] = 0$.

Substituting Eq. 6.2 into Eq. 6.4, leads to

$$\sigma_e^2 = \mathrm{var}\left[\hat{Z} - Z\right] = \sum_{i=1}^{N}\sum_{j=1}^{N}\lambda_i\lambda_j c_{ij} - 2\sum_{i=1}^{N}\lambda_i c_{i0} + c_{00} \tag{6.5}$$

where $c_{ij} = C\left(\left|\mathbf{x}_i - \mathbf{x}_j\right|\right)$ is the covariance between $Z(\mathbf{x}_i)$ and $Z(\mathbf{x}_j)$, $c_{i0} = C\left(\left|\mathbf{x}_i - \mathbf{x}_0\right|\right)$ is the covariace between $Z(\mathbf{x}_i)$ and $Z(\mathbf{x}_0)$ and $c_{00} = C\left(\left|\mathbf{x}_0 - \mathbf{x}_0\right|\right) = C(0) = \sigma^2$ is the variance of $Z(\mathbf{x}_0)$, which is estimated at the target location $\mathbf{x}_0$. By using Eq. 6.3, Eq. 6.5 can be rearranged as

$$\sigma_e^2 = \mathrm{var}\left[\hat{Z} - Z\right] = \sum_{i=1}^{N}\sum_{j=1}^{N}\lambda_i\lambda_j(c_{ij} - \sigma^2) - 2\sum_{i=1}^{N}\lambda_i(c_{i0} - \sigma^2) + (c_{00} - \sigma^2)$$
$$= \sum_{i=1}^{N}\sum_{j=1}^{N}\lambda_i\lambda_j\left(C\left(\left|\mathbf{x}_i - \mathbf{x}_j\right|\right) - \sigma^2\right) - 2\sum_{i=1}^{N}\lambda_i\left(C\left(\left|\mathbf{x}_i - \mathbf{x}_0\right|\right) - \sigma^2\right)$$
$$+ \left(C\left(\left|\mathbf{x}_0 - \mathbf{x}_0\right|\right) - \sigma^2\right) \tag{6.6}$$
$$= -\sum_{i=1}^{N}\sum_{j=1}^{N}\lambda_i\lambda_j\gamma\left(\left|\mathbf{x}_i - \mathbf{x}_j\right|\right) + 2\sum_{i=1}^{N}\lambda_i\gamma\left(\left|\mathbf{x}_i - \mathbf{x}_0\right|\right) - \gamma\left(\left|\mathbf{x}_0 - \mathbf{x}_0\right|\right)$$

This rearrangement makes use of the relationship between a variogram $\gamma(\boldsymbol{\tau})$ and a covariance function $C(\boldsymbol{\tau})$ (Eq. 3.6), that is

$$\gamma(\boldsymbol{\tau}) = C(0) - C(\boldsymbol{\tau}) = \sigma^2 - C(\boldsymbol{\tau}) \tag{6.7}$$

To minimise the error variance (i.e. Eq. 6.6), the Lagrange method is used (Wackernagel, 2003). An objective function $\phi(\lambda_i, \mu)$ is defined by introducing the Lagrangian parameter μ and including the condition that the weights satisfy Eq. 6.3, i.e.

$$\phi(\lambda_i, \mu) = \sigma_e^2 = \sigma_e^2 - 2\mu\left(\sum_{i=1}^{N}\lambda_i - 1\right) \tag{6.8}$$

The weights can then be found by setting the partial derivatives of the objective function, with respect to all weights λ_i and μ, to zero. This leads to a system of equations of size $N+1$, for a constant mean:

$$\begin{pmatrix} \gamma(\mathbf{x}_1 - \mathbf{x}_1) & \cdots & \gamma(\mathbf{x}_1 - \mathbf{x}_N) & 1 \\ \vdots & \ddots & \vdots & \vdots \\ \gamma(\mathbf{x}_N - \mathbf{x}_1) & \cdots & \gamma(\mathbf{x}_N - \mathbf{x}_N) & 1 \\ 1 & \cdots & 1 & 0 \end{pmatrix}\begin{pmatrix} \lambda_1 \\ \vdots \\ \lambda_N \\ \mu \end{pmatrix} = \begin{pmatrix} \gamma(\mathbf{x}_1 - \mathbf{x}_0) \\ \vdots \\ \gamma(\mathbf{x}_N - \mathbf{x}_0) \\ 1 \end{pmatrix} \tag{6.9}$$
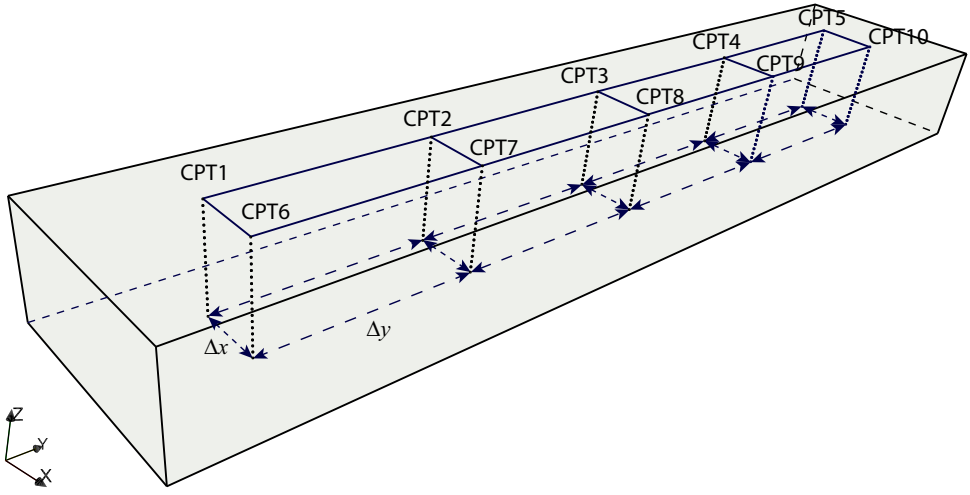
Figure 6.1: Example CPT sampling strategy ($k = 2$, $m = 5$)

For a mean following some trend, the modification to Eq. 6.9 is straightforward, and interested readers are referred to Chapter 4 in Fenton (2007).

According to Eq. 6.9, the Lagrangian parameter μ can be expressed by

$$\mu = -\sum_{j=1}^{N} \lambda_j \gamma\left(\left|\mathbf{x}_1 - \mathbf{x}_j\right|\right) + \gamma\left(\left|\mathbf{x}_1 - \mathbf{x}_0\right|\right) = -\sum_{j=1}^{N} \lambda_j \gamma\left(\left|\mathbf{x}_2 - \mathbf{x}_j\right|\right) + \gamma\left(\left|\mathbf{x}_2 - \mathbf{x}_0\right|\right) = \dots$$
$$= -\sum_{j=1}^{N} \lambda_j \gamma\left(\left|\mathbf{x}_N - \mathbf{x}_j\right|\right) + \gamma\left(\left|\mathbf{x}_N - \mathbf{x}_0\right|\right)$$
(6.10)

Rearranging Eq. 6.6 and making use of Eq. 6.10 and Eq. 6.3 leads to

$$\sigma_e^2 = \mu + \sum_{i=1}^{N} \lambda_i \gamma\left(\left|\mathbf{x}_i - \mathbf{x}_0\right|\right) - \gamma(0)$$
(6.11)

where $\gamma(0) = 0$ from Eq. 6.7.

Eq. 6.9 may be expressed as

$$\boldsymbol{\gamma}_{lhs}\boldsymbol{\lambda}_x = \boldsymbol{\gamma}_{rhs}$$
(6.12)

Once Eq. 6.9 is solved, the estimation variance can be expressed by

$$\sigma_e^2 = \left(\boldsymbol{\gamma}_{lhs}^{-1}\boldsymbol{\gamma}_{rhs}\right)^{\mathrm{T}}\boldsymbol{\gamma}_{rhs}$$
(6.13)

where λ_i is essentially a function of the relative positioning of $\mathbf{x}_i$ and $\mathbf{x}_0$. Note that the left-hand-side matrix $\boldsymbol{\gamma}_{lhs}$ is a function of only the observation point locations and co-variance between them. Therefore, it only needs to be inverted once, and then Eqs. 6.9 and 6.2 used repeatedly for building up the field of best estimates at different locations in space. In contrast, the right-hand-side vector $\boldsymbol{\gamma}_{rhs}$ changes as a function of the spatial point $\mathbf{x}_0$, resulting in different weight vectors $\boldsymbol{\lambda}_x$ that are used in Eq. 6.2 to get the estimates point by point in the domain of interest.

(a)

A1 — 1 2 3 m — A1

A2 — m+1 m+2 m+3 2m — A2

(b)

A1

1	n+1	2n+1	(m-1)n+1
2	n+2	2n+2	(m-1)n+2
3	n+3	2n+3	(m-1)n+3
4	n+4	2n+4	(m-1)n+4
5	n+5	2n+5	(m-1)n+5
n-1	2n-1	3n-1	mn-1
n	2n	3n	mn

(c)

A2

mn+1	(m+1)n+1	(m+2)n+1	(2m-1)n+1
mn+2	(m+1)n+2	(m+2)n+2	(2m-1)n+2
mn+3	(m+1)n+3	(m+2)n+3	(2m-1)n+3
mn+4	(m+1)n+4	(m+2)n+4	(2m-1)n+4
mn+5	(m+1)n+5	(m+2)n+5	(2m-1)n+5
(m+1)n-1	(m+2)n-1	(m+3)n-1	2mn-1
(m+1)n	(m+2)n	(m+3)n	2mn
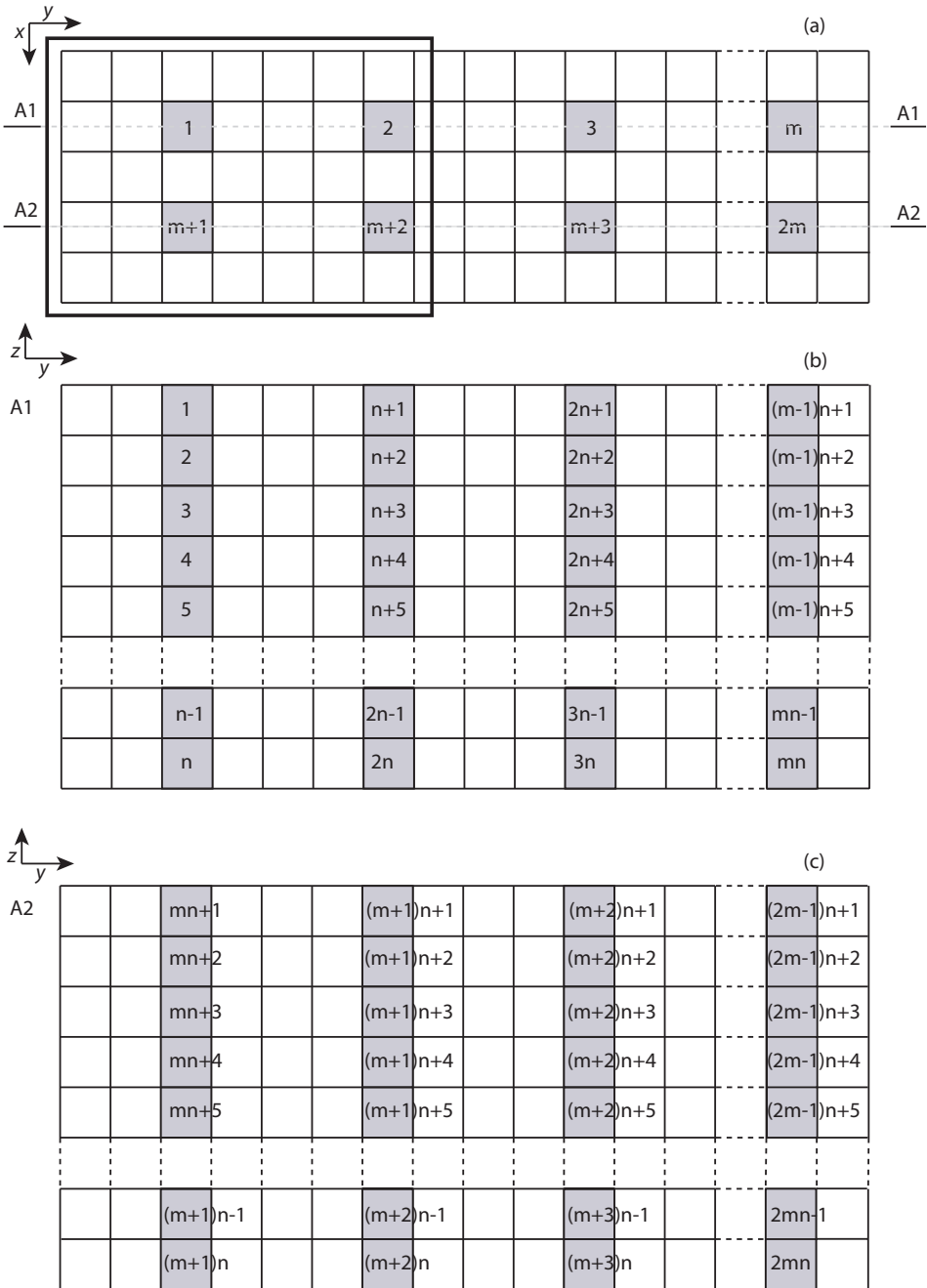
Figure 6.2: Example CPT data grid ($k = 2$): (a) plan view showing CPT locations; (b) global numbering of data points at section A1; (c) global numbering of data points at section A2

6.4. Kriging Implementation in 3D

In geotechnical engineering, a sampling strategy following some pattern is generally adopted (DeGroot and Baecher, 1993). For example, CPT sampling is often planned in the form of a regular grid on the ground surface (Jaksa et al., 1999). It is therefore desirable to implement the above Kriging algorithm in the context of some sampling design with a regular pattern. While it is straightforward to implement in 2D, it is less so when implemented in 3D. The most fundamental part is how the left-hand-side matrix of Eq. 6.12 is formed. This chapter shows an implementation of 3D Kriging for the regular grid sampling strategy shown in Fig. 6.1. The following will be devoted to setting up the left-hand-side matrix and the right-hand-side vector.

Suppose there are $k \times m$ CPT locations that follow a rectangular grid at the ground surface. That is, there are k rows in the x direction and, within each row, m CPT profiles in the y direction (Fig. 6.1). Assuming that there are n data points for each CPT profile, the global numbering scheme for all the CPT data points is shown in Fig. 6.2 for the case of $k = 2$.

6.4.1. Forming LHS matrix

Following the basic Eq. 6.12, of size $N+1 = kmn+1$, the left-hand-side matrix is formulated as

$$\boldsymbol{\gamma}_{lhs} = \begin{pmatrix} \mathbf{v}_{1,1} & \mathbf{v}_{1,2} & \mathbf{v}_{1,3} & \cdots & \mathbf{v}_{1,m} & \mathbf{v}_{1,m+1} & \mathbf{v}_{1,m+2} & \mathbf{v}_{1,m+3} & \cdots \\ \mathbf{v}_{2,1} & \mathbf{v}_{2,2} & \mathbf{v}_{2,3} & \cdots & \mathbf{v}_{2,m} & \mathbf{v}_{2,m+1} & \mathbf{v}_{2,m+2} & \mathbf{v}_{2,m+3} & \cdots \\ \mathbf{v}_{3,1} & \mathbf{v}_{3,2} & \mathbf{v}_{3,3} & \cdots & \mathbf{v}_{3,m} & \mathbf{v}_{3,m+1} & \mathbf{v}_{3,m+2} & \mathbf{v}_{3,m+3} & \cdots \\ \vdots & \vdots & \vdots & \ddots & \vdots & \vdots & \vdots & \vdots & \ddots \\ \mathbf{v}_{km,1} & \mathbf{v}_{km,2} & \mathbf{v}_{km,3} & \cdots & \mathbf{v}_{km,m} & \mathbf{v}_{km,m+1} & \mathbf{v}_{km,m+2} & \mathbf{v}_{km,m+3} & \cdots \\ 1 & 1 & 1 & \cdots & 1 & 1 & 1 & 1 & \cdots \end{pmatrix}$$

$$\begin{pmatrix} \mathbf{v}_{1,2m} & \cdots & \mathbf{v}_{1,(k-1)m+1} & \mathbf{v}_{1,(k-1)m+2} & \mathbf{v}_{1,(k-1)m+3} & \cdots & \mathbf{v}_{1,km} & 1 \\ \mathbf{v}_{2,2m} & \cdots & \mathbf{v}_{2,(k-1)m+1} & \mathbf{v}_{2,(k-1)m+2} & \mathbf{v}_{2,(k-1)m+3} & \cdots & \mathbf{v}_{2,km} & 1 \\ \mathbf{v}_{3,2m} & \cdots & \mathbf{v}_{3,(k-1)m+1} & \mathbf{v}_{3,(k-1)m+2} & \mathbf{v}_{3,(k-1)m+3} & \cdots & \mathbf{v}_{3,km} & 1 \\ \vdots & \ddots & \vdots & \vdots & \vdots & \ddots & \vdots & \vdots \\ \mathbf{v}_{km,2m} & \cdots & \mathbf{v}_{km,(k-1)m+1} & \mathbf{v}_{km,(k-1)m+2} & \mathbf{v}_{km,(k-1)m+3} & \cdots & \mathbf{v}_{km,km} & 1 \\ 1 & \cdots & 1 & 1 & 1 & \cdots & 1 & 0 \end{pmatrix} \quad (6.14)$$

in which $\mathbf{v}_{i,j}$ is a matrix representing the correlation structure between CPT_i and CPT_j (where each CPT has n data points),

$$\mathbf{v}_{i,j} =$$

$$\begin{pmatrix} d_{(i-1)n+1,(j-1)n+1} & d_{(i-1)n+1,(j-1)n+2} & d_{(i-1)n+1,(j-1)n+3} & \cdots & d_{(i-1)n+1,(j-1)n+n} \\ d_{(i-1)n+2,(j-1)n+1} & d_{(i-1)n+2,(j-1)n+2} & d_{(i-1)n+2,(j-1)n+3} & \cdots & d_{(i-1)n+2,(j-1)n+n} \\ d_{(i-1)n+3,(j-1)n+1} & d_{(i-1)n+3,(j-1)n+2} & d_{(i-1)n+3,(j-1)n+3} & \cdots & d_{(i-1)n+3,(j-1)n+n} \\ \vdots & \vdots & \vdots & \ddots & \vdots \\ d_{(i-1)n+n,(j-1)n+1} & d_{(i-1)n+n,(j-1)n+2} & d_{(i-1)n+n,(j-1)n+3} & \cdots & d_{(i-1)n+n,(j-1)n+n} \end{pmatrix}$$
$$(6.15)$$

where $(i, j) = 1, 2, 3, \ldots, m, m+1, m+2, m+3, \ldots, 2m, \ldots, (k-1)m+1, (k-1)m+2, (k-1)m+3, \ldots, km$ and $d_{r,s}$ $(r = (i-1)n+1, \ldots, (i-1)n+n)$ $(s = (j-1)n+1, \ldots, (j-1)n+n)$ are the components of the submatrix $\mathbf{v}_{i,j}$, which can be expressed in the form of a variogram between data points r and s (Eq. 6.7 and 3.6).

6.4.2. FORMING RHS VECTOR AND SOLVING FOR UNKNOWN VECTOR

The right-hand-side vector is formulated as

$$
\boldsymbol{\gamma}_{rhs} = \begin{pmatrix} \mathbf{v}_1 \\ \mathbf{v}_2 \\ \mathbf{v}_3 \\ \vdots \\ \mathbf{v}_{km} \\ 1 \end{pmatrix}
\tag{6.16}
$$

in which $\mathbf{v}_p$ is a vector representing the correlation structure between the estimation point and CPT_p,

$$
\mathbf{v}_p = \begin{pmatrix} d_{(p-1)n+1} \\ d_{(p-1)n+2} \\ d_{(p-1)n+3} \\ \vdots \\ d_{(p-1)n+n} \end{pmatrix}
\tag{6.17}
$$

where $p = 1, 2, 3, \ldots, m, m+1, m+2, m+3, \ldots, 2m, \ldots \ldots, (k-1)m+1, (k-1)m+2, (k-1)m+3, \ldots, km$ and d_t $(t = (p-1)n+1, \ldots, (p-1)n+n)$ are the components of the subvector $\mathbf{v}_p$, which can be expressed in the form of a variogram (Eq. 6.7 and 3.6) between data points t and the point at which the value is to be estimated (Fig. 6.2).

In Fig. 6.3, the spatial variability of the soil property is represented by a series of discrete values assigned to cubic cells. The black cell denotes one of the cell values that are to be estimated, whereas the red cells denote the CPT measurements.

The unknown weights vector is

$$
\boldsymbol{\lambda}_x = \begin{pmatrix} \boldsymbol{\lambda}_1 \\ \boldsymbol{\lambda}_2 \\ \boldsymbol{\lambda}_3 \\ \vdots \\ \boldsymbol{\lambda}_{km} \\ \mu \end{pmatrix}
\tag{6.18}
$$
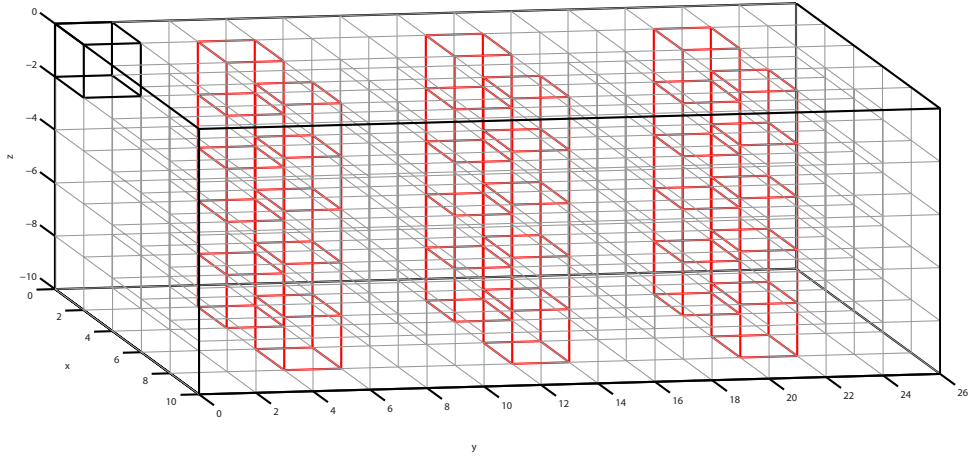
Figure 6.3: CPT sampling profile ($k = 2$, $m = 3$, $n = 5$)

in which $\boldsymbol{\lambda}_q$ is the weights subvector for CPT$_q$,

$$\boldsymbol{\lambda}_q = \begin{pmatrix} \lambda_{(q-1)n+1} \\ \lambda_{(q-1)n+2} \\ \lambda_{(q-1)n+3} \\ \vdots \\ \lambda_{(q-1)n+n} \end{pmatrix} \tag{6.19}$$

where $q = 1, 2, 3, \ldots, m, m+1, m+2, m+3, \ldots, 2m, \ldots, (k-1)m+1, (k-1)m+2, (k-1)m+3, \ldots, km$.

6.4.3. COMPUTING EFFICIENCY

There are two aspects involved in the computational efficiency of the above Kriging implementation. One is the total number of equations, which depends on the total number of data points ($N = k \times m \times n$, where k and m are the number of CPT rows in the x and y directions respectively, and n is the number of data points for each CPT profile, see Fig. 6.1) contributing to the left-hand-side matrix; the other is the number of points in the field ($n_f = n_x \times n_y \times n_z$, where n_x, n_y and n_z are the number of points in the three Cartesian directions) that need to be Kriged (i.e. how many times the algorithm will need to be repeated, except for inverting the left-hand-side matrix). The higher the required field resolution (n_f) and total number of known data points (N), the longer the Kriging will take. In the case of the CPT arrangement in Fig. 6.1, the size of matrix $\boldsymbol{\gamma}_{lhs}$ (see Eq. 6.9 or Eq. 6.14) and the size of vector $\boldsymbol{\gamma}_{rhs}$ (see Eq. 6.9 or Eq. 6.16) in 3D are m^2 and m times larger than those in 2D (i.e. a cross-section in the xz plane) respectively. The time it takes to Krige a full 3D field depends on the processing time of each individual step and the number of times each step has to be performed. To Krige a field of size n_f,

conditional to N measurement points, the total time may be approximated by

$$t(N, n_f) \approx c_1 n_f N^2 + c_2 N^3 \tag{6.20}$$

where the first term represents the time needed for solving the system of equations for all field points (i.e. n_f times) ($O(N^2)$) and the second represents the time needed for inverting the matrix $\boldsymbol{\gamma}_{lhs}$ (i.e. only once) ($O(N^3)$). The constants c_1 and c_2 are functions of the CPU speed and the operation, and in this case are in a ratio of approximately 4:1. Additionally, in all practical cases, $n_f \gg N$, so that the calculation time depends mainly on the first term in the above equation; that is, on the number of times (i.e. n_f times) that the matrix–vector multiplication operation, $\boldsymbol{\lambda}_x = \boldsymbol{\gamma}_{lhs}^{-1} \boldsymbol{\gamma}_{rhs}$, needs to be performed. Note that $n_f = n_x \times n_y \times n_z$ in 3D is n_y times $n_f = n_x \times n_z$ in 2D and $N = k \times m \times n$ in 3D is m times $N = k \times n$ in 2D. In the examples reported in Section 6.6, all problems investigated are very long in the third dimension compared to the cross-section. Therefore, the time consumed in a 3D analysis is theoretically $n_y \times m^2$ times that of a 2D analysis, when neglecting the relatively fast, one-off matrix inversion operation and other computation overheads, such as reading/writing and memory operations.

However, despite the greater run-time requirements for Kriging in 3D, it is far less than the time consumed in a nonlinear finite element analysis where plasticity iterations are needed. For Example 1 in Section 6.6, where $n_x = 20$, $n_y = 100$ and $n_z = 20$, it took, in serial and on average, 134 hours in total for the 500 finite element analyses forming each Monte Carlo simulation (3.0 GHz CPU), whereas Kriging 500 times took about 2.4 hours. In contrast, 500 Kriging interpolations for a 2D cross-section analysis took approximately 8.5 seconds. It is noted that the computation time used for Kriging 500 times is significant in comparison with a single finite element analysis, and therefore should not be considered a pre-processing step if utilising parallel computation for the finite element analyses. Therefore, the computing strategy developed (Chapter 3 and Appendix A) to carry out the analyses for Examples 1 and 2 in Section 6.6 (comprising around 30,000 realisations in total, and involving 30,000 3D Kriging interpolations) was to run the analyses in parallel (each Kriging and finite element analysis serially on a single computation node) on the Dutch national grid e-infrastructure with high performance computing clusters (Li et al., 2015d).

Note that it is possible to prescribe an appropriate neighbourhood size in the algorithm to reduce the computational burden for 3D Kriging. For example, a neighbourhood size of $5 \times 7 \times n$ may be used to construct the left-hand-side matrix (see the neighbourhood denoted as a rectangle in Fig. 6.2), i.e. by using only the nearest 4 CPT profiles). That is, only those CPT profiles that have a significant influence (i.e. a lag distance within the range of the scale of fluctuation in Eq. 6.7) on the point to be estimated are used to construct the left-hand-side (LHS) matrix. However, using this strategy, for each point (or each subset of points) to be estimated, the left-hand-side matrix is different and will need to be inverted accordingly, so this could increase the computational time if there are a large number of points or cells to be estimated. Therefore, a choice has to be made, to make sure that the time saved by inverting a smaller matrix, instead of a bigger one, outweighs the time consumed by inverting the left-hand-side matrices for all the (subgroups of) cells to be estimated for the case in which a neighbourhood is used. And, of course, there is a trade-off between the estimation accuracy and time saved when

Table 6.1: Comparison of uncertainty reduction ratio for using a local neighbourhood and using all the CPT profiles

	$\theta_h = 6$ m	$\theta_h = 12$ m	$\theta_h = 24$ m
u_n (local neighbourhood)	0.7231	0.5449	0.3953
u_a (all CPTs)	0.7220	0.5442	0.3946
E_u	1.5‰	1.3‰	1.8‰

such a neighbourhood approach is used. The accuracy will increase as more available data are used to do the Kriging estimation, and so the neighbourhood size depends on the required accuracy and the scales of fluctuation.

Due to the relatively fast inversion of the LHS matrix in the current investigation (the maximum size investigated is $N = 500$), all CPT profiles have been used for the Kriging in the examples in Section 6.6. However, one neighbourhood strategy was investigated by using the 4 nearest CPT profiles, and the following uncertainty reduction ratio (a 3D extension to the 1D definition in van den Eijnden and Hicks (2011)) has been used to assess the approximation error:

$$u = \frac{\sum_{i=1}^{n_x} \sum_{j=1}^{n_y} \sum_{k=1}^{n_z} \sigma_e(i, j, k)}{n_x n_y n_z \sigma} \tag{6.21}$$

The approximation error may be evaluated by

$$E_u = \frac{|u_n - u_a|}{u_a} \tag{6.22}$$

where u_n and u_a are the uncertainty reduction ratios when using a neighbourhood and when all CPT profiles have been used, respectively.

One of the sampling strategies from Example 1 (Section 6.6, Fig. 6.11(b)) was used to evaluate the approximation error and the results are listed in Table 6.1. It can be seen that using a neighbourhood of the 4 nearest CPT profiles has been sufficient in this case.

6.5. VALIDATION OF CONDITIONAL RANDOM FIELDS

The conditional simulation of a 5 m high (z), 5 m wide (x) and 25 m long (y) clay block, characterised by a spatially varying undrained shear strength, is presented in this section to demonstrate the procedure and the validity of the implementation described in Section 6.4. The idea is to show how the measured values are honoured, and to check whether or not the statistical properties (e.g. covariance) of the random fields are maintained after conditioning.

The block is discretised into 20×100×20 cubic cells, with each cell of dimension 0.25 m. The mean of the undrained shear strength is 40 kPa, and the standard deviation is 8 kPa. The degree of anisotropy of the heterogeneity is $\xi = 3$, in which $\xi = \theta_h/\theta_v$ and $\theta_v = 1.0$ m. Five CPT measurement locations in the y direction are available, each comprising
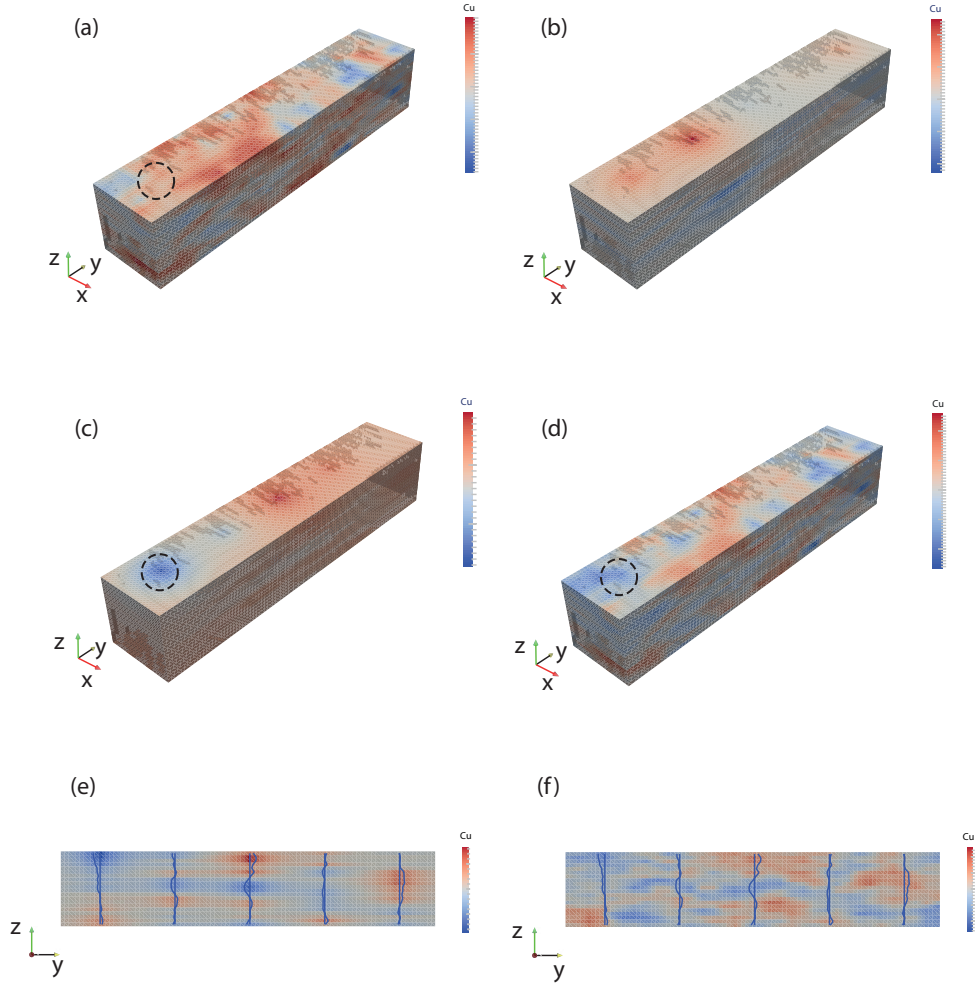
Figure 6.4: Example illustrations of the unconditional random field (a), the Kriged field based on the randomly simulated data (b), the Kriged field based on the CPT data (c), the conditional random field (d), cross-sections (e and f) in the longitudinal direction taken from the Kriged field (c) and from the conditional random field (d), respectively. Dashed circle indicates the position of the first CPT in subfigures (a) and (c-d)
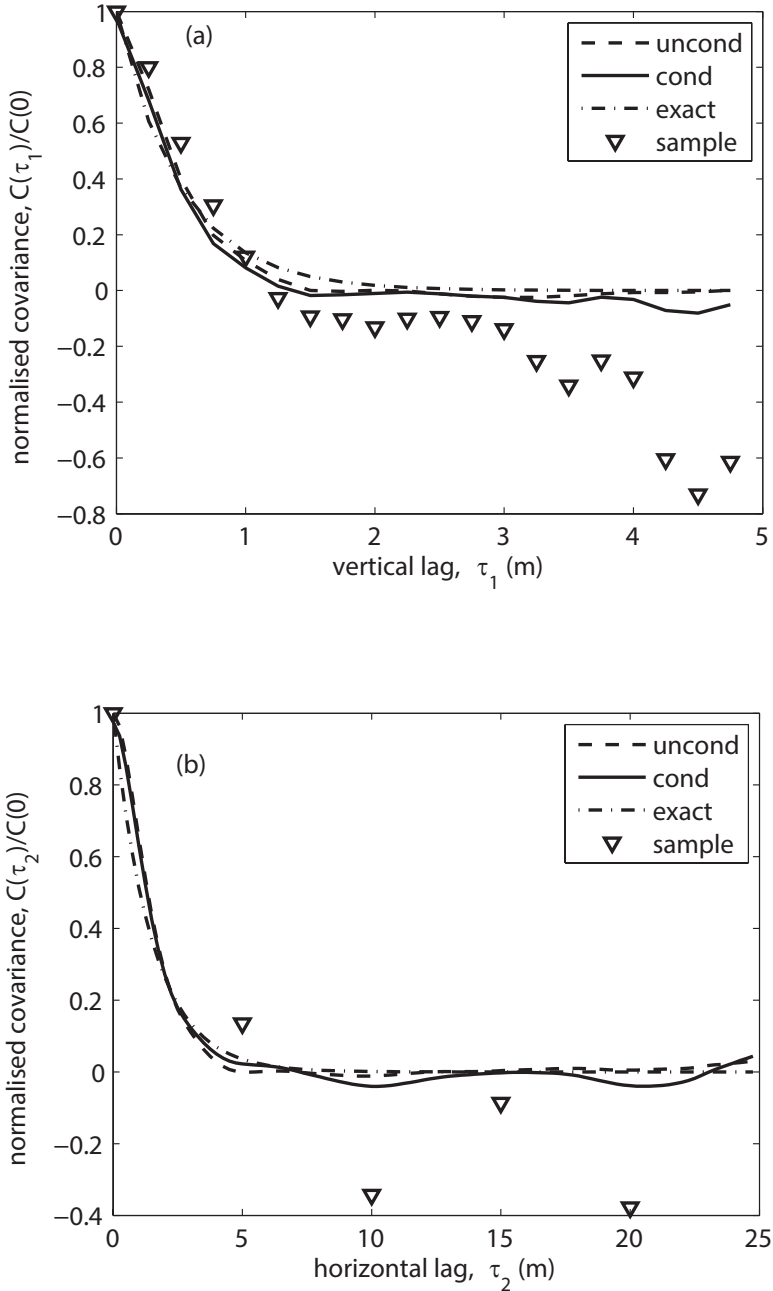
Figure 6.5: Vertical (a) and horizontal (b) covariance functions averaged over 200 realisations ($\theta_v = 1.0$ m, $\theta_h = 3.0$ m)

$n = 20$ data points at 0.25 m spacing in the vertical direction. These 'measured' data have been obtained by sampling from a single independent realisation of the spatial variability (i.e. representing the 'actual' in-situ variability). The interval distance between CPTs in the horizontal direction is $\Delta_y = 5$ m, and the first CPT is located at $y = 2.5$ m.

Fig. 6.4 shows an example realisation, to illustrate the stages involved in constructing the conditional random field. It shows (a) the unconditional field generated using LAS, (b) the Kriged field based on the unconditionally simulated cell values at the measurement locations, (c) the Kriged field based on the measured data (taken from the reference field), and (d) the conditional random field. It can be seen that the conditional field eliminates unrealistic values from the unconditional simulation by honouring the measurement data at the measurement locations (e.g. corresponding to the centre of the dashed circle in the case of the first CPT). The cross-section from which the CPTs were taken is also shown in Fig. 6.4 (e) and (f), together with the known CPT profiles. It is seen that the known CPT profiles are honoured in the conditional random field. Note that, in order to better visualise the fields, a local colour scale is used for all sub-figures in Fig. 6.4.

In order to validate the consistency of conditioning, apart from the PDFs of the target distribution before and after conditioning (these have been shown to be consistent, although not shown herein), the following estimator of the correlation structure along the vertical or horizontal direction of the random field is used to back-figure the covariance structure:

$$\hat{C}(\tau_j = j\Delta\tau) = \frac{1}{n-j} \sum_{i=1}^{n-j} \left(Z_i - \hat{\mu}_Z \right) \left(Z_{i+j} - \hat{\mu}_Z \right) \tag{6.23}$$

where $j = 0, 1, \ldots, n-1$, n is the number of data points in the vertical or horizontal direction, τ_j is the lag distance between cells at x_i and x_{i+j} (vertical or horizontal component of positions $\mathbf{x}_i$ and $\mathbf{x}_{i+j}$), $\Delta\tau$ is the distance between two adjacent cells vertically or horizontally, $\hat{\mu}_Z$ is the estimated mean, Z is the random soil property and Z_i is the sample of Z. The correlation function is then $\hat{\rho}(\tau_j) = \hat{C}(\tau_j)/\hat{C}(0)$, where $\hat{C}(0) = \hat{\sigma}_Z^2$ and $\hat{\sigma}_Z^2$ is the estimated variance (Fenton, 1999b).

Fig. 6.5 shows the back-figured (a) vertical and (b) horizontal covariances for the unconditional and conditional random fields averaged over 200 realisations, as well as the sample (i.e. CPT) covariances and exact covariances (i.e. equation 3.6 with only those terms that are associated with the vertical or horizontal direction in 1D). It can be seen that the conditional random field preserves the covariance structure reasonably well in both the horizontal and vertical directions, and that the correlation function fits well the sample correlation for the first quarter of the data points (i.e. $n/4$) (Jaksa et al., 1999; Uzielli et al., 2005). It is also seen that the covariance for the conditional field lies between those for the unconditional field and the sampling points.

6.6. GEOTECHNICAL APPLICATION

Two simple examples concerning slope stability are presented in this section, in order to illustrate how the technique presented in this chapter may be used as an aid to geotechnical design. The first involves finding the optimum locations for CPT profiles, in order to minimise the uncertainty in assessing the reliability of a slope. The second involves

6
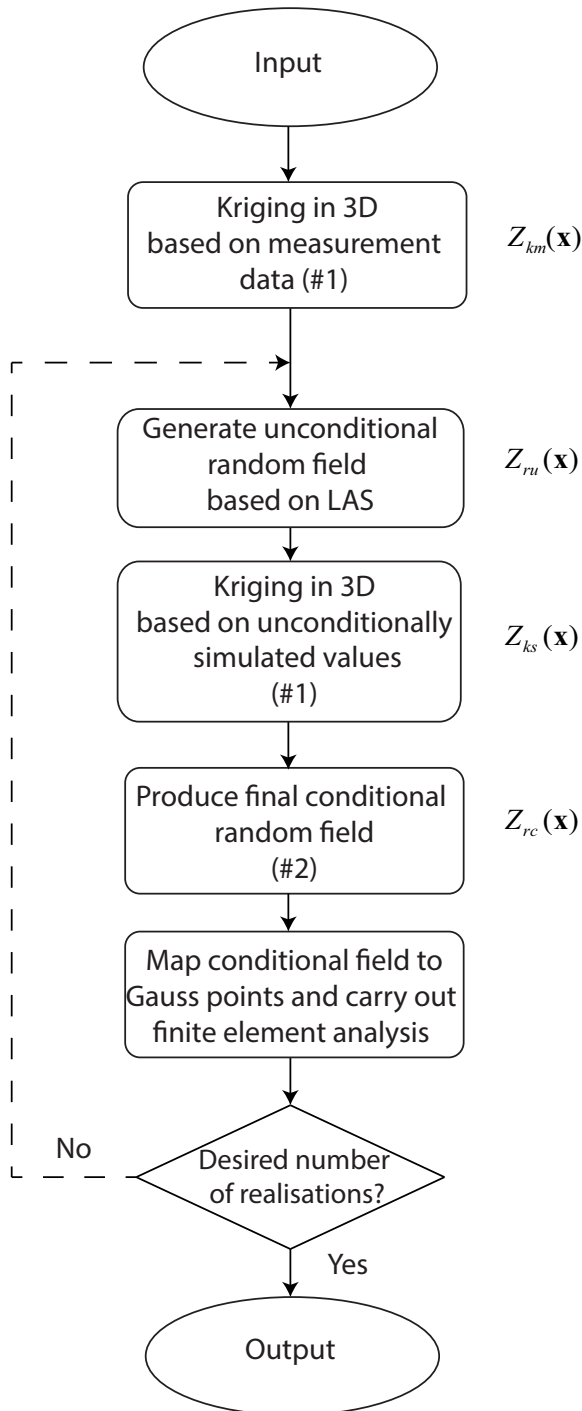
Figure 6.6: Flowchart for conditional RFEM simulation (#1: via Eqs. 6.9 and 6.2; #2: via Eq. 6.1)

a cost-effective design with regard to the slope angle when field measurements have already been made (i.e. the positions where the CPT data were taken are already known).

Both examples are presented in terms of the uncertainties in the slope response (with respect to factor of safety). The factors of safety are calculated by 3D finite elements using the strength reduction method (Smith and Griffiths, 2005), with the analyses being undertaken within a probabilistic (RFEM) framework; a flowchart for carrying out such a simulation is shown in Fig. 6.6. The undrained clay behaviour has been modelled using a linear elastic, perfectly plastic Tresca soil model. The clay has a unit weight of 20 kN/m^3, a Young's modulus of 100 MPa and a Poisson's ratio of 0.3. With reference to Figs. 6.7 and 6.15, the finite element boundary conditions are: a fixed base, rollers on the back of the domain preventing displacements perpendicular to the back face, and rollers on the two ends of the domain, allowing only settlements and preventing movements in the other two directions (i.e. the out-of-slope-face and longitudinal directions). A full explanation of these boundary conditions is given in Spencer (2007) and Hicks and Spencer (2010).

The random field cell values are mapped onto the $2 \times 2 \times 2$ Gauss points in each 20-node finite element, in order to simulate the spatial variability more accurately (Hicks and Samy, 2002; Hicks and Spencer, 2010). Note that the random fields (both conditional and unconditional) have been mapped onto a finite element mesh with an element aspect ratio equal to 2.0 (see Fig. 6.7) to save time for the finite element analyses (Spencer, 2007). A detailed description of how the random field cell values, in this case based on a cell size of $0.25 \times 0.25 \times 0.25$ m, are mapped onto the larger non-cubic finite elements is given in Hicks and Spencer (2010).

Note that CPT data, i.e. cone resistance and sleeve friction, cannot be used directly in the analyses reported here. A conversion or transformation model is needed to relate the test measurement to an appropriate design property (e.g. the undrained shear strength) (Phoon and Kulhawy, 1999b). As this chapter theoretically shows how such converted data can be used, artificial data of undrained shear strength have been used in the following examples.

6.6.1. EXAMPLE 1–COST-EFFECTIVE DESIGN OF SITE EXPLORATION PROGRAMMES

The first example considers a proposed 45°, 5 m high, 50 m long slope, that is to be cut from a heterogeneous clay deposit characterised by an undrained shear strength with the following statistics: mean 20 kPa (corresponding to a traditional/deterministic factor of safety of $F_T = 1.23$), standard deviation 4 kPa, vertical SOF of $\theta_v = 1.0$ m and horizontal SOF of $\theta_h = 6.0$ m. A question arises as to how to design the sampling strategy for the soil deposit. For example, if 5 CPTs are to be conducted in a straight line along the axis of the proposed slope, where is the best location to site the CPTs such that the designed slope will have the smallest uncertainty in the realised factor of safety F_R? Hence, this example first investigates the influence of the CPT locations on the standard deviation of the realised factor of safety, followed by the influence of CPT intensity. Fig. 6.7 shows a cross-section through the slope, and 10 possible positions to locate the CPTs ($i = 0, 1, \ldots, 9$). Note that the CPTs are taken to be equally spaced (i.e. at 10 m centres) in the third dimension, and that the first and fifth CPTs are located at 5 m and 45 m along the slope axis (see Fig. 6.11(a)). Furthermore, the CPTs are carried out before the slope
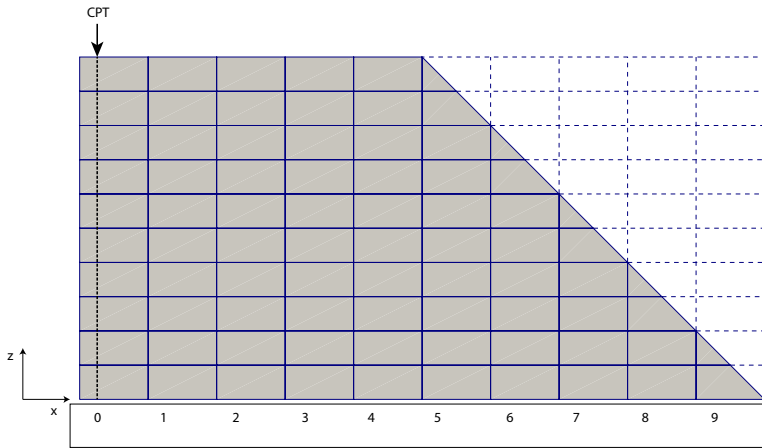
Figure 6.7: Finite element mesh and possible numbered CPT locations at a cross-section through the proposed 50 m long slope (dashed lines indicate the excavated soil mass and numbers correspond to Gauss point locations within the finite elements)

is excavated, in a block of soil of dimensions $10 \times 50 \times 5$ m as indicated in the figure.

Both conditional and unconditional RFEM simulations were carried out, using 500 realisations per simulation, to investigate how the structure response (in this case, the realised factor of safety) changes as the conditioning location changes. Fig. 6.8(a) shows that the uncertainty in the realised factor of safety reduces after conditioning, i.e. after making use of the available CPT information about the soil variability, as indicated by the narrower distribution of realised factor of safety for the conditional simulation. In this figure, the reduction in uncertainty is due to CPT data being taken from location $i = 5$.

Fig. 6.8(b) shows the sampling efficiency indices with respect to the different CPT locations, in which the sampling efficiency index is defined as

$$I_{se} = \frac{\sigma_u}{\sigma_i} \tag{6.24}$$

where σ_u is the standard deviation of the realised factor of safety for the unconditional simulation, and σ_i is the standard deviation of the realised factor of safety for the conditional simulation based on column position i. Hence $I_{se} = 1$ if the simulation is not conditioned. Clearly, there exists an optimum position (in this case, $i = 5$) to locate the CPTs; i.e. the uncertainty is a minimum if the CPTs are located along the crest of the proposed slope. In contrast, when $i = 0$ and 1, there is little improvement, because the potential failure planes (in the various realisations) generally pass through zones where the shear strength is, at most, only weakly correlated to values at the left-hand boundary (due to θ_h being only 6 m in this case). It is interesting to note that, although there is not much information included in the slope stability calculation when $i = 9$, i.e. for the CPTs at the slope toe, the reduction in uncertainty is still noticeable, due to the CPTs being located in the zone where slope failure is likely to initiate. This observation highlights that the location of additional information may matter more than how much additional
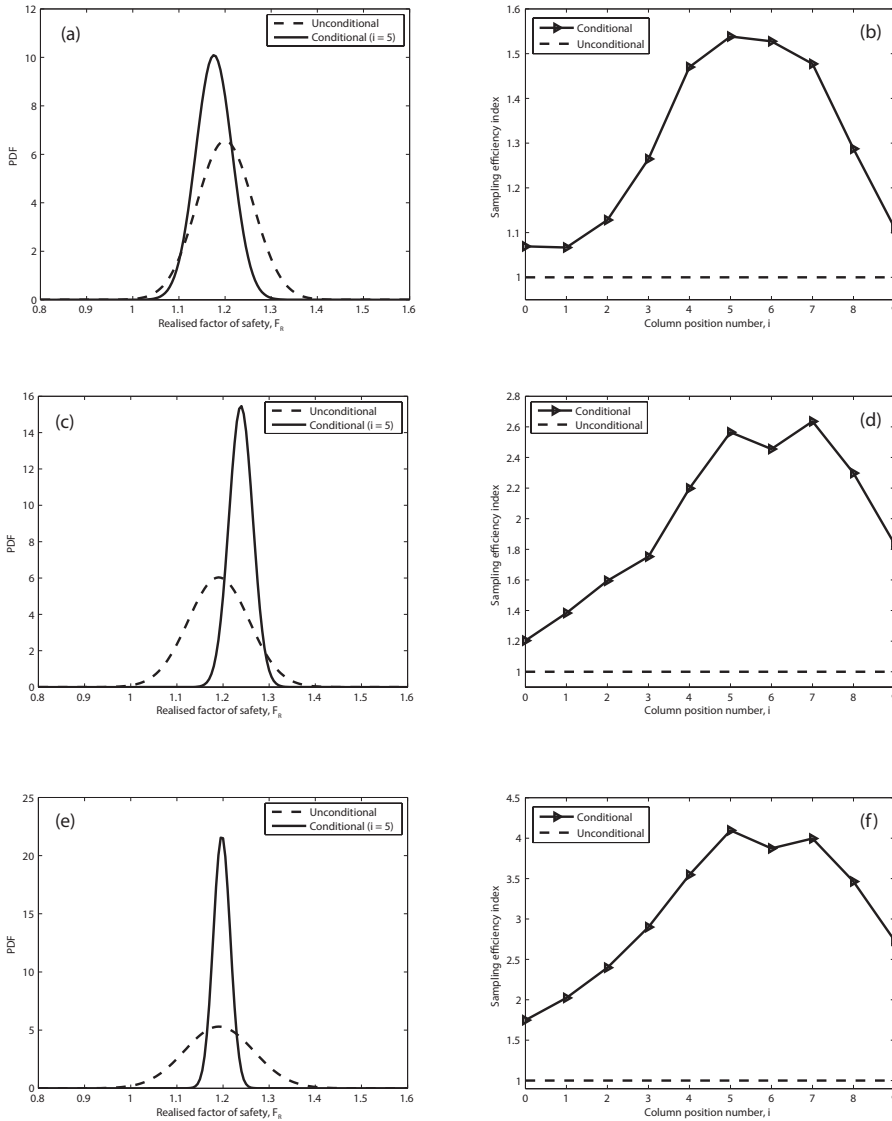
Figure 6.8: Simulation results of Example 1 (based on $\theta_v = 1.0$ m and 500 realisations per simulation): probability density functions of realised factor of safety ($\xi = 6$) (a), influence of CPT location ($\xi = 6$) (b), probability density functions of realised factor of safety ($\xi = 12$) (c), influence of CPT location ($\xi = 12$) (d), probability density functions of realised factor of safety ($\xi = 24$) (e), and influence of CPT location ($\xi = 24$) (f)
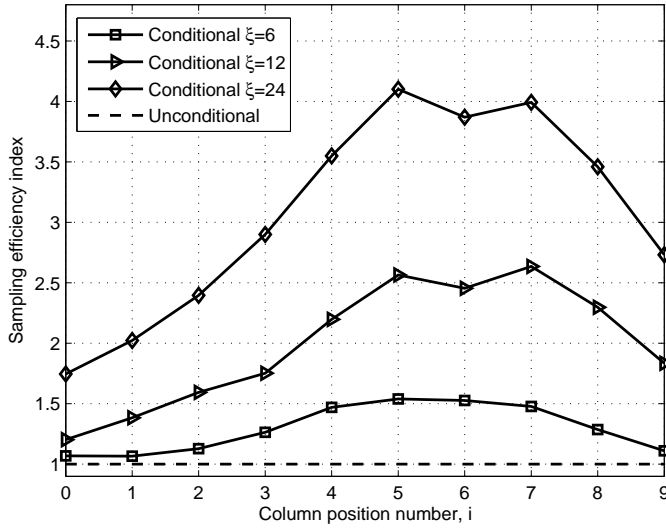
Figure 6.9: Sampling efficiency indices for various values of ξ

6

information there is (e.g. contrast the large difference in the amount of directly utilised data between CPT locations $i = 0$ and $i = 9$).

However, it should be remembered that Figs. 6.8 (a)-(b) are for the case of $\xi = 6$ and that ξ often takes a larger value in practice. Figs. 6.8 (c)-(f) show that, for $\xi = 12$ and $\xi = 24$, the reduction in uncertainty relative to the unconditional case is greater. Moreover, improved values of I_{se} are obtained for CPT locations near the right and left boundaries, due to the higher correlation of soil properties in the horizontal direction.

Fig. 6.9 summarises the results as a function of the degree of anisotropy of the heterogeneity ξ. It is seen that the best locations for carrying out the 5 CPTs are at $i = 5$, 6 and 7. As the value of ξ increases, the sampling efficiency indices increase due to the decreasing Kriging variance σ_e^2, as illustrated in Fig. 6.10 for a $y-z$ slice at $i = 5$ (i.e. corresponding to where the CPTs are located). It is seen that, for larger values of ξ, the Kriging variance between CPTs can drop well below the input variance of the shear strength (i.e. $\sigma_e^2 \leq 16\,\text{kPa}^2$). Note also that the input variance of shear strength is $4^2 = 16\,\text{kPa}^2$). Moreover, carrying out CPTs at some distance to the left or right of the slope crest for higher values of ξ can have similar effects to carrying out CPTs near the crest for smaller values of ξ. For example, the sampling efficiency index for $\xi = 24$ at $i = 2$ is approximately the same as that for $\xi = 12$ at $i = 5$, 6 and 7.

Note that the same reference 3D random field is used to represent the 'real' field situation in conditioning the random fields in each RFEM analysis. The 3D random fields are conditioned before being mapped onto the finite element mesh, so that they are consistent with sampling the ground before the slope is cut. Hence, for $i = 6$, 7, 8 and 9, although the CPT measurements are directly used for fewer cells in the FE mesh, they nevertheless have an impact on all cell values via the lateral spatial correlation of soil
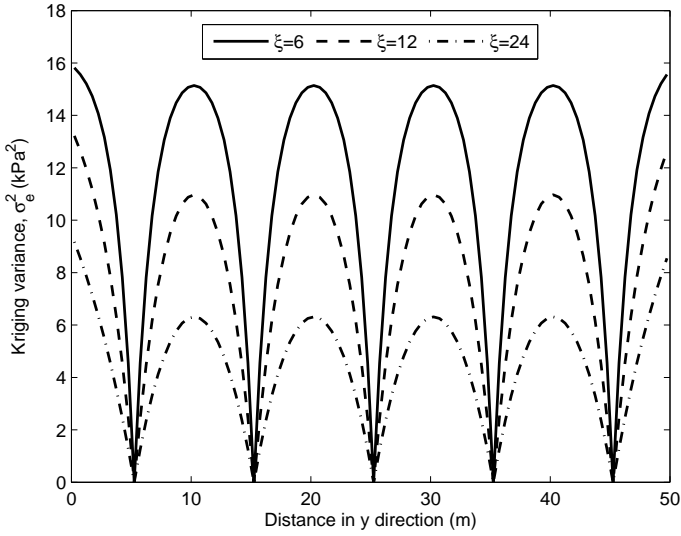
Figure 6.10: Kriging variance for various values of ξ ($y - z$ slice at $i = 5$)

(a) $i=5$

(b) $i=5$, $j=0$
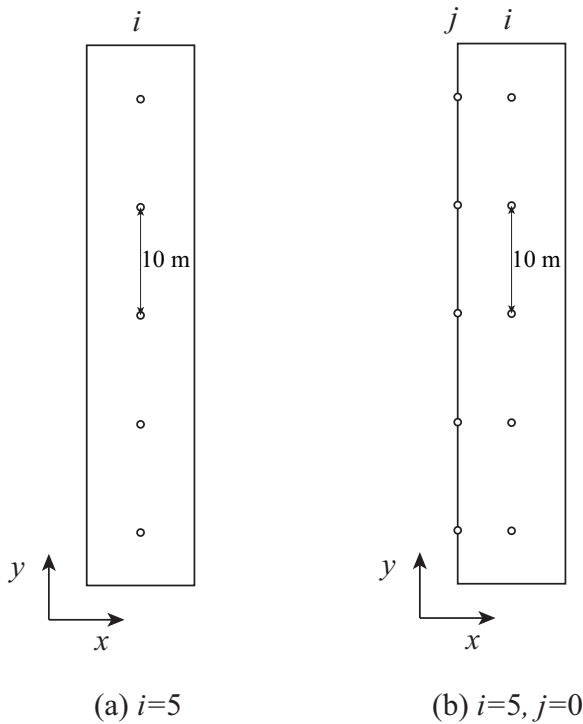
Figure 6.11: CPT layout illustration (plan view) for a single row (a) and two rows (b)
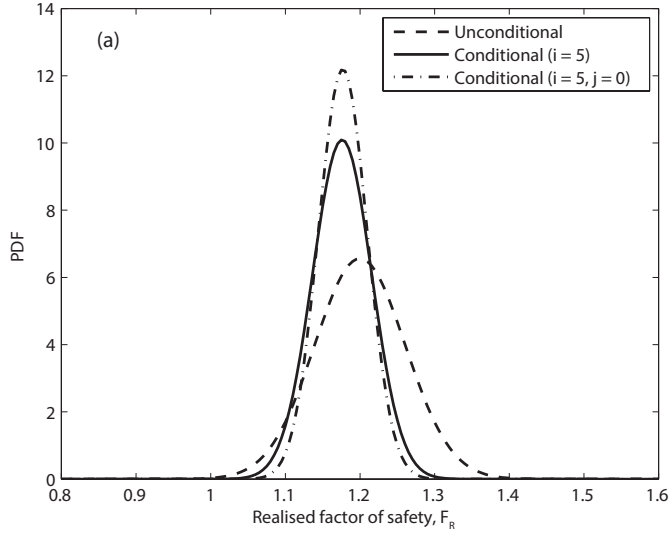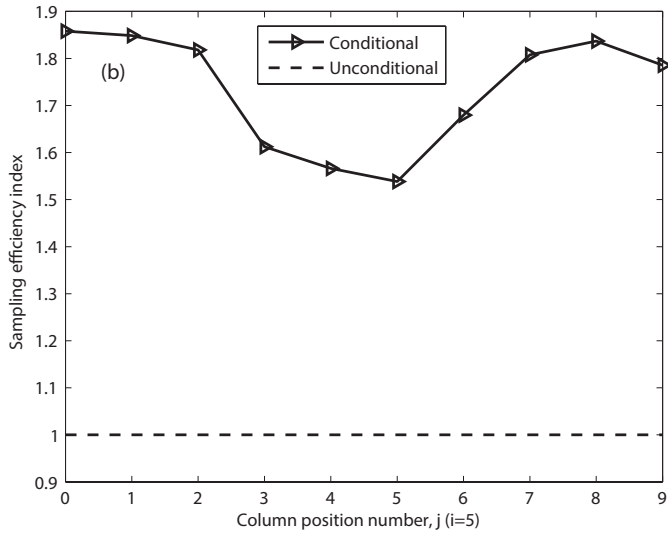
Figure 6.12: Influence of CPT location j during the second phase of site investigation (based on $\theta_v = 1.0$ m and 500 realisations per simulation): probability density function of realised factor of safety ($\xi = 6$) (a); influence of CPT location j with $i = 5$ ($\xi = 6$) (b)
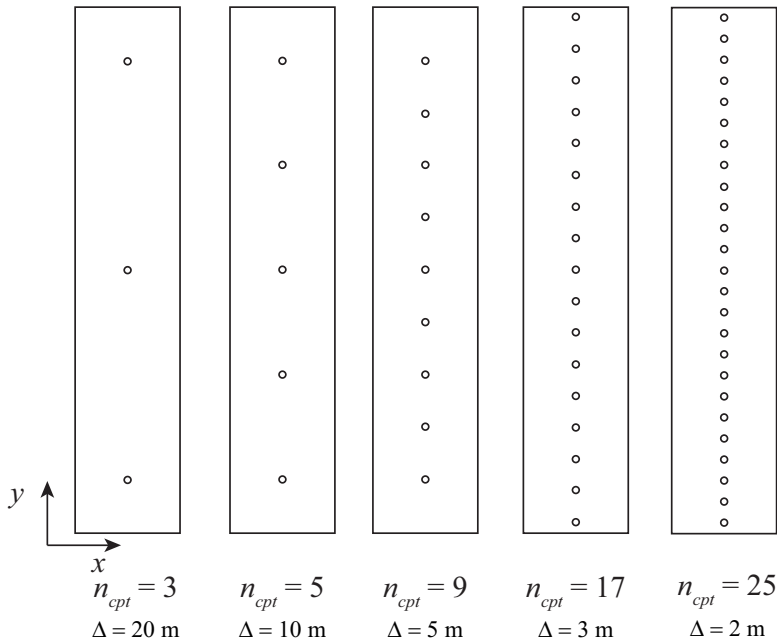
Figure 6.13: CPT layouts (plan views) for various numbers of boreholes (n_{cpt} = 3, 5, 9, 17, 25 and Δ denotes the distance between CPTs)

properties in the original ground profile.

If a second row of CPT tests (at position j) is to be performed in a second phase of the site investigation (e.g. as illustrated in Fig. 6.11(b)), the above procedure can be repeated by changing j in the range 0–9 to locate the best positions for the new CPTs, assuming that the position of the first set of CPT profiles has been set to $i = 5$. This is shown in Fig. 6.12 for the case of $\xi = 6$. Fig. 6.12(a) shows the probability distributions of the realised factor of safety for the unconditional simulation, the conditional simulation for one row of CPTs at $i = 5$ and the conditional simulation for an additional row of CPTs at position $j = 0$. It is seen that the confidence level in the project has been further increased by the second phase of site investigation. Fig. 6.12(b) shows the sampling efficiency indices for various locations j of the second row of CPTs. It suggests that the best location for carrying out the second phase of site investigation can be at either side of the slope crest (at approximately 3 m distance from the crest for the input parameters used in this example, i.e. $\theta_h = 6$ m). To further investigate the influence of CPT intensity on the uncertainty in the realised factor of safety, conditional simulations involving different numbers of CPTs (and thereby different distances (Δ) between adjacent CPTs) have been carried out for the case of $\xi = 6$, 12 and 24. Fig. 6.13 shows the plan views of CPT layouts for $n_{cpt} = 3$, 5, 9, 17 and 25 (corresponding to CPT spacings of $\Delta = 20$, 10, 5, 3 and 2 m, respectively), with the locations of the CPTs in the x-direction being fixed at $i = 5$. Fig. 6.14 shows the influence of CPT density on the sampling efficiency indices for the three values of

ξ. It is seen that there is only a marginal benefit in increasing the scope of investigation by having CPT spacings less than $\Delta \approx \theta_h/2$ especially for the $\xi = 6$ and 12 cases. For $\xi = 24$, the sampling efficiency index is as high as 4 when $\Delta \approx \theta_h/2$ although more CPTs (i.e. $\Delta \approx \theta_h/4$, $n_{cpt} = 9$) may improve the sampling efficiency to a value of 4.5. However, the general finding from Figs 6.9(b) and 6.11 is that the optimal sampling distance is around $\theta_h/2$ for the problem investigated, based on the assumed correlation function.

6.6.2. EXAMPLE 2−COST-EFFECTIVE DESIGN OF SLOPE GEOMETRY

In the second example, a soil deposit characterised by spatially varying undrained shear strength is to be excavated to form a slope of a certain angle. Site investigations have been conducted based on CPT tests. The question is: In order to satisfy a target reliability level of, for example, 95%, as suggested in Eurocode 7 (CEN, 2004) and discussed in Hicks and Nuttall (2012), how steep should the slope be designed?

Fig. 6.15 shows three possible slope angles, with the corresponding finite element mesh discretisations. The slope is 5 m high and 50 m long in the third dimension, and the left-hand boundary is taken to be 15 m from the slope toe. Five CPTs were taken along the length of the slope at 10 m centres, at the location of the column of Gauss points nearest the slope crest, for the 1:1 slope, as seen in the figure. The clay soil has a mean undrained shear strength of 21 kPa, a coefficient of variation of 0.2, a vertical scale of fluctuation of 1 m and a horizontal scale of fluctuation of 12 m.

The three candidate slopes are (vertical:horizontal) 1:2, 1:1 and 2:1. Based on only the mean undrained shear strength, these three slopes have deterministic factors of safety F_T of 1.73, 1.29 and 1.07. Both conditional and unconditional simulations were carried out to investigate the reliability of each slope, and, for each simulation, 500 realisations were analysed. Note that, as in the previous example, one reference random field is generated first and assumed to represent the real field situation. The conditional random fields used in the RFEM analyses are therefore based on CPT measurements taken from this 'real' field.

The stability of the slopes were calculated by the strength reduction method by applying gravitational loading. The probability density distributions of the realised factor of safety are shown in Fig. 6.16 for the three slopes, for both conditional and unconditional simulations. The deterministic factors of safety F_T, i.e. the factors of safety based on the mean property values, are also shown. It is seen that, if unconditional simulation is used, there is a significant chance that the 2:1 slope will fail (the probability of failure is the area under the pdf for the realised factor of safety smaller than 1.0). Unsurprisingly, the gentlest (i.e. 1:2) slope has the lowest probability of failure. However, once again, conditional simulations significantly reduce the uncertainty in the structural response, as clearly demonstrated by the narrower probability distributions. In particular, the reliability of the steepest slope increases from 77% to 99% when the CPT measurements are taken into account.

The results show that, if unconditional simulations are used, the 1:1 and 1:2 slopes satisfy a target reliability level of 95%, whereas the 2:1 slope does not. However, when the additional information from the CPT profiles is used, all three cases meet the target reliability. The message here is that the embankment may be designed to a slope angle of 2:1 if the CPT measurements are used in the simulation, which is, of course, a more
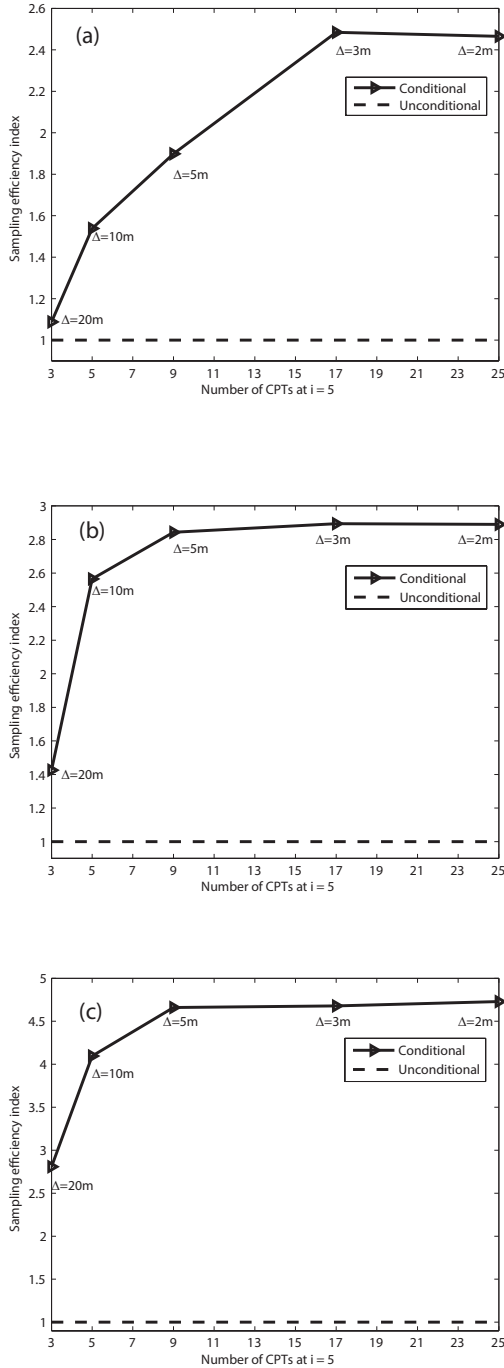
Figure 6.14: Influence of number of CPTs (at $i = 5$) on sampling efficiency for various values of ξ and $\theta_v = 1.0$ m (denotes the distance between CPTs): (a) $\xi = 6$ ($\theta_h = 6$ m); (b) $\xi = 12$ ($\theta_h = 12$ m); (c) $\xi = 24$ ($\theta_h = 24$ m)
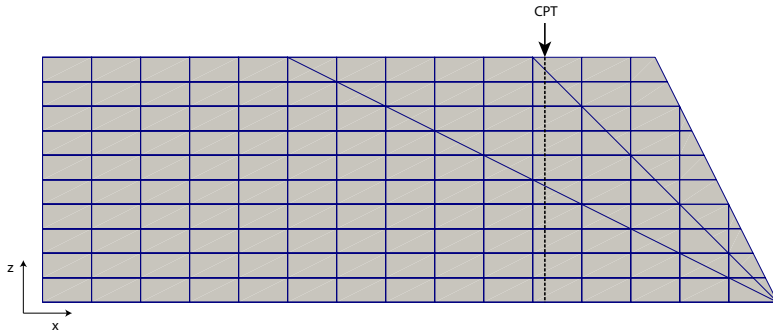
Figure 6.15: Finite element mesh for different slope geometries
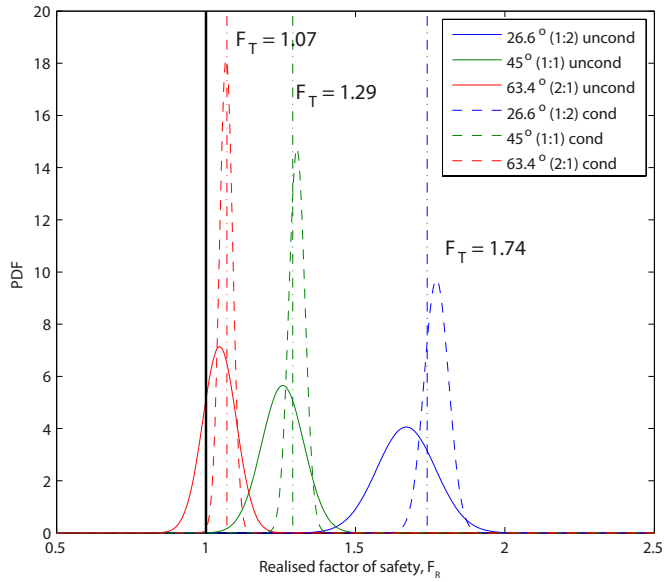
Figure 6.16: PDFs of realised factor of safety for three slopes, based on conditional and unconditional simulations (cond: conditional; uncond: unconditional)

logical thing to do, and this has implications for the soil volume to be excavated and thereby cost, although the cost can be site dependent (e.g. on whether there are nearby structures). A best design is a design that meets the requirements set by standards, while, at the same time, minimising the cost. In this case, the steepest slope may be a cost effective design.

6.7. CONCLUSIONS

An approach for conditioning 3D random fields based on CPT measurements has been implemented and validated, and then applied to two numerical examples to illustrate its potential use for geotechnical site exploration and cost-effective design. It has been shown that conditional simulations based on CPT data are able to increase the confidence in a design's success or failure. Indeed, the reliability from a conditional simulation can be thought of as a conditional reliability (or conditional probability of failure not occurring), i.e. based on a 'posterior' distribution of the structure performance after taking account of the spatial distribution of all the measured CPT data points. In contrast, the unconditional simulation based on random field theory only results in a 'prior' distribution of the structure response. This was clearly demonstrated by the updating of the probability density distributions in the two numerical examples. Although Bayesian updating is not used in this chapter, the effect is similar.

If further CPT measurements are required, the approach can be repeated for updating the response probability density function. In this way, the confidence in the probability of failure or survival will be further increased. In fact, in many cases a multi-stage site investigation may be carried out, with the results of the initial analysis guiding further field tests. As demonstrated in the first example, if a second stage of site exploration were to be conducted, it is possible to find out the optimum location for the additional testing. This highlights the method's potential use in directing site exploration programmes and thereby improving the efficient use of field measurements. For the first example considered in this chapter, an optimal sampling distance of half the horizontal scale of fluctuation was identified when an exponential correlation function is used. For the second example, the conditional simulation led to a more cost-effective design.

6

7

CONCLUSIONS

7.1. INTRODUCTION

Geotechnical engineers are now paying more attention to material heterogeneity in designs. For example, the probabilistic analysis of slope stability is becoming routine engineering practice in the Netherlands for the (strengthening) design of dike systems. Design tools incorporating spatial variability considerations (e.g. the Calle (1985) model) are available, as in software developed by Deltares (2016). By representing the soil properties as random fields, characterised by probability distributions and spatial correlation structures, a probabilistic assessment is possible; e.g. in the case of slope stability, the probability of failure (or, alternatively, reliability) can be computed, and, when combined with a consideration of failure consequence, give rise to an understanding of the risk involved.

However, while current probabilistic design tools provide a useful aid in the design process, there are certain simplifications in these models that require examination. For example, a rigid cylindrical failure is assumed in the models proposed by Vanmarcke (1977b) and Calle (1985). It is therefore important to identify when these simplifications are reasonable approximations and when some caution is needed. This thesis has sought to investigate this issue for 3D slope stability analysis by comparing the performance of these simpler probabilistic methods with the more advanced, but computationally more expensive, random finite element method (RFEM). Indeed, it is only in recent years, with the increasing power of computers, that more advanced methods such as RFEM can be used to thoroughly investigate the influence of spatial variability on long 3D slope failures. The thesis follows on from previous investigations, including those by Hicks and Spencer (2010) and Hicks et al. (2014), who conducted parametric studies into the influence of different aspects of heterogeneity and slope geometry on slope reliability and performance.

Focusing specifically on 3D spatial variability in slope stability analysis, the primary goal of this thesis has been to investigate the performance of RFEM and the two simpler limit equilibrium based models. In short, it contains the following:

- An evaluation of the models of Vanmarcke (1977b) and Calle (1985), in which the failure mechanisms have been idealised as a single cylindrical failure; in the former case from a 3D perspective, and in the latter case from a 2D perspective with an extension in the third dimension.

- An investigation of slope stability problems for very long 3D slopes, in order to evaluate the length effect.

- A step towards more realistic random field realisations of soil properties, in which field measurements are utilised directly in the realised random fields in order to reduce uncertainties in material variability and structural performance.

- An investigation of factors influencing the optimal sampling locations in site investigations.

Section 7.2 lists the main research conclusions from the thesis, while Section 7.3 gives recommendations for further study.

7.2. Research Conclusions

7.2.1. Random field generator and Kriging

Fully working 2D and 3D LAS random field generators were inherited by the Author from Spencer (2007). Kriging algorithms in 2D and 3D were implemented by the Author based on well-known mathematics in geostatistcs, and these were combined with the random field generators to enable the generation of 2D and 3D conditional random fields. The validity of the conditional simulator was demonstrated by an examination of the covariance structure. Moreover, the conditional random fields were shown to match measurement data at borehole locations and honour the spatial correlations of the soil properties. In this way, the simulations are fully consistent with the field data at the measurement locations, thereby making best use of the measurement data.

7.2.2. Parallelisation

When the problem size is scaled up (as in going from 2D to 3D simulations), it is necessary to parallelise the process so that the desired analyses can be run in a reasonable time. The Author has implemented a parallelised Monte Carlo method based on two schemes:

- Cloud computing with a master–slave relationship;

- Grid computing with a CouchDB pool server.

This allowed analyses to be run in a timely fashion, shortening job times from years/months to days. The computing strategies can be modified without much effort to cope with other types of application.

7.2.3. Comparative investigation of slope model performance

The first part of the research work in this thesis related to comparing the performance of RFEM with Vanmarcke's (1977b) simplified model for a geometrically long 'linear' slope. The ability of 3D RFEM analysis to model failure surfaces of varying geometry, thereby accounting for the wide range of possible failure surfaces over which strength values are averaged (rather than simple spatial averages over a single predefined failure surface of one critical length, such as the cylindrical surface assumed in Vanmarcke's solution) was highlighted as a contributing factor to the differences observed between the two models. A second factor is the ability of RFEM to seek out semi-continuous weak zones, thereby reducing the average shear strength over the failure surface. Thirdly, the rigid cylindrical failure in Vanmarcke's model gives rise to an exaggerated prediction of the slide's end resistance, especially for smaller values of the horizontal scale of fluctuation.

The second part of the work concerned an investigation of length effects on the reliability of very long slopes. The analyses demonstrated that, for a stationary random process, the reliability changes in line with the principles of probability of multiple independent events. It was shown that a power law equation based on the assumption of a series system composed of multiple independent elements gives a close fit to the computed results, demonstrating that the probability of failure for long slopes may be estimated from the detailed analysis of shorter and computationally less intensive 3D slopes (as previously highlighted by Hicks and Spencer (2010), albeit for slopes of shorter

length). The ability of RFEM to account for the possibility of failure at any location along the analysed domain stimulated the comparison of RFEM with the length-dependent models of Vanmarcke (1977b) and Calle (1985). It was shown that the three methods can give significantly different results, depending on the value of the horizontal scale of fluctuation (SOF) relative to the slope length and height, with RFEM predicting a lower slope reliability than the two simpler methods in all cases. However, for large horizontal SOFs compared to slope length, the results of the three methods are generally closer. Discrete failure lengths were quantified using RFEM and compared with the failure lengths provided by the Vanmarcke (1977b) and Calle (1985) models, with the differences in failure length (coupled with an evaluation of the different model assumptions) providing a possible reason for the differences in reliability indices. The effect of the α factor, used by Dutch practice in Calle's method, was thoroughly investigated and explained by variance reduction theory. It was shown to be a function of the horizontal and vertical SOFs, and of the slope dimensions. By incorporating this factor into the correlation function used in Calle's model, the reliability indices were shown be closer to the RFEM predictions.

7.2.4. INVESTIGATION OF SITE INVESTIGATION PLANS AND SLOPE DESIGNS

The conditional simulator was applied to two numerical examples to illustrate its potential use for geotechnical site exploration and cost-effective design. It has been shown that conditional simulations based on CPT data are able to increase the confidence in a design's success or failure. Optimum locations can be identified for the testing, as was illustrated in the first example for 2 phases of site exploration. This highlights the method's potential use in directing site exploration programmes and thereby improving the efficient use of field measurements. Sampling intensity was also investigated in the first example, with an optimal sampling distance of half the horizontal scale of fluctuation being identified based on an exponential correlation function. For the second example, conditional simulation led to the more cost-effective design of a slope (i.e. the steepest slope), by meeting the design standards with respect to reliability while reducing the soil volume that needed to be excavated.

7.3. RECOMMENDATIONS FOR FURTHER WORK

Based on the Author's experience, the following recommendations are made for future work:

- Most of this thesis is devoted to reliability; that is, one minus the probability of failure. However, further developments of the framework have included the quantification of slide volumes and lengths (i.e. the consequence) using a threshold displacement approach, thereby providing a first step towards quantifying the risks involved in a project, i.e. the probability of failure multiplied by the failure consequence. So, a next step would be to quantify the risks involved in the design of long slopes.

- The developed framework for 3D conditional simulation has been used in two simple examples, but the same framework can be extended to include more complicated examples (e.g. irregular sampling strategies such as stratified sampling,

nested sampling, random sampling, and so on) for cost effective site investigation plans and designs. Note also that the values obtained at the precise locations of the measurements are rather far from being deterministic, because of measurement uncertainties and model transformation errors. Hence, a next step could be to add some noise on these measurements, i.e. to develop techniques to generate random fields which are conditional, but not in an absolute manner; for example, Li et al. (2015b) used the Markov Chain Monte Carlo method to generate conditional samples of geologic profiles in a 2D plane. The resulting random fields would then be random everywhere, but much less so in the neighborhood of the measurements themselves. Moreover, although it has been found in this thesis that the optimum CPT sampling space is around half of the horizontal scale of fluctuation, the horizontal scale of fluctuation is, of course, unknown before carrying out a site investigation. Therefore, the site investigation plans should preferably be an iterative process: an initial plan based on engineering judgment should be carried out first; the point and spatial statistics can then be estimated from the initial investigation; then the site investigation plan can be refined to update the estimates of the relevant statistics. Also, only 'direct' measurements corresponding to input variables have been used in the current implementation of the conditional random field simulator; the next step could be to incorporate indirect measurements corresponding to system responses, such as deformations and pore pressure measurements (e.g. for c-ϕ slopes), i.e. inverse modelling.

- The random finite element method is able to simulate multiple failures along the length of a slope, although only a single failure is assumed in Vanmarcke's and Calle's models, so this is one point of inconsistency in the comparison analyses performed in this thesis. An interesting direction would be to develop, analytically, a model that is simply an extension of Vanmarcke's model to be able to take account of, e.g. two failures.

- The end effect in Vanmarcke's and Calle's models is likely to be overestimated, especially for relatively short slope failures. It may be intuitive to think that short failures are less likely to occur due to larger end effects, but would the end effects really be that large (in reality) when one thinks about the weakest path mechanism? It would be interesting to look at the uncertainties associated with the end faces in the two semi-analytical models.

- Different decisions (e.g. target reliability) need to be made, based on the different length scales in a geotechnical structure. The present framework can be extended to a larger scale, e.g. regional or national scale, based on the research presented in Vanmarcke and Otsubo (2013), i.e. for longer slopes with multiple segments having distinctly different properties (e.g. strength, load and geometry).

- The investigation carried out in this thesis has mainly focused on the short term (i.e. undrained) behavior of a slope. More practical scenarios would be effective stress analyses taking account of pore pressure accumulation and dissipation during construction of a new structure, or during rainfall infiltration and evaporation in the case of an existing structure.

- At a small target probability of failure (e.g. as when the factor of safety based on the mean shear strength is relatively large), the number of Monte Carlo realisations should be large in order to get more accurate and meaningful results around $F \approx 1.0$. In this case, subset simulation (or other estimator variance reduction techniques) may be used to improve the performance of the Monte Carlo Method. This has been done in 2D by various researchers. However, the gain in 3D would be more apparent due to 3D analysis being very expensive (see for example, Xiao et al. (2016) for the so-called auxiliary random finite element method (ARFEM)).

- A systematic comparative analysis with respect to FORM analysis for 3D slope reliability (e.g. Ji and Chan (2014); Ji (2014) used FORM to analyse 3D slope reliability by considering only the longitudinal spatial variability) can be carried out using the methodology presented in this thesis. In this way, the influence of spatial variability in the other two directions may be investigated and the justification provided for a simplified FORM analysis that ignores the variability in the cross-sectional plane, thereby bypassing the high-dimensional problem that would otherwise be encountered.

7

REFERENCES

Ahmed, A. and Soubra, A.-H. (2012). "Probabilistic analysis of strip footings resting on a spatially random soil using subset simulation approach." *Georisk: Assessment and Management of Risk for Engineered Systems and Geohazards*, 6(3), 188–201.

Ang, A. H. and Tang, W. H. (1984). *Probability concepts in engineering planning and design. Vol. II: Decision, risk, and reliability*. John Wiley & Sons, New York.

Arnold, P., Fenton, G. A., Hicks, M. A., Schweckendiek, T., and Simpson, B. (2012). *Modern geotechnical design codes of practice: Implementation, application and development*. IOS Press, Amsterdam.

Arnold, P. and Hicks, M. A. (2011). "A stochastic approach to rainfall-induced slope failure." *Proceedings of the 3rd International Symposium on Geotechnical Safety and Risk (ISGSR)*, Munich, Germany, 107–115.

Arregui-Mena, J. D., Margetts, L., Griffiths, D. V., Lever, L., Hall, G., and Mummery, P. M. (2015). "Spatial variability in the coefficient of thermal expansion induces pre-service stresses in computer models of virgin gilsocarbon bricks." *Journal of Nuclear Materials*, 465, 793–804.

Asaoka, A. and Grivas, D. A. (1982). "Spatial variability of the undrained strength of clays." *Journal of Geotechnical Engineering Division*, ASCE, 108(5), 743–756.

Auvinet, G. and Gonzalez, J. L. (2000). "Three-dimensional reliability analysis of earth slopes." *Computers and Geotechnics*, 26(3), 247–261.

Babu, G. S. and Srivastava, A. (2007). "Reliability analysis of allowable pressure on shallow foundation using response surface method." *Computers and Geotechnics*, 34(3), 187–194.

Baecher, G. B. (1983). "Simplified geotechnical data analysis." *Reliability theory and its application in structural and soil mechanics*, Springer, 257–277.

Baecher, G. B. and Christian, J. T. (2005). *Reliability and statistics in geotechnical engineering*. John Wiley & Sons, New York.

Bergado, D. T., Patron, B. C., Youyongwatana, W., Chai, J.-C., et al. (1994). "Reliability-based analysis of embankment on soft Bangkok clay." *Structural Safety*, 13(4), 247–266.

Box, G. E. and Wilson, K. B. (1951). "On the experimental attainment of optimum conditions." *Journal of the Royal Statistical Society: Series B (Methodological)*, 13(1), 1–45.

Broere, W. (2001). "Tunnel face stability and new CPT applications." Ph.D. thesis, Delft University of Technology, Delft, Netherlands.

Cafaro, F. and Cherubini, C. (2002). "Large sample spacing in evaluation of vertical strength variability of clayey soil." *Journal of Geotechnical and Geoenvironmental Engineering*, 128(7), 558–568.

Calle, E. O. F. (1985). "Probabilistic analysis of stability of earth slopes." *Proceedings of the 11th International Conference on Soil Mechanics and Foundation Engineering*, San Francisco, California, USA, 809–812.

Catalan, J. M. and Cornell, C. A. (1976). "Earth slope reliability by a level-crossing method." *Journal of Geotechnical and Geoenvironmental Engineering*, 102(GT6), 591–604.

CEN (2004). "Eurocode 7: Geotechnical design–part 1: General rules." *EN 1997-1, European Committee for Standardisation (CEN)*.

Chiasson, P., Lafleur, J., Soulié, M., and Law, K. T. (1995). "Characterizing spatial variability of a clay by geostatistics." *Canadian Geotechnical Journal*, 32(1), 1–10.

Chiles, J.-P. and Delfiner, P. (2009). *Geostatistics: modeling spatial uncertainty*. John Wiley & Sons, New York.

Ching, J. and Phoon, K.-K. (2013a). "Effect of element sizes in random field finite element simulations of soil shear strength." *Computers and Structures*, 126, 120–134.

Ching, J. and Phoon, K.-K. (2013b). "Multivariate distribution for undrained shear strengths under various test procedures." *Canadian Geotechnical Journal*, 50(9), 907–923.

Ching, J., Phoon, K.-K., and Hu, Y.-G. (2009). "Efficient evaluation of reliability for slopes with circular slip surfaces using importance sampling." *Journal of Geotechnical and Geoenvironmental Engineering*, 135(6), 768–777.

Cho, S. E. (2007). "Effects of spatial variability of soil properties on slope stability." *Engineering Geology*, 92(3), 97–109.

Cho, S. E. (2009). "Probabilistic assessment of slope stability that considers the spatial variability of soil properties." *Journal of Geotechnical and Geoenvironmental Engineering*, 136(7), 975–984.

Christian, J. T. and Baecher, G. B. (2011). "Unresolved problems in geotechnical risk and reliability." *Proceedings of GeoRisk 2011: Geotechnical Risk Assessment and Management*, Atlanta, Georgia, USA, 50–63.

Christian, J. T., Ladd, C. C., and Baecher, G. B. (1994). "Reliability applied to slope stability analysis." *Journal of Geotechnical Engineering*, 120(12), 2180–2207.

Cressie, N. (1990). "The origins of kriging." *Mathematical geology*, 22(3), 239–252.

DeGroot, D. J. (1996). "Analyzing spatial variability of in situ soil properties." *Uncertainty in the Geologic Environment: from Theory to Practice*, ASCE, Madison, Wisconsin, USA, 210–238.

DeGroot, D. J. and Baecher, G. B. (1993). "Estimating autocovariance of in-situ soil properties." *Journal of Geotechnical Engineering*, 119(1), 147–166.

Deltares (2016). *D-Geo Stability: Slope stability software for soft soil engineering - User Manual*. Delft, Netherlands.

Der Kiureghian, A. and Ke, J.-B. (1987). "The stochastic finite element method in structural reliability." *Stochastic Structural Mechanics*, Springer, 84–109.

Ditlevsen, O. (1981). *Uncertainty modeling with applications to multidimensional civil engineering systems.* McGraw-Hill, New York.

Duncan, J. M. (2000). "Factors of safety and reliability in geotechnical engineering." *Journal of Geotechnical and Geoenvironmental Engineering*, 126(4), 307–316.

Duncan, J. M., Navin, M., and Wolff, T. F. (2003). "Discussion on 'probabilistic slope stability analysis for practice'." *Canadian Geotechnical Journal*, 40(4), 848–850.

EGEE (2005). "Job description language attributes specification for the gLite workload management system." *surfsara wikipage link*. https://grid.surfsara.nl/wiki/index.php/Job_Description_Language. Accessed: 2015-12-8.

El-Ramly, H. (2002). "Probabilistic analyses of landslide hazards and risks: Bridging theory and practice." Ph.D. thesis, University of Alberta, Edmonton, Alberta, Canada.

El-Ramly, H., Morgenstern, N. R., and Cruden, D. M. (2002). "Probabilistic slope stability analysis for practice." *Canadian Geotechnical Journal*, 39(3), 665–683.

El-Ramly, H., Morgenstern, N. R., and Cruden, D. M. (2003). "Probabilistic stability analysis of a tailings dyke on presheared clay shale." *Canadian Geotechnical Journal*, 40(1), 192–208.

El-Ramly, H., Morgenstern, N. R., and Cruden, D. M. (2006). "Lodalen slide: a probabilistic assessment." *Canadian Geotechnical Journal*, 43(9), 956–968.

Elkateb, T. M. (2003). "Quantification of soil heterogeneity." Ph.D. thesis, University of Alberta, Edmonton, Alberta, Canada.

Elkateb, T. M., Chalaturnyk, R., and Robertson, P. K. (2003). "An overview of soil heterogeneity: quantification and implications on geotechnical field problems." *Canadian Geotechnical Journal*, 40(1), 1–15.

Fenton, G. A. (1990). "Simulation and analysis of random fields." Ph.D. thesis, Princeton University, New Jersey, USA.

Fenton, G. A. (1994). "Error evaluation of three random-field generators." *Journal of Engineering Mechanics*, 120(12), 2478–2497.

Fenton, G. A. (1999a). "Estimation for stochastic soil models." *Journal of Geotechnical and Geoenvironmental Engineering*, 125(6), 470–485.

Fenton, G. A. (1999b). "Random field modeling of CPT data." *Journal of Geotechnical and Geoenvironmental Engineering*, 125(6), 486–498.

Fenton, G. A. (2007). "Data analysis/geostatistics." *Probabilistic Methods in Geotechnical Engineering*, Springer, 51–73.

Fenton, G. A. and Griffiths, D. V. (2002). "Probabilistic foundation settlement on spatially random soil." *Journal of Geotechnical and Geoenvironmental Engineering*, 128(5), 381–390.

Fenton, G. A. and Griffiths, D. V. (2003). "Bearing-capacity prediction of spatially random c–φ soils." *Canadian Geotechnical Journal*, 40(1), 54–65.

Fenton, G. A. and Griffiths, D. V. (2005). "Three-dimensional probabilistic foundation settlement." *Journal of Geotechnical and Geoenvironmental Engineering*, 131(2), 232–239.

Fenton, G. A. and Griffiths, D. V. (2008). *Risk assessment in geotechnical engineering*. John Wiley & Sons, New York.

Fenton, G. A. and Griffiths, D. V. (2010). "Reliability-based geotechnical engineering." *GeoFlorida 2010: Advances in Analysis, Modeling & Design*, ASCE, West Palm Beach, Florida, USA, 14–52.

Fenton, G. A., Griffiths, D. V., and Urquhart, A. (2003). "A slope stability model for spatially random soils." *Proceedings of the 9th International Conference on Applications of Statistics and Probability in Civil Engineering*, San Francisco, California, USA, 1263–1269.

Fenton, G. A., Hicks, M. A., Wang, X., and Griffiths, D. V. (2013). "Effect of slope height and gradient on failure probability." *Geo-Congress 2013: Stability and Performance of Slopes and Embankments III*, ASCE, San Diego, California, USA, 972–981.

Fenton, G. A. and Vanmarcke, E. H. (1990). "Simulation of random fields via local average subdivision." *Journal of Engineering Mechanics*, 116(8), 1733–1749.

Fenton, G. A. and Vanmarcke, E. H. (1998). "Spatial variation in liquefaction risk." *Géotechnique*, 48(6), 819–831.

Firouzianbandpey, S., Griffiths, D. V., Ibsen, L. B., and Andersen, L. V. (2014). "Spatial correlation length of normalized cone data in sand: case study in the north of Denmark." *Canadian Geotechnical Journal*, 51(8), 844–857.

Frank, R. (2004). *Designers' guide to EN 1997-1 Eurocode 7: Geotechnical design-General rules*. Thomas Telford, London.

Frimpong, S. and Achireko, P. K. (1998). "Conditional LAS stochastic simulation of regionalized variables in random fields." *Computational Geosciences*, 2(1), 37–45.

Gavin, H. P. and Yau, S. C. (2008). "High-order limit state functions in the response surface method for structural reliability analysis." *Structural Safety*, 30(2), 162–179.

GeoDelft (1994). *User's Manual PC-Model MproStab: Probabilistic analysis of stability of earth slopes.* Delft, Netherlands.

Griffiths, D. V. and Fenton, G. A. (1995). "Observations on two-and three-dimensional seepage through a spatially random soil." *Proceedings of the 7th International Conference on Applications of Statistics and Probability in Civil Engineering*, Paris, France, 65–70.

Griffiths, D. V. and Fenton, G. A. (1997). "Three-dimensional seepage through spatially random soil." *Journal of Geotechnical and Geoenvironmental Engineering*, 123(2), 153–160.

Griffiths, D. V. and Fenton, G. A. (1998). "Probabilistic analysis of exit gradients due to steady seepage." *Journal of Geotechnical and Geoenvironmental Engineering*, 124(9), 789–797.

Griffiths, D. V. and Fenton, G. A. (2004). "Probabilistic slope stability analysis by finite elements." *Journal of Geotechnical and Geoenvironmental Engineering*, 130(5), 507–518.

Griffiths, D. V., Fenton, G. A., and Denavit, M. D. (2007). "Traditional and advanced probabilistic slope stability analysis." *Proceedings of Geo-Denver 2007: Probabilistic Applications in Geotechnical Engineering*, ASCE, Denver, Colorado, USA, 1–10.

Griffiths, D. V., Huang, J., and Fenton, G. A. (2009a). "Influence of spatial variability on slope reliability using 2-D random fields." *Journal of Geotechnical and Geoenvironmental Engineering*, 135(10), 1367–1378.

Griffiths, D. V., Huang, J., and Fenton, G. A. (2009b). "On the reliability of earth slopes in three dimensions." *Proceedings of the Royal Society A: Mathematical, Physical and Engineering Sciences*, The Royal Society, 465(2110), 3145–3164.

Griffiths, D. V. and Lane, P. A. (1999). "Slope stability analysis by finite elements." *Géotechnique*, 49(3), 387–403.

Griffiths, D. V., Paiboon, J., Huang, J., and Fenton, G. A. (2012). "Homogenization of geomaterials containing voids by random fields and finite elements." *International Journal of Solids and Structures*, 49(14), 2006–2014.

Haldar, S. and Babu, G. S. (2009). "Design of laterally loaded piles in clays based on cone penetration test data: a reliability-based approach." *Géotechnique*, 59(7), 593–607.

Hasofer, A. M. and Lind, N. C. (1974). "Exact and invariant second-moment code format." *Journal of the Engineering Mechanics Division*, 100(1), 111–121.

Hassan, A. M. and Wolff, T. F. (1999). "Search algorithm for minimum reliability index of earth slopes." *Journal of Geotechnical and Geoenvironmental Engineering*, 125(4), 301–308.

Hicks, M. A. (2007). *Risk and variability in geotechnical engineering*. Thomas Telford, London.

Hicks, M. A., Chen, J., and Spencer, W. A. (2008). "Influence of spatial variability on 3D slope failures." *Proceedings of the 6th International Conference on Computer Simulation in Risk Analysis and Hazard Mitigation*, Kefalonia, Greece, 335–342.

Hicks, M. A. and Nuttall, J. D. (2012). "Influence of soil heterogeneity on geotechnical performance and uncertainty: A stochastic view on EC7." *Proceedings of the 10th International Probabilistic Workshop, Universität Stuttgart, Stuttgart*, 215–227.

Hicks, M. A., Nuttall, J. D., and Chen, J. (2014). "Influence of heterogeneity on 3D slope reliability and failure consequence." *Computers and Geotechnics*, 61, 198–208.

Hicks, M. A. and Onisiphorou, C. (2005). "Stochastic evaluation of static liquefaction in a predominantly dilative sand fill." *Géotechnique*, 55(2), 123–133.

Hicks, M. A. and Samy, K. (2002). "Influence of heterogeneity on undrained clay slope stability." *Quarterly Journal of Engineering Geology and Hydrogeology*, 35(1), 41–49.

Hicks, M. A. and Samy, K. (2004). "Stochastic evaluation of heterogeneous slope stability." *Italian Geotechnical Journal*, 38(2), 54–66.

Hicks, M. A. and Spencer, W. A. (2010). "Influence of heterogeneity on the reliability and failure of a long 3D slope." *Computers and Geotechnics*, 37(7), 948–955.

Honjo, Y. and Kuroda, K. (1991). "A new look at fluctuating geotechnical data for reliability design." *Soils and Foundations*, 31(1), 110–120.

Hooper, J. A. and Butler, F. G. (1966). "Some numerical results concerning the shear strength of London clay." *Géotechnique*, 16(4), 282–304.

Hsu, S.-C. and Nelson, P. P. (2006). "Material spatial variability and slope stability for weak rock masses." *Journal of Geotechnical and Geoenvironmental Engineering*, 132(2), 183–193.

Huang, J., Lyamin, A. V., Griffiths, D. V., Krabbenhoft, K., and Sloan, S. W. (2013). "Quantitative risk assessment of landslide by limit analysis and random fields." *Computers and Geotechnics*, 53, 60–67.

Huang, S. and Kou, X. (2007). "An extended stochastic response surface method for random field problems." *Acta Mechanica Sinica*, 23(4), 445–450.

Huang, S., Mahadevan, S., and Rebba, R. (2007). "Collocation-based stochastic finite element analysis for random field problems." *Probabilistic Engineering Mechanics*, 22(2), 194–205.

Huang, S. P., Liang, B., and Phoon, K. K. (2009). "Geotechnical probabilistic analysis by collocation-based stochastic response surface method: An excel add-in implementation." *Georisk: Assessment and Management of Risk for Engineered Systems and Geohazards*, 3(2), 75–86.

Jaksa, M. B. and Fenton, G. A. (2002). "Assessment of fractal behavior of soils." *International Conference on Probabilistics in GeoTechnics: Technical and Economic Risk Estimation*, Graz, Austria, 47–54.

Jaksa, M. B., Goldsworthy, J. S., Fenton, G. A., Kaggwa, W. S., Griffiths, D. V., Kuo, Y. L., and Poulos, H. G. (2005). "Towards reliable and effective site investigations." *Géotechnique*, 55(2), 109–121.

Jaksa, M. B., Kaggwa, W. S., and Brooker, P. I. (1999). "Experimental evaluation of the scale of fluctuation of a stiff clay." *Proceedings of the 8th International Conference on Applications of Statistics and Probability*, Sydney, Australia, 415–422.

Jamshidi Chenari, R. and Oloomi Dodaran, R. (2010). "New method for estimation of the scale of fluctuation of geotechnical properties in natural deposits." *Computational Methods in Civil Engineering*, 1(1), 55–64.

Ji, J. (2014). "A simplified approach for modeling spatial variability of undrained shear strength in out-plane failure mode of earth embankment." *Engineering Geology*, 183, 315–323.

Ji, J. and Chan, C. L. (2014). "Long embankment failure accounting for longitudinal spatial variation–a probabilistic study." *Computers and Geotechnics*, 61, 50–56.

Ji, J., Liao, H. J., and Low, B. K. (2012). "Modeling 2-D spatial variation in slope reliability analysis using interpolated autocorrelations." *Computers and Geotechnics*, 40, 135–146.

Jiang, S.-H., Li, D.-Q., Cao, Z.-J., Zhou, C.-B., and Phoon, K.-K. (2014). "Efficient system reliability analysis of slope stability in spatially variable soils using Monte Carlo simulation." *Journal of Geotechnical and Geoenvironmental Engineering*, 141(2), 04014096(1–13).

Jongejan, R., Maaskant, B., ter Horst, W., Havinga, F., Roode, N., and Stefess, H. (2013). "The VNK2-project: a fully probabilistic risk analysis for all major levee systems in the Netherlands." *IAHS-AISH publication*, 75–85.

Journel, A. G. (1974). "Geostatistics for conditional simulation of ore bodies." *Economic Geology*, 69(5), 673–687.

Journel, A. G. and Huijbregts, C. J. (1978). *Mining geostatistics.* Academic press, San Francisco.

Keaveny, J. M., Nadim, F., and Lacasse, S. (1989). "Autocorrelation functions for offshore geotechnical data." *Proceedings of the 5th International Conference on Structural Safety and Reliability (ICOSSAR)*, ASCE, San Francisco, USA, 263–270.

Kenarsari, A. E., Chenari, R. J., and Eslami, A. (2013). "Characterization of the correlation structure of residual CPT profiles in sand deposits." *International Journal of Civil Engineering, Transaction B: Geotechnical Engineering*, 11(1), 29–37.

Kim, H. (2005). "Spatial variability in soils: stiffness and strength." Ph.D. thesis, Georgia Institute of Technology, Atlanta, Georgia, USA.

Krige, D. G. (1951). "A statistical approach to some mine valuation and allied problems on the witwatersrand." M.S. thesis, University of the Witwatersrand, Johannesburg, Gauteng, South Africa.

Kulatilake, P. H. and Ghosh, A. (1988). "An investigation into accuracy of spatial variation estimation using static cone penetrometer data." *Proceedings of the 1st International Conference on Penetration Testing*, Orlando, Florida, USA, 815–821.

Kuo, Y. L., Jaksa, M. B., Kaggwa, G., Fenton, G. A., Griffiths, D. V., and Goldsworthy, J. S. (2004). "Probabilistic analysis of multi-layered soil effects on shallow foundation settlement." *Proceedings of the 9th Australia–New Zealand Conference on Geomechanics*, Auckland, New Zealand, 541–547.

Kutschke, W. (2011). "Investigation of lateral stress relief on the stability of $\varphi = 0°$ slopes using laboratory, fracture mechanics, and finite element method approaches." Ph.D. thesis, University of Pittsburgh, Pennsylvania, USA.

Lacasse, S. and de Lamballerie, J. Y. (1995). "Statistical treatment of CPT data." *Proceedings of the International Symposium on Cone Penetration Testing*, Linköping, Sweden, 369–377.

Lacasse, S. and Nadim, F. (1997). "Uncertainties in characterising soil properties." *Publikasjon-Norges Geotekniske Institutt*, 201, 49–75.

Lee, I. K., White, W., Ingles, O. G., et al. (1983). *Geotechnical engineering*. Pitman Publishing, Melbourne.

Li, C.-C. and Der Kiureghian, A. (1993). "Optimal discretization of random fields." *Journal of Engineering Mechanics*, 119(6), 1136–1154.

Li, D.-Q., Chen, Y.-F., Lu, W.-B., and Zhou, C.-B. (2011). "Stochastic response surface method for reliability analysis of rock slopes involving correlated non-normal variables." *Computers and Geotechnics*, 38(1), 58–68.

Li, D.-Q., Jiang, S.-H., Cao, Z.-J., Zhou, W., Zhou, C.-B., and Zhang, L.-M. (2015a). "A multiple response-surface method for slope reliability analysis considering spatial variability of soil properties." *Engineering Geology*, 187, 60–72.

Li, X. Y., Zhang, L. M., and Li, J. H. (2015b). "Using conditioned random field to characterize the variability of geologic profiles." *Journal of Geotechnical and Geoenvironmental Engineering*, 142(4), 04015096(1–11).

Li, Y. J. and Hicks, M. A. (2014). "Comparative study of embankment reliability in three dimensions." *Proceedings of the 8th European Conference on Numerical Methods in Geotechnical Engineering (NUMGE)*, Delft, Netherlands, 467–472.

Li, Y. J., Hicks, M. A., and Nuttall, J. D. (2013). "Probabilistic analysis of a benchmark problem for slope stability in 3D." *Proceedings of the 3rd International Symposium on Computational Geomechanics (COMGEO III)*, Krakow, Poland, 641–648.

Li, Y. J., Hicks, M. A., and Nuttall, J. D. (2015c). "Comparative analyses of slope reliability in 3D." *Engineering Geology*, 196, 12–23.

Li, Y. J., Hicks, M. A., and Vardon, P. J. (2015d). "High performance computing strategies for nonlinear finite element analysis of long heterogeneous soil slopes." *Proceedings of the 23rd UK Conference of the Association for Computational Mechanics in Engineering*, Swansea, UK, 427–430.

Li, Y. J., Hicks, M. A., and Vardon, P. J. (2015e). "Three dimensional discrete failures in long heterogeneous slopes." *Proceedings of the 5th International Symposium on Geotechnical Safety and Risk*, Rotterdam, Netherlands, 666–670.

Li, Y. J., Hicks, M. A., and Vardon, P. J. (2016). "Uncertainty reduction and sampling efficiency in slope designs using 3D conditional random fields." *Computers and Geotechnics*, 79, 159–172.

Liu, W. K., Belytschko, T., and Mani, A. (1986). "Random field finite elements." *International Journal for Numerical Methods in Engineering*, 23(10), 1831–1845.

Lloret-Cabot, M., Fenton, G. A., and Hicks, M. A. (2014). "On the estimation of scale of fluctuation in geostatistics." *Georisk: Assessment and Management of Risk for Engineered Systems and Geohazards*, 8(2), 129–140.

Lloret-Cabot, M., Hicks, M. A., and Van den Eijnden, A. P. (2012). "Investigation of the reduction in uncertainty due to soil variability when conditioning a random field using Kriging." *Géotechnique Letters*, 2, 123–127.

Low, B. K. (2014). "FORM, SORM, and spatial modeling in geotechnical engineering." *Structural Safety*, 49, 56–64.

Low, B. K., Gilbert, R. B., and Wright, S. G. (1998). "Slope reliability analysis using generalized method of slices." *Journal of Geotechnical and Geoenvironmental Engineering*, 124(4), 350–362.

Low, B. K., Lacasse, S., and Nadim, F. (2007). "Slope reliability analysis accounting for spatial variation." *Georisk: Assessment and Management of Risk for Engineered Systems and Geohazards*, 1(4), 177–189.

Low, B. K. and Tang, W. H. (1997a). "Efficient reliability evaluation using spreadsheet." *Journal of Engineering Mechanics*, 123(7), 749–752.

Low, B. K. and Tang, W. H. (1997b). "Reliability analysis of reinforced embankments on soft ground." *Canadian Geotechnical Journal*, 34(5), 672–685.

Low, B. K. and Tang, W. H. (2004). "Reliability analysis using object-oriented constrained optimization." *Structural Safety*, 26(1), 69–89.

Low, B. K. and Tang, W. H. (2007). "Efficient spreadsheet algorithm for first-order reliability method." *Journal of Engineering Mechanics*, 133(12), 1378–1387.

Low, H. E., Lunne, T., Andersen, K. H., Sjursen, M. A., Li, X., and Randolph, M. F. (2010). "Estimation of intact and remoulded undrained shear strengths from penetration tests in soft clays." *Géotechnique*, 60(11), 843–859.

Lumb, P. (1966). "The variability of natural soils." *Canadian Geotechnical Journal*, 3(2), 74–97.

Lundberg, A. B. and Li, Y. J. (2015). "Probabilistic characterization of a soft scandinavian clay supporting a light quay structure." *Proceedings of the 5th International Symposium on Geotechnical Safety and Risk*, Rotterdam, Netherlands, 170–175.

Matsuo, M. (1976). "Reliability in embankment design." Ph.D. thesis, MIT, Cambridge, USA.

Matthies, H. G., Brenner, C. E., Bucher, C. G., and Soares, C. G. (1997). "Uncertainties in probabilistic numerical analysis of structures and solids-stochastic finite elements." *Structural Safety*, 19(3), 283–336.

Mollon, G., Dias, D., and Soubra, A.-H. (2010). "Probabilistic analysis of pressurized tunnels against face stability using collocation-based stochastic response surface method." *Journal of Geotechnical and Geoenvironmental Engineering*, 137(4), 385–397.

Nguyen, V. U. and Chowdhury, R. N. (1984). "Probabilistic study of spoil pile stability in strip coal mines–two techniques compared." *International Journal of Rock Mechanics and Mining Sciences & Geomechanics Abstracts*, 21(6), 303–312.

Nuttall, J. D. (2011). "Parallel implementation and application of the random finite element method." Ph.D. thesis, The University of Manchester, Manchester, UK.

O'Connor, A. J. and Kenshel, O. (2012). "Experimental evaluation of the scale of fluctuation for spatial variability modeling of chloride-induced reinforced concrete corrosion." *Journal of Bridge Engineering*, 18(1), 3–14.

Olea, R. A. (1984). "Sampling design optimization for spatial functions." *Journal of the International Association for Mathematical Geology*, 16(4), 369–392.

Paiboon, J., Griffiths, D. V., Huang, J., and Fenton, G. A. (2013). "Numerical analysis of effective elastic properties of geomaterials containing voids using 3D random fields and finite elements." *International Journal of Solids and Structures*, 50(20), 3233–3241.

Paice, G. M. and Griffiths, D. V. (1997). "Reliability of an undrained clay slope formed from spatially random soil." *Proceedings of the 9th International Conference of the International Association for Computer Methods and Advances in Geomechanics (9th IACMAG)*, Wuhan, China, 543–548.

Papoulis, A. and Pillai, S. U. (2002). *Probability, random variables, and stochastic processes.* McGraw-Hill, New York.

Phoon, K.-K. (2008). *Reliability-based design in geotechnical engineering: computations and applications.* CRC Press, Boca Raton.

Phoon, K. K., Huang, S. P., and Quek, S. T. (2002). "Simulation of second-order processes using Karhunen–Loeve expansion." *Computers and Structures*, 80(12), 1049–1060.

Phoon, K.-K. and Kulhawy, F. H. (1999a). "Characterization of geotechnical variability." *Canadian Geotechnical Journal*, 36(4), 612–624.

Phoon, K.-K. and Kulhawy, F. H. (1999b). "Evaluation of geotechnical property variability." *Canadian Geotechnical Journal*, 36(4), 625–639.

Phoon, K.-K., Quek, S.-T., and An, P. (2003). "Identification of statistically homogeneous soil layers using modified Bartlett statistics." *Journal of Geotechnical and Geoenvironmental Engineering*, 129(7), 649–659.

Popescu, R., Prévost, J. H., and Deodatis, G. (1997). "Effects of spatial variability on soil liquefaction: some design recommendations." *Géotechnique*, 47(5), 1019–1036.

Popescu, R., Prevost, J. H., and Vanmarcke, E. H. (1995). "Numerical simulations of soil liquefaction using stochastic input parameters." *Proceedings of the 3rd International Conference on Recent Advances in Geotechnical Earthquake Engineering and Soil Dynamics*, Missouri S&T, St. Louis, Missouri, USA, 275–280.

Pyrcz, M. J. and Deutsch, C. V. (2014). *Geostatistical reservoir modeling.* Oxford university press, Oxford.

Rackwitz, R. and Flessler, B. (1978). "Structural reliability under combined random load sequences." *Computers and Structures*, 9(5), 489–494.

Rogers, J. D. (2016). "Mississippi river levee." *Missouri S&T weblink*. http://web.mst.edu/~rogersda/levees/. Accessed: 2016-02-18.

Ronold, K. O. (1990). "Random field modeling of foundation failure modes." *Journal of Geotechnical Engineering*, 116(4), 554–570.

Rosenblatt, M. (1952). "Remarks on a multivariate transformation." *The Annals of Mathematical Statistics*, 470–472.

Salgado, R. and Kim, D. (2013). "Reliability analysis of load and resistance factor design of slopes." *Journal of Geotechnical and Geoenvironmental Engineering*, 140(1), 57–73.

Schweckendiek, T. (2014). "On reducing piping uncertainties: A Bayesian decision approach." Ph.D. thesis, Delft University of Technology, Delft, the Netherlands.

Schweiger, H. F. and Peschl, G. M. (2005). "Reliability analysis in geotechnics with the random set finite element method." *Computers and Geotechnics*, 32(6), 422–435.

Smith, I. M. and Griffiths, D. V. (2005). *Programming the finite element method*. John Wiley & Sons, New York.

Soulie, M., Montes, P., and Silvestri, V. (1990). "Modelling spatial variability of soil parameters." *Canadian Geotechnical Journal*, 27(5), 617–630.

Spencer, W. A. (2007). "Parallel stochastic and finite element modelling of clay slope stability in 3D." Ph.D. thesis, University of Manchester, Manchester, UK.

Spencer, W. A. and Hicks, M. A. (2006). "3D stochastic modelling of long soil slopes." *Proceedings of the 14th Conference of the Association for Computational Mechanics in Engineering (ACME)*, Belfast, UK, 119–122.

Spencer, W. A. and Hicks, M. A. (2007). "A 3D finite element study of slope reliability." *Proceedings of the 10th International Symposium on Numerical Models in Geomechanics, Rhodes, Greece*, 539–543.

Suchomel, R., Mašín, D., et al. (2010). "Comparison of different probabilistic methods for predicting stability of a slope in spatially variable c–φ soil." *Computers and Geotechnics*, 37(1), 132–140.

Tandjiria, V., Teh, C. I., and Low, B. K. (2000). "Reliability analysis of laterally loaded piles using response surface methods." *Structural Safety*, 22(4), 335–355.

Tang, W. H. (1979). "Probabilistic evaluation of penetration resistances." *Journal of the Geotechnical Engineering Division*, 105(10), 1173–1191.

Tantalla, J., Prevost, J.-H., and Deodatis, G. (2001). "Spatial variability of soil properties in slope stability analysis: Fragility curve generation." *Proceedings of the 8th International Conference on Structural Safety and Reliability (ICOSSAR)*, Newport Beach, California, USA, 287–292.

TAW (2001). *Technical report on Water Retaining Earth Structures*. Netherlands.

Taylor, D. W. (1937). "Stability of earth slopes." *Journal of the Boston Society of Civil Engineers*, 24, 197–246.

Uzielli, M., Vannucchi, G., and Phoon, K. K. (2005). "Random field characterisation of stress-nomalised cone penetration testing parameters." *Géotechnique*, 55(1), 3–20.

van den Eijnden, A. P. and Hicks, M. A. (2011). "Conditional simulation for characterizing the spatial variability of sand state." *Proceedings of the 2nd International Symposium on Computational Geomechanics, Dubrovnik, Croatia*, 288–296.

Vanmarcke, E. H. (1975). "On the distribution of the first-passage time for normal stationary random processes." *Journal of Applied Mechanics*, 42(1), 215–220.

Vanmarcke, E. H. (1977a). "Probabilistic modeling of soil profiles." *Journal of the Geotechnical Engineering Division*, 103(11), 1227–1246.

Vanmarcke, E. H. (1977b). "Reliability of earth slopes." *Journal of the Geotechnical Engineering Division*, 103(11), 1247–1265.

Vanmarcke, E. H. (1978). "Probabilistic characterization of soil profiles." *Site Characterization & Exploration*, ASCE, Evanston, Illinois, USA, 199–219.

Vanmarcke, E. H. (1980). "Probabilistic stability analysis of earth slopes." *Engineering Geology*, 16(1), 29–50.

Vanmarcke, E. H. (1983). *Random fields: Analysis and synthesis*. MIT Press, Cambridge, MA.

Vanmarcke, E. H. (2011). "Risk of limit-equilibrium failure of long earth slopes: How it depends on length." *Proceedings of Geo-Risk 2011: Risk Assessment and Management*, Atlanta, Georgia, USA, 1–24.

Vanmarcke, E. H. and Fenton, G. A. (1991). "Conditioned simulation of local fields of earthquake ground motion." *Structural Safety*, 10(1), 247–264.

Vanmarcke, E. H. and Grigoriu, M. (1983). "Stochastic finite element analysis of simple beams." *Journal of Engineering Mechanics*, 109(5), 1203–1214.

Vanmarcke, E. H. and Otsubo, Y. (2013). "Reliability analysis of long multi-segment earth slopes." *Proceedings of Geo-Congress: Foundation Engineering in the Face of Uncertainty: Honoring Fred H. Kulhawy*, ASCE, San Diego, California, USA, 520–529.

Vrouwenvelder, T. (2006). "Spatial effects in reliability analysis of flood protection systems." *Proceedings of the 2nd International Forum on Engineering Decision Making (IFED)*, Lake Louise, Canada.

Wackernagel, H. (2003). *Multivariate geostatistics: An introduction with applications*. Springer, New York.

Wang, B., Hicks, M. A., and Vardon, P. J. (2016). "Slope failure analysis using the random material point method." *Géotechnique Letters*, 6(2), 113–118.

Wang, Y., Cao, Z., and Au, S.-K. (2010). "Practical reliability analysis of slope stability by advanced Monte Carlo simulations in a spreadsheet." *Canadian Geotechnical Journal*, 48(1), 162–172.

Wickremesinghe, D. and Campanella, R. G. (1993). "Scale of fluctuation as a descriptor of soil variability." *Proceedings of the Conference on Probabilistic Methods in Geotechnical Engineering*, Canberra, Australia, 233–239.

Wolff, D. (2008). "Reliability of levee systems." *Reliability-based design in geotechnical engineering*, Taylor & Francis, 448–496.

Wong, F. S. (1985). "Slope reliability and response surface method." *Journal of Geotechnical Engineering*, 111(1), 32–53.

Wong, S. Y. (2004). "Stochastic characterisation and reliability of saturated soils." Ph.D. thesis, University of Manchester, Manchester, UK.

Wu, T. H. (1974). "Uncertainty, safety, and decision in soil engineering." *Journal of the Geotechnical Engineering Division*, ASCE, 100(3), 329–348.

Xiao, T., Li, D.-Q., Cao, Z.-J., Au, S.-K., and Phoon, K.-K. (2016). "Three-dimensional slope reliability and risk assessment using auxiliary random finite element method." *Computers and Geotechnics*, 79, 146–158.

Xu, B. and Low, B. K. (2006). "Probabilistic stability analyses of embankments based on finite-element method." *Journal of Geotechnical and Geoenvironmental Engineering*, 132(11), 1444–1454.

Youssef Abdel Massih, D. S. and Soubra, A.-H. (2008). "Reliability-based analysis of strip footings using response surface methodology." *International Journal of Geomechanics*, 8(2), 134–143.

Yücemen, M. S. and Al-Homoud, A. S. (1990). "Probabilistic three-dimensional stability analysis of slopes." *Structural Safety*, 9(1), 1–20.

Zhang, J., Huang, H. W., and Phoon, K. K. (2012). "Application of the kriging-based response surface method to the system reliability of soil slopes." *Journal of Geotechnical and Geoenvironmental Engineering*, 139(4), 651–655.

Zhao, H. F., Zhang, L. M., Xu, Y., and Chang, D. S. (2013). "Variability of geotechnical properties of a fresh landslide soil deposit." *Engineering Geology*, 166, 1–10.

A

HPC CLOUD AND GRID COMPUTING

In the Monte Carlo simulation of a dyke, thousands of realisations of soil properties that satisfy the point and spatial statistics of the soil often need to be generated using a random field generator, so that the designed dyke reliability and risk (consequence) can be assessed. However, the subsequent nonlinear finite element analysis for each realisation generally requires hundreds of plastic iterations before reaching an equilibrium state, which is a time consuming process. Thus, running the analysis serially on a desktop computer would be unfeasible. In order to make the calculations feasible, the Author has developed a suitable framework for carrying out this kind of computational task, which, in this case, is based on high performance computing (HPC) Cloud and Grid computing. This annex presents the development of the computing framework for geotechnical computations involving multiple realisations of physically large nonlinear problems, which has been used in Chapters 4, 5 and 6 of this thesis.

A.1. INTRODUCTION

The Author has mainly investigated dyke safety using the random finite element method (Li and Hicks, 2014; Li et al., 2013). For this purpose, thousands of realisations of soil properties that satisfy the point and spatial statistics of the soil may be generated using a random field generator based on local average subdivision (Fenton and Vanmarcke, 1990), so that the designed dyke reliability and risk can be assessed. However, the subsequent nonlinear finite element analysis for each realisation often requires hundreds of plastic iterations before reaching an equilibrium state (Smith and Griffiths, 2005; Spencer, 2007), which is a time consuming process. In order to make the calculations feasible, the Author needed to develop a suitable framework for carrying out this kind of computational task, which, in this case, is based on high performance computing (HPC) Cloud and Grid computing. This chapter presents the development of the computing framework for geotechnical computations involving multiple realisations of physically large nonlinear problems.

There are basically two computing strategies for these largely independent calculations: i.e. Cloud computing and Grid computing. They will be discussed in Sections A.2 and A.3, respectively. The Author had access to the Dutch HPC Cloud service and Grid e-infrastructures for carrying out the investigation presented in this annex.

A.2. CLOUD COMPUTING

In basic terms, Cloud computing can be seen as a virtualising environment where users can build their own cluster comprised of multiple virtual machines (Infrastructure as a Service, IaaS paradigm). Each virtual machine used by the user is created from a template. This template is created from predefined resources (Orange color) provided by surfSARA[1] and user defined resources (Green color), see Fig. A.1. To deploy their applications, Cloud users install operating system images and their application software on the Cloud infrastructure. Users are free to build their computing nodes (virtual machines) themselves by arranging CPU, memory, network and storage together. They can interconnect them in their own private network (private cluster), or make (part of) them reachable from the internet. The Cloud infrastructure has 960 HPC cores and 80 Light cores (8GB RAM/core).

A.2.1. HARDWARES

The Dutch Cloud system is based on the following hardware (based on Februry, 2014):

- 30 High Performance Computing nodes:

    - 19 nodes with 32 cores @ 2.13 GHz (Intel Xeon E7 "Westmere-EX")
    - 11 nodes with 32 cores @ 2.70 GHz (Intel Xeon CPU E5-4650 0)
    - 256 Gbyte RAM
    - 2 × 10GE network

---

[1]SURFsara is a Dutch foundation that provides supercomputers, colocation, networks and high-end visualisation to academic institutions. https://www.surf.nl/en/about-surf/subsidiaries/surfsara/
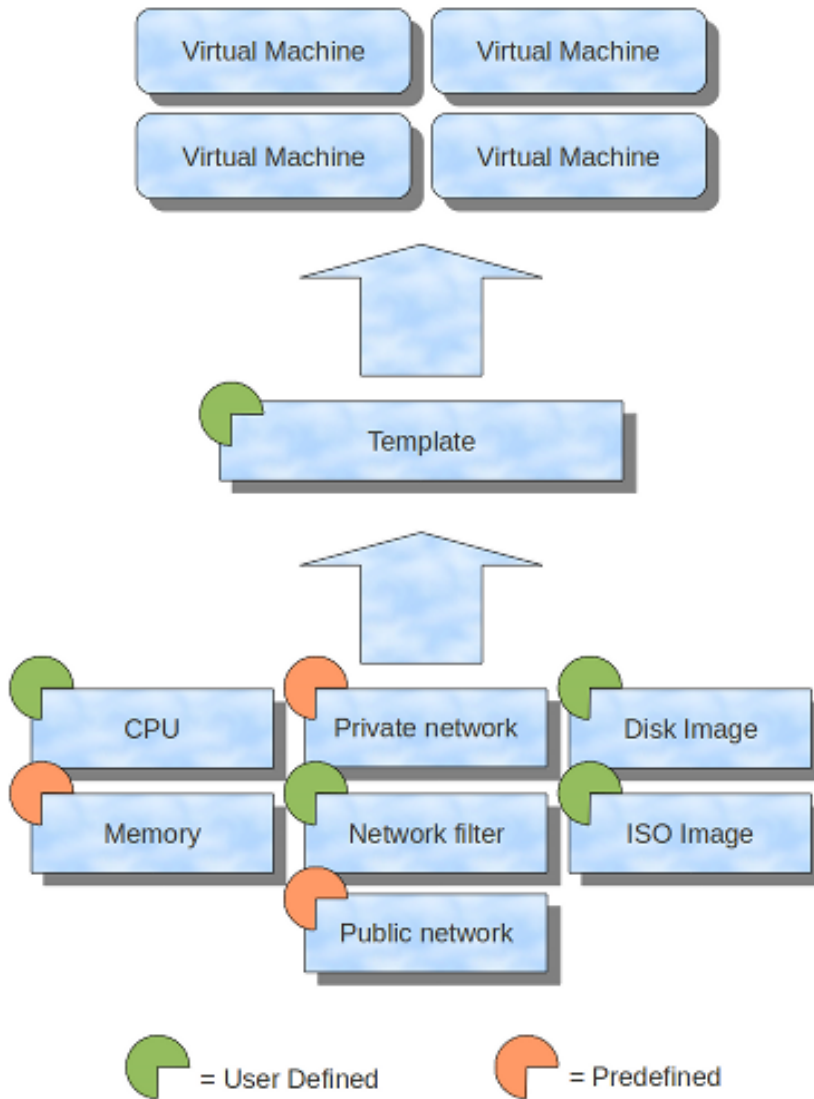
Figure A.1: Creation of Virtual Machines (source: Surfsara)

- 10 "light" nodes:

  – 8 cores (AMD Opteron 6212)

  – 64 GByte RAM

  – 1 × 10GE network

  – 6 TByte local disk

- 1 High-Memory node:

  – 40 cores @ 2.00 GHz (Intel Xeon CPU E7-4850)

  – 2 TByte RAM

  – 2 × 10GE network

  – 6.4 TB local disk

  – 851 SPecInt

A.2.2. ALLOCATED RESOURCES

The following resources were allocated for the Author's project on the Cloud:

- 40,000 core hours of Cloud;

- 100GB of disk storage;

- 1TB of VirDir storage (i.e. virtual directory storage).

A.2.3. STRATEGY DESIGN

A master/worker design is implemented and adopted here. Shell scripts were written to distribute all the jobs to the detected hosts. Once finished, the results are collected to the master node, where the data in the separated files are loaded into one data file. This data file is then transferred back to the virtual directory for backup and downloading to the local machine for post processing. The procedure is shown in Fig. A.2.

The advantage is that the users control their own private environment and have full control over their operating system (OS), libraries, etc. The disadvantage is that users are responsible for all of the installation and maintenance. It requires significant effort to get familiar with a few concepts, set up the virtual machines and design the workflow pipelines, but once everything works the benefits are apparent, with effectively a linear speed up.

A.3. GRID COMPUTING

The computing capacity on the Cloud is not as large as on the Grid, so it was decided to also investigate using the Grid. Grid computing is a collection of geographically distributed computers, data storage facilities and services that can be dynamically joined to reach a common goal involving non-interactive workloads with a large number of files. A Grid user is able to use all this computing power simultaneously, without having to log
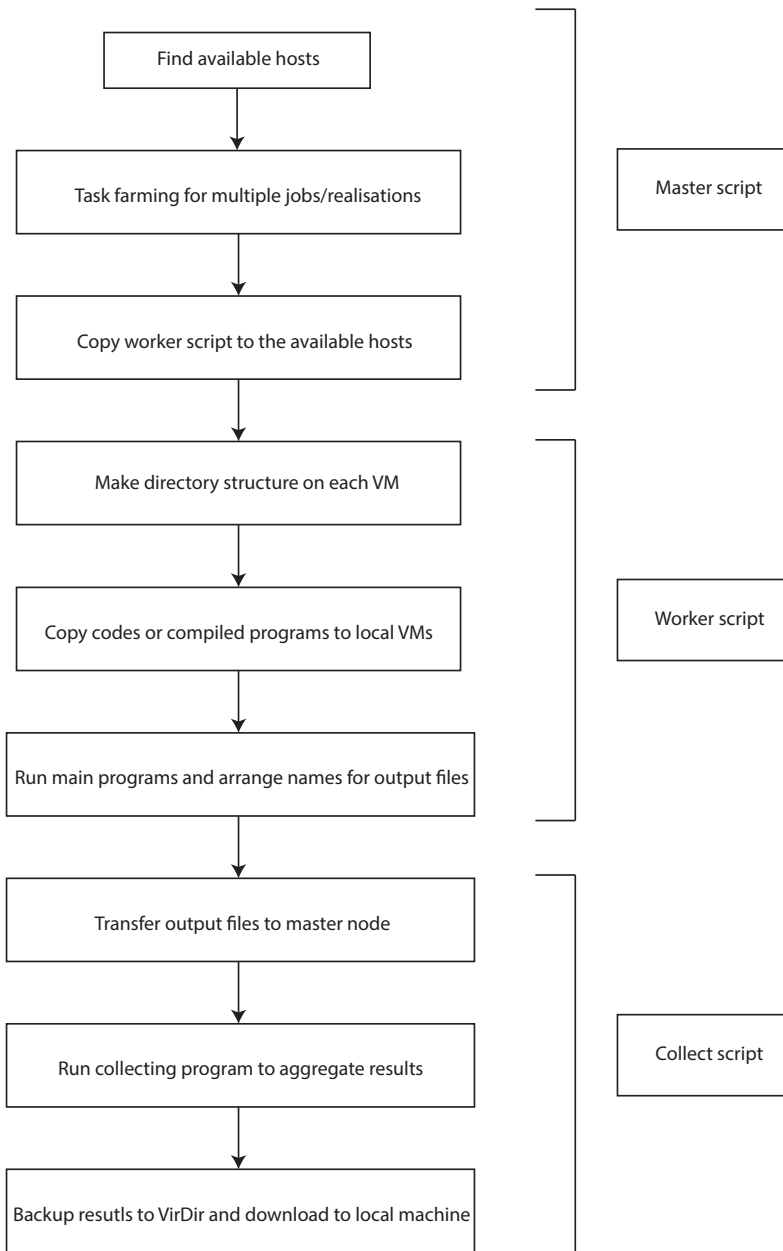
Figure A.2: Flow chart for Cloud computing: master/worker design

in at all the different sites. For assessing the reliability of longer and longer dykes, typically 1000 realisations are needed to ensure a converged solution. As each realisation or job is able to be run independently on a single serial computer, Grid computing is ideally suitable for such a computational task.

Before starting to use the Grid, there are three steps that need to be finished. Firstly, a Grid certificate needs to be authorized; secondly, a user interface account for submitting jobs needs to be applied; thirdly, users should join a Virtual Organisation (VO) which determines what resources the user can use.

A.3.1. ALLOCATED RESOURCES

The Author was granted access to the national computing and data storage environment with the following resources (based on December, 2014):

- 500,000 core hours of Grid

- 500 GB of Disk storage

- 500 GB of Tape

- Computing clusters (4,400 cores for gina cluster, 900 cores for rug cluster and 3,800 cores for nikhef cluster).

All of the clusters are heterogeneous and, for example, the gina cluster has nodes with Intel Xeon(R) CPU E5-2650 @ 2.60GHz, RAM memory 3-8 GB/core.

At first, the Author did not have a pre-knowledge about Linux and bash scripting. After trying out the tutorials available at surfsara wiki[2], the Author was able to adapt the problem and design an implementation considering memory, wall clock time and available storage space.

A.3.2. GRID STRATEGY DESIGN

Two approaches were tested for the Monte Carlo simulation involved in assessing the reliability and risk of long 3D slopes:

1. Using parametric jobs through WMS;

2. Using the PiCaS (explained later) token pool server.

JDL PARAMETRIC JOBS USING WMS

The computational jobs are submitted by a JDL (job description language) file. A job description language file is a file (called JDL file) used to describe jobs and their requirements, consisting of attribute value pairs. Grid middleware takes care of the distribution of all the 'jobs' a user submits. Each job in the form of a JDL file is then submitted to the Workload Management System (WMS). This system schedules the jobs and knows which computer clusters in the Grid are ready to accept the jobs. These clusters each consist of several machines. The Compute Element (CE) is the server which communicates with the WMS and accepts jobs. It then distributes the jobs to other machines

---

[2]https://grid.surfsara.nl/wiki/index.php/Using_the_Grid/

A

in the cluster, called Worker Nodes (WNs). These WNs are the machines which do the actual work. When finished with a job they will report back to the CE, which in turn will inform the user about the status of the job. In addition, Clusters have a storage server, called the Storage Element (SE). These servers can be used to store files on a permanent basis. Data on the SE's can be replicated at other sites and jobs can be told to land only on Worker Nodes which are close to data the jobs will operate upon.

A document about the attributes specification for the GLITE WMS is available (EGEE, 2005). One job type worth mentioning is the parametric job. A parametric job causes a set of jobs to be generated from one JDL file. This is invaluable in cases where many similar (but not identical) jobs must be run, as in the case of a Monte Carlo simulation where many realisations need to be initiated from different seeds. This is achieved by the parametric job having one or more parametric attributes described in the JDL. These attributes are identified by the value of the key word _PARAM_; this value will be replaced by the actual value of Parameters during the JDL expansion. The JobType in the JDL should be Parametric.

The approach follows the procedures below:

1. Define a parametric job consisting of 50 realisations;

2. Submit 10 parametric jobs using a single bash script;

3. Check status of submitted jobs and retrieve the output results;

4. Download output files to local computer for post-processing.

The input data in this case are transferred to the Worker Nodes by sandbox (an attribute in a JDL file), and the output data transferred from the WNs to the User interface server using sandbox (if the amount of data are less than 10 MB). In the case that the output data are more than 10 MB for each realisation, the Grid storage is needed.

THE PILOT FRAMEWORK USING PICAS

While the above approach works quite well, there are inevitably some jobs that fail (due to time limit, system problems, etc.). It is a cumbersome task to track down these failed jobs and resubmit them, with the potential risk of ending up with some of the resubmitted jobs also failing. The Pilot framework (PiCaS[3], developed by Jan Bot, is a Python module using couchDB as token pool server, see Fig A.3) was developed to handle failed jobs automatically. The user should not look at the pilot jobs he/she has submitted, but to the number of tokens being processed. There is no need to keep track of submitted jobs and those (and only those) that fail are automatically identified and resubmitted.

In addition, when submitting a large number of jobs, users will often find that they need to operate on the same database or some other static data source. For every job submission this database then has to be copied to the node the job is running on. This introduces a large overhead per job. A second advantage of using PiCas is the reduced overhead of job submission. Once a pilot job is in place it will consume tokens as long as there are any, or its wall clock time (the maximum time a job is allowed to run) is up. This can also be advantageous for jobs that need to transfer a large data file. In those examp-

---

[3]https://github.com/jjbot/picasclient

A
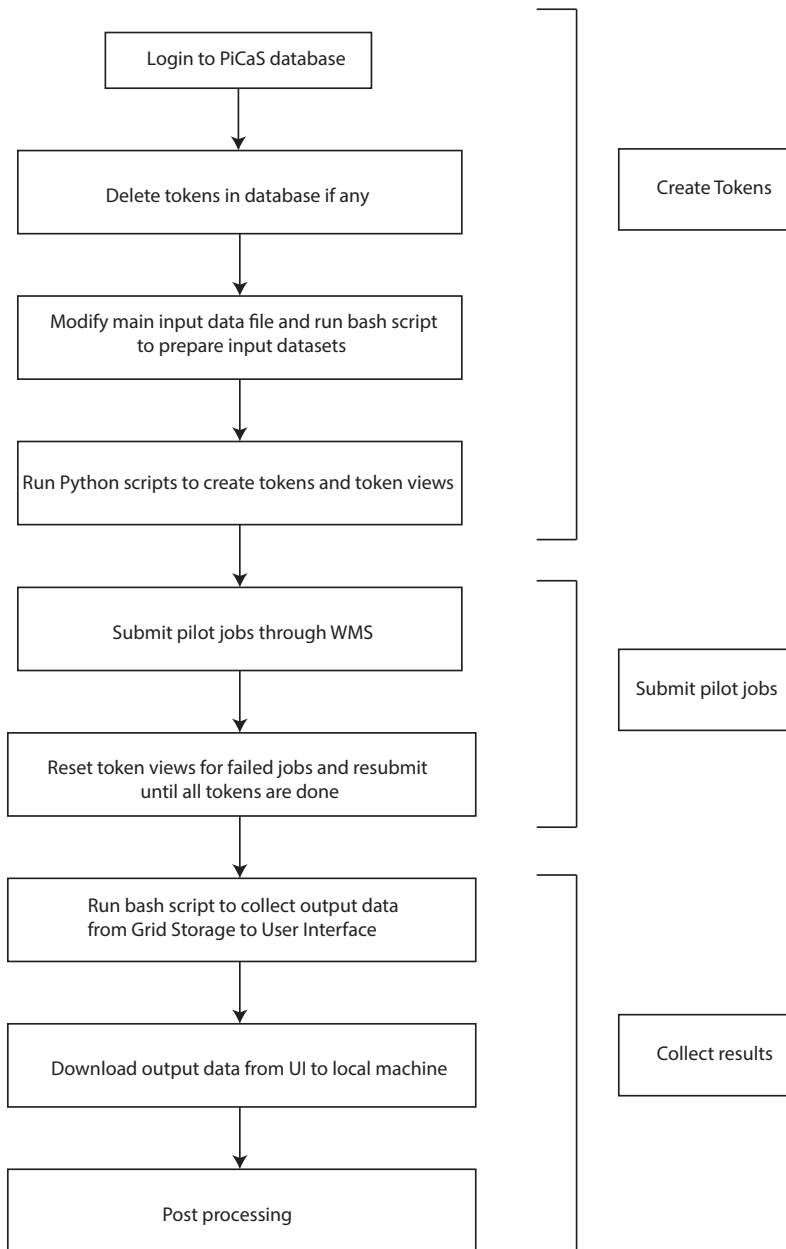
Figure A.3: Flow chart for Grid computing: pilot framework

A
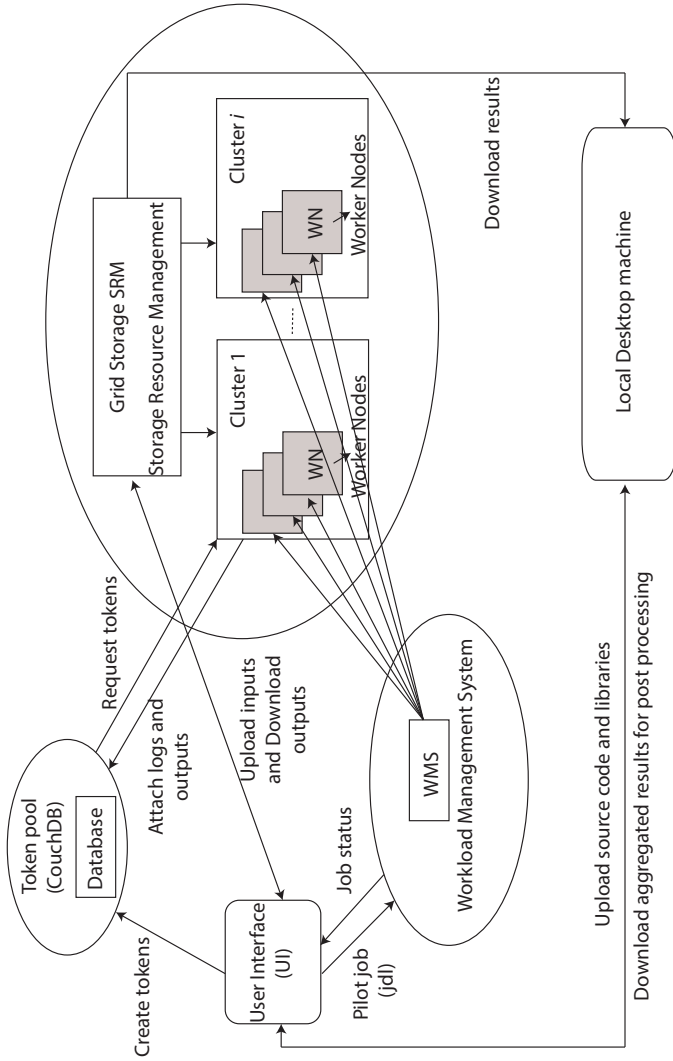
Figure A.4: A global overview of the pilot job framework

A

les where a database should be downloaded from a SE to the Worker Node where the job is running, it only needs to be downloaded once if the pilot framework is used.

Whenever a token is requested, couchDB returns the next document which is available (i.e. a token with attributes lock=0 and done=0). If a document is processed with the Python/PiCaS script, the 'lock' is set to the current time. Whenever the script is done, it sets 'done' to the current time. This allows multiple instances of your scripts on different locations to work on different samples from the same collection (pool).

The working philosophy of the pilot framework is shown in Fig. A.4.

As seen in Fig. A.4, a filled token pool is needed. The CouchDB is used for this. First, request a database with SurfSARA. Once the database is in place it should be empty. It can be popluated using the createtokens.py script. For PiCaS to know which tokens it whould request, a view needs to be created in CouchDB. First go to the couchdb pool server[4] and select the database. A Python script has been written to create the views.

A.4. IMPLEMENTATION OF A PILOT FRAMEWORK FOR RFEM

The pilot framework for Monte Carlo simulation has been implemented particularly for the computational work of this thesis. The implementation makes use of the Python library modules couchdb and picas. A number of shell scripts (.sh files) and Python script (.py files) were written to automate the whole process.

The directory tree on the UI is:

```
geomodel
├─Runprocess
│  ├─sandbox
│  │  ├─couchdb.tar
│  │  ├─picas.tar
│  │  ├─scripts.tar
│  │  ├─pilot.sh
│  │  ├─runprocess.py
│  │  ├─runprocess.sh
│  │  ├─p67exe
│  │  ├─input1
│  │  └─input2
│  ├─runprocess.jdl
│  ├─jobsubmit.sh
│  └─collect2ui
│     └─copyDirfromGrid.sh
└─Tokens
   ├─couchdb
   ├─picas
   ├─datasets
   ├─createTokens.py
   ├─createViews.py
   └─resetTokens.py
```

---

[4]https://picas.grid.sara.nl:6984/_utils/index.html

A

```
    └─deletedocs.py
    └─p67.dat
    └─prepinputdata.sh
```

The steps are:

1. Start a Grid session

2. Prepare tokens in the pool server and add input data to the tokens. This is done in the <Tokens> dir in the Grid user interface:

    (a) Upload p67.dat (the input data file) and run prepinputdata.sh to generate the input files in sub-dir <datasets>

    (b) In directory <Tokens>, run createTokens.py and createViews.py, check on the server if the Tokens and Token views have been generated successfully

3. Try to run on the UI (the user interface computer as a computing node):

    (a) Compile source code in directory <yourdirname>; this will produce an executable, say, p67exe

    (b) Copy p67exe to folder Runprocess/sandbox

    (c) Run . pilot.sh $PICAS_DB $PICAS_USR $PICAS_USR_PWD

    (d) If any locked tokens after some time: go back to <Tokens> directory run resetTokens.py and rerun pilot.sh

4. Run on the Grid by JDL:

    (a) Go back to <Runprocess> dir

    (b) Modify runprocess.jdl and runprocess.sh (basically the name of .exe and output files names and the directory name on the Grid storage

    (c) Submit jobs/job status and results retrieval

A.5. PERFORMANCE

For high memory jobs (as is the case in the current investigation), it is the gina cluster that is used. The computing capacity is 4400/2 = 2200 jobs (it has 3-8 GB memory per core on the gina cluster and 2 free cores are needed for a single 6 GB job).

In order to investigate the length effect, various slope lengths with the same soil property statistics need to be analysed. Here, an example of slope length L = 50-500 m with an interval of 50 m is presented (with all cases comprising 1,000 realisations). The timings for the 10 cases are shown in Fig. A.5 in terms of probability density functions. Also, the average time and maximum time for a single realisation are tabulated in Table A.1 in seconds, minutes and hours.

The average time of one realisation for the different cases is in the range of 15 minutes to 3 hours, and the maximum time is in the range of 1 to 9 hours. The wall clock time should be considered carefully, as, in the Grid system, short queues are limited to 4 hours
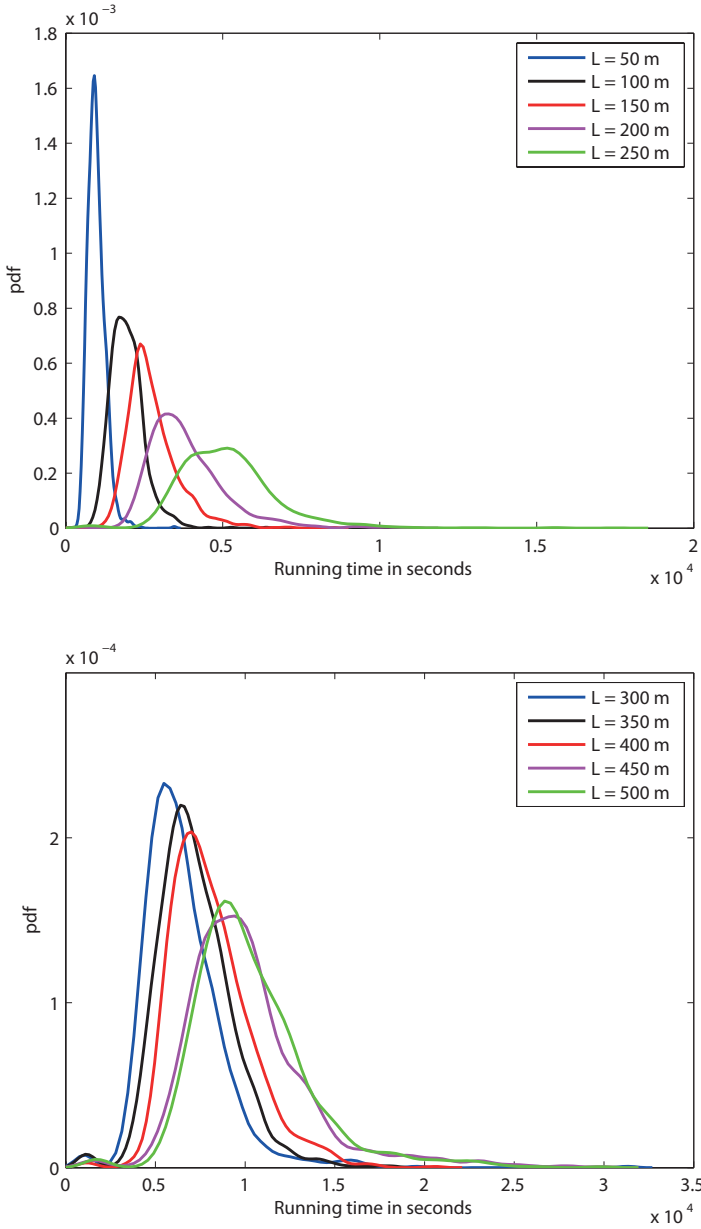
Figure A.5: Timings for slope stability calculations with various slope lengths L

Table A.1: Average and maximum time (t_a and t_m) for different slope lengths L on 2 cores on the Grid

L (m)	50	100	150	200	250	300	350	400	450	500
t_a (s)	977	1958	2768	3850	5182	6546	7217	8096	10134	10349
(min)	(16.3)	(32.6)	(46.1)	(64.2)	(86.4)	(109.1)	(120.3)	(134.9)	(168.9)	(172.5)
(hour)	(0.3)	(0.5)	(0.8)	(1.1)	(1.4)	(1.8)	(2.0)	(2.2)	(2.8)	(2.9)
t_m (s)	3456	6382	8506	11067	17476	31313	18204	20528	29886	29850
(min)	(57.6)	(106.4)	(141.8)	(184.5)	(291.3)	(521.9)	(303.4)	(342.1)	(498.1)	(497.5)
(hour)	(1.0)	(1.8)	(2.4)	(3.1)	(4.9)	(8.7)	(5.1)	(5.7)	(8.3)	(8.3)

and medium queues to 36 hours. The decision on the requirement for jobs to be submitted to the Grid is based upon the maximum time. For example, for the first 4 cases (i.e. L ranging from 50 m to 200 m), the short queues suffice. However, for the other cases, the medium queues must be specified in the JDL file. There is no point in submitting short jobs to medium queues, as the waiting time is usually longer in the medium queues. On the other hand, if a long job is submitted to a short queue, it could result in a large proportion of job failures. So, a general idea of how long one realisation takes for each case helps to improve the calculation efficiency.

With all the available resources, it is possible to carry out a detailed investigation for a 500 m long slope. Usually it takes 15-18 hours to finish 2,000 jobs for the 500 m case, including the waiting time in the queue and the actual calculation time (i.e. 2.9 hours on average). In comparison, running the analysis serially would be unfeasible, taking 250 days (3 hours × 2000 realisations / 24 = 250), which clearly demonstrates the power of Grid computing. Even the 50 m case could take as long as 25 days (0.3 × 2000 / 24 = 25) on a standard desktop computer, which is still unacceptable in most cases.

For scientific purposes, it is always necessary to carry out a sensitivity analysis for several sets of statistics. For example, when investigating the influence of anisotropy of the heterogeneity on the reliability of a long 3D slope, about 10 cases are needed. In such cases, the benefits are clearly more apparent. It is worth mentioning that, for the 50 m case, it takes about 30 minutes per realisation on the Cloud virtual machines, which is 2 times slower than on the Grid. This is the penalty of using virtual machines to ensure the portability of Cloud applications across all types of real hardware.

One may choose to run 10 realisations for 1 job instead of 1 realisation per job to reduce the job submitting overhead (i.e. mainly the waiting time in the queue, which could take 0-5 hours depending how busy the clusters are at that moment). However, the latter has the advantage of downloading and post-processing the output results for one set of input data, while, at the same time, submitting a second job and waiting for the results for a second set of input data.

A.6. CONCLUSIONS

Two computational computing strategies have been developed to cope with a traditionally challenging computational task using desktop computers; one based on HPC Cloud (small capacity) and the other based on Grid computing (larger capacity). They are particularly suitable for many largely independent calculations for physically large and time consuming problems. These HPC strategies are readily applicable for researchers demanding a great deal of workload in various scientific fields and they provide a way for researchers to work 'out of the box' to achieve their scientific goals. Although it takes some time to get familiar with the computing environment that is not commonly used by researchers in, say, the engineering field, it is well worth the effort. Bash scripts and Python scripts developed by the Author can be easily modified. The modification is only limited to organising the input and output files according to the user's particular project.

Due to the high computational requirements for a probabilistic analysis of such a physically large problem, as presented in this thesis, Grid computing technologies were used to conduct the investigation, meaning that 1 year of serial computational analysis could be undertaken in a single day in parallel.

B

MEAN AND STANDARD DEVIATION OF F_R VERSUS NUMBER OF MC REALISATIONS

This appendix shows the convergence plots of the mean and standard deviation (SD) of the realised factor of safety (F_R) from the RFEM analyses in Chapters 4 and 5.
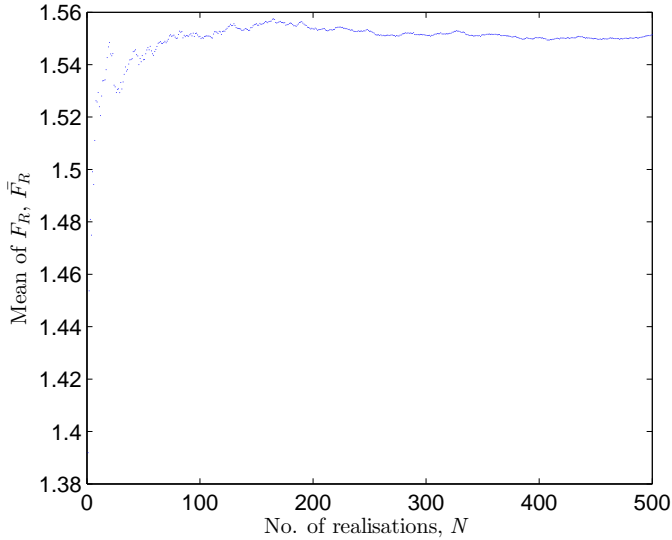
Figure B.1: Mean of the realised factor of safety versus number of MC realisations (θ_h = 6 m, L = 50 m)
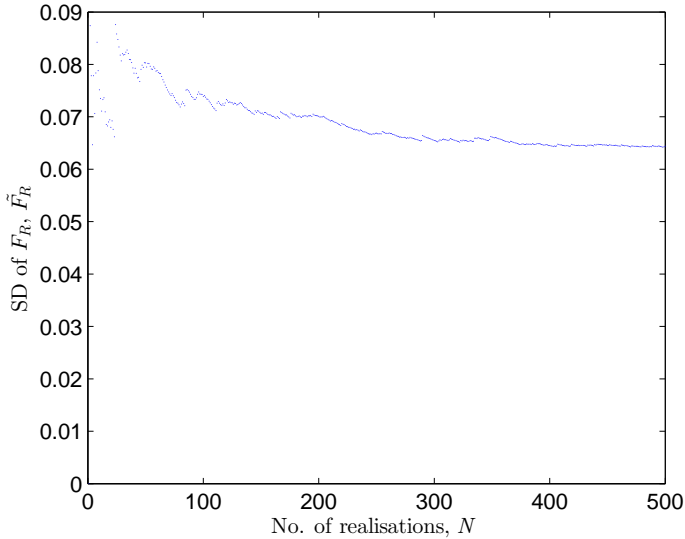
Figure B.2: SD of the realised factor of safety versus number of MC realisations (θ_h = 6 m, L = 50 m)
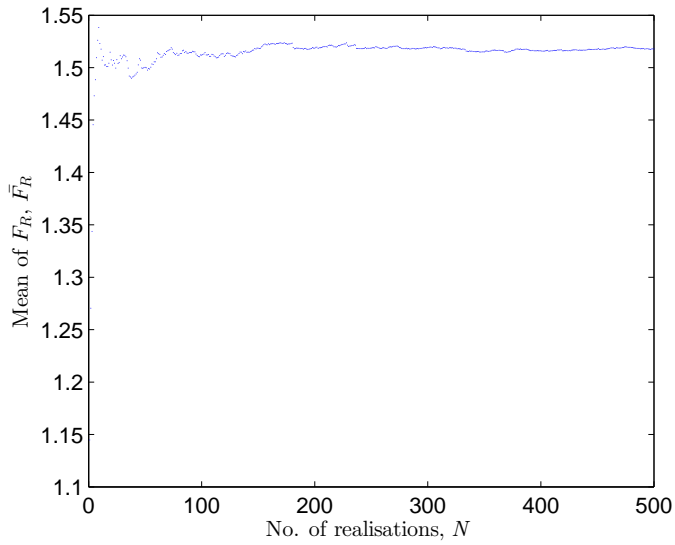
Figure B.3: Mean of the realised factor of safety versus number of MC realisations (θ_h = 24 m, L = 50 m)
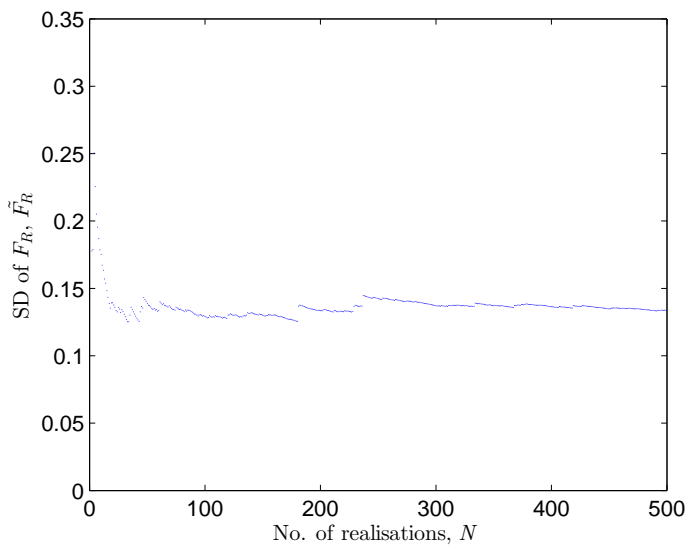
Figure B.4: SD of the realised factor of safety versus number of MC realisations (θ_h = 24 m, L = 50 m)
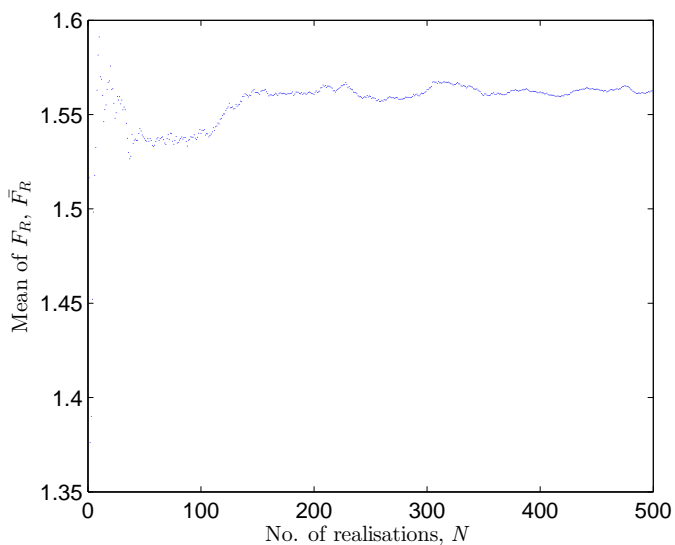
Figure B.5: Mean of the realised factor of safety versus number of MC realisations (θ_h = 100 m, L = 50 m)
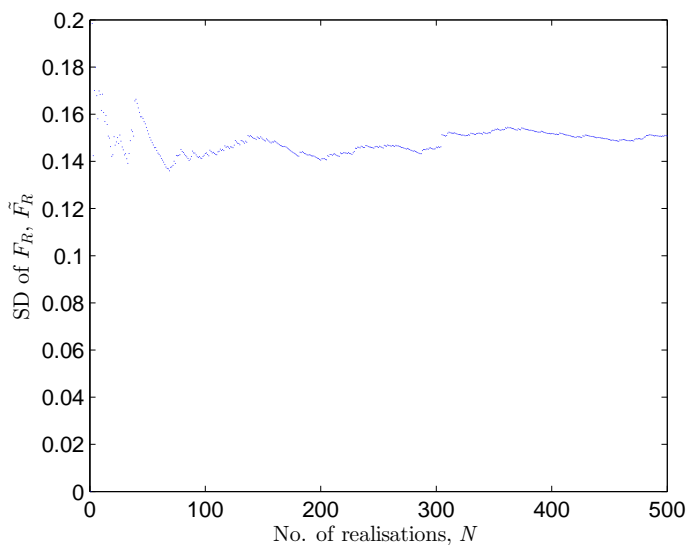
Figure B.6: SD of the realised factor of safety versus number of MC realisations (θ_h = 100 m, L = 50 m)
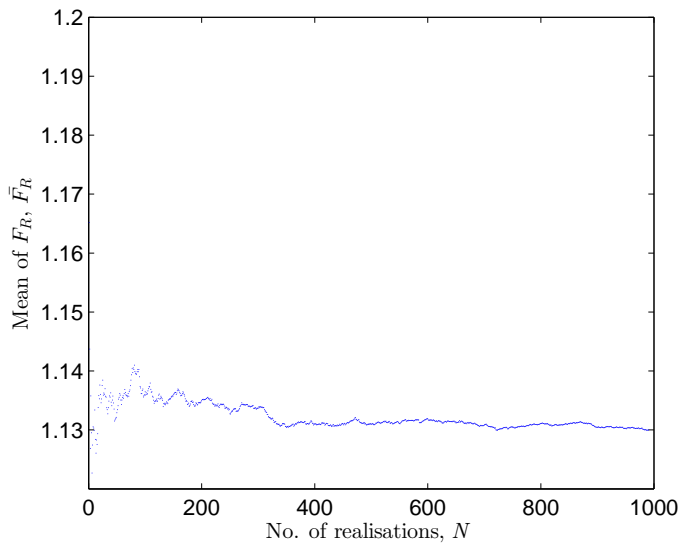
Figure B.7: Mean of the realised factor of safety versus number of MC realisations (θ_h = 12 m, L = 500 m)
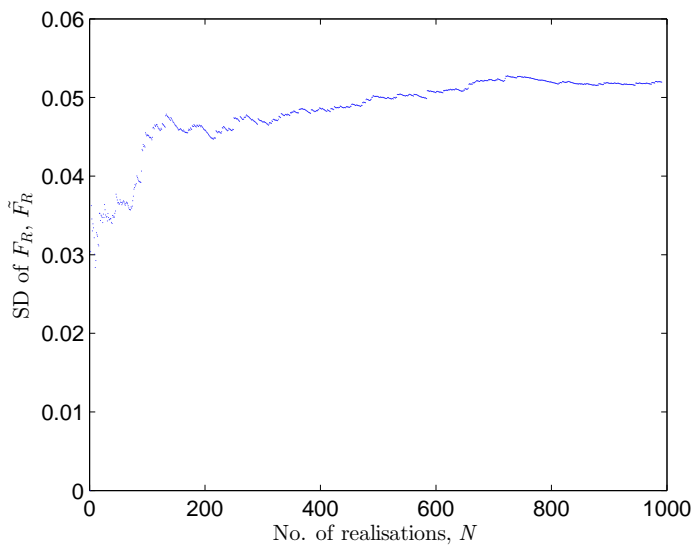
Figure B.8: SD of the realised factor of safety versus number of MC realisations (θ_h = 12 m, L = 500 m)
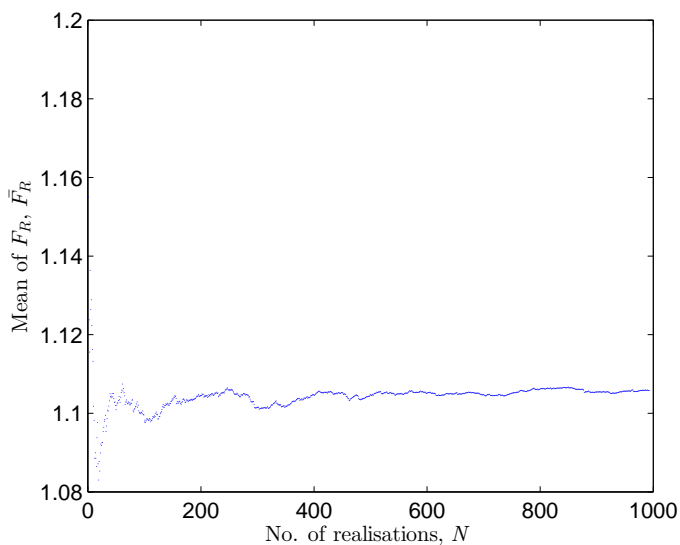
Figure B.9: Mean of the realised factor of safety versus number of MC realisations (θ_h = 24 m, L = 500 m)
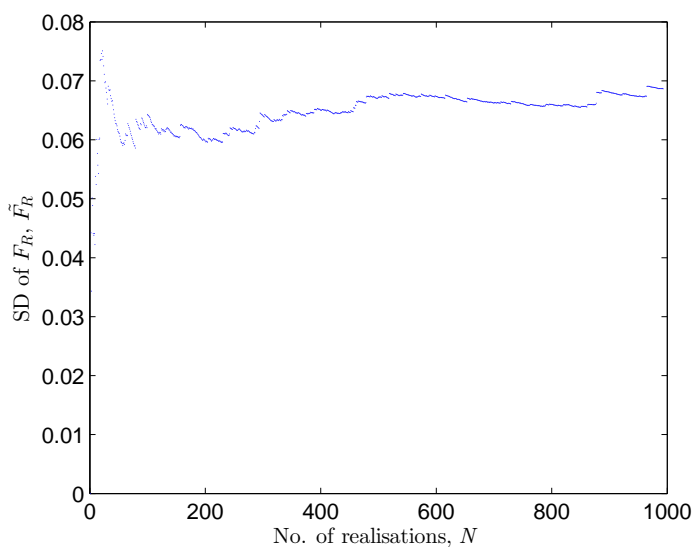
Figure B.10: SD of the realised factor of safety versus number of MC realisations (θ_h = 24 m, L = 500 m)
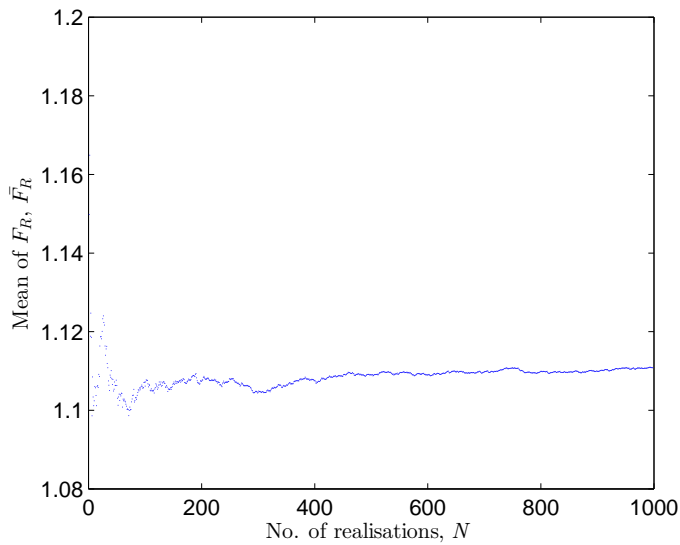
Figure B.11: Mean of the realised factor of safety versus number of MC realisations (θ_h = 50 m, L = 500 m)
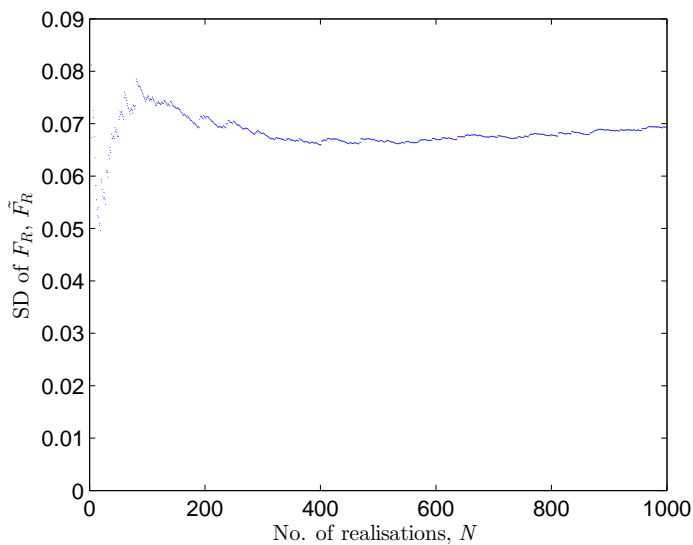
Figure B.12: SD of the realised factor of safety versus number of MC realisations (θ_h = 50 m, L = 500 m)
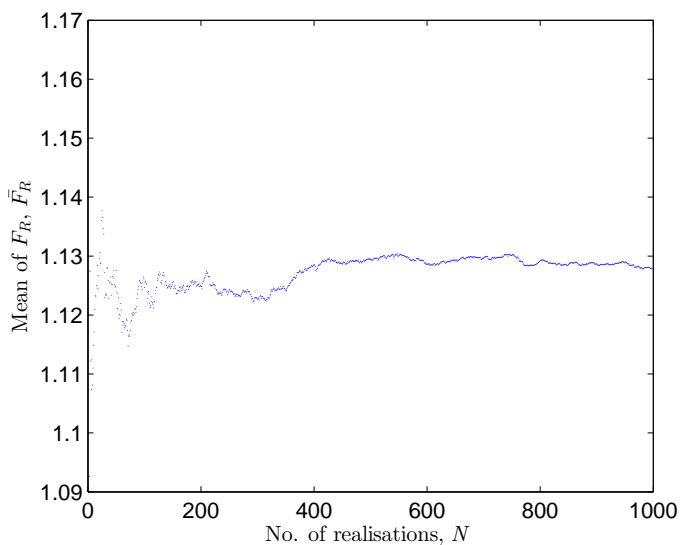
Figure B.13: Mean of the realised factor of safety versus number of MC realisations (θ_h = 100 m, L = 500 m)
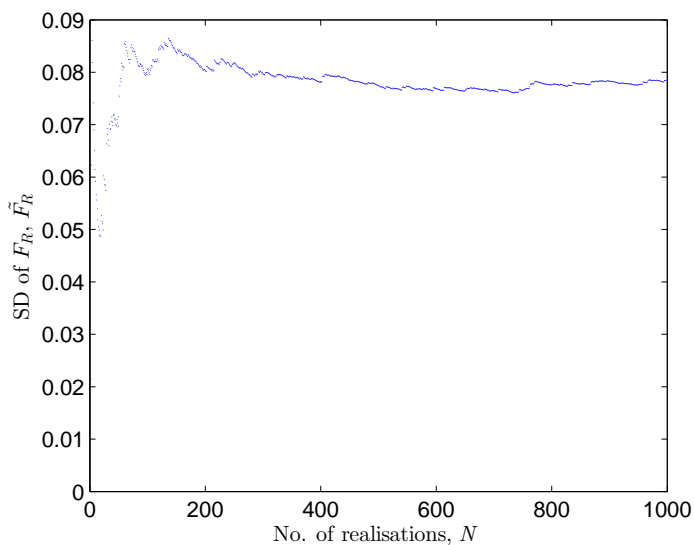
Figure B.14: SD of the realised factor of safety versus number of MC realisations (θ_h = 100 m, L = 500 m)

C

DERIVATION OF VARIANCE RELATION (EQ. 5.14)

Hereafter, and with reference to the notation used in Chapter 5, $\sigma_t^2 = \tilde{s}^2$, $\sigma_v^2 = \tilde{s}_v^2$, $\sigma_h^2 = \tilde{s}_h^2$.

Consider 3 CPT profiles, where each consists of n data points: $a_1, a_2, \ldots, a_n$; $b_1, b_2, \ldots, b_n$; $c_1, c_2, \ldots, c_n$. The mean of each CPT profile is as follows:

$$m_a = \frac{1}{n} \sum_{i=1}^{n} a_i;$$

$$m_b = \frac{1}{n} \sum_{i=1}^{n} b_i; \qquad \text{(C.1)}$$

$$m_c = \frac{1}{n} \sum_{i=1}^{n} c_i.$$

The mean of all data points from the 3 CPT profiles is

$$\mu = \left(\sum_{i=1}^{n} a_i + \sum_{i=1}^{n} b_i + \sum_{i=1}^{n} c_i \right)/3n = (m_a + m_b + m_c)/3 \qquad \text{(C.2)}$$

The variance of each CPT profile is as follows:

$$\sigma_{v1}^2 = \frac{1}{n} \sum_{i=1}^{n} a_i^2 - m_a^2;$$

$$\sigma_{v2}^2 = \frac{1}{n} \sum_{i=1}^{n} b_i^2 - m_b^2; \qquad \text{(C.3)}$$

$$\sigma_{v3}^2 = \frac{1}{n} \sum_{i=1}^{n} c_i^2 - m_c^2.$$

The average of the 3 vertical variances is

$$\sigma_v^2 = \frac{1}{3} \left(\sigma_{v1}^2 + \sigma_{v2}^2 + \sigma_{v3}^2 \right) = \frac{1}{3} \left(\frac{1}{n} \sum_{i=1}^{n} a_i^2 - m_a^2 + \frac{1}{n} \sum_{i=1}^{n} b_i^2 - m_b^2 + \frac{1}{n} \sum_{i=1}^{n} c_i^2 - m_c^2 \right)$$
$$\text{(C.4)}$$

The horizontal variance (of the 3 means) is

$$\sigma_h^2 = \frac{1}{3} \left(m_a^2 + m_b^2 + m_c^2 \right) - \mu^2 \qquad \text{(C.5)}$$

Hence,

$$\sigma_h^2 + \sigma_v^2 = \frac{1}{3} \left(\frac{1}{n} \sum_{i=1}^{n} a_i^2 + \frac{1}{n} \sum_{i=1}^{n} b_i^2 + \frac{1}{n} \sum_{i=1}^{n} c_i^2 \right) - \mu^2 = \frac{1}{3n} \left(\sum_{i=1}^{n} a_i^2 + \sum_{i=1}^{n} b_i^2 + \sum_{i=1}^{n} c_i^2 \right) - \mu^2 = \sigma_t^2$$
$$\text{(C.6)}$$

SUMMARY

Highway embankments, river dykes and sea dykes usually have a uniform cross-section and extend for a long distance in the third dimension. These long soil structures are generally characterised by spatially varying soil properties, i.e. soil heterogeneity. Slope stability failures of these structures may have significant economic and societal consequences. Thus, it is of particular interest for engineers to investigate the influence of soil spatial variability on the stability and failure mechanisms of long 'linear' structures. For example, earthen levee flood protection systems can be viewed as series systems, where failure at one location, or failure of one component, can result in catastrophic failure of the entire flood protection system and result in tragic loss of life, damage to fundamental infrastructure, and substantial economic impact to the immediate and surrounding regions. In order to ensure the desired level of flood protection system performance, standards in the Netherlands explicitly require probabilistic designs. For example, this may include the use of semi-analytical tools, such as Calle's 2.5D method and the 3D method of Vanmarcke. However, these (semi-) analytical models make certain simplifying assumptions; in particular, that of a finite length cylindrical failure mechanism.

The random finite element method (RFEM) has found increasing use for long engineered slopes in recent years, due to its conceptual simplicity to implement and its capability to comprehensively analyse the effects of soil spatial variability. As a simulation method, RFEM can be applied to large and complex systems, without the need to include some of the rigid idealisations and/or simplifications necessary for analytical solutions, resulting in more realistic models. Therefore, RFEM can be used as a comparative tool in investigating the performance of simpler methods. Its biggest disadvantage is that it tends to be computationally expensive.

The main body of this thesis is devoted to comparative studies (in terms of statistics of the realised factor of safety, the reliability and the failure consequences with respect to potential failure length and volume) of the three above models, for a range of spatial statistics of the soil shear strength. In particular, the relative performance of RFEM and Vanmarcke's model is investigated for a relatively short slope (of length 10 times the height) for which the length effect may be ignored. For horizontal scales of fluctuation that are large compared to the slope length, the two approaches give similar results, because most of the failure surfaces computed in the RFEM analyses are then approximately cylindrical and propagate along the entire length of the slope, thereby matching Vanmarcke's assumption and resulting failure length for this limiting condition. In contrast, for smaller values (i.e. less than the slope length), the two approaches can give significantly different results, with the RFEM response of the slope generally being much weaker than the Vanmarcke solution, apparently due to different predicted failure lengths and the influence of the cylinder ends in the simpler model.

A second comparative study using all three models involves the so-called length effect (i.e. the increase of the probability of failure as the total slope length increases) for

very long slopes (of length up to 100 times the height), using HPC strategies developed in this thesis. In contrast to the level crossing approach adopted in the two (semi-) analytical models, a simple power law equation was utilised with RFEM, which was validated based on the principles of probability of multiple independent (failure) events within the length of the slope. It is shown that RFEM predicts the smallest reliability indices for the range of cases considered. However, the solutions predicted by Vanmarcke's and Calle's models move closer to the RFEM results at larger horizontal scales of fluctuation. Discrete failure lengths have been quantified in RFEM and compared with predicted failure lengths using the simpler models, in order to provide a rational explanation for the differences observed. Moreover, the α factor used with Calle's model in Dutch practice was investigated thoroughly via random fields for various degrees of spatial variability, enabling a comprehensive evaluation of its influence.

While the unconditional RFEM is used as a baseline stochastic method to make the comparative studies, the conditional RFEM was implemented and applied in the last part of the thesis to two example geotechnical applications. The first example focuses on the efficient design of site investigation plans (i.e. optimum locations and sampling intensity) in a 3D soil deposit. A sampling efficiency index was defined and used as an indicator of the efficiency of a site's plan. A 'posterior' distribution of the structure performance, after taking account of the spatial distribution of all the measured CPT data, was derived and showed a significant reduction in the uncertainty compared to the 'prior' distribution of the structure response by using the unconditional simulation based on random field theory. An optimal sampling position for the excavation of a slope was identified, both for a single stage of site investigation and a two stage site investigation. Moreover, an optimal sampling distance of half the horizontal scale of fluctuation was identified when an exponential correlation function is used. The second example is devoted to cost-effective designs of an excavated 3D slope. For the problem analysed, a steeper slope was found to be sufficiently reliable (i.e. in line with Eurocode 7) when conditional random fields were used. This was in contrast to the finding of unconditional simulations, due to the greater uncertainty due to only making partial use of available measurement data. The potential benefit of a 3D conditional simulation in geotechnical cost-effective designs has therefore been highlighted.

SAMENVATTING

Rivier- en zeedijken en andere infrastructurele taluds hebben vaak een uniforme dwarsdoorsnede en zijn langgerekt in de richting haaks op deze doorsnede. Deze langgerekte taluds kennen over het algemeen ruimtelijke variatie van grondeigenschappen, ofwel heterogeniteit van de grond. Hellinginstabiliteit van deze taluds kan grote economische en sociale gevolgen hebben. Het is om die reden van bijzonder belang dat ingenieurs de invloed van ruimtelijke variabiliteit van de grond op de stabiliteit en bezwijkingsmechanismes van deze langgerekte werken onderzoeken. Een rivierdijk bijvoorbeeld, kan gezien worden als een aaneenschakeling van compartimenten, waarbij het bezwijken van één compartiment leidt tot het falen van de volledige waterkering, met mogelijk verlies van mensenlevens, beschadiging van cruciale infrastructuur en substantiële economische schade aan directe en aangrenzende regio's tot gevolg. Ten einde het gewenste niveau van waterkerende functie te kunnen garanderen, vereisen toetsingsnormen in Nederland probabilistische ontwerpmethodes. Mogelijke probabilistische ontwerpmethodes zijn Calle's 2.5D methode of de 3D methode van Vanmarcke. Deze (semi-)analytische methodes zijn echter gebaseerd op een aantal vereenvoudigende aannames, met name die van een cilindrisch bezwijkingsmechanisme van eindige lengte.

De random eindige elementen methode (RFEM) wordt de laatste jaren meer en meer gebruikt voor het doorrekenen van ontwerpen van langgerekte taluds vanwege de conceptueel eenvoudige implementatie en het vermogen de effecten van variabiliteit in de grond volledig in rekening te brengen. Als simulatiemethode kan RFEM toegepast worden op grote en gecompliceerde systemen, zonder de conceptuele vereenvoudigingen die nodig zijn voor analytische methodes. Dit resulteert in een realistischer model van het te analyseren systeem en zodanig kan RFEM gebruikt worden als referentie in het onderzoek naar de prestaties van eenvoudigere methoden. Het grootste nadeel is echter dat RFEM veel rekenkracht kan eisen.

De hoofdmoot van dit proefschrift is gewijd aan vergelijkingsstudies tussen de drie eerdergenoemde modellen, voor een reeks statistieken van de ruimtelijke verdeling van schuifsterkte van de grond. Deze vergelijkingsstudies zijn gedaan met betrekking op de statistische verdeling van de berekende veiligheidsfactoren, de betrouwbaarheid van de methode en de verdeling van bezwijkingslengte en –volume. Met name de onderlinge vergelijking tussen de prestaties van RFEM en het Vanmarcke model is onderzocht. Dit is gedaan voor relatief korte taluds (met een lengte-hoogte verhouding van 10), waarvoor het zogenaamde lengte-effect verwaarloosd kan worden. Deze methodes blijken vergelijkbare resultaten te geven voor horizontale correlatielengtes die groot zijn ten opzichte van de taludlengte, doordat de berekende glijvlakken in RFEM bij benadering cilindrisch zijn en daarbij de volledige lengte van het talud beslaan. Zodoende komen ze overeen met de aannames in de Vanmarcke methode. Voor kleinere correlatielengtes (kleiner dan de taludlengte) kunnen beide modellen sterk afwijkende resultaten geven, waarbij RFEM een veel zwakker gedrag voorspelt dan het Vanmarcke model. Dit blijkt

te verklaren door het verschil in bezwijkingslengte en de invloed van de einden van het cilindrisch schuiflichaam in het simpelere model.

Een tweede vergelijkende studie tussen de drie modellen gaat in op het zogenoemde lengte-effect (de toenemende kans op bezwijken bij een toenemende taludlengte) voor zeer lange taluds (tot 100 keer de taludhoogte). Hierbij wordt gebruik gemaakt van een HPC strategie, waarvan de ontwikkeling staat beschreven in dit proefschrift. In tegenstelling tot de 'level-crossing approach' die gebruikt wordt in de twee (semi-)analytische modellen, wordt voor RFEM een eenvoudige machtsvergelijking gebruikt. Deze machtsvergelijking is gevalideerd aan de hand van de waarschijnlijkheid meerdere onafhankelijke afschuivingen te vinden over de lengte van het talud. Simulaties tonen aan dat RFEM leidt tot de kleinste betrouwbaarheidsindices voor de reeks aan onderzochte cases. De resultaten van de Vanmarcke en Calle modellen blijken de resultaten van RFEM echter te benaderen voor grotere horizontale correlatielengtes. Discrete bezwijklengtes zijn bepaald in RFEM en vergeleken met de bezwijklengtes die voorspeld worden door de eenvoudigere modellen om zo een rationele verklaring te geven voor de waargenomen verschillen. Tevens is de α-factor zoals deze in Nederland in de praktijk gebruikt wordt voor Calle's model, grondig onderzocht met behulp van random velden voor een variatie aan karakteristieke waarden voor ruimtelijke variabiliteit. Dit maak een uitgebreide gevoeligheidsanalyse mogelijk.

Als referentie voor de stochastische methodes in de vergelijkingsstudies is ongeconditioneerde RFEM gebruikt. In het laatste deel van dit proefschrift is ook geconditioneerde RFEM geïmplementeerd. De geconditioneerde RFEM is vervolgens toegepast in twee voorbeelden van geotechnische problemen. Het eerste voorbeeld gaat in op het opzetten van een plan voor efficiënt bodemonderzoek (de optimalisatie van locatie en intensiteit van metingen) in een driedimensionaal grondvolume. Een efficiëntie-index voor individuele metingen is gedefinieerd en gebruikt als indicator voor de efficiëntie van het plan voor een verkennend bodemonderzoek. De vergelijking van de waarschijnlijkheidsverdeling van het taludgedrag met en zonder het conditioneren aan de hand van de sonderingsdata heeft een significante afname van onzekerheid als gevolg van conditioneren aangetoond. Een optimale plaatsing van veldmetingen voor het ontwerp van een talud is bepaald, voor verkennend bodemonderzoek bestaand uit zowel één als twee meetrondes. Tevens is, onder aanname van een exponentiele correlatiefunctie, de optimale meetdichtheid bepaald op een half keer de horizontale correlatielengte. Het tweede voorbeeld is gewijd aan het 3D modelleren van een ontgraven talud. In dit voorbeeld blijkt een steiler talud voldoende betrouwbaar te zijn (volgens Eurocode 7) wanneer geconditioneerde random fields worden gebruikt. Dit in tegenstelling tot ongeconditioneerde simulaties, waar de onzekerheid groter is ten opzichte van geconditioneerde simulaties door het niet optimaal benutten van beschikbare data. Hiermee is het mogelijke voordeel van het gebruik van geconditioneerde simulaties in een kosten-efficiënt geotechnisch ontwerp gedemonstreerd.

ACKNOWLEDGMENT

NOTATION LIST

This list defines acronyms and symbols used within the body of the thesis.

Acronyms

ARFEM auxiliary random finite element method

BLUE   best linear unbiased estimation

CR   centre of rotation

CIUC   consolidated isotropic undrained triaxial compression test

COV   coefficient of variation

CPT   cone penetration test

DMT   dilatometer test

DST   direct shear test

FE   finite element

FORM first order reliability method

FOSM first order second moment method

HPC   high performance computing

LAS   local average subdivision

LHS   left hand side

MC   Monte Carlo

MCS   Monte Carlo simulation

PDF   probability density function

QRA   quantitative risk assessment

RFEM random finite element method

RHS   right hand side

RSM   response surface method

RVE   representative volume element

SD   standard deviation

SOF   scale of fluctuation

SPT   standard penetration test

SRSM   stochastic response surface method

UC   unconfined compression test

UU   unconsolidated undrained triaxial compression test

VM   Vanmarcke

VST   vane shear test

Greek letters

α factor used in Calle's model, Chapter 5

β_{b_c} reliability index for critical failure length b_c, Chapters 4, 5

β reliability index, Chapters 2, 4; reliability index in 2D, Chapter 5

β_l reliability index considering the end effect, Chapter 5

β_b reliability index for failure length b, Chapter 5

β_{lc} reliability index considering length and end effects (or level crossing), Chapter 5

Δx 'effective horizontal' segment length along failure arc, Chapter 4

Δy lag distance between local averages s_b or s_1 in the slope length direction, Chapter 5

Δz lag distance in the vertical direction, Chapter 5

Δz_1 'effective vertical' segment length along failure arc near slope crest, Chapter 4

Δz_2 'effective vertical' segment length along failure arc near slope toe for a slope with a foundation layer, Chapter 4

δ 'characteristic distance', Chapter 4

δ_h horizontal correlation distance, Chapter 5

δ_v vertical correlation distance, Chapter 5

Δ_x, Δ_y interval distances between CPTs in the horizontal plane, Chapter 6

$\gamma(\boldsymbol{\tau})$ variogram, Chapter 6

$\gamma(T)$ variance function, Chapter 4

$\Gamma^2()$ variance reduction factor, Chapters 4, 5

$\boldsymbol{\gamma}_{lhs}$ left-hand-side matrix, Chapter 6

$\boldsymbol{\gamma}_{rhs}$ right-hand-side vector, Chapter 6

λ_i unknown weighting factor associated with observation point $\mathbf{x}_i$, Chapter 6

$\boldsymbol{\lambda}_q$ weights subvector for CPT$_q$, Chapter 6

$\boldsymbol{\lambda}_x$ weights vectors, Chapter 6

μ mean value of soil property, Chapter 2; Lagrangian parameter, Chapter 6

μ_i mean value of variable x_i, Chapter 2

$\boldsymbol{\mu}$ vector of mean values of variables, Chapter 2

∇F_s gradient vector storing derivatives of F with respect to s_i, Chapter 5

ν Poisson's ratio, Chapters 4, 5

∇_g gradient vector, Chapter 2

$\phi(\lambda_i, \mu)$ objective function, Chapter 6

Φ cumulative standard normal distribution function, Chapters 4, 5

ϕ friction angle, Chapter 2

$\hat{\rho}$ experimental correlation function, Chapter 6

ρ correlation coefficient, Chapter 2

$\rho()$ correlation function, Chapters 4, 5

ρ_b correlation function of local average variables, Chapter 5

ρ_F correlation function of averaged shear strength over cross-sections, Chapter 5

σ_e^2 variance of the Kriging error , Chapter 6

σ standard deviation of soil property, Chapter 2

σ_h^2 variance of the average values of individual boreholes, Appendix C

σ_i standard deviation of variable x_i, Chapter 2; standard deviation of the realised factor of safety for the conditional simulation based on column position i, Chapter 6

σ_t^2 total 'point' variance, Appendix C

σ_u standard deviation of the realised factor of safety for the unconditional simulation, Chapter 6

σ_v' effective vertical stress, Chapter 2

σ_v^2 average of the variances of different individual boreholes, Appendix C

$\hat{\sigma}_X^2$ estimated variance, Chapter 6

τ lag distance, Chapters 2, 4, 5

τ_1 lag distance in the vertical direction, Chapters 4, 5

τ_2, τ_3 lag distances in the lateral directions, Chapters 4, 5

θ scale of fluctuation, Chapters 2, 4, 5

θ_1 vertical SOF, Chapter 4

θ_2, θ_3 lateral SOF, Chapter 4

θ_e equivalent SOF, Chapter 4

θ_h horizontal scale of fluctuation, Chapters 2, 4, 5

θ_v vertical scale of fluctuation, Chapters 2, 4, 5

θ_{iso} isotropic scale of fluctuation, Chapter 3

v_{β_b} average number of excursions per unit length or mean (decay) rate of threshold level down-crossings, Chapter 5

ξ anisotropy of the heterogeneity, Chapters 4, 5

Latin letters

A coefficient matrix in LAS, Chapter 3

A cross-sectional area above the sliding arc, Chapters 4, 5

a spatial range, Chapter 2

B covariance matrix in LAS, Chapter 3

b failure length, Chapters 4, 5

b_c critical failure length, Chapters 4, 5

$\hat{C}$ experimental covariance function, Chapter 6

C covariance matrix, Chapter 2; coefficient matrix in LAS, Chapter 3

c cohesion, Chapter 2; factor defining the variance associated with the end resistance, Chapter 5

c_1, c_2 constants used in approximation of time spent in Kriging, Chapter 6

c_i soil cohesion, Chapter 2

CI compressibility index, Chapter 2

C covariance function, Eq. 3.6, Chapter 3

c_{00} variance of $Z(\mathbf{x}_0)$ estimated at the target location $\mathbf{x}_0$, Chapter 6

c_{i0} covariace between $Z(\mathbf{x}_i)$ and $Z(\mathbf{x}_0)$, Chapter 6

c_{ij} covariance between $Z(\mathbf{x}_i)$ and $Z(\mathbf{x}_j)$, Chapter 6

$[C]$ covariance matrix, Chapter 5

D domain size, Chapter 3

d horizontal distance from the centre of rotation to the centre of gravity of the rotating body, Chapter 4

d_0 factor representing the end effect, Chapter 4

d_c random cell size, Chapter 3

$d_{r,s}$ components of the submatrix $\mathbf{v}_{i,j}$, Chapter 6

d_t components of the subvector $\mathbf{v}_p$, Chapter 6

E elastic modulus, Chapters 4, 5

E_u approximation error, Chapter 6

E[]   expectation operator, Chapters 2, 6

$\bar{F}', \tilde{F}'$ mean and standard deviation of F', Chapter 5

$\bar{F}_b$ mean factor of safety for failure length b, Chapters 4, 5

$\bar{F}_l, \tilde{F}_l$ mean and standard deviation of F_l, Chapter 5

$\bar{F}_R$ mean realised factor of safety, Chapters 4, 5

$\bar{F}$ mean factor of safety for the plane strain condition, Chapter 4

$\bar{F}, \tilde{F}$ mean and standard deviation of factor of safety for plane strain condition, Chapter 5

$\bar{F}_{b_c}$ mean factor of safety for critical failure length b_c, Chapters 4, 5

$\tilde{F}_b$ standard deviation of factor of safety for failure length b, Chapters 4, 5

$\tilde{F}_R$ standard deviation of realised factor of safety, Chapters 4, 5

$\tilde{F}_{b_c}$ standard deviation of factor of safety for critical failure length b_c, Chapters 4, 5

F failure domain, i.e. $G(\mathbf{x}) \le 0$, Chapter 2; cross-sectional safety factor, Chapter 5

F' first order approximation of cross-sectional safety factor, Chapter 5

F^+, F^- value of F evaluated using strength parameter values equal to the mean plus or minus one standard deviation, Chapter 5

F_b factor of safety associated with failure length b, Chapters 4, 5

F_l factor of safety for finite failure of length l, Chapter 5

F_R realised factor of safety, Chapters 4, 5

F_T traditional factor of safety based on the mean property value, Chapter 5

F_{b_c} factor of safety for critical failure length b_c, Chapters 4, 5

FS factor of safety, Chapter 2

$\bar{G}', \tilde{G}'$ mean and standard deviation of G', Chapter 5

G limit state surface/function or performance function, Chapters 2, 5

g limit state surface/function or performance function, Chapter 2

G' approximate performance function, Chapters 2, 5

g_c critical value of limit state surface/function, Chapter 2

H slope height, Chapters 4, 5

i, j numbering subscripts; sampling column position, Chapter 6

I_{se} sampling efficiency index, Chapter 6

k number of rows in the x direction, Chapter 6

l expected length of a potentially unstable zone, Chapter 5

L slope length in the third dimension, Chapters 4, 5

l, m_i, n_i coefficients in the polynomial performance function, Chapter 2

L_a length of the assumed circular failure arc, Chapters 4, 5

L_A, L_B two slope lengths having the same statistical strength characteristics, Chapter 5

m factor used in FOSM and RSM, Chapter 2; number of CPT profiles within each row in the y direction, Chapter 6

M_e end resisting moment for one of the two end boundaries of the cylinder, Chapter 5

M_o overturning moment, Chapters 4, 5

M_r resisting moment, Chapters 4, 5

$M_{o,b}$ overturning moment for failure length b, Chapter 5

$M_{r,b}$ resisting moment for failure length b, Chapter 5

N SPT blow count value, Chapter 2; total number of Monte Carlo realisations, Chapters 4, 5; number of measurement locations, Chapter 6

n number of data points for each CPT profile, Chapter 6

N_β average number of excursions per unit length (or mean down-crossing rate), Chapter 5

n_f number of points in the field, Chapter 6

N_f number of realisations where slope failed (i.e. realised factor of safety is smaller than 1.0), Chapter 5

n_x, n_y, n_z number of points in the three Cartesian directions, Chapter 6

n_{cpt} number of CPTs in y direction, Chapter 6

$O(N^2)$ big O notation (the algorithm has order of N^2 time complexity for a problem of size Z), Chapter 6

$O(N^3)$ big O notation (the algorithm has order of N^3 time complexity for a problem of size Z), Chapter 6

P   vector of parent cells, Chapter 3

$P()$ probability of an event, Chapters 4, 5

p, q numbering subscripts, Chapter 6

P_F system probability of failure, Chapter 5

P_f probability of failure, Chapter 5

p_f probability of failure, Chapter 2

$p_f(b_c)$ probability of failure for critical failure length b_c, Chapters 4, 5

$P_f(L_A)$ probability of failure for a slope of length L_A, Chapter 5

P_o DMT lift-off pressure, Chapter 2

P_S system probability of survival (i.e. reliability), Chapter 5

P_i parent cell values in LAS, Chapter 3

P[]   probability of an event, Chapter 2

Q   vector of child cells, Chapter 3

q_c CPT tip resistance, Chapter 2

Q_j child cell values in LAS, Chapter 3

R	correlation matrix, Chapter 2; covariance matrix in LAS, Chapter 3
R	reliability in RFEM, Chapter 5
r	autocorrelation distance, Table 2.1, Chapter 2; radius of the failure arc, Chapters 4, 5
r'	'effective' lever arm length for the end faces, Chapter 5
r, s, t	numbering subscripts, Chapter 6
R, r	ellipse radius in FORM, Fig. 2.5, Chapter 2
R_e	contribution to the resisting moment from the end sections, Chapters 4, 5
$\bar{s}_b$	mean of s_b, Chapter 4
$\bar{s}$	mean undrained shear strength, Chapters 4, 5
$\bar{\mathbf{s}}$	vector of the means of n random variables, Chapter 5
S	covariance matrix in LAS, Chapter 3
s	vector of n random variables (i.e. undrained shear strength), Chapter 5
$\tilde{s}$	standard deviation of undrained shear strength, Chapters 4, 5
$\tilde{s}_h^2$	variance of the average strength values of individual boreholes, Chapter 5
$\tilde{s}_v^2$	average of the strength variances of different individual boreholes, Chapter 5
s	undrained shear strength, Chapters 4, 5
s_1	average shear strength over unit length, Chapters 4, 5
s_b	average shear strength over length b, Chapters 4, 5
S_p	state parameter, Chapter 2
s_u	undrained shear strength, Chapter 2
T	averaging interval, Chapter 4
$t(N, n_f)$	total time spent in Kriging, Chapter 6
U	standardised random variable, Chapters 4, 5
u	uncertainty reduction ratio, Chapter 6
u_a	uncertainty reduction ratio when all CPT profiles have been used, Chapter 6
u_n	uncertainty reduction ratio when using a neighbourhood, Chapter 6
V	coefficient of variation of soil properties, Chapter 2

V_F coefficient of variation of the plane strain factor of safety, Chapter 5

V_s coefficient of variation of the 'point' shear strength, Chapters 4, 5

V_{M_r} coefficient of variation of the plane strain resisting moment, Chapter 5

V_{s_1} coefficient of variation of the average strength over the failure surface with a unit length, Chapters 4, 5

$\mathbf{v}_{i,j}$ matrix representing the correlation structure between CPT_i and CPT_j, Chapter 6

$\mathbf{v}_p$ vector representing the correlation structure between the estimation point and CPT_p, Chapter 6

var[]   variance operator, Chapter 6

W weight per unit length of the material located above the sliding surface, Chapter 4

$\mathbf{x}$ vector representing the set of random variables, Chapter 2; location point in space, Chapter 6

$\mathbf{x}^N$ standardised or reduced $\mathbf{x}$, Chapter 2

x out-of-slope-face direction, Chapters 4, 5

x_i, X_i random variable, Chapter 2

x_i^N component of $\mathbf{x}^N$, Chapter 2

y slope length direction, Chapters 4, 5

y_o centre position of the failure surface, Chapter 5

$\hat{Z}(\mathbf{x}_0)$ best linear unbiased estimation (BLUE) of the soil property at location $\mathbf{x}_0$, Chapter 6

z slope height direction, Chapter 5

Z soil properties, Chapter 6

$Z_1, Z_2, \ldots, Z_N$ observations of the random field $Z(\mathbf{x})$ at points $\mathbf{x}_1, \mathbf{x}_2, \ldots, \mathbf{x}_N$, Chapter 6

Z_i equal to $Z(\mathbf{x}_i)$ $(i = 1, 2, \ldots, N)$, Chapter 6

$Z_{km}(\mathbf{x})$ Kriged field based on measured values at $\mathbf{x}_i (i = 1, 2, \ldots, N)$, Chapter 6

$Z_{ks}(\mathbf{x})$ Kriged field based on unconditionally (or randomly) simulated values at sampling positions $\mathbf{x}_i (i = 1, 2, \ldots, N)$, Chapter 6

$Z_{rc}(\mathbf{x})$ conditionally simulated random field, Chapter 6

$Z_{ru}(\mathbf{x})$ unconditional random field, Chapter 6

LIST OF FIGURES

LIST OF TABLES

183

CURRICULUM VITÆ

Yajun LI (李亚军)

07-02-1987   Born in Shanxi, China.

EDUCATION

2005–2009   Undergraduate in Agricultural Hydraulic Engineering
College of Water Resources and Architectural Engineering
Northwest A&F University
Yangling, Shaanxi, China

2009–2011   Postgraduate in Hydraulic Structure Engineering
Department of Water Conservancy and Hydropower Engineering
Hohai University
Nanjing, Jiangsu, China

2011–2016   PhD in Geotechnics
Geo-Engineering Section
Department of Geoscience and Engineering
Faculty of Civil Engineering and Geosciences
Delft University of Technology
Delft, the Netherlands
Thesis: Reliability of Long Heterogeneous Slopes in 3D:
Model Performance and Conditional Simulation
Promotor: Prof. dr. M. A. Hicks

2016   PostDoc researcher
Geo-Engineering Section
Department of Geoscience and Engineering
Faculty of Civil Engineering and Geosciences
Delft University of Technology
Delft, the Netherlands
Project: Technical Feasibility of a Dutch Radioactive
Waste Repository in Boom Clay (OPERA)
Supervisors: Dr. P. J. Vardon, Prof. dr. M. A. Hicks

LIST OF PUBLICATIONS

JOURNAL PUBLICATIONS

3. **Y. Li**, M.A. Hicks, J.D. Nuttall. *Comparative analyses of slope reliability in 3D*, Engineering Geology **196**, 12–23 (2015).

2. **Y. Li**, M.A. Hicks, P.J. Vardon. *Uncertainty reduction and sampling efficiency in slope designs using 3D conditional random fields*, Computers and Geotechnics **79**, 159–172 (2016).

1. **Y. Li**, M.A. Hicks. *Influence of length effect on embankment slope reliability in 3D*, Submitted for publication (2016).

CONFERENCE PUBLICATIONS

7. **Y. Li**, P.J. Vardon, M.A. Hicks. *Probabilistic performance assessment of a deep tunnel for a radioactive waste repository in French COx claystone*, Proceedings of the 2nd Petrus-OPERA PhD and Early Stage Researcher Conference, p. 61–63 (2016). Delft, the Netherlands.

6. P.J. Vardon, J. Yuan, M.A. Hicks, **Y. Li**. *Initial plug and seal design for the Dutch repository concept*, Dopas (full scale demonstration of plugs and seals) Seminar, Session 4 (2016). Turku, Finland.

5. **Y. Li**, M.A. Hicks, P.J. Vardon. *Three dimensional discrete failures in long heterogeneous slopes*, Proceedings of the 5th International Symposium on Geotechnical Safety and Risk (ISGSR5), p. 666–670 (2015). Rotterdam, the Netherlands.

4. A.B. Lundberg, **Y. Li**. *Probabilistic characterization of a soft Scandinavian clay supporting a light quay structure*, Proceedings of the 5th International Symposium on Geotechnical Safety and Risk (ISGSR5), p. 170–175 (2015). Rotterdam, the Netherlands.

3. **Y. Li**, M.A. Hicks, P.J. Vardon. *High performance computing strategies for nonlinear finite element analysis of long heterogeneous soil slopes*, Proceedings of the 23rd UK Conference of the Association for Computational Mechanics in Engineering (ACME), p. 427–430 (2015). Swansea, UK.

2. **Y. Li**, M.A. Hicks. *Comparative study of embankment reliability in three dimensions*, Proceedings of the 8th European Conference on Numerical Methods in Geotechnical Engineering (NUMGE), p. 467–472 (2014). Delft, the Netherlands.

1. **Y. Li**, M.A. Hicks, J.D. Nuttall. *Probabilistic analysis of a benchmark problem for slope stability in 3D*, Proceedings of the 3rd International Symposium on Computational Geomechanics (ComGeo III), p. 641–648 (2013). Krakow, Poland.